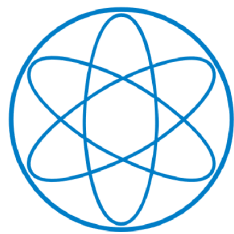# Geometric Perturbation Theory: Internally Coupled Ears, Tsunamis, and Organ Pipes

David Heider

München, Januar 2019

Physik Department

Lehrstuhl für theoretische Biophysik T35

Geometric Perturbation Theory: Internally Coupled Ears, Tsunamis, and Organ Pipes

David (Thomas) Heider

Vollständiger Abdruck der von der Fakultät für Physik der Technischen Universität München zur Erlangung des akademischen Grades eines

Doktors der Naturwissenschaften (Dr. rer. nat.)

genehmigten Dissertation

Vorsitzender:	Prof. Dr. Matthias Rief
Prüfer der Dissertation:	1. Prof. Dr. J. Leo van Hemmen
	2. Prof. Dr. Folkmar Bornemann

Contents

List of Figures

Acknowledgement

Abstract

This doctoral thesis investigates physical causes and consequences of geometric perturbations by three case studies embedded in the field of continuum mechanics.

The model of internally coupled ears consists of two membranes coupled through a cylindrical acoustic duct. In the model, the membranes' displacement is a response to the pressure difference between the inner and outer membrane surface. The equations of motion for the internal pressure and the membrane displacements are formulated exactly in the language of analysis on manifolds. The widely used stationary domain approximation for the pressure field is derived explicitly. Picard iteration allows the decoupling of the reduced problem's governing equations as well as an assessment of the accuracy of Vedurmudi et al.'s piston approximation which gained popularity in auditory research.

In the context of tsunamis, the tsunami-induced perturbation of the underwater velocity field triggers the formation of a turbulent layer of vorticity directly above the surface of the continental plate. The vortex-plate surface interaction generates a small transverse dislocation of the plate surface from its equilibrium position. Calculations of arrival time differences and sound pressure level equivalents indicate that seismic tsunami detection in elephants is not only possible but also in reasonable agreement with experimental results.

Last, the end-correction in open-ended organ pipes is derived from the combined experimental and theoretical assessment of vortex phenomena at the pipe's open end and interpreted from a hydrodynamic perspective. A stochastic model for the onset of turbulence in the geometric jet disturbance, that a jet exiting the windway is subject to, yields a broadband frequency distribution. From the latter, the pipe's resonance body selects its resonance frequencies which generate the characteristic power spectrum for a given organ pipe.

Zusammenfassung

Ziel dieser Doktorarbeit ist die Untersuchung physikalischer Ursachen und Folgen geometrischer Störung in drei dem Gebiet der Kontinuumsmechanik zuzurechnenden Fallstudien.

Das Modell der Intern Gekoppelten Ohren besteht aus zwei, über einen zylindrischen Hohlraum gekoppelten Membranen, die auf die Druckdifferenz zwischen Innen- und Außenseite durch Auslenkung aus ihrer jeweiligen Gleichgewichtslage antworten. Mittels einer Beschreibung in der Sprache der Analysis auf Mannigfaltigkeiten werden die Modellgleichungen für den Innendruck und die Membranauslenkungen exakt formuliert und die vielfach verwendete Approximation eines stationären, statt zeitabhängigen, akustischen Hohlraums hergeleitet. Picard-Iteration erlaubt die Entkopplung der Modellgleichungen sowie eine Untersuchung der Güte der Kolbenapproximation von Vedurmudi et al..

Im Kontext der Tsunamis führt die Störung des Unterwassergeschwindigkeitsfeldes zu einer turbulenten Wirbelregion direkt oberhalb der Kontinentalplatte. Die Wechselwirkung zwischen Wirbel und Plattenoberfläche erzeugt eine kleine transversale Auslenkung der Plattenoberfläche aus der Gleichgewichtslage. Berechnungen von Ankunftszeitdifferenzen und seismischen Schallpegeläquivalenten zeigen, dass die Tsunamiortung durch Detektion geometrischer Störungen theoretisch möglich ist und mit experimentellen Befunden zum Verhalten von Elefanten vor Ankunft des Tsunamis in Einklang steht.

Ausgehend von sowohl experimentellen als auch theoretischen Untersuchungen von Wirbelphänomenen am offenen Ende der Labialorgelpfeife wird die Endkorrektur für die Pfeifenlänge hergeleitet und hydrodynamischen interpretiert. Ein stochastisches Modell für die Turbulenzentwicklung des aus der Kernspalte austretenden Jets liefert eine breitbandige Frequenzverteilung. Aus dieser filtert der Pfeifenkörper die Resonanzfrequenzen, die das für eine gegebene Orgelpfeife charakteristische Spektrum definieren.

Chapter 1

Introduction

Continuum physics is no canonical part of the physics curriculum. Yet, its governing equations provide the language templates upon which the models in the subsequent chapters build.

After a short presentation of the individual three projects that form the body of the thesis, a selection of topics in continuum physics is presented. The starting point is Euler's first axiom, $d_t\mathbf{p} = \mathbf{F}_{\mathrm{body}}$ [86], which states the change in total momentum of continuous body equates to the sum of all forces, body or surface ones, it experiences. Through the continuum assumption, Euler's first axiom gives rise to the local momentum balance law. The latter is supplemented by a, typically linear, material model for the stress tensor storing information about surface forces in the mechanical continuum [72, 71].

Upon appropriate modeling, the Navier-Stokes equations of hydrodynamics [71] and the Cauchy-Navier equations of elastodynamics [86] follow. Together with the closely related membrane theory [142, 139, 138] and the theories of acoustics [72, 131], they and appropriate special cases to-be-discussed serve as the equations of motion for the mechanical key notions that underlie the concrete modeling presented in later chapters.

1.1   Thesis overview

Organization of the thesis   The thesis comprises three different projects connected through the general theme that they all are cases studies regarding "Geometric perturbation theory". For each project, a short manuscript has been prepared that constitutes a chapter of the thesis' main body.

Some additional comments and more elaborate derivations that would exceed typical threshold page limitations for journal publications, $\approx$ 12 pages, have been condensed into appendices accompanying the three main chapters. By outsourcing some of the lengthier, but still insightful derivations to appendices, the author hopes to shepherd the reader as quickly as possible to the main results and make the thesis self-contained.

The remainder of this section shall introduce the individual projects and questions underlying their design.

Chapter two: Project "Geometric perturbation theory"   Originally inspired from the model of internally coupled ears [157, 158, 145, 147, 148, 146], the project investigates the dynamics of partial differential equations coupled through acoustic boundary conditions [8, 7]: Suppose one has a, for the sake of concreteness, cylindrical cavity. The endcaps of the cylinder are supposed to be locally reacting surfaces. As long as the system is at rest, it maintains its cylindrical shape.

As soon as the system is stimulated, say by an externally impinging acoustic pressure, the locally reacting surfaces exhibit a motion coupled through the cavity. The geometrically interesting question concerns the evolution of the cavity, and the pressure wave it hosts, after external stimulus exposition. Based on the no-penetration conditions [86, 71], the motion of the locally reacting surfaces is coupled to the pressure inside the cavity and through a pressure difference receiver source term [5, 6, 141], the motion of the locally reacting surface is coupled to the cavity's internal pressure.

While decoupling techniques for linear partial differential equations are available (see e.g. perturbation theory as described in [60]), they are confined to partial differential equations defined on joint domains. However, this is not the case for the problem under consideration. Even more so, by conservation of mass inside the cavity, the formation of a pressure wave is due to a local change in volume, thus in local mass density and ultimately in pressure. Although the equations of motion for the locally reacting surfaces live on a stationary domain, the domain of the wave equation is, strictly speaking, a cylinder undergoing small undulations or "perturbations". These impacts are un-arguably small but absent in the acoustics literature.

Therefore, we rephrase the question on how the acoustic pressure wave inside the cavity behaves like mathematically in the language of analysis on manifolds [68, 96] and use the notion of a fiber bundle to obtain an explicit expression for the impacts of the cavity's undulations on the acoustic wave equation. The smallness of undulation

amplitudes finally leads to re-establishing the - correct - formulation of vibrational acoustics problems through Beale's acoustic boundary conditions where all mechanical fields live on exclusively stationary domains.

Putting semi-group techniques from mathematics [144, 24, 25] into practice, a de-coupling strategy for the model equations results. Through algebraic operator calculus, an iteration in a very physical parameter, the mass-per-volume density ratio of fluid in the cavity and the wall solid, results. See [83, 84] for a similar definition of a smallness parameter.

To gratify academic playfulness, snapshots of the undulating three-dimensional cavity are presented as well.

Chapter three: Project "Tsunami localization" Unlike humans, elephants are seemingly capable of foreseeing, or better fore-sensing, tsunamis [66, 65]. One key difference between the sensual system of humans and elephants lies in the employment of seismic sensing, see [103, 97]: A human can hear sound generated by vibrations of the ground but typically does not sense the vibrations themselves. In some sense, one may regard an elephant as a tuning fork, placed on the continental plate, that detects seismic vibrations of the continental plate [125, 92, 55].

Physically, tsunamis are perturbations of the velocity field of the ocean water due to a seismic event such as a seaquake or a landslide on the continental margin [87]. Thus, one may arrive at the hasty conclusion that the seismic event generates a cue that the elephant detects, see [54] for a similar view.

Unfortunately, the explanation has some drawbacks: First, seismic waves propagate at $\sim$ km s^{-1} whereas tsunamis need hours to arrive at the shoreline. But elephants do not take flight until a couple of minutes before the tsunami strikes the shoreline [159]. Second, reports of both, scientific [159, 105, 64] and everyday-observation quality (note [160] on this issue), describe that elephants' arousal increased over time.

If the tsunami-generating event takes place at one isolated spot in time, does the elephant have the capability of performing a calculation to estimate when the tsunami ultimately arrives at the shoreline? Most likely, no.

Instead of focusing on the seismic event, the tsunami's seismic impacts deserve more attention. The perturbation of the ocean water's velocity leads to the formation of a small turbulent layer close to the seafloor. In the boundary layer, a region of vorticity forms that functions as a an acoustic dipole source for underwater sound [119, 120, 90,

91]. Since the region of vorticity is situated almost directly on the continental plate - ocean water interface, it can also exert a force on the surface of the continental plate similar to the vortex force [127] used in Howe's vortex acoustics [69].

Metaphorically, the vorticity region impacts the surface of the continental plate as a vast region of small hammers knocking on the plate's surface. For a similar idea applied to the coupling between air and the continental plate's vibrations, see [121].

Via bounds from above by the tsunami's frequency and from below by turbulence estimates, the frequencies can be shown to be (a) in the infrasound range characteristic for natural hazards and (b) be out of human hearing range [131] but in the hearing range of elephants [103]. Using a linear depth profile, we calculate the arrival time differences [54] between tsunami and seismic wave generated by the turbulent vorticity.

It agrees reasonably with the available experimental data. In the scenario, that elephants' feet have an impedance matching function [104] as conjectured by biologists, the sound pressure level equivalent of the signal that arrives at the elephant allows a comparison of how "loud" an equivalent acoustic signal would be for human, see [104, 102, 109, 106, 59, 4, 107, 108, 110, 105, 64] just to name a few prominent references using this method as well. At maximum, the elephant senses the tsunami as a human hears the traffic sound at a big street.

Chapter four: Project "Organ pipes"   Chapter four presents results on a larger and cross-disciplinary research project on the open-ended organ pipe. The organ pipe has originally been modeled by Helmholtz [156] and later also by Rayleigh at the end of the 19th and beginning of the 20th century [133].

For the musical properties of organ pipes, the acoustic wave equation on an axi-symmetric cylindrical cavity, of a given length and with Neumann boundary conditions, is a sensible zeroth-order approximation [156, 47, 28]. At the bottom of the resonant cavity, Neumann boundary conditions are plausible as the bottom endcap is a hard wall which does not undergo significant vibrations caused by a pressure wave of reasonable sound pressure level.

At the open-end, a justification of Neumann boundary conditions seemingly was akin to "It works there reasonably well!". Although it had already been known in Rayleigh's time that acoustically speaking, the pipe systematically sounds "longer" than it physically is [133], it took until the middle of 20th century until J. Schwinger and H. Levine [88] derived the end-correction $\delta_e \cdot R = 0.61 \cdot R$ which was corrected by

Howe [70] and Ando [2] numerically. An attempt dating back to the 1860s is mentioned in [1] and can be found in [27]. The cumbersome derivation is based on the Wiener-Hopf technique to solve partial differential equations in semi-infinite geometries.

The first part of chapter four focuses on obtaining a value for the end-correction based on a physical method that allows generalization to other setups. At the pipe's open end, *Bernhardt Edskes* observed during cleaning an organ pipe that a gold particle was moving along the open end circle when the pipe was under play. The motion along a circular line can be explained by the presence of (at least) one vortex ring centered around the open end.

A preliminary experiment in Wageningen hinted at the existence of even two vortex rings, one at the inner and the other one at the outer edge of the pipe's open end. The thesis contributes a physical derivation of the double vortex ring based on an actual definition of the acoustic volume inside the pipe's resonance body and an experimental test confirming the existence of the vortex structure as predicted by theory.

Furthermore, a numerical simulation of the potential flow field shows that the symmetric double vortex ring structure gives rise to a so-called sphere of separation: It encloses a spherical volume that lies inside the resonance body and outside in equal parts. In the ideal case of no background flow in the pipe, the total volume enclosed in the hemisphere on top of the pipe allows the definition of a cylindrical end-correction $2/3 \cdot R \approx 0.67 \cdot R$. Up to $\lesssim 10\,\%$ relative error with respect to Levine and Schwinger's $0.61 \cdot R$ [88, 70], this is the end-correction derived from a boundary phenomenon at the open-end of the pipe.

The second part of the organ pipe project intends to better understand the sound production [31, 32, 36, 35, 38, 150, 153, 151, 152, 44, 45, 46] in organ pipe's. As also in other flue-like instruments, the responsible process is that a stream of air, a so-called jet [44, 153], hits a sharp obstacle, the upper labial lip. The latter destroys the jet structure but has been shown to be responsible for the production of sound [119, 19].

From a theoretical perspective, the data to explain is the power spectrum of the pipe measured either slightly above the open end of the pipe or in the vicinity of the organ pipe's mouth, see [3] for many examples. In either case, one observes the presence of several peaks at the resonance frequencies of the cavity, subject to several corrections such as damping effects and wall losses [28] as well the end- [47, 88] and mouth-correction [47, 74], to name the most important causes of deviations from the ideal theory.

Even today, the height of the measured peaks in the power spectrum as well as the fact, that the fundamental frequency and higher harmonics are excited, is bewildering. Seemingly, the sound production mechanism is universal so as to the pipe filters out only its preferred frequencies from a broadband acoustic signal. The second part of the chapter on organ pipes contributes a phenomenological turbulence model inspired by [98, 100, 82, 81] that predicts the existence of multiple peaks and allows the systematic definition of a fit function to reproduce theoretically the measured power spectrum. In contrast to other approaches, the data, gathered in collaboration with *Bernhardt Edskes* and *Bernhard Seeber* and used for the analysis, had been taken at a sound-pressure level such that nonlinear processes [12] in the pipe's resonance body could be excluded.

In combination, the two theoretical models, one for the vortex phenomena at the open end and the sound production mechanism in the pipe, give a *linear* explanation based on physical insight rather than algebraic brute-force computation.

Greatest common divisor   What does connect the three projects? All of them feature a small effect at the geometric boundary of the model's geometry, that is, geometric perturbations.

For the first project, the small geometric effect is a perturbation of a cylindrical cavity from equilibrium. The geometric perturbation of the second project is the elastic displacement of the surface of the continental plate which finally generates the seismic signal to be sensed by elephants as a tsunami precursor signal. In the third project, the perturbation from the ideal organ pipe is given by the existence of a vortex structure *at the open end of the pipe* that leads, via the sphere of separation, to a correction of the effective acoustic volume of the pipe, that is, makes the pipe sound longer than it is solely on geometric grounds.

1.2   General continuum mechanics

The starting point is Newton's second law which states that the temporal change in momentum equates to the total force $\mathbf{F}_{\text{tot}}$, $d_t\mathbf{p} = \mathbf{F}_{\text{tot}}$. The object $\mathbf{F}_{\text{tot}}$ is called force and, in the continuum case, consists of two contributions.

First, the are surface forces [72] acting on the surface ∂V of a control volume V moving at the same local speed as the continuum's constituent mass particles. The body forces are represented by a vector-valued quantity $\mathbf{f}$ storing the force per volume

applied to the mechanical continuum under consideration.

Second, there are body forces that act on each point of the control volume. The surfaces forces are modeled by a rank 2 tensor field, the so-called *stress tensor* [71] defined throughout the continuum: It can be defined through $dF_i = \sigma_{ij}dA_j$ in a small cubic parcel with Einstein summation over repeated indices implied. The stress tensor $\boldsymbol{\sigma} = (\sigma_{ij})_{1 \leq i \leq j}$ captures the force exerted in i-direction upon changing a surface with normal vector in j direction by dA_j.

Newton's second law takes a differential formulation:

$$\frac{d}{dt} \int_V dV \, \rho \mathbf{v} = \int_{\partial V} \langle d\mathbf{S}, \boldsymbol{\sigma} \rangle_{\mathbb{R}^3} + \int_V dV \, \mathbf{f} \tag{1.1}$$

in which $\rho = \rho(t, \mathbf{x})$ denotes the mass-per-volume density of the medium and $\mathbf{v} = \mathbf{v}(t, \mathbf{x})$ is the velocity of the constituent particles at a physical point $\mathbf{x}$ at time t.

The right-hand side of (1.1) features the stress tensor $\boldsymbol{\sigma}$ in a Euclidean product understood so as to produce the exerted force. The left-hand side can be massaged in a better form using Reynold's transport theorem [126] for volumes.

Since a particle is characterized by a momentum and a position in phase space, the total derivative with respect to time for the velocity of the continuum's constituents features an additional contribution. Denoting the total derivative with respect to time by D/Dt, the acceleration $\mathbf{a} = \mathbf{a}(t, \mathbf{x})$ satisfies [71]

$$\mathbf{a} \equiv \frac{D\mathbf{v}}{Dt} = \partial_t \mathbf{v} + \langle d_t \mathbf{x}, \nabla \rangle_{\mathbb{R}^3} \mathbf{v} = \partial_t \mathbf{v} + \langle \mathbf{v}, \nabla \rangle_{\mathbb{R}^3} \mathbf{v}. \tag{1.2}$$

As short-hand notation, $D_t \equiv D/Dt = \partial_t + (\mathbf{v} \cdot \nabla)$. The differential operator D/Dt is called *material derivative*.

Next, the Reynold's transport theorem states that the time derivative for the co-moving control volume can be pulled inside the integral and becomes the material derivative operator acting on the product of the function inside the integral and the infinitesimal, but, since co-moving, also time-dependent, volume element dV.

$$\frac{d}{dt} \int_V dV \, \rho \mathbf{v} = \int_V \left(dV \cdot \frac{D(\rho \mathbf{v})}{Dt} + \frac{D(dV)}{Dt} \cdot (\rho \mathbf{v}) \right) \tag{1.3}$$

$$= \int_V dV \left(\frac{D(\rho \mathbf{v})}{Dt} + (\nabla \cdot \mathbf{v}) \rho \mathbf{v} \right) \tag{1.4}$$

Inside the volume, we have conservation of mass at each point. A corresponding local balance law is termed continuity equation of mass. Let us take a fixed, stationary

volume V' with stationary boundary $\partial V'$. Clearly, the change in mass in V' equates to the net mass flux through $\partial V'$,

$$\frac{d}{dt} \int_{V'} dV' \, \rho = - \int_{\partial V'} \langle d\mathbf{S}', \mathbf{j}_{\text{mass}} \rangle_{\mathbb{R}^3} \,. \tag{1.5}$$

Since V' is fixed, the total time derivative outside the integral simply becomes the partial derivative upon commutation with the volume integral.

Gauss' theorem of integration can be applied, taking suitable regularity properties of V' and the mass per surface area $\mathbf{j}_{\text{mass}} = \rho \mathbf{v}$ for granted. The minus sign on the right-hand side is a result of specifying the orientation for $\partial V'$ through the outward unit normal such that a mass flux from V' to $V'^{\complement}$ results in a mass loss inside V'.

The above equation is readily re-arranged to yield:

$$\int_{V'} dV' \left(\frac{\partial \rho}{\partial t} + \nabla(\rho \mathbf{v}) \right) = 0. \tag{1.6}$$

By arbitrariness of V', $\partial_t \rho + \nabla(\rho \mathbf{v}) = D_t \rho + \rho \nabla \mathbf{v} = 0$ everywhere, particularly, in the co-moving V. The product rule of differentiation and the definition of the material derivative D_t have been utilized in the second step.

Using $D_t \rho = -\rho \nabla \mathbf{v}$ in (1.4), the product rule of vector calculus yields

$$\frac{d}{dt} \int_V dV \, \rho \mathbf{v} = \int_V dV \, \rho D_t \mathbf{v}. \tag{1.7}$$

The right-hand side of Newton's second law in differential formulation (1.1) is processed by application of Gauss' theorem to convert the surface integral into a volume integral. In doing so, $\boldsymbol{\sigma} = \boldsymbol{\sigma}_i \hat{e}_i$ is used with vector valued coefficients $\boldsymbol{\sigma}_i$. Linearity of the surface integral operator allows to apply Gauss' theorem as usual to the components $\boldsymbol{\sigma}_i$ for $1 \leq i \leq 3$ then.

Then

$$\int_{\partial V} \langle d\mathbf{S}, \boldsymbol{\sigma} \rangle_{\mathbb{R}^3} + \int_V dV \, \mathbf{f} = \int_V dV \, (\nabla \boldsymbol{\sigma} + \mathbf{f}) \,. \tag{1.8}$$

Insertion of (1.7) and (1.8) into (1.1) yields:

$$\int_V dV \, (\rho D_t \mathbf{v} - \nabla \boldsymbol{\sigma} + \mathbf{f}) = \mathbf{0} \tag{1.9}$$

or, by arbitrariness of V and definition of the material derivative,

$$\rho \partial_t \mathbf{v} + \rho (\mathbf{v} \cdot \nabla) \mathbf{v} = \nabla \boldsymbol{\sigma} + \mathbf{f}. \tag{1.10}$$

This is the sought-after balance equation for momentum from which the continuum mechanical theories of fluid dynamics [71] and elasticity [86, 62] as well as simplifications such as acoustics [72, 12] are recovered. The only ingredients we still have to add is a model for the stress tensor $\boldsymbol{\sigma}$ and another model for the force density $\mathbf{f}$.

Such models are the subject of the next two paragraphs: The case of elastic waves in solids is treated as a special case of (1.10) first. Gaseous and liquid media, known under the common notion "fluids" in physics, is covered afterwards.

1.3 Elastodynamics and membranes

Elastodynamics Microscopically, a solid is built up from atoms and molecules sitting at fixed positions in a fixed volume [86]. Focusing on the classical physics side, this defines an equilibrium coordinate system. We use the notation $\mathbf{x} = (x_1, x_2, x_3)$ to refer to a mass parcel, a continuum physical building block of the solid, that is at equilibrium in $\mathbf{x}$.

Let us perturb the constituents by a small but classical length $\mathbf{u} = \mathbf{u}(t, \mathbf{x})$ from the equilibrium $\mathbf{x}$. In the solid, $\mathbf{x}$ is independent of time, such that $\mathbf{v}(t, \mathbf{x}) = \partial_t \mathbf{u}(t, \mathbf{x})$. The smallness requirement of the perturbation from spatial equilibrium permits the neglection of the nonlinear contribution $(\mathbf{v} \cdot \nabla)\mathbf{v}$ against the contributions linear in $\mathbf{v}$ in (1.10). We find

$$\rho \partial_t^2 \mathbf{u} = \nabla \boldsymbol{\sigma} + \mathbf{f}. \tag{1.11}$$

Next, we assume homogeneity and isotropy of the medium. By homogeneity, ρ becomes a constant mass per volume density. Under the additional restriction to elastic deformations only, Hooke's law can be used to relate $\boldsymbol{\sigma}$ to the linear *strain tensor*, $\boldsymbol{\epsilon} = (\epsilon_{ij})_{i,j}$:

$$\epsilon_{ij} = \frac{1}{2}\left(\frac{\partial u_i}{\partial x_j} + \frac{\partial x_j}{\partial x_i}\right). \tag{1.12}$$

The assumption of isotropy settles $\boldsymbol{\sigma}$ to be symmetric [86]. By smallness of the perturbation $\mathbf{u}$, we can confine the further treatment to linear contributions. Assuming an (external) pressure p acting as a surface force density in the solid volume,

$$\sigma_{ij} = -p\delta_{ij} + \Lambda_{ij;kl}\epsilon_{kl} \tag{1.13}$$

where δ_{ij} is the Kronecker symbol and $\Lambda_{ij;kl}$ is the Hooke matrix.

Isotropy and homogeneity settle the number of, at most $3^4 = 81$ independent components, to be just 2, the *Lamé constants* λ, μ, [62].

$$\sigma_{ij} = -p\delta_{ij} + \mu(\partial_i u_j + \partial_j u_i) + \lambda(\partial_k u_k)\delta_{ij} \tag{1.14}$$

The stress tensor $\boldsymbol{\sigma}$ defined that way is called *Cauchy-Navier stress tensor*, cf. [86].

Insertion of (1.14) into (1.11) yields

$$\rho\partial_t^2 \mathbf{u}(t,\mathbf{x}) = (\lambda + 2\mu)\nabla(\nabla \cdot \mathbf{u})(t,\mathbf{x}) - \mu\nabla \times \nabla \times \mathbf{u}(t,\mathbf{x}) = -\nabla p + \mathbf{f}. \tag{1.15}$$

In the absence of p and $\mathbf{f}$, the equation becomes

$$\partial_t^2 \mathbf{u} = c_p^2 \nabla(\nabla \mathbf{u}) - c_s^2 \nabla \times \nabla \times \mathbf{u}. \tag{1.16}$$

The objects $c_p^2 = (\lambda + 2\mu)/\rho$ and $c_s^2 = \mu/\rho$ define the squares of the phase velocity of primary and secondary elastic waves.

Up to a harmonic function, we can decompose $\mathbf{u} = \mathbf{u}_p + \mathbf{u}_s$ such that $\mathbf{u}_p$, the primary wave, has zero rotation, $\nabla \times \mathbf{u}_p = \mathbf{0}$, and the secondary wave, $\mathbf{u}_s$, has zero divergence, $\nabla \cdot \mathbf{u}_s = 0$.

The decomposition gives rise to two separate wave equations: Denoting by $\Delta_v = \nabla^2 = \nabla(\nabla\cdot) - \nabla \times \nabla\times$ the vector Laplace operator, the insertion yields

$$\partial_t^2 \mathbf{u}_p = c_p^2 \Delta_v \mathbf{u}_p \text{ and } \partial_t^2 \mathbf{u}_s = c_s^2 \Delta_v \mathbf{u}_s. \tag{1.17}$$

The first one describes a longitudinal wave, a *p*-wave in seismological jargon, the second one a transverse wave, an *s*-wave for seismologists [86]. The inhomogeneities from (1.15) can be included by decomposing into contributions with zero rotation and zero divergence.

A notable special case that will, however, not be studied further is that of a harmonic external force $\Delta_v \mathbf{f} = \mathbf{0}$. In the static case, $\mathbf{u} = \mathbf{u}(\mathbf{x})$, in the absence of an external pressure p, application of Δ_v to (1.15) yields by constancy of ρ, μ and λ

$$\Delta_v^2 \mathbf{u} \equiv \Delta_v(\Delta_v \mathbf{u}) = \mathbf{0}. \tag{1.18}$$

The object on the left-hand side is the so-called *biharmonic operator* [86].

Membranes and curvature corrections   For membranes, variants of (1.15) can be derived from energy considerations. Suppose a surface of area A is dislocated by a

function $u(t, x_1, x_2)$ in transverse direction, i.e., parallel to $\hat{e}_{x_3}$ at each point (x_1, x_2). This displacement is assumed to be elastic and small - a flexible membrane.

In harmonic approximation, we will take a quadratic potential energy functional in u. The corresponding density e_{pot} shall include area changes and corrections due to impacts of curvature on the potential energy such that the lowest order contribution is quadratic.

This settles $dA' e_{\text{pot}} = T dA'(1 + \lambda_1 H^2 + \lambda_2 K)$ where dA' denotes the area element of the graph of u. H and K denote the graph's *mean curvature* and *Gaussian curvature* respectively, see [68, 143] for an introduction. λ_1, λ_2 are constants, T is the so-called *membrane tension*, the proportionality constant to mitigate work and area deformation as $\delta W = -T dA'$. Denoting by $A' = \text{graph}(u)$ the t-dependent family of graph hypersurfaces in $\mathbb{R}^3$, the Lagrangian L follows from the definition:

$$L = E_{\text{kin}} - E_{\text{pot}} = \int_{A'} dA' \frac{\rho(\partial_t u)}{2} - T \int_{A'} dA' \left(1 + \lambda_1 H[\text{graph}(u)]^2 + \lambda_2 K[\text{graph}(u)]\right).$$

(1.19)

The potential energy still lacks a contribution. Namely, we have not accounted for contributions from the boundary of A' so far.

Now, we do so by adding an extra potential energy contribution, namely

$$\partial E_{\text{pot}} = T\lambda_2 \int_{\partial A'} ds' \, k_g.$$

(1.20)

k_g denotes the excess geodetic curvature generated by permitting the boundary to be perturbed as well.

Gauss-Bonnet's theorem [68] states that over regular, oriented two-dimensional surfaces in three-dimensional embedding space, the Euler characteristic of a surface is proportional to the sum of integrated Gauss curvature and the integrated geodetic curvature. If A' was closed, the contribution from the boundary curve was absent. Gauss-Bonnet's theorem [143, Appendix] cancels the contribution from Gauss curvature from the equations of motion. The addition of the boundary contribution ∂E_{pot} to potential energy reflects the fact that already the deformation of the boundary requires work. The proportionality constants have been chosen so as to compensate contributions from the Gaussian curvature K.

Explicitly for small u with bounded and sufficiently small first and second spatial

partial derivatives in a local Cartesian coordinate system (x_1, x_2, x_3),

$$K = \frac{\partial_{x_1}^2 u \partial_{x_2}^2 u - (\partial_{x_1 x_2}^2 u)^2}{\sqrt{1 + (\partial_{x_1} u)^2 + (\partial_{x_2} u)^2}^4} \tag{1.21}$$

$$\simeq \partial_{x_1}^2 u \partial_{x_2}^2 u - (\partial_{x_1 x_2}^2 u)^2 + \mathcal{O}((\partial u)^4) \tag{1.22}$$

$$H = \frac{(1 + (\partial_{x_2} u)^2)\partial_{x_1 x_1}^2 u - 2\partial_{x_1} u \partial_{x_2} u \partial_{x_1 x_2}^2 u + (1 + (\partial_{x_1} u)^2)\partial_{x_2 x_2}^2 u}{2\sqrt{1 + (\partial_{x_1} u)^2 + (\partial_{x_2} u)^2}} \tag{1.23}$$

$$\simeq 0.5\Delta u + \mathcal{O}((\partial u)^3) \tag{1.24}$$

$$dA' = dA \sqrt{1 + (\partial_{x_1} u)^2 + (\partial_{x_2} u)^2} \tag{1.25}$$

$$\simeq dA \left(1 + \frac{1}{2}\left((\partial_{x_1} u)^2 + (\partial_{x_2} u)^2\right)\right) + \mathcal{O}((\partial u)^4) \tag{1.26}$$

We drop the additive contribution leading to the Euler characteristic from the Lagrangian L. Only the mean curvature contribution survives.

To apply Hamilton's principle to the Lagrangian with boundary curvature correction, L is integrated over time and the functional derivative with respect to u of the (quadratic) functional in u and derivatives thereof is considered. Integration by parts leads, upon requiring $\partial_{\mathbf{n}} u = 0$ or $u = 0$ at the boundary $\partial A'$, to

$$\rho \partial_t^2 u - T\Delta u + T\lambda_1 \Delta^2 u = 0, \tag{1.27}$$

an equation we call *curvature-corrected elastic membrane equation*.

The "or" is seen by performing the relevant integration by parts and inserting a partial eigenfunction expansion of u in terms of eigenfunctions of the Dirichlet or the Neumann Laplacian on A. We require the corresponding eigenvalue problem to be well-defined on an open domain $B \supset A$ but impose boundary conditions at ∂A. This regularity assumption avoids an equation in the bi-harmonic operator Δ^2 and $-\Delta = \sqrt{\Delta^2}$ rather than the Laplacian Δ. It is unclear whether the problem featuring the bi-harmonic operator is solvable analytically although numeric schemes are available.

When curvature corrections are small in the sense that the $\sim \Delta^2$ contribution is small compared to the $\sim \Delta$ contribution, (1.27) admits an interpretation as a perturbation of the elastic membrane equation $\rho \partial_t^2 u - T\Delta u$ by the perturbation operator $\mathsf{V}[u] = T\lambda_1 \Delta^2 u$.

For the membrane objects under consideration, we interpret (1.27) as an equation featuring a polynomial of the Laplacian Δ with either Dirichlet or Neumann conditions imposed.

Clearly, a well-defined initial-boundary value problem still needs initial conditions for u and $\partial_t u$.

1.4 Fluid dynamics and acoustics

Newtonian fluid dynamics Newtonian fluid dynamics [62, 71] is based on a similar decomposition as utilized for the derivation of the general Cauchy-Navier equation (1.15) in the pre-to-last section 1.2.

The difference is that, here, we use the symmetric part of the velocity gradient $\tilde{\boldsymbol{\epsilon}}$ in place of the linear strain tensor $\boldsymbol{\epsilon}$. In a fluid, no stress is generated by the rotation of the fluid such that the symmetric part $\tilde{\boldsymbol{\epsilon}} = (\tilde{\epsilon}_{ij})_{i,j}$ of the velocity gradient $\nabla \otimes \mathbf{v} = (\partial_i v_j)_{i,j}$ suffices.

Explicitly, the components $\tilde{\epsilon}_{ij}$ read

$$\tilde{\epsilon}_{ij} = \frac{1}{2}\left(\frac{\partial v_i}{\partial x_j} + \frac{\partial v_j}{\partial x_i}\right). \tag{1.28}$$

The material model used in Newtonian fluid dynamics builds on a *linearly* viscous fluid, that is, it assumes a stress tensor $\boldsymbol{\sigma} = (\sigma_{ij})_{i,j}$

$$\sigma_{ij} = -p\delta_{ij} + \eta(\partial_i v_j + \partial_j v_i) + \zeta(\partial_k v_k)\delta_{ij} \tag{1.29}$$

η is called the *shear viscosity* and ζ is called the *bulk viscosity* [71].

Insertion of (1.29) into (1.10) yields the famous *Navier-Stokes equations*

$$\rho\partial_t\mathbf{v} + \rho(\mathbf{v}\nabla)\mathbf{v} = -\nabla p + \eta\Delta_v\mathbf{v} + (\zeta + \eta/3)\nabla(\nabla \cdot \mathbf{v}) + \mathbf{f}. \tag{1.30}$$

There is a hypothesis due to Stokes that states $\zeta \approx 0$ for "reasonable" fluids [71]. We will only deal with these "reasonable fluids" and adopt Stokes' hypothesis.

Accordingly, the Navier-Stokes equations (1.30) take the form

$$\rho\partial_t\mathbf{v} + \rho(\mathbf{v}\nabla)\mathbf{v} = -\nabla p + \eta\Delta_v\mathbf{v} + \eta/3\nabla(\nabla \cdot \mathbf{v}) + \mathbf{f}. \tag{1.31}$$

The nonlinear contribution from the material derivative, the so-called convective term, enters: $(\mathbf{v}\nabla)\mathbf{v}$ renders the solution of the Navier-Stokes equations somewhat difficult in general.

Together with the continuity equation of mass, $D_t\rho = -\rho\nabla\mathbf{v}$, and a thermal equation of state relating the pressure p to the mass density ρ, the equations are a coupled

set of nonlinear partial differential equations. In the main body of this thesis, only analytic special cases are treated.

An important special case is the *Euler equation* which is obtained as $\mu = 0$ in (1.31) (*inviscid fluid dynamics*):

$$\rho D_t \mathbf{v} = -\nabla p + \mathbf{f}. \tag{1.32}$$

In conjunction with the continuity equation of mass $D_t \rho = -\rho \nabla \cdot \mathbf{v}$, they serve as the starting point to derive several acoustics theories. A physical fluid can be both a gas or a liquid.

The distinction between continuum mechanical descriptions of the two kinds of fluids lies in compressibility. We focus on liquids, and more specifically water. In contrast to gases, many liquids most notably water are under reasonable conditions *incompressible*. The requirement is formalized through $D_t \rho = 0$ mathematically and physically by the requirement of the mass density to be constant along mass parcel trajectories. The mass continuity equation then states $D_t \rho = 0 = -\rho \nabla \mathbf{v}$.

Recall that $\mathbf{v}$ is a vector field in three-dimensional space. As such it admits a decomposition as $\mathbf{v} = \nabla \Phi + \nabla \times \mathbf{\Psi}$ in terms of a scalar velocity potential Φ and a vector-valued stream function $\mathbf{\Psi}$. The incompressibility condition turns into $\Delta \Phi = 0$, the *Laplace equation* of potential theory.

Acting with the curl operator $\nabla \times$ on the decomposition $\mathbf{v} = \nabla \Phi + \nabla \times \mathbf{\Psi}$ and imposing the Coulomb gauge $\nabla \cdot \mathbf{\Psi} = 0$ to eliminate a redundant degree of freedom, one finds $\nabla \times \nabla \times \mathbf{\Psi} = -\Delta_v \mathbf{\Psi} = \nabla \times \mathbf{v}$. The quantity on the right-hand side is denoted by $\boldsymbol{\omega}$ and called *vorticity*

$$\boldsymbol{\omega} \equiv \nabla \times \mathbf{v}. \tag{1.33}$$

Through application of Stokes' theorem, the flow Γ of $\boldsymbol{\omega}$ through an oriented surface A with boundary ∂A gives

$$\int_A \langle d\mathbf{A}, \boldsymbol{\omega} \rangle_{\mathbb{R}^3} \equiv \Gamma = \int_{\partial A} \langle d\mathbf{s}, \mathbf{v} \rangle_{\mathbb{R}^3} \tag{1.34}$$

such that the flow Γ serves as a measure for the "circulation" of fluid around the boundary curve ∂A. Therefore, Γ is referred to as *circulation*.

If $\partial A = \emptyset$, $\Gamma = 0$ which is one of *Kelvin's circulation theorem*s. Φ and $\mathbf{\Psi}$ need not be time-independent such that also $\Gamma = \Gamma(t)$ is possible in general.

Although for many liquids such as water, incompressibility is a sensible assumption, inviscidity leads to problems. Despite the nonlinear convection contribution in Euler's equation (1.32) does not predict *turbulence.* Turbulence can be described as the transport of energy from, predominantly, large length scales to small length scales and, ultimately, dissipation (due to viscosity) into heat. The wave number range in which the transport of energy takes place from one length scale to another is called *inertial range* and the transport of energy is called *energy cascade.*

The impacts of viscosity leading to turbulence manifest themselves especially at solid boundaries [128, 98]. At solid boundaries, Euler's equation (1.32) can be given the *no-penetration* boundary conditions, $\mathbf{v}_n^{\text{fluid}} = \mathbf{v}_n^{\text{wall}}$ and no restriction on the component parallel to the wall, whereas the Navier-Stokes equations (1.31) require *no-slip boundary conditions*, $\mathbf{v}_\parallel = \mathbf{0}$ at the solid-liquid interface [71] additionally.

Viscosity matters: The adhesive forces between the fluid and solid boundary particles exceed the cohesive forces between the liquid particles due to viscosity. Since this phenomenon is confined to a small *boundary layer*, one can regard the impact of the boundary layers and the formation of vorticity in there as a correction to incompressible, inviscid (*ideal*), fluid dynamics.

We note that ideal fluid dynamics predicts a wrong flow around sharp edges such as a plate of finite length, say D, placed as an obstacle in a flow of velocity V. If the *Reynolds number*, [71, 86, 98],

$$\text{Re} \equiv \frac{\rho D V}{\eta} \gtrsim \text{Re}_c = 90, \tag{1.35}$$

a vortex street can form out past the obstacle although the flow itself is far from fully turbulent. At the termination of the plate, *side eddies* form out and the background flow leads to dissolution of individual vortices which form the vortex street.

Another characteristic number can be associated with the flow. Denoting the frequency of vortex shedding by f, one can define the *Strouhal number*, [71],

$$\text{St} = \frac{f D}{V} \tag{1.36}$$

which has been measured to be approximately $\text{St} \approx 0.2$ for a variety of flows, including flows around cylinders.

In the case of an isotropic fluid and conservative body forces with constant mass density ρ but in the presence of viscosity, one can derive a simple differential equation for

the vorticity $\boldsymbol{\omega}$ from (1.30) by taking the curl. The result is a vector-valued advection-diffusion equation

$$\rho D_t \boldsymbol{\omega} = (\boldsymbol{\omega}\nabla)\mathbf{v} + \eta\Delta_v\boldsymbol{\omega}. \tag{1.37}$$

In the inviscid case, $\eta = 0$, the above equation reduces to

$$D_t\boldsymbol{\omega} = (\boldsymbol{\omega}\nabla)\mathbf{v}. \tag{1.38}$$

If, even more, $\mathbf{v}$ is small such that convective effects are negligible, then $\partial_t\boldsymbol{\omega} = \mathbf{0}$ and the vorticity is a time-independent quantity and stays at fixed positions, e.g., when there is a considerably slow flow from an orifice.

The next paragraph on introductory material revolves around acoustic theories. These theories study the propagation of material waves in media.

Acoustic theories Let us consider an inviscid fluid described by Euler's equation $\rho D_t\mathbf{v} = -\nabla p + \mathbf{f}$ and the mass continuity equation $\partial_t\rho + \nabla(\rho\mathbf{v}) = q$ with a source pumping mass inside the volume V. The classical *acoustic wave equation* studies small, irrotational $\nabla \times \mathbf{v} = \mathbf{0}$ fluctuations around a simple hydrodynamic background.

For a sufficiently small $\delta \ll 1$, the linearization procedure [72] is specified through

$$\mathbf{v} \to \delta\mathbf{v}\,,\ p \to P_0 + \delta p\,,\ \rho \to \rho_0 + \delta\rho\,,\ \mathbf{f} \to \mathbf{0} + \delta\mathbf{f}\,,\ q \to 0 + \delta q. \tag{1.39}$$

By insertion of (1.39) in the mass continuity equation and the Euler equation and keeping only contributions linear in δ one obtains

$$\rho_0\partial_t\mathbf{v} = -\nabla p + \mathbf{f} \tag{1.40}$$

$$\partial_t\rho + \rho_0\nabla\mathbf{v} = q. \tag{1.41}$$

In linear order in δ the thermal equation of state becomes, $p(\rho) \simeq c^2\rho$ where c^2 denotes the *speed of sound* [72, 127]. For air, $c \approx 343\,\text{ms}^{-1}$ while for water $c \approx 1481\,\text{ms}^{-1}$.

The equations can be combined upon acting with $\nabla\cdot$ on (1.40) and ∂_t on (1.41). Then, Schwarz' theorem allows to commute partial derivatives. The result is the acoustic wave equation:

$$-c^{-2}\partial_t^2 p + \Delta p = \nabla\mathbf{f} + c^{-2}\partial_t q. \tag{1.42}$$

In the absence of sources for acoustic dipoles ($\nabla\mathbf{f} = 0$) and acoustic monopoles ($\partial_t q = 0$), the standard homogeneous wave equation is recovered [72]:

$$\partial_t^2 p - c^2\Delta p = 0. \tag{1.43}$$

The equation is to be solved for the pressure fluctuation p around the hydrostatic equilibrium pressure P_0.

Notice that the physical nature of the liquid under consideration is stored in the thermal equation of state as is the thermodynamic nature of the fluctuation. They can be packaged as an isentropic or an isothermal process, to name two important instances. For the reference values of the speed of sound given above, isentropic processes have been assumed as underlying processes.

A more general approach to acoustics is formalized in the *Lighthill equation* [90, 91, 40]. The latter typically serves as a starting point to systematically investigate refinements of the standard acoustic wave equation (1.43).

The compressible Navier-Stokes equations and the continuity equation of mass function as the starting point for the derivation:

$$\partial_\rho + \nabla(\rho\mathbf{v}) = q, \tag{1.44}$$

$$\rho\partial_t\mathbf{v} + \rho(\mathbf{v}\nabla)\mathbf{v} = -\nabla p + \nabla\boldsymbol{\sigma} + \mathbf{f}. \tag{1.45}$$

Multiplication of (1.44) with $\mathbf{v}$ and addition to (1.45) makes the product rule of vector calculus differentiation applicable. The result of the addition is

$$\partial_t(\rho\mathbf{v}) + \nabla(\rho(\mathbf{v}\otimes\mathbf{v})) = -\nabla p + \nabla\boldsymbol{\sigma} + \tilde{\mathbf{f}} \tag{1.46}$$

where $\tilde{\mathbf{f}} = q\mathbf{v} + \mathbf{f}$ denotes the sum of forces exerted on the fluid body by externally caused mass influx ($\sim q\mathbf{v}$) and other externally applied body forces ($\sim \mathbf{f}$).

Subtraction of the partial derivative with respect to time of (1.44) from the divergence of (1.46) results in

$$\partial_t^2\rho - \Delta p = (\nabla\otimes\nabla)(\rho\mathbf{v}\otimes\mathbf{v} - \boldsymbol{\sigma}) + (\partial_t q - \nabla\cdot\tilde{\mathbf{f}}) \tag{1.47}$$

Last, we subtract on both sides of the equation $c^2\Delta\rho - \Delta p$ where c denotes the speed of sound in the quiescent state of the fluid under consideration.

Upon utilizing $\boldsymbol{\delta} = (\delta_{ij})_{i,j}$ as representation for the identity matrix, (1.47) takes the form

$$\partial_t^2\rho - c^2\Delta\rho = (\nabla\otimes\nabla)(\rho\mathbf{v}\otimes\mathbf{v} - \boldsymbol{\sigma} + (p - c^2\rho)\boldsymbol{\delta}) + (\partial_t q - \nabla\cdot\tilde{\mathbf{f}}). \tag{1.48}$$

Defining $\mathsf{T} = (T_{ij})_{i,j} \equiv \rho\mathbf{v}\otimes\mathbf{v} - \boldsymbol{\sigma} + (p - c^2\rho)\boldsymbol{\delta}$ and $g_{\text{ext}} \equiv (\partial_t q - \nabla\cdot\tilde{\mathbf{f}})$, the above equation can be condensed to an inhomogeneous wave equation for ρ. With Einstein summation convention over repeated indices implied,

$$\partial_t^2\rho - c^2\Delta\rho = \partial_{i,j}^2 T_{ij} + q_{\text{ext}}. \tag{1.49}$$

The object T is called the *Lighthill (turbulence) stress tensor*.

If $q_{\mathrm{ext}} = 0$, the above result simplifies to the *Lighthill equation* governing modern aero-acoustics

$$\partial_t^2 \rho - c^2 \Delta \rho = \partial_{i,j}^2 T_{ij}. \tag{1.50}$$

Observe that the equation is an exact rewriting of the compressible Navier-Stokes equations without further assumptions imposed on the flow. The turbulent contribution is stored in $\rho \mathbf{v} \otimes \mathbf{v}$ in the Lighthill turbulence stress tensor.

The Lighthill equation serves as a starting point to determine the v^8-law for the acoustic intensity of the sound field generated by a turbulent flow of velocity v in a region of length l in the far-field [72]. A discussion is postponed to section 3.3 when it will be required.

Unfortunately, direct analytic solution techniques for Lighthill's equation are not available in general. The importance of the equation is rather conceptual. First, it connects the fields of fluid dynamics and acoustics directly by re-arranging the governing equations underlying both, the Navier-Stokes equations and the continuity equation of mass, into one wave equation. Second, the investigation of special cases based on simplifications and model-specific adaptation of the Lighthill turbulence stress tensor leads to a variety of acoustic theories which permit to study the impacts of, say, viscosity, background fluid motion, vortices and non-linear equations of state on the production of sound.

If, for example, the equation of state is expanded up to quadratic contributions, $\rho = c^2(p + c_2 p^2)$ and damping through thermal conduction is included, $\rho = c^2(p + c_2 p^2 + c_3 \partial_t \rho)$, the assumption of "plane-wave relations" from linear acoustics leads [12] to the so-called *Westervelt equation*. It has the structure

$$\partial_t^2 p + \wp(-\Delta)\partial_t p - c^2 \Delta p = \aleph \partial_t^2(p^2) + (\text{Source}). \tag{1.51}$$

This is a non-linear equation to be solved for the acoustic pressure p. $\wp$ is the viscous-thermal damping coefficient accounting for damping according to the frequency-dependent Stokes-Kirchhoff law [12]. We call $\aleph$ the coefficient of nonlinearity.

The equation is a generalization of the acoustic wave equation at exceptionally high sound amplitudes such that a linearization process as used for the derivation of the acoustic wave equation turns somewhat questionable. As a nonlinear partial differential equations, analytic solutions are only possible in special cases, predominantly in $D =$

$1 + 1$, or via a perturbative treatment for sound waves with amplitudes such that the non-linear contribution $\sim \aleph \partial_t^2 p^2$ can be interpreted in the sense of perturbation theory. We won't encounter a problem in this thesis that requires the solution of Westervelt's equation although there was a point in the actual research on organ pipes where the usage of a nonlinear acoustics theory could not be discarded offhand.

The second simplification of (1.50) concerns the generation of sound by vortices. This branch of acoustics is called *vortex acoustics* [70, 120]. The subsequent derivation follows [127].

Define the *specific enthalpy* $i = e + \rho^{-1}p$ where e is the energy density. With the aid of the total specific enthalpy $B = i + \frac{1}{2}\mathbf{v}^2$, Euler's equation can be recast to take *Crocco's form* [33],

$$\partial_t \mathbf{v} + \nabla B = -\boldsymbol{\omega} \times \mathbf{v}. \tag{1.52}$$

Rearranging the continuity equation $D_t \rho + \rho \nabla \mathbf{v} = 0$ to separate mass density ρ and fluid velocity $\mathbf{v}$ results in

$$-\rho^{-1} D_t \rho = \nabla \cdot \mathbf{v}. \tag{1.53}$$

We take the divergence of (1.52) and the time derivative of (1.53). These operations result in the following two equations

$$\frac{\partial}{\partial t} (\nabla \mathbf{v}) + \nabla^2 B = -\nabla (\boldsymbol{\omega} \times \mathbf{v}) \tag{1.54}$$

$$-\frac{\partial}{\partial t} \left(\frac{1}{\rho} \frac{D\rho}{Dt} \right) = \frac{\partial}{\partial t} (\nabla \mathbf{v}). \tag{1.55}$$

As usual, Schwarz' theorem permitted us to commute the gradient operator ∇ with the partial time derivative operator ∂_t.

Insertion of (1.55) in (1.54) gives

$$-\frac{\partial}{\partial t} \left(\frac{1}{\rho} \frac{D\rho}{Dt} \right) + \nabla^2 B = -\nabla (\boldsymbol{\omega} \times \mathbf{v}). \tag{1.56}$$

A wave equation for B requires some additional information on the flow. We assume a locally isentropic flow such that $ds = 0$ for the entropy density s. Linearization of the thermal equation of state for p as a function of ρ and s produces $dp = c^2 d\rho + \partial_s p|_{\rho=\text{const.}}\, ds = c^2 d\rho$.

Next, the second fundamental theorem of thermodynamics says that, for adiabatic changes, the local heat satisfies $dq = Tds$. The further assumption of isentropy produces $dq = 0$. The specific work satisfies $dw = -pd\rho^{-1}$ such that the first fundamental

theorem of thermodynamics produces $dq = Tds = 0 = de + pd\rho^{-1}$. Legendre transforming in order to exchange the thermodynamic variables $p \leftrightarrow \rho^{-1}$, we arrive at $di = \rho^{-1}dp$ for the *specific enthalpy* $i = e + \rho^{-1}p$ as defined in the beginning of the derivation.

The two thermodynamic considerations allow us to replace $\rho^{-1}D_t\rho \leftrightarrow \partial_t(c^{-2}D_ti)$ in the main derivation of the vortex sound equation. The result of the replacement is

$$\frac{\partial}{\partial t}\left(\frac{1}{c^2}\frac{Di}{Dt}\right) - \nabla^2 B = \nabla\left(\boldsymbol{\omega} \times \mathbf{v}\right). \tag{1.57}$$

Let us consider a background flow $\mathbf{v}_0$ with constant stagnation enthalpy B_0. Define $B' \equiv B - B_0$. First, we re-express the equation in terms of B' rather than B. Second, we subtract the enthalpy contribution on both sides and add an extra contribution $c^{-2}\mathcal{D}_t^2 B'$ for the enthalpy difference B' on both sides of the equation in order to ensure validity of the equality sign. The operator $\mathcal{D}_t \equiv \partial_t + \mathbf{v}_0\nabla$ is a convective derivative with convective term $\sim \mathbf{v}_0\nabla$ along the background flow with velocity field $\mathbf{v}_0$.

The procedure outlined before gives a wave equation for the enthalpy difference B' with reference enthalpy B_0,

$$c^{-2}\mathcal{D}_t^2 B' - \nabla^2 B' = \nabla\left(\boldsymbol{\omega} \times \mathbf{v}\right) + c^{-2}\mathcal{D}_t^2 B' - \partial_t(c^{-2}D_ti) \tag{1.58}$$

In the low Mach number - see [72] for the concept of Mach number - regime $\|\mathbf{v}\|/c \equiv \mathrm{Ma} \ll 1$, the last two contributions on the right hand side of the equation cancel each other. We are thus left with the wave equation

$$c^{-2}\mathcal{D}_t^2 B' - \nabla^2 B' = \nabla\left(\boldsymbol{\omega} \times \mathbf{v}\right). \tag{1.59}$$

Let us assume that outside the source vorticity region, we have $\mathbf{v}_0 = \mathbf{0}$. Upon neglection of small fluctuations in the mass density, $B = i = p/\rho_0$ where p denotes the acoustic pressure.

Ultimately, we have the *vortex acoustics equation*

$$c^{-2}\partial_t^2 p - \nabla^2 p = \rho_0\nabla\left(\boldsymbol{\omega} \times \mathbf{v}\right), \tag{1.60}$$

for the acoustic pressure p.

We notice that $\mathbf{f}_v \equiv \rho_0\left(\boldsymbol{\omega} \times \mathbf{v}\right)$ has the structure of a Coriolis force density and the physical dimensions of a force per volume [127]. As such it can be regarded as a force density in a region filled with vortices that triggers the formation of a pressure wave or acts on solid boundaries.

Concluding remark   The theories sketched in this section are used as basic physical equations for the models to be studied in the sequel main chapters of the thesis. It is precisely the vivid interplay of the governing equations from elasticity, membrane theory, fluid dynamics or acoustics that makes continuum mechanics widely applicable to properly describe natural phenomena in the world that surrounds us directly.

Chapter 2

Acoustic boundary conditions and geometric perturbation theory

Numerous practical and academic applications of acoustics require not only the study of an acoustic wave equation in isolation but also the accounting for its interaction with locally reacting surfaces described by elasticity equations. The model equations are coupled via so-called acoustic boundary conditions, accounting for the pressure in, say, an acoustic enclosure and the displacement of the locally reacting parts of the enclosure's walls from equilibrium.

In the geometric context of the bio-acoustic model of Internally Coupled Ears (ICE), we aspire to complement Beale's original mathematical definition of acoustic boundary conditions with the physical definition of the notion "acoustic pressure" as a small local change in mass density in the Eulerian respectively a small local change in available volume per fixed mass in the Lagrangian picture of fluid dynamics. The notion of a perturbation bundle is defined as an idealization of a cavity with locally reacting walls undergoing small fluctuations. It is the natural geometric stage for a systematic perturbation theory to study the cavity's evolution. The full, exemplary model is reduced to a set of three decoupled partial differential equations. A full treatment of the relaxation dynamics of the ICE model as typical vibrational acoustics and the presentation of the spinning mode series expansion, a generalization of the duct acoustic cut-off criterion to the case of thick cylinders, conclude the analysis.

The chapter aspires to serve as a bridge between the different formalisms employed by engineers, mathematicians and physicists. The geometric approach signifies geometry as the natural language of mechanics in general, acoustics in specific.

Note: Fig. 2.2 and Fig.2.3 have already been utilized in [61].

2.1   Introductory material

Internally coupled ears   Though omnipresent, geometric perturbation theory has hardly been discerned as such, if at all. We start by describing a typical situation, viz., that of Internally Coupled Ears (ICE), which is present in more than half of the terrestrial vertebrates. Though ICE has been observed and described since long, it has attracted considerable attention only recently [147, 147, 158, 141]. It is used here as a typical example from the field of acoustics to illustrate the general idea of geometric perturbation theory.

Terrestrial animals perform azimuthal sound localization through neuronally determining the time difference between left and right eardrums, the so-called interaural time difference (ITD). Whereas mammals have independent ears, which do not influence each other, most of the terrestrial vertebrates have ICE at their disposal, which means an internal, air-filled, cavity that connects the two eardrums. ICE allows in particular small animals with small head and, hence, small ITD to greatly increase it; typically, for low frequencies by 2–4 [141]. What the animal then actually perceives is the so-called the internal time difference (iTD) as the superposition of the external auditory stimulus p_{ext} operating at the two eardrums, say, at $x = 0$ and $x = L$, and the internal pressure p; see Fig. 2.1.

The eardrums are driven by the superposition of p_{ext} and p, and are part of the boundary conditions to the wave equation governing the internal pressure p. In the, for the sake of clarity, concrete situation of ICE analyzed here as well as in any other acoustic problem, the time-dependent deviations from equilibrium (defined to be $x = 0$ respectively $x = L$) are extremely small, in the nm range and thus orders of magnitude smaller than any other physical quantity involved. Since an exact solution to the coupled dynamics of outside stimulus, inside pressure, and both eardrums is nearly always out of range and the tympanic deviations from equilibrium are small (nm), a perturbation theory seems natural.

Acoustic boundary conditions   As early as 1938, Herbert Frölich [49] published a short paper with the title "A solution of the Schröinger equation by a perturbation of the boundary conditions", where he initiated a perturbation theory for the change in

eigenfunctions and eigenvalues by changing the boundary conditions but still fixing the domain, and also by changing the domain as well. Both types of change, however, did not depend on time. Neither did they in the succinct analyses [22, 23, 39, 17, 18, 73]. In the acoustic context of the above examples, they do and we are also interested in a general treatment of the ensuing time evolution but, despite the small amplitudes involved, until now a systematic, time-dependent, perturbation theory did not exist. That is what we do here.

Starting with the work of Beale and Rosencrans [8], which Beale [7] has extended and worked out, the approach was different. In view of the nm deviations from equilibrium, the boundary was fixed to be the original one and assumed to be "locally reacting" in the sense that is was covered by independent oscillators satisfying a separate damped harmonic-oscillator equation coupled linearly to p [8]. A typical example of a setup, though different from ours, is treated in [112, 113]. Beale and Rosencrans [8] called the final construct Acoustic Boundary Conditions or, for short, ABC. In so doing they have started the mathematical analysis of ABC.

Though their construct can be handled mathematically and Beale and Rosencrans [8] and particularly Beale [7] could prove the existence of a dynamical evolution, it does not correspond to the underlying physics. Nor was it possible to obtain any explicit solution, valuable as it is for practical work. In fact, many concrete situations in vibro-acoustics have been analyzed in a similar spirit [73, 24, 25, 50, 89] - to name just a few outstanding papers, though even these allow neither a dynamics nor a dynamical coupling.

Objective and scope of this work   Here we return to the essential physics of the problem by taking the volume fluctuations due to the dynamics of the eardrums as our starting point and incorporating them as time-dependent perturbations of the Laplacian, a procedure that seems to be novel and, more importantly, allows for a systematic perturbation theory. We develop a time-dependent perturbation theory in the style of Dirac [34], whose key idea is nicely described by Dirac himself in his classic on quantum mechanics [34, §44]. Not only do we present a mathematical perturbation theory for handling time-varying domains and allowing for explicit solutions but also for obtaining the full dynamical evolution for all times $t \geq 0$, including the asymptotics as $t \to \infty$. In a sense, we extend Beale's ABC [8, 7] to ABCD, i.e., Acoustic Boundary Condition Dynamics, with the geometric perturbation theory as the physical foundation.
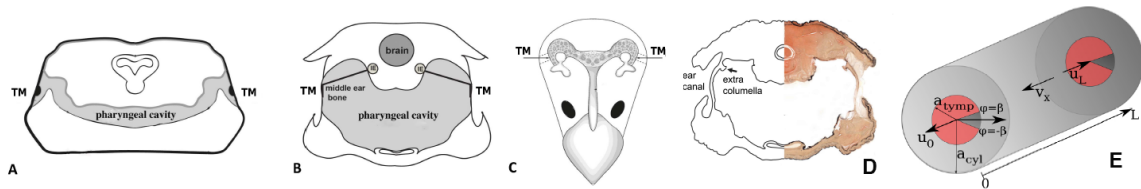
Figure 2.1: Schematic representation of Internally Coupled Ears (ICE) in frogs (a), lizards (b), and birds (c). The bird in (c) is seen from the top, the other two in (a) and (b) show a cross section, and all three exhibit the interaural cavity as a gray tube. (d) Cross section of a real Gecko cavity as it occurs in Nature. The extracolumella in (d) is embedded in the eardrum and the beginning of the middle-ear bone in (b) that picks up the eardrum vibrations and transports them through the air-filled cavity to the cochlea. The latter is quite near to the neuronal information processing area of sound in the brain. The mathematical idealization of (d) is depicted in (e) where the cylindrical cavity $\mathcal{Z}_{\text{stat}}$ of length L and radius a_{cyl} are as used in the ICE model that is used here as example. The circular sectors Γ_0 and Γ_L with radius $a_{\text{tymp}} \leq a_{\text{cyl}}$ and opening angle β are situated at $x = 0$ and $x = L$. The left and right membrane-displacement in x-direction are indicated by u_0 and u_L, respectively. The arrow at the bottom of Figure 1 (e) denotes orientation in positive x-direction. Figures 1 (a)–(c) have been adapted from Christensen-Dalsgaard [29], (d) stems from Carr, Tang [30], and Christensen-Dalsgaard and (e) has been taken from Vedurmudi et al. [147].

2.2   Geometric considerations

Assumptions   Due to the complexity in the formulation, some overall assumptions are needed: Physical regularity behavior of mathematical objects is assumed throughout. The internal acoustic pressure p and the displacements u_0, u_L are assumed to be bounded and regular such as to permit continuation.

Stationary cavity model   Let $\mathcal{Z}_{\text{stat}} = \{(x, y, z) \in \mathbb{R}^3 | 0 < x < L, y^2 + z^2 < a_{\text{cyl}}\}$ denote the cylinder for which the x-axis of the Cartesian coordinate system is the axis of symmetry. Up to a set of measure 0, $\mathcal{Z}_{\text{stat}}$ can be expressed as a *normal domain* in $\mathbb{R}^3$, i.e., there exist sufficiently regular (at least $\mathcal{C}^2$ here) $\mathbb{R}$-valued functions $q_2^-, q_2^+, q_3^-, q_3^+$ for reals q_1^-, q_1^+ such that $\mathcal{Z}_{\text{stat}} \equiv \{(q_1, q_2, q_3) \in \mathbb{R}^3 | q_1^- < q_1 < q_1^+, q_2^- < q_2(q_1) < q_2^+(q_1), q_3^-(q_1, q_2) < q_3 < q_3^+(q_1, q_2)\}$.

In the case of the cylinder, the normal domain property is readily seen in cylindrical coordinates $\mathcal{Z}_{\text{stat}} = \{(r, \phi, x) \in \mathbb{R}_0^+ \times [0, 2\pi] \times \mathbb{R} | 0 < r < a_{\text{cyl}}, 0 < \phi < 2\pi, 0 < x < L\}$. The equality of sets holds to a set of measure zero. In the cylindrical coordinates, the cylinder attains the form of an open cuboid.

Inclusion of locally reacting surfaces   Let us define the left and right endcap of the cylinder by $\mathcal{F}_0 \equiv \{(x = 0, y, z) \in \mathbb{R}^3\} \cap \partial\mathcal{Z}_{\text{stat}}$ and $\mathcal{F}_L \equiv \{(x = 0, y, z) \in \mathbb{R}^3\} \cap \partial\mathcal{Z}_{\text{stat}}$. Both endcaps are open balls of radius a_{tymp} situated in an affine subspace of $\mathbb{R}^3$, namely in $(0, 0, 0) + \lim_{\mathbb{R}}\{\hat{e}_y, \hat{e}_z\}$ and $(0, 0, L) + \lim_{\mathbb{R}}\{\hat{e}_y, \hat{e}_z\}$ of the same dimension.

We define $\Gamma_0 \subseteq \mathcal{F}_0$ and $\Gamma_L \subseteq \mathcal{F}_L$ to be cuboids in the cylindrical coordinate system. Furthermore, we let $(u_0)_t : \Gamma_0 \to \mathbb{R}$ and $(u_L)_t : \Gamma_L \to \mathbb{R}$ be a $\mathcal{C}^2$ $\mathbb{R}^+$-family of functions, each of which is $\mathcal{C}^2$. We consent on abusing notation to denote by $(u_0)_t$, $(u_L)_t$ also the function families' null-continuation from Γ_0 to $\mathcal{F}_0$ and from Γ_L to $\mathcal{F}_L$. Apart from a set of measure 0, namely $\partial\Gamma_0 \cap \mathcal{F}_0$ and $\partial\Gamma_L \cap \mathcal{F}_L$, the above null-continuations are $\mathcal{C}^2$ as well. Since $(u_0)_t$ and $(u_L)_t$ are in particular continuous and defined on a compact domain, the maximum principle from real analysis applied to $\text{abs} \circ (u_0)_t$ and $\text{abs} \circ (u_L)_t$ ensures that $\|(u_0)_t\|_\infty \equiv U_0(t)$ and $\|(u_L)_t\|_\infty \equiv U_L(t)$ define $\mathcal{C}^0$-functions for all and, by the imposed t-regularity, even $\mathcal{C}^2$-functions for almost all $t > 0$.

Finally, we suppose that there is an $0 < \epsilon' < 0.5$, preferentially a small number, such that $U_0(t) < \epsilon' L$ and $U_L(t) < \epsilon' L$ for all t. The equation states that $(u_0)_t$, $(u_L)_t$ are "physically" small compared to L.

Next, let

$$\mathcal{Z}(t) \equiv \left\{ (r, \phi, x) \in \mathbb{R}_0^+ \times [0, 2\pi] \times \mathbb{R} \,|\, 0 < r < a_{\text{cyl}}, 0 < \phi < 2\pi, -u_0(t, r, \phi) < x < L + u_L(t, r, \phi) \right\}. \tag{2.1}$$

We use $(u_0)_t(\bullet) = u_0(t, \bullet)$ and $(u_L)_t(\bullet) = u_L(t, \bullet)$ to store the t-dependency in the argument of the function. By the requirement $\epsilon' < 0.5$, the topological properties of $\mathcal{Z}_{\text{stat}}$ carry over to $\mathcal{Z}(t)$ for $t > 0$ and in particular $\mathcal{Z}(t)$ stays simply connected, compact, oriented and suitably regular with a suitable piecewisely regular boundary $\partial \mathcal{Z}(t)$.

Geometric configuration space of the undulating cavity   Dynamically, $u_0(t = 0, \bullet) = 0 = u_L(t = 0, \bullet)$ is required together with $\partial_t u_0(t = 0, \bullet) = 0 = \partial_t u_L(t = 0, \bullet)$ where $\bullet$ denotes a point in the cuboids Γ_0, Γ_L respectively. On $\mathcal{F}_0 \setminus \bar{\Gamma}_0$ and $\mathcal{F}_L \setminus \bar{\Gamma}_L$ $u_L(t, \bullet) = u_0(t, \bullet) \equiv 0$.

We define the objects

$$\mathcal{M} \equiv \mathbb{R}^+ \times \mathcal{Z}_{\text{stat}} \subset \mathbb{R}^+ \times \mathbb{R}^3, \tag{2.2}$$

$$\mathcal{M}(t) \equiv \bigcup_{t \in \mathbb{R}^+} \{t\} \times \mathcal{Z}(t) \subset \mathbb{R}^+ \times \mathbb{R}^3. \tag{2.3}$$

$\mathcal{M}$ and $\mathcal{M}(t)$ are trivial fiber bundles [60] over $\mathbb{R}^+$ where $\mathcal{M}$ is even a product manifold and $\mathcal{M}(t)$ is not a product manifold.

The notion of a manifold is understood in a smooth sense upon assuming smoothing out edges and corners of the fiber manifolds $\mathcal{Z}_{\text{stat}}$ and $\mathcal{Z}(t)$ by mollification.

For our purposes, the existence of edges in cylinders is unproblematic. Accordingly, we will treat the fibers as smooth manifolds as if they had been mollified.

Perturbation bundle $\mathcal{M}(t)$ is called a *perturbation bundle* with *unperturbed bundle* $\mathcal{M}$.

Topological observation   Let $\psi_{t,r,\phi} : (-u_0(t, r, \phi), L + u_L(t, r, \phi)) \to (0, L)$ be defined through

$$x \equiv \psi_{t,r,\phi}(x_t) \equiv \frac{L x_t}{L + u_0(t, r, \phi) + u_L(t, r, \phi)}. \tag{2.4}$$

Since $0 < |x| < L|x_t|/(L - 2\epsilon) < \infty$ by $\epsilon < 0.5$, this map is well-defined. It is a bijection and smooth with smooth inverse, i.e., a diffeomorphism between domain and range.

Ultimately, define $\Psi : \mathcal{M}(t) \to \mathcal{M}$ through the coordinate prescription

$$(t, r, \phi, x) \equiv \Psi(t_t, r_t, \phi_t, x_t) \equiv (t, r, \phi, \psi_{t,r,\phi}(x_t)). \tag{2.5}$$

Ψ inherits the diffeomorphism property from $\psi_{t,r,\phi}$: It declares a diffeomorphism between the fiber bundles' total spaces $\mathcal{M}(t)$ and $\mathcal{M}$. Both $\psi_{t,r,\phi}$ and Ψ preserve the orientation that domain and range inherit from the embedding Euclidean respectively Lorentzian space.

Metrics As a model for cavities with locally reacting wall elements $\mathcal{M}(t)$ and its stationary counterpart are by construction embedded in $\mathbb{R}^+ \times \mathbb{R}^3$. Let c denote the speed of sound in air, $c \approx 343\,\mathrm{ms}^{-1}$.

Endowing $\mathbb{R}^+ \times \mathbb{R}^3$ with a Lorentzian signature metric $\eta \equiv \mathrm{diag}(+1, -c^2, -c^2, -c^2)$ and exploiting the cylindrical symmetry of the fiber spaces $\mathcal{Z}_{\mathrm{stat}}$ and $\mathcal{Z}(t)$ for $t > 0$, we find in the adequate coordinates within the framework of the Einstein summation convention

$$\mathsf{G} = G_{MN} dx^M dx^N = dt^2 - c^2 \left(dr^2 + r^2 d\phi^2 + dx^2 \right) \tag{2.6}$$

with $dx^0 = dt$ and $dx^1 = dr$, $dx^2 = d\phi$, $dx^3 = dx$. After restriction to $\mathcal{M}$ respectively $\mathcal{M}(t)$ as Lorentzian sub-manifolds of $(\mathbb{R}+ \times \mathbb{R}^3, \mathsf{G})$, we obtain induced Lorentzian metrics $\mathsf{G}_{0,0} : T\mathcal{M} \times T\mathcal{M} \to C^\infty(\mathcal{M} \to \mathbb{R})$ respectively $\mathsf{G}_{0,t} : T\mathcal{M}(t) \times T\mathcal{M}(t) \to C^\infty(\mathcal{M}(t) \to \mathbb{R})$.

The assignment of $\mathsf{G}_{0,0}$ turns the bundles' total spaces $\mathcal{M}$ and $\mathcal{M}(t)$ into Lorentzian manifolds $(\mathcal{M}, \mathsf{G}_{0,0})$ and $(\mathcal{M}(t), \mathsf{G}_{0,t})$. For two isometric Lorentzian manifolds (M_1, g_1) and (M_2, g_2), we write $(M_1, \mathsf{g}_1) \cong (M_2, \mathsf{g}_2)$.

By the last paragraph in the previous section, $\mathcal{M} \simeq \mathcal{M}(t)$ whereas $(\mathcal{M}, \mathsf{G}_{0,0}) \not\cong (\mathcal{M}(t), \mathsf{G}_{0,t})$. This means although topologically, the fiber bundles are diffeomorphic via Ψ, i.e., topologically equivalent, they are not isometric via Ψ, i.e., their local geometric properties differ.

We note $\mathcal{M} = (\Psi^{-1})^* (\mathcal{M}(t))$ as a pull-back manifold. The associated pull-back metric $\mathsf{G}_{t,0} \equiv (\Psi^{-1})^* \mathsf{G}_{0,t}$ defines a Lorentzian metric on $\mathcal{M}$ such that $(\mathcal{M}, \mathsf{G}_{t,0}) \cong (\mathcal{M}(t), \mathsf{G}_{0,t})$. We observe that the scalar d'Alembertian for $\mathsf{G}_{0,t} = G_{MN} dx^M dx^N$ is just

the usual d'Alembertian in cylindrical coordinates:

$$\Box_{0,t} = \sqrt{-\det G}^{-1} \partial_M \left(\sqrt{-\det G}\, G^{MN} \partial_N \right) \tag{2.7}$$

$$= \partial_t^2 - c^2 \left(\partial_r^2 + r^{-1} \partial_r + r^{-2} \partial_\phi^2 + \partial_x^2 \right) \tag{2.8}$$

$$\equiv c^2 \left(\partial_\chi^2 - \partial_r^2 + r^{-1} \partial_r + r^{-2} \partial_\phi^2 + \partial_x^2 \right) \tag{2.9}$$

where $\chi = ct$ has the physical dimension of a length.

For the subsequent argument, we will work with χ as a temporal variable in place of t. Additionally, we will non-dimensionalize through normalization to the length scale set by the cylinder's length L.

The metric $\mathsf{G}_{0,t}$ becomes

$$G_{MN} dx^M dx^N = c^2 L^2 (d\chi_0^2 - dr_0^2 - r_0^2 d\phi^2 - dx_0^2) \tag{2.10}$$

where $\chi_0 = \chi/L$, $r_0 = r/L$, $x_0 = x/L$. The functional matrix $\Lambda_{M'}^M$ for the differential $d\Psi^{-1}$ is found with $u \equiv (u_0 + u_L)/L$ for which $\|u\|_\infty < 2\epsilon < 1$

$$\left(\Lambda_{M'}^M \right) = \left(\delta_{M'}^M \right) + \left(\lambda_{M'}^M \right). \tag{2.11}$$

$$\left(\lambda_{M'}^M \right) = \begin{pmatrix} 0 & 0 & 0 & 0 \\ 0 & 0 & 0 & 0 \\ 0 & 0 & 0 & 0 \\ x_0 \partial_{\chi_0} u & x_0 \partial_{r_0} u & x_0 \partial_\phi u & u \end{pmatrix} \tag{2.12}$$

in the non-dimensional units defined above. The pull-back metric $\mathsf{G}_{t,0} = (\Psi^{-1})^*(\mathsf{G}_{0,t})$ evaluates to

$$g_{M'N'} = G_{MN} \Lambda_{M'}^M \Lambda_{N'}^N = G_{M'N'} + \delta G_{M'N'}, \tag{2.13}$$

$$\delta G_{M'N'} = G_{M'N} \lambda_{N'}^N + G_{MN'} \lambda_{M'}^M + G_{MN} \lambda_{M'}^M \lambda_{N'}^N. \tag{2.14}$$

$\delta G_{M'N'}$ is symmetric in its indices.

Let us assume $\|\partial_{\chi_0} u\|_\infty, \|\partial_{r_0} u\|_\infty, \|\partial_\phi u\|_\infty < 2\epsilon$. This means the boundary perturbation undulates not too fast neither temporally nor spatially. Since $0 < x_0 < 1$, then $\|G^{K'N'} \cdot \delta G_{M'N'}\| \leq \|\delta G_{M'N'}\| \cdot \|G_{M'N'}\|^{-1} < \epsilon < 0.5 < 1$ in the Frobenius matrix norm [122] with the maximum norm imposed on the individual coefficients of the matrix. Through expansion of the determinant, we have $\det(-g) = \det(-G) \det(\mathbb{1} + G^{-1} \cdot \delta G) = (\det(-G))(1 + \text{Tr}[G^{-1} \cdot \delta G])$ up to contributions of order ϵ^2.

Similarly, $g^{M'N'} = G^{M'N'} - \delta G^{M'N'}$, with indices raised and lowered via $\mathsf{G}_{0,t}$, holds up to contributions of order ϵ^2.

d'Alembertian   Dropping primes on indices, we find with $-\det g = -g$

$$\Box_{t,0} \equiv \sqrt{-g}^{-1}\partial_M\left(\sqrt{-g}g^{MN}\partial_N\right) = \Box_{0,t} + \mathsf{V}. \tag{2.15}$$

With the abbreviation $-G = -\det G$, $\Box_{0,t}$ denotes the d'Alembertian on $\mathcal{M}$ in the metric $\mathsf{G}_{0,t}$ and V is interpreted as a perturbation operator.

Both partial differential operators are given explicitly:

$$\Box_{0,t} = \sqrt{-G}^{-1}\partial_M\left(\sqrt{-G}G^{MN}\partial_N\right) \tag{2.16}$$

$$\begin{aligned}
\mathsf{V} = &-\mathrm{Tr}\left[G^{-1}\cdot\delta G\right]\sqrt{-G}^{-1}\partial_M\left(G^{MN}\sqrt{-G}\partial_N\right) \\
&+ \sqrt{-G}^{-1}\partial_M\left(G^{MN}\sqrt{-G}\mathrm{Tr}\left[G^{-1}\cdot\delta G\right]\partial_N\right) \\
&- \sqrt{-G}^{-1}\partial_M\left(\delta G^{MN}\sqrt{-G}\partial_N\right).
\end{aligned} \tag{2.17}$$

At most second order derivatives of u appear in V.

The requirement of suitable boundedness of second order derivatives of u as $\sim \epsilon$ allows us to regard V as a $\Box_{0,t}$-bounded small perturbation in a second-order Sobolev space in which $\Box_{0,t}$ is bounded as a linear operator [124]. The regularity requirement consented in the beginning enables us to impose this rather strong regularity behavior.

V will not be needed explicitly for the rest of the chapter. In the following, we understand it as being written out in the physical variables t, r, ϕ, x for $\mathcal{M}$.

Back in the physical variables, we have

$$\partial_t^2 p - c^2(\partial_r^2 p + r^{-1}\partial_r p + r^{-2}\partial_\phi^2 p + \partial_x^2 p) + \mathsf{V}[p] = 0 \tag{2.18}$$

for p at least $\mathcal{C}^2$ on $\mathcal{M} = \mathbb{R}^+ \times \mathcal{Z}_{\mathrm{stat}}$. The object in round brackets is the Laplace-Beltrami operator on $\mathcal{Z}_{\mathrm{stat}}$ expressed in cylindrical coordinates.

Equation (2.18) is the acoustic wave equation [135] to-be-studied. It needs boundary conditions.

Boundary conditions   The boundary conditions need to be derived physically in the coordinates of (2.18). Physical background material can be found in [135].

We focus on the $x = 0$ and $x = L$ endcaps of $\mathcal{Z}_{\mathrm{stat}}$, i.e., on $\mathcal{F}_0$ and $\mathcal{F}_L$. We have $p(t, r, \phi, x + \Delta x) - p(t, r, \phi, x) = f_{\mathrm{fluid}}(t, r, \phi, x)\Delta x$ in mechanical equilibrium, i.e., after Taylor expansion $\partial_x p(t, r, \phi, x) = f_{\mathrm{fluid}}$. The pressure gradient in x-direction equates to the volume density of force in the fluid. From the continuum version of Newton's second law, $f_{\mathrm{fluid}} = -\rho_0\partial_t v_x$ in acoustic linearization. This means that the acoustic

pressure compensates the small velocity fluctuations induced by the local reaction of the surfaces.

At $x = 0$ and $x = L$, $v_x = \dot{u}_0$ respectively $v_x = \dot{u}_L$. Indeed, the force per volume density acting on a point on the $x = 0$ stored in the motion of the locally reacting surface has only a non-trivial x-component $f_{\text{fluid}} = \rho_0 \partial_t \dot{u}_0$ in acoustic linearization.

The mechanical equilibrium condition now states that the acoustic pressure forms such as to compensate this force density. Saying that the acoustic pressure p forms to ensure mechanical equilibrium means working in coordinates such that the cylinder does not change its shape in time, i.e., $\mathcal{Z}_{\text{stat}}$ pertains its form. $\partial \mathcal{Z}_{\text{stat}} \setminus (\mathcal{F}_0 \cup \mathcal{F}_L)$ models walls which are acoustically hard. I.e., the subset of the boundary of $\mathcal{Z}_{\text{stat}}$ currently under consideration does not undergo vibrations. The mechanical equilibrium condition from above thus reduces to $\partial_r p = 0$ on $\partial \mathcal{Z}_{\text{stat}} \setminus (\mathcal{F}_0 \cup \mathcal{F}_L)$.

Explicitly, the boundary conditions to the Laplace-Beltrami operator read

$$\partial_x p = -\rho_0 \partial_t \dot{u}_0 \text{ on } \mathcal{F}_0 \tag{2.19}$$

$$\partial_x p = -\rho_0 \partial_t \dot{u}_L \text{ on } \mathcal{F}_L \tag{2.20}$$

$$\partial_r p = 0 \text{ on } \partial \mathcal{Z}_{\text{stat}} \setminus (\mathcal{F}_0 \cup \mathcal{F}_L) . \tag{2.21}$$

Furthermore, the cylindrical symmetry is incorporated in the periodicity condition imposed on the azimuthal variable ϕ, $p(t, r, \phi, x) = p(t, r, \phi + 2\pi, x)$ for all values of coordinates (t, r, ϕ, z) for $\mathcal{M} = \mathbb{R}^+ \times \mathcal{Z}_{\text{stat}}$.

Initial conditions   The initial conditions are obtained from physical deliberations as well. The cavity model's wall react locally to an external pressure signal incident on the walls. If this signal is absent, the locally reacting surfaces in the cavity's wall do not undulate. The mathematical translation gives homogeneous initial conditions for the acoustic pressure, that is, $p(t = 0, r, \phi, x) = 0$ and $\partial_t p(t = 0, r, \phi, x) = 0$.

Physical comments   The main question underlying the treatment is how to apply the notion of acoustic pressure rather strictly. Acoustic pressure is defined as a small fluctuation around a hydrostatic equilibrium pressure. It can alternatively be described as the dynamic pressure generated by small local fluctuations in mass density.

In the cavity model described above, parts of the boundary are allowed to undergo small perturbations around their equilibrium position. This impacts the acoustic wave equation in so far that the Laplacian is in fact time-dependent and small volumes have

to be added to viz. subtracted from $\mathcal{Z}_{\text{stat}}$. On the other hand, the momentum balance given by Euler's equation in acoustic linearization just states that the acoustic pressure ensures equilibrium: $\nabla p = -\rho_0 \partial_t \mathbf{v}$. However, the position where we evaluate the fluid velocity and the acoustic pressure's gradient still fluctuates since we are perturbing from the fluid rest frame but Euler's equation accounts for the whole fluid motion, including perturbations.

This led us to infer that the impact of the locally reacting surface becomes visible two times. First, by boundary conditions to ensure the mechanical equilibrium and second, by a suitable perturbation operator which stores the impacts of the full three-dimensional local changes in volume.

The result of the further treatment is anticipated here: The V can be safely neglected as being out of range for the acoustic linearization procedure. Intuitively, this has been used in [8, 7] who coined the notion of acoustic boundary conditions. In the next section, we will support this view by combining Dirac perturbation theory [34] and Picard iteration [60].

2.3   Perturbation theory

Locally reacting surfaces   For simplicity, only one of the two endcaps' locally reacting wall elements with equilibrium position $\mathcal{F} \in \{\Gamma_0, \Gamma_L\}$ is considered.

Physically, the local reaction of the membranes gives rise to a kinetic energy density (per volume) of the constituent molecules. Working on classical scales above $a_0 \simeq 10^{-10}\,\text{m}$, the kinetic energy density is given by $\rho_m (\partial_t u)^2 / 2$. In that expression, ρ_m denotes the mass density of the membrane and is assumed constant due to the smallness of vibrations under consideration. The quantity u symbolizes the transverse membrane displacement and corresponds to u_0 or u_L in the model of the cylindrical cavity vibrating endcaps. The kinetic energy stored in an infinitesimal volume dV of the membrane thus is $dE_{\text{kin}} = dV\, \rho_m (\partial_t u)^2 / 2$.

In the absence of external energy injection, the kinetic energy stored in a membrane volume dV is accompanied by a potential energy term. The $p(\mathsf{H}) = \det(\mathbb{1}_2 + \kappa \sigma_3 \mathsf{H}[u])$ is found to produce in quadratic expansion a spatial dependency of the potential energy term that includes (mean) curvature $\mathsf{H}[u]$ contributions of the hyper-surface defined by u to the potential energy dE_{pot} as well. It has been chosen only on the basis of giving the correct result, see e.g. [142], and although it has the same structure as the

polynomial from which physicists derive the Chern characteristic classes, the coinciding mathematical structure does not "hide" a deep secret.

Let κ be a small length scale and set

$$p(\mathsf{H}) = \det\left(\mathbb{1}_2 + \kappa\sigma_3\mathsf{H}[u]\right) = 1 + \frac{\kappa^2(\Delta_\partial u)^2}{4} + \mathcal{O}(\kappa^3). \tag{2.22}$$

because in linear approximation, $2\mathsf{H}[u] = \Delta_\partial u$ where Δ_∂ is the Laplace-Beltrami operator defined. Keeping only quadratic terms, it remains to introduce the membrane tension T_0 as a dimensional constant to ensure that the resulting infinitesimal potential energy dE_{pot} in the volume dV has the correct physical dimension of an energy. dE_{pot} is expressed up to quadratic order in κ as

$$dE_{\text{pot}} = dV\,T_0 p(\mathsf{H}) \approx dV\,T_0\left(1 + \frac{\kappa^2(\Delta_\partial u)^2}{4}\right). \tag{2.23}$$

We focus on dV. Let us idealize the membrane as having uniform thickness d in perpendicular direction to an infinitesimal surface element dA. Then $dV = d_m dA$ and if dA_0 denotes the equilibrium surface $\mathcal{F}$ which is stretched during surface undulation we have $dA = dA_0\sqrt{1 + (\nabla_\partial u)^2}$ in addition. Taylor expansion up to including contributions at most quadratic in derivatives of u yields

$$dV \approx dA_0\,d_m\left(1 + \frac{(\nabla_\partial u)^2}{2}\right). \tag{2.24}$$

The objects of interest are the infinitesimal kinetic and potential energy. Keeping only contributions of at most quadratic order in u and derivatives thereof and dropping an overall constant term $\sim dA_0\,d_m$ to the potential energy dE_{pot}, we arrive at

$$dE_{\text{pot}} = dA_0\frac{T_0 d_m}{2}\left((\nabla_\partial u)^2 + \kappa^2\frac{(\Delta_\partial u)^2}{2}\right), \tag{2.25}$$

$$dE_{\text{kin}} = dA_0\frac{\rho_m d_m(\partial_t u)^2}{2}. \tag{2.26}$$

In order to circumvent the problem of having to impose "plate" boundary conditions, we observe that

$$\int_{\mathcal{F}} dA_0\,(\Delta_\partial u)^2 = \int_{\partial\mathcal{F}}\langle d\mathbf{s}, \nabla_\partial u\rangle\rangle(\Delta_\partial u) - \int_{\mathcal{F}} dA_0\,\langle\nabla_\partial u, \nabla_\partial\Delta_\partial u\rangle. \tag{2.27}$$

We assume to be able to integrate the first integral on the right-hand side by parts one more. Since $\partial(\partial\mathcal{F}) = \emptyset$, we find in this case

$$\int_{\partial\mathcal{F}}\langle d\mathbf{s}, \nabla_\partial u\rangle\rangle(\Delta_\partial u) = -\int_{\partial\mathcal{F}}\langle d\mathbf{s}, \nabla_\partial\Delta_\partial u\rangle u. \tag{2.28}$$

We then require $u = 0$ on $\partial\mathcal{F}$.

Consider the case that Δ_∂ admits eigenfunctions which can be continued into a small environment on $\mathcal{F}$. The alternative, $\Delta_\partial u = 0$ on $\partial\mathcal{F}$ and, furthermore, boundary condition $u = 0$ on $\partial\mathcal{F}$, gives rise to the same solution as does the requirement of simply $u = 0$ on $\partial\mathcal{F}$. We will address this later on again.

If we require $u = 0$ on $\partial\mathcal{F}$ and $\Delta_\partial u = 0$ on $\partial\mathcal{F}$, we have for the full potential energy after integration by parts

$$E_{\text{pot}} = \frac{T_0 d_m}{2} \int_{\mathcal{F}} dA_0 \, u \left(-\Delta_\partial u + \kappa^2 \frac{\Delta_\partial^2 u}{2} \right). \tag{2.29}$$

The total kinetic energy is obtained by trivial integration of dE_{kin} over spatial degrees of freedom. Its time integral can only be brought into a form that permits application of Hamilton's variational principle if $u = 0$ is demanded for $t = 0$ and for $t \to \infty$. The latter asymptotic behavior can be ensured by the phenomenological inclusion of damping, the first requirement reproduces one of the two conditions that we have already imposed on the displacement of locally reacting surfaces. Denoting by δu the variation of u, Hamilton's principle finally yields the condition

$$0 = \delta S = -\int_{\mathbb{R}^+ \times \mathcal{F}} dt dA_0 \, \delta u \left[\rho_m d_m \partial_t^2 u - T_0 d_m \left(\Delta_\partial u + \kappa^2 \frac{\Delta_\partial^2 u}{2} \right) \right]. \tag{2.30}$$

By the fundamental lemma of variational calculus an, albeit preliminary, equation of motion follows:

$$0 = \rho_m d_m \partial_t^2 u - T_0 d_m \left(-\Delta_\partial u + \kappa^2 \frac{\Delta_\partial^2 u}{2} \right). \tag{2.31}$$

Damping can be included by a slight modification of ∂_t^2. Let $\Sigma : \mathbb{R}^+ \to I \subset \mathbb{R}^+$ be an orientation preserving diffeomorphism of $\mathbb{R}^+$ onto one of its open intervals, say I, and replace

$$\partial_t^2 \to \mathsf{D}_t^2 \equiv \Sigma(t)^{-1} \partial_t (\Sigma(t) \partial_t). \tag{2.32}$$

The choice $\Sigma(t) = \exp(2\alpha t)$ $(\alpha > 0)$ reproduces linear damping. Note that D_t^2 is not symmetric and thus does not permit a Friedrichs extension.

It remains to model the coupling with the acoustic pressure p and the outside signal p_{ex}. This is accomplished by noting that $\delta W = -p\Delta V$ represents the thermodynamic differential volume work. Since from the outside of the cavity, an external pressure stimulus p_{ex} impinges on the membrane, the internal acoustic pressure forms to ensure

overall mechanical equilibrium by the discussion in the previous section. The net work is $\delta W = -\delta p \Delta V$ where $\delta p = p_{\text{ex}} - p$. The coordinates chosen above permit to evaluate the pressure difference on the fixed $\mathcal{F}$ rather than the undulating surface defined by u. The local volume change ΔV is to be understood in the sense of thermodynamics rather than the geometrical volume dV used in the previous part of the derivation. Locally, for both p_{ex} and p, the available air volume changes as $\Delta V = u \, dA_0$ where u denotes the amplitude of the undulation. Inclusion of δW in dE_{pot} and variation of the modified quadratic action S with respect to u, results in an inhomogeneity to the formerly homogeneous equation for u.

Upon modification to account for damping, the dynamics of the locally reacting surface u is governed by

$$p_{\text{ex}} - p = \rho_m d_m \mathsf{D}_t^2 u - T_0 d_m \left(\Delta_\partial u - \kappa^2 \frac{\Delta_\partial^2 u}{2} \right). \qquad (2.33)$$

Division through $\rho_m d$ yields, in conjunction with $\kappa = 0$ and $\Sigma(t) = \exp(2\alpha t)$ $(\alpha = 0)$, the damped membrane equation used in [147, 148, 158]: Set $c_m^2 = T_0/(\rho_m d_m) \equiv T_0/\sigma_m$ with the surface mass density σ_m and $\Phi = (p_{\text{ex}} - p)/(\rho_m d_m)$ to find

$$\partial_t^2 u + 2\alpha \partial_t u - c_m^2 \Delta_\partial u = \Phi. \qquad (2.34)$$

Eigenfunctions and eigenvalues   Let $\mathbf{k} = (k_1, k_2) \in \mathbb{N} \times \mathbb{N}$. The eigenfunctions and eigenvalues for the Laplace-Beltrami operator Δ_∂ on $\mathcal{F} \in \{\Gamma_0, \Gamma_L\}$ with homogeneous Dirichlet boundary conditions on $\partial \mathcal{F}$ can be found by separation of variables [123, 124]:

$$\psi_{\mathbf{k}}^\partial(r, \phi) = \frac{J_{\frac{k_1 \pi}{2\pi - 2\beta}} \left(\frac{\nu_{k_1 k_2} r}{a_{\text{tymp}}} \right) \sin \left(\frac{k_1 \pi (\phi - \beta)}{2\pi - 2\beta} \right)}{\frac{\sqrt{2(\pi - \beta)} a_{\text{tymp}}}{2} \left| J'_{\frac{k_1 \pi}{2\pi - 2\beta}} \left(\nu_{k_1 k_2} \right) \right|}, \qquad (2.35)$$

$$\left(\omega_{\mathbf{k}}^\partial \right)^2 = c_m^2 \left(\frac{\nu_{k_1 k_2}^2}{a_{\text{tymp}}^2} \right) \qquad (2.36)$$

where only eigenfunctions which exhibit regular behavior as $r \to 0$ as $\lim_{r \to 0} |\Phi_{k_1, k_2}(r, \phi)| < \infty$ are kept and the "trivial" eigenfunction 0 is omitted. Let $\mathbf{n} \equiv (n_1, n_2, n_3) \in \mathbb{N}_0 \times \mathbb{Z} \times \mathbb{N}_0$.

The eigenfunctions and eigenvalues for the Laplace-Beltrami operator on $\mathcal{Z}_{\text{stat}}$ with homogeneous Neumann boundary conditions on $\partial \mathcal{Z}_{\text{stat}}$ can be found by an analysis of cases in a treatment by separation of variables. The distinction by cases is indicated

as (Letter) and the case condition is given below the expression for the eigenfunctions and eigenvalues in questions:

$$\psi_{\mathbf{n}}(r,\phi,z) = \begin{cases} \dfrac{1}{\sqrt{\pi a_{\text{cyl}}^2 L}} & \text{(A)} \\[2ex] \dfrac{J_{n_1}\left(\frac{\mu_{n_1 0} r}{a_{\text{cyl}}}\right)}{\sqrt{2\pi L}\sqrt{\mu_{n_1 0}^2 - n_1^2}\left|J_{n_1}(\mu_{n_1 0})\right|} & \text{(B)} \\[3ex] \dfrac{J_{n_1}\left(\frac{\mu_{n_1 |n_2|} r}{a_{\text{cyl}}}\right)e^{in_2\phi}}{\sqrt{\pi L}\sqrt{\mu_{n_1|n_2|}^2 - n_1^2}\left|J_{n_1}(\mu_{n_1|n_2|})\right|} & \text{(C)} \\[3ex] \dfrac{\sqrt{2}\cos\left(\frac{n_3\pi x}{L}\right)}{\sqrt{\pi a_{\text{tymp}}^2 L}} & \text{(D)} \\[3ex] \dfrac{\sqrt{2}J_{n_1}\left(\frac{\mu_{n_1|n_2|} r}{a_{\text{cyl}}}\right)e^{in_2\phi}\cos\left(\frac{n_3\pi x}{L}\right)}{\sqrt{\pi L}\sqrt{\mu_{n_1|n_2|}^2 - n_1^2}\left|J_{n_1}(\mu_{n_1|n_2|})\right|} & \text{(E)} \end{cases} \tag{2.37}$$

$$\omega_{\mathbf{n}}^2 = c^2\left(\frac{\mu_{n_1 n_2}^2}{a_{\text{cyl}}^2} + \frac{n_3^2\pi^2}{L^2}\right) \tag{2.38}$$

(A) requires $0 = n_1 = n_2 = n_3$, (B) necessitates $n_1 \neq 0$ and $n_2 = n_3 = 0$, (C) is applicable if $n_1 \neq 0$, $n_2 \neq 0$ and $n_3 = 0$, (D) means $n_1 = n_2 = 0$ and $n_3 \neq 0$ and (E) captures the remaining possibility $n_1 \neq 0$, $n_2 \neq 0$, $n_3 \neq 0$.

Each set of both eigenfunctions $\{\psi_{\mathbf{k}}^\partial\}_{\mathbf{k}}$ and $\{\psi_{\mathbf{n}}\}_{\mathbf{n}}$ is a complete system of normalized, pairwisely orthogonal functions on the corresponding domain with respect to the L^2-inner product, the L^2-norm, respectively. The two systems of functions do not satisfy mutual orthogonality.

The discussion of the boundary conditions for the locally reacting surfaces' equations of motion needs to be completed: Let $\delta > 0$ be sufficiently small and $\Gamma_{0,\delta} \equiv \{\text{pt} \in \mathcal{F}_0 : \text{dist}_2(\text{pt},\Gamma_0) < \delta\}$ and $\Gamma_{L,\delta} \equiv \{\text{pt} \in \mathcal{F}_L : \text{dist}_2(\text{pt},\Gamma_0) < \delta\}$. Obviously, $\{\psi_{k_1 k_2}^\partial\}_{k_1,k_2}$ can be extended at least $\mathcal{C}^2$-regularly from Γ_0 and Γ_L to $\Gamma_{0,\delta}$ and $\Gamma_{L,\delta}$ for the sufficiently small $\delta > 0$ - a consequence of the physical regularity behavior of the involved objects. Then we can evaluate the algebraic expression $\Delta_\partial \psi_{k_1 k_2}(r,\phi) = -c_m^{-2}(\omega_{k_1 k_2}^\partial)^2\psi_{k_1 k_2}(r,\phi)$ on $\partial\mathcal{F}$ for the $\mathcal{F} \in \{\Gamma_0,\Gamma_L\}$ employed in the derivation in the previous paragraph. The eigenvalue of the Dirichlet Laplacian is nonzero for non-trivial eigenfunctions such that $\Delta_\partial u = 0$ is equivalent to $u = 0$ on $\partial\mathcal{F}$ in terms of an eigenfunction expansion of u in eigenfunctions of the Dirichlet Laplace-Beltrami operator studied in the beginning of the paragraph.

Physically, the condition $\Delta^\partial u = 0$ on $\partial\mathcal{F}$ can be understood as a linearization of the requirement that the undulating locally reacting surface has vanishing mean curvature at the boundary - for small-amplitude vibrations in the ICE context, biology

has already implemented the requirement by clamping a given tympanum to the much heavier surrounding bony structure at its boundary.

Perturbation expansion   The full problem consists of the perturbed acoustic wave equation on $\mathcal{Z}_{\mathrm{stat}}$ for the acoustic pressure p forming out in the, by now, stationary cavity

$$\partial_t^2 p - c^2 \left(\partial_r^2 p + r^{-1}\partial_r p + r^{-2}\partial_\phi^2 p + \partial_x^2 p \right) + \mathsf{V}[p] = 0. \tag{2.39}$$

Setting $P(\heartsuit) = \heartsuit - \kappa^2 \heartsuit^2/2$, the locally reacting surfaces u_0, u_L are described

$$\mathsf{D}_t^2 u_0 - c_m^2 P(\Delta_\partial)u_0 = \sigma_m^{-1}\left(p_{\mathrm{ex}} - p\right)\big|_{x=0} \tag{2.40}$$

$$\mathsf{D}_t^2 u_L - c_m^2 P(\Delta_\partial)u_L = \sigma_m^{-1}\left(p_{\mathrm{ex}} - p\right)\big|_{x=L} \tag{2.41}$$

where $\Delta_\partial = \partial_r^2 + r^{-1}\partial_r + r^{-2}\partial_\phi^2$ is the Laplace operator on Γ_0, Γ_L expressed in those polar coordinates that agree with the polar part of the cylindrical coordinates utilized for the economic description of $\mathcal{Z}_{\mathrm{stat}}$.

Note that although algebraically $\Delta_\partial + \partial_x^2$ reproduces the Laplace-Beltrami operator on $\mathcal{Z}_{\mathrm{stat}}$, the operators are different as can already be inferred from the different boundary conditions (Neumann vs. Dirichlet) assigned to them. The non-homogeneity in the boundary conditions occurs only for the perturbed acoustic wave equation at the $x = 0$ face through $\partial_x p = -\rho_0 \partial_t \dot{u}_0$ and at the $x = L$ face through $\partial_x p = -\rho_0 \partial_t \dot{u}_L$. The rest of boundary and initial data for the three equations is homogeneous.

We set $p_{\mathrm{ex}}(t, x = 0) = p_0 \exp(i\omega t + i\phi_0)$ and $p_{\mathrm{ex}}(t, x = L) = p_0 \exp(i\omega t + i\phi_L)$ with two phases $\phi_0, \phi_L \in [0, 2\pi)$ which bear auditory information in the context of the ICE model and have been surveyed exhaustively [147, 148, 158, 140]. Here, p_{ex} corresponds to a time-harmonic pressure signal that impinges on the cavity from the acoustic far-field.

The solution strategy consists of using the smallness of the perturbation V compared to $\square_{0,t}$ to handle the acoustic wave equation by time-dependent perturbation theory in the style of Dirac [34][§44]. Indeed, since $\mathsf{V} \sim \delta G \sim \epsilon$ in terms of scaling relative to $\square_{0,t}$-like operators,

$$\partial_t^2 p - c^2(\partial_r^2 + r^{-1}\partial_r + r^{-2}\partial_\phi^2 + \partial_x^2)p = -\epsilon \mathsf{V}_0[p] \tag{2.42}$$

where $\mathsf{V}_0 \equiv \epsilon^{-1}\mathsf{V}$ denotes a re-scaling of V such as to obtain the scaling $\mathsf{V} \sim \square_{0,t}$. In most applications of vibrational acoustics, $\epsilon \ll 1$. E.g., in the ICE context the

membrane displacement can be measured to be $\sim 10^{-9}$ m whereas the length of the cavity $\mathcal{Z}_{\text{stat}}$ is $\sim 10^{-2}$ m.

Acoustically, the impact of the perturbation is negligible on the sound pressure level of the internal pressure p. More formally, the smallness of the perturbation can be used to invert the wave operator on the left-hand side of the equation and iterate the equation.

Let $\mathsf{G}_0 = \Box_{0,t}^{-1}$ denote the inverse operator to the wave-operator $\Box_{0,t}$ on the left-hand side of the above equation. Assuming high-enough regularity behavior of p and the displacements u_0, u_l, we can write the inverse operator $\mathsf{G} = (\Box_{0,t} + \mathsf{V})^{-1}$ as

$$\mathsf{G} = \sum_{n=0}^{\infty} (-\epsilon)^n (\mathsf{G}_0 \cdot \mathsf{V}_0)^n \cdot \mathsf{G}_0. \tag{2.43}$$

where $\cdot$ denotes the (non-commutative!) composition of operators. G_0 acts on a suitable function f as

$$\mathsf{G}_0[f] = \sum_{\mathbf{n}} \psi_{\mathbf{n}}(r, \phi, x) \int_0^t d\tau \, \frac{\sin\left((t - \tau)\omega_{\mathbf{n}}\right)}{\omega_{\mathbf{n}}} \int_{\mathcal{Z}_{\text{stat}}} d(\rho, \varphi, \zeta) \, \rho \psi_{\mathbf{n}}^{\dagger}(\rho, \varphi, \zeta) f(\tau, \rho, \varphi, \zeta).$$

$$\tag{2.44}$$

The expression is obtained by Duhamel's principle, treating the Laplace-Beltrami operator Δ on $\mathcal{Z}_{\text{stat}}$ in the sense of Borel's functional calculus [122, 123, 124]. Afterwards, the spectral theorem is invoked to obtain the summation over the eigenvalues of Δ.

So far nothing has been solved because we do not know the perturbation operator V. The latter operator depends explicitly on the unknown functions u_0, u_L. The above perturbation expansion is based on the overall setup assumptions that there are suitably regular solutions (p, u_0, u_L) and u_0, u_L and derivatives thereof are suitably small compared to L.

Fixed-point iteration The general damping $\Sigma = \Sigma(t)$ inscribed in $\mathsf{D}_t^2 = \Sigma^{-1} \partial_t (\Sigma \partial_t)$ permits an analytic treatment, too. The restrictions on the choice of Σ ensures that its natural logarithm and its square root as well as the composition of natural logarithm and square root on Σ are well-defined. Since Σ depends only on t it represents a constant with respect to the Laplace-Beltrami operator Δ on $\mathcal{Z}_{\text{stat}}$. The inverse operator $\mathsf{H}_0 \equiv (\mathsf{D}_t^2 - c_m^2 P(\Delta_\partial))^{-1}$ is then found by reduction of the equation of motion for u_0 respectively u_L to a Klein-Gordon type equation.

Conversion into a first-order operator differential equation shows that the t-dependent matrices in the operator differential equation commute at different t's. Upon definition

of $Q(t) \equiv -(\partial_t \log \sqrt{\Sigma(t)})^2 + \partial_t^2 \log \sqrt{\Sigma(t)}$, we find that H_0 acts on suitable functions, say g, as

$$
\begin{aligned}
\mathsf{H}_0[g] = \sum_{\mathbf{k}} \psi_{\mathbf{k}}^{\partial}(r, \phi) \int_0^t d\tau \sqrt{\frac{\Sigma(\tau)}{\Sigma(t)}} \frac{\sin\left((t - \tau)\sqrt{I_{\mathbf{k}}}\right)}{\sqrt{I_{\mathbf{k}}}} \\
\times \int_{\mathcal{F} \in \{\Gamma_0, \Gamma_L\}} d(\rho, \varphi)\, \rho \left(\psi_{\mathbf{k}}^{\partial}\right)^{\dagger}(\rho, \varphi) g(\rho, \varphi).
\end{aligned}
\tag{2.45}
$$

where $I_{\mathbf{k}} = I_{\mathbf{k}}(t - \tau)$ is given for a $\mathbf{k} \in \mathbb{N} \times \mathbb{N}$ through the following integral representation

$$
I_{\mathbf{k}} = \int_0^1 d\xi \left[c_m^2 P\left(-c_m^{-2} \left(\omega_{\mathbf{k}}^{\partial}\right)^2\right) + Q(\xi(t - \tau)) \right].
\tag{2.46}
$$

In the case of linear damping $\sim 2\alpha \partial_t$, i.e., $\Sigma(t) = \exp(2\alpha t)$ ($\alpha > 0$) and $\kappa = 0$, i.e., in the model of damped flexible membranes as locally reacting surfaces, the formula reduces to the inverse operator for the damped wave-equation on a circular sector $\mathcal{F} \in \{\Gamma_0, \Gamma_L\}$:

$$
\begin{aligned}
\mathsf{H}_0[g] = \sum_{\mathbf{k}} \int_0^t \frac{d\tau\, e^{-\alpha(t - \tau)} \sin\left((t - \tau)\sqrt{\left(\omega_{\mathbf{k}}^{\partial}\right)^2 - \alpha^2}\right)}{\sqrt{\left(\omega_{\mathbf{k}}^{\partial}\right)^2 - \alpha^2}} \\
\times \psi_{\mathbf{k}}^{\partial}(r, \phi) \int_{\mathcal{F}} d(\rho, \varphi)\, \rho \left(\psi_{\mathbf{k}}^{\partial}\right)^{\dagger}(\rho, \varphi) g(\rho, \varphi).
\end{aligned}
\tag{2.47}
$$

In order to obtain an explicit solution in the end, we need a method to decouple the three equations. Consequently, the next step is an iteration procedure. Recall that solutions need to satisfy in particular the homogeneous initial conditions $p(t = 0) = 0$, $\dot{p}(t = 0) = 0$ and $u_0(t = 0) = 0$, $\dot{u}_0(t = 0) = 0$ as well as $u_L(t = 0) = 0$, $\dot{u}_L(t = 0) = 0$. If $p^{(0)} = 0$, $u_0^{(0)} = 0$ and $u_L^{(0)} = 0$ are chosen to be the starting points for a fixed point iteration. The partial differential equations decouple in first iteration and we find

$$
p^{(1)} = 0, \quad u_0^{(1)} = \mathsf{H}_0 \left[\frac{p_{\text{ex}}|_{x=0}}{\sigma_m} \right], \quad u_L^{(1)} = \mathsf{H}_0 \left[\frac{p_{\text{ex}}|_{x=L}}{\sigma_m} \right].
\tag{2.48}
$$

To give the full iteration scheme, it is useful to include the locally reacting surfaces u_0, u_L explicitly in the perturbation operator by setting $\mathsf{V}[\bullet] = \mathsf{V}[u_0, u_L, \bullet]$. The idea is to use the smallness of the perturbation to perform a fixed point iteration in the spirit of the Picard-iteration: Assuming physical regularity of the involved quantities, the fixed point iteration converges - see e.g. [95, 26] for convergence estimates in the context of the Magnus series [14, 13] which is equivalent to our Ansatz. Typical estimates as the one for the Magnus series involve (towers of) Sobolev spaces.

Accordingly, the assumption of physical, i.e., at best smooth, regularity ensures convergence although the assumption is not optimized in the sense that it does not specify the minimum regularity needed to ensure convergence of the iteration scheme we are about to present:

$$p^{(k+1)} = \mathsf{G}_0[\mathsf{V}[u_0^{(k)}, u_L^{(k)}, p^{(k)}]] + \partial\mathcal{G}^{(k)}[u_0^{(k)}, u_L^{(k)}], \tag{2.49}$$

$$u_0^{(k+1)} = \mathsf{H}_0\left[\sigma_m^{-1}\left(p_{\mathrm{ex}} - p^{(k)}\right)\big|_{x=0}\right], \tag{2.50}$$

$$u_L^{(k+1)} = \mathsf{H}_0\left[\sigma_m^{-1}\left(p_{\mathrm{ex}} - p^{(k)}\right)\big|_{x=L}\right]. \tag{2.51}$$

The symbol $\partial\mathcal{G}^{(k)}$ denotes that also the boundary conditions to the Laplace-Beltrami operator in the perturbed wave equation for p yields a non-trivial contribution at the endcaps $\Gamma_0 \subset \mathcal{F}_0$ and $\Gamma_L \subset \mathcal{F}_L$. Notice that a priori a suitably modified version of the full operator G acts on the boundary conditions.

In the next paragraph, the smallness of the perturbation, loosely denoted as "$\mathsf{V} \sim \epsilon$" in physicists' terminology, will aid at reducing the full, nonlinear problem to a problem of three linearly coupled partial differential equations.

Reduced problem Typical, low-amplitude acoustics takes place at sufficiently "low" sound pressure levels $\lesssim 130\,\mathrm{dB}$ and, accordingly, is governed by small amplitude vibrations of the air particles $\sim (10^0 - 10^1)\,\mathrm{nm}$ and as such also the typical vibration amplitudes of the locally reacting surfaces are in this range. This is a cue for an overall linear treatment of the problem although the physics is - strictly speaking - requiring a nonlinear description including the perturbation V.

Given our assumptions on the behavior of u_0, u_L, we need to ensure that the first derivatives are suitably small. A typical vibration amplitude over the length of the cylindrical cavity in the ICE model is $\epsilon \sim U/L \lesssim 10^{-6}$ for a cavity of length $L \simeq 10^0\,\mathrm{cm}$ and vibration amplitudes $U \simeq 10^{-9}\,\mathrm{m}$. The iteration scheme above produces in every step additional contributions scaling a factor of ϵ higher. We can determine the leading order contribution to the internal pressure p from the second iteration around the starting values $p^{(0)} = 0$, $u_0^{(0)} = 0$ and $u_L^{(0)} = 0$. This yields (2.48).

Insertion of $p^{(1)}, u_0^{(1)}, u_L^{(1)}$ in the second iteration, i.e., determining $p^{(2)}$, yields

$$p^{(2)} = \partial\mathsf{G}^{(1)}[u_0^{(1)}, u_L^{(1)}] \tag{2.52}$$

where we repeat the expressions for $u_0^{(1)}$ and $u_L^{(1)}$ for the reader's convenience

$$u_0^{(1)} = \mathsf{H}_0\left[\frac{p_{\mathrm{ex}}|_{x=0}}{\sigma_m}\right], \quad u_L^{(1)} = \mathsf{H}_0\left[\frac{p_{\mathrm{ex}}|_{x=L}}{\sigma_m}\right]. \tag{2.53}$$

Next, the symbol $\partial \mathcal{G}^{(k)}$ awaits specification of its meaning. The differential equation satisfied by $p^{(2)}$ is

$$\partial_t^2 p^{(2)} - c^2(\partial_r^2 + r^{-1}\partial_r + r^{-2}\partial_\phi^2 + \partial_x^2)p^{(2)} + \mathsf{V}[u_0^{(1)}, u_L^{(1)}, p^{(1)}] \tag{2.54}$$

$$= \partial_t^2 p^{(2)} - c^2(\partial_r^2 + r^{-1}\partial_r + r^{-2}\partial_\phi^2 + \partial_x^2)p^{(2)} = 0 \tag{2.55}$$

by noting linearity of V in its third argument, i.e., $\mathsf{V}[u^{(1)}, u_L^{(1)}, p^{(1)} = 0] = 0$. Consistency of the iteration scheme requires that object $\partial\mathsf{G}^{(k)}$ respect the iteration employed to solve the coupled system of partial differential equations in a yet to be settled sense. For $k \in \mathbb{N}$, we define:

$$(\partial\mathcal{G})^{(k)} \equiv \mathsf{G}_0|_{\mathbb{R}^+ \times \partial \mathcal{Z}_{\mathrm{stat}}} \tag{2.56}$$

and understand this as a truncation of the boundary integral in Green's theorem applied to Neumann boundary value problems.

For a suitable function f on $\bar{\mathcal{M}}$, the above prescriptions are shorthand for

$$\partial\mathsf{G}^{(k)}[f] = \sum_{\mathbf{n}} \psi_{\mathbf{n}}(r, \phi, x) \int_0^t d\tau \frac{\sin((t-\tau)\omega_{\mathbf{n}})}{\omega_{\mathbf{n}}} \int_{\partial\mathcal{Z}_{\mathrm{stat}}} dO\, \rho \psi_{\mathbf{n}}^\dagger(\rho, \varphi, \zeta) f(\tau, \rho, \varphi, \zeta) \tag{2.57}$$

The definition ensures that the boundary conditions to the differential equation for p contribute linearly and the perturbation term $\mathsf{G}_0[\mathsf{V}[u_0^{(k)}, u_L^{(k)}, p^{(k)}]]$ is responsible for introducing corrections to the boundary conditions in higher orders of ϵ in further iterations. Since these corrections can be neglected compared to the leading $\sim \epsilon$ contribution, the internal pressure $p^{(2)}$ is given through

$$p^{(2)} = -\rho_0 \sum_{\mathbf{n}} \psi_{\mathbf{n}}(r, \phi, x) \int_0^t d\tau \frac{\sin((t-\tau)\omega_{\mathbf{n}})}{\omega_{\mathbf{n}}} \int_{\Gamma_0} d(\rho, \phi)\, \rho \psi_{\mathbf{n}}^\dagger(\rho, \varphi, 0) \partial_t \dot{u}_0^{(1)}(\tau, \rho, \varphi)$$
$$- \rho_0 \sum_{\mathbf{n}} \psi_{\mathbf{n}}(r, \phi, x) \int_0^t d\tau \frac{\sin((t-\tau)\omega_{\mathbf{n}})}{\omega_{\mathbf{n}}} \int_{\Gamma_L} d(\rho, \phi)\, \rho \psi_{\mathbf{n}}^\dagger(\rho, \varphi, 0) \partial_t \dot{u}_L^{(1)}(\tau, \rho, \varphi) \tag{2.58}$$

where the fact that $\dot{u}_0^{(1)}$, $\dot{u}_L^{(1)}$ are non-zero only on $\Gamma_0 \subset \mathcal{F}_0$ and $\Gamma_L \subset \mathcal{F}_L$ has already been incorporated.

It is worth noting that the above equation is also the Green's function representation for the Neumann initial boundary value problem on $\mathcal{M} = \mathbb{R}^+ \times \mathcal{Z}_{\mathrm{stat}}$

$$\partial_t^2 p^{(2)} + c^2(\partial_r^2 + r^{-1}\partial_r + r^{-2}\partial_\phi^2 + \partial_x^2)p^{(2)} = 0 \tag{2.59}$$

with homogeneous initial and homogeneous Neumann boundary conditions for $p^{(2)}$ except on Γ_0, Γ_L where $\partial_x p^{(2)}(t, r, \phi, x_0) = -\rho_0 \partial_t \dot{u}_{x_0}^{(1)}(t, r, \phi)$ for $x_0 \in \{0, L\}$.

Quasi-stationary solution in the case of linear damping The specific case of the damping function $\Sigma(t) = \exp(2\alpha t)$ with $\alpha > 0$ and κ a fixed but very small ($\kappa < \epsilon$) length scale is tractable and a frequent case in applications. It accounts for a linear damping $\sim 2\alpha\partial_t$ in the equations of motion of the displacements of the locally reacting surfaces. Due to the damping, the system exhibits for stimuli frequencies $\omega \notin \left\{\omega | -\omega^2 + 2\alpha i\omega - c_m^2 P\left(-c_m^{-2}\left(\omega_{\mathbf{k}}^{\partial}\right)^2\right) = 0\right\}$ and $t \gg \alpha^{-1}$ a quasi-stationary state.

The first condition corresponds to excluding resonances, the second condition allows us to neglect an overall contribution scaling as $\sim \exp(-\alpha t)$. The displacements of the locally reacting surfaces follows with the so-called mass coupling constant $\rho_0/\rho_m \equiv \mathfrak{g}$ from (2.53): Abbreviating $u_{0,\text{q.s.}}^{(1)}(t, r, \phi) = U_{0,\text{q.s.}}^{(1)}(r, \phi) \exp(i\omega t + i\phi_0)$ and $u_{L,\text{q.s.}}^{(1)}(t, r, \phi) = U_{L,\text{q.s.}}^{(1)}(r, \phi) \exp(i\omega t + \phi_L)$ with "q.s" indicating the quasi-stationary state, it holds that

$$U_{0,\text{q.s.}}^{(1)}(r, \phi) = \frac{-\mathfrak{g}p_0}{\rho_0 d} \sum_{\mathbf{k}} \frac{\psi_{\mathbf{k}}^{\partial}(r, \phi) \int_{\Gamma_0} d(\rho, \varphi)\, \rho \left(\psi_{\mathbf{k}}^{\partial}\right)^{\dagger}(\rho, \varphi)}{-\omega^2 + 2\alpha i\omega - c_m^2 P\left(-c_m^{-2}\left(\omega_{\mathbf{k}}^{\partial}\right)^2\right)}, \tag{2.60}$$

$$U_{L,\text{q.s.}}^{(1)}(r, \phi) = \frac{-\mathfrak{g}p_0}{\rho_0 d} \sum_{\mathbf{k}} \frac{\psi_{\mathbf{k}}^{\partial}(r, \phi) \int_{\Gamma_L} d(\rho, \varphi)\, \rho \left(\psi_{\mathbf{k}}^{\partial}\right)^{\dagger}(\rho, \varphi)}{-\omega^2 + 2\alpha i\omega - c_m^2 P\left(-c_m^{-2}\left(\omega_{\mathbf{k}}^{\partial}\right)^2\right)}. \tag{2.61}$$

for (r, ϕ) polar coordinates on Γ_0, Γ_L.

Using only the above quasi-stationary state solution, insertion of (2.60) and (2.61) into (2.58) yields $p^{(2)}$ as

$$p_{\text{q.s.}}^{(2)} = -\rho_0 c^2 \omega^2 \sum_{\mathbf{n}} \frac{[e^{i\omega t} - R_{\mathbf{n}}(t)]\, \psi_{\mathbf{n}}(r, \phi, x) \sum_{x_0 \in \{0, L\}} e^{i\phi_{x_0}} \int_{\Gamma_{x_0}} d(\rho, \varphi)\, \rho\psi_{\mathbf{n}}^{\dagger}(\rho, \varphi, x_0) U_{x_0}^{(1)}(\rho, \varphi)}{-\omega^2 + \omega_{\mathbf{n}}^2}.$$

$$\tag{2.62}$$

where $R_{\mathbf{n}}(t) \equiv \omega_{\mathbf{n}}^{-1}\left(i\omega \sin\left(\omega_{\mathbf{n}}t\right) + \omega_{\mathbf{n}} \cos\left(\omega_{\mathbf{n}}t\right)\right)$ ensures that $p^{(2)}$ stay finite during resonance, $\lim_{\omega \to \omega_{\mathbf{n}}} |p^{(2)}(t)| < \infty$.

For the next paragraph, we note that $p^{(2)}$ scales as $\mathfrak{g}$, which is readily seen by insertion of $U_{0,\text{q.s.}}^{(1)}$ and $U_{0,\text{q.s.}}^{(1)}$ in the above formula.

Relaxation behavior An assessment of the full system during relaxation in the quasi-stationary state yields a sharper criterion for the time which is needed to neglect phase-like contributions from frequencies other than the stimulus' frequency ω. For $x_0 \in \{0, L\}$, the difference $\delta u_{x_0}^{(1)} \equiv u_{x_0}^{(1)} - u_{x_0,\text{q.s}}^{(1)}$ between the full and the quasi-stationary state solution is the quantity of interest.

Let us define the reduced surface eigenfrequency $\omega_{r,\mathbf{k}}^{\partial} \equiv \sqrt{c_m^2 P\left(-c_m^{-2}\left(\omega_{\mathbf{k}}^{\partial}\right)^2 - \alpha^2\right)}$ and the transient function $t_{\mathbf{k}}(t) \equiv (\omega_{r,\mathbf{k}}^{\partial})^{-1}\left(\omega_{r,\mathbf{k}}^{\partial}\cos\left(\omega_{r,\mathbf{k}}^{\partial}t\right) + (\alpha + i\omega)\sin\left(\omega_{r,\mathbf{k}}^{\partial}t\right)\right)$. The latter serves as a mathematical storage for phase-like contributions at the reduced eigenfrequency $\omega_{r,\mathbf{k}}^{\partial}$ of the locally reacting surface rather than the stimulus' frequency ω.

We anticipate that the most relevant object is the transient coupling strength, defined through $\mathfrak{h}(t) \equiv \mathfrak{g}\exp(-\alpha t)$. The coupling strength $\mathfrak{g}$ is used as an expansion parameter in vibrational acoustics to quantify the coupling of an air parcel of mass density ρ_0 to a material parcel of mass density ρ_m. By the inscription of the locally reacting surfaces' inherent damping $\sim \exp(-\alpha t)$ into the transient coupling strength $\mathfrak{h}(t)$, a dynamically evolving smallness parameter in units of the usual coupling strength $\mathfrak{g}$ is devised.

For $\delta u_{x_0}^{(1)}$, we find

$$\delta u_{x_0}^{(1)} = \frac{p_0 \mathfrak{h}(t)}{\rho_0 d}\sum_{\mathbf{k}}\frac{t_{\mathbf{k}}(t)\psi_{\mathbf{k}}^{\partial}(r,\phi)\int_{\Gamma_{x_0}}d(\rho,\varphi)\,\rho\left(\psi_{\mathbf{k}}^{\partial}\right)^{\dagger}(\rho,\varphi)}{-\omega^2 + 2\alpha i\omega - c_m^2 P\left(-c_m^{-2}\left(\omega_{\mathbf{k}}^{\partial}\right)^2\right)}. \tag{2.63}$$

It scales as $\sim \mathfrak{h}(t)$. Following the above logic, the difference between the full internal pressure $p^{(2)}$ and its quasi-stationary counterpart $p_{\text{q.s.}}^{(2)}$, that is, $\delta p^{(2)} \equiv p^{(2)} - p_{\text{q.s.}}^{(2)}$, is investigated.

A variation of physically insignificant smallness in the material parameters ensure the validity of the following mathematical assumption: $\omega_{r,\mathbf{k}}^{\partial} \notin \sigma\left(\sqrt{-c^2\Delta}\right)$ for all $\mathbf{k} \in \mathbb{N}\times\mathbb{N}$. This way, divergences in the subsequent formulas can be excluded a priori.

Let us define the auxiliary quantities $C_{\mathbf{n},\text{o}} \equiv (\omega_{r,\mathbf{k}}^{\partial})\left((\alpha^2 - (\omega_{r,\mathbf{k}}^{\partial})^2)(\alpha + i\omega) + 2\alpha(\omega_{r,\mathbf{k}}^{\partial})\right)$. $C_{\mathbf{n},\text{e}} \equiv \alpha^2 - (\omega_{r,\mathbf{k}}^{\partial})^2 - 2\alpha(\alpha + i\omega)$, $k_{\mathbf{n},\mathbf{k}} \equiv \left((i\omega_{r,\mathbf{k}}^{\partial} - \alpha)^2 - \omega_{\mathbf{n}}^2\right)^{-1}$. Upon modal expansion and seeking for a specific solution to the resulting harmonic oscillator equations by the Ansatz $\sim \exp(i\omega_{r,\mathbf{k}}t)$, we find that $\delta p^{(2)}$ satisfies

$$\delta p^{(2)} = -\frac{p_0 \mathfrak{h}(t)c^2}{d}\sum_{x_0\in\{0,L\},\mathbf{k},\mathbf{n}}\left\{\left[C_{\mathbf{k},\text{e}}\Re\left(k_{\mathbf{n},\mathbf{k}}e^{i\omega_{r,\mathbf{k}}^{\partial}t}\right) + C_{\mathbf{k},\text{o}}\Im\left(k_{\mathbf{n},\mathbf{k}}e^{i\omega_{r,\mathbf{k}}^{\partial}t}\right)\right]\psi_{\mathbf{n}}(r,\phi,x)\right.$$
$$\left.\times\frac{\int_{\Gamma_{x_0}}d(\rho,\varphi)\,\rho'\psi_{\mathbf{n}}^{\dagger}(\rho,\varphi,x_0)\psi_{\mathbf{k}}^{\partial}(\rho,\varphi)\int_{\Gamma_{x_0}}d(\rho',\varphi')\,\rho'\left(\psi_{\mathbf{k}}^{\partial}\right)^{\dagger}(\rho',\varphi')}{-\omega^2 + 2\alpha i\omega - c_m^2 P\left(-c_m^{-2}\left(\omega_{\mathbf{k}}^{\partial}\right)^2\right)}\right\}.$$
$$\tag{2.64}$$

Again, it scales as $\sim \mathfrak{h}(t)$.

Since for $x_0 \in \{0, L\}$, the quasi-stationary displacement $u^{(1)}_{x_0,\text{q.s.}}$ of the locally reacting surfaces and $p^{(2)}$ scale as $\sim \mathfrak{g}$ in terms of the vibrational acoustics' smallness parameter $\mathfrak{g}$, neglection of contributions scaling as $\sim \mathfrak{g}^2$ is possible after the equilibration time $T_{\text{eq}} \equiv -\alpha^{-1} \log \mathfrak{g}$. After T_{eq}, $\delta u^{(1)}_{x_0}, \delta p^{(2)} \sim \mathfrak{g}^2$ and thus are negligible in terms of their $\mathfrak{g}$-scaling behavior against the quasi-stationary state solutions $u^{(1)}_{x_0}$, $p^{(2)}$ scaling as $\mathfrak{g}^1$.

Fig. 2.2 shows the dynamics of the fundamental mode ψ^{∂}_{11} for *Gecko gekko* (A) and *Varanus salvator* (B). In (A) as well as (B) the relaxation to the quasi-stationary, or harmonic, asymptotics is fast: after 1 and 5 ms, respectively. For data see [147, 148, 158].

Piston approximation Since two elements of the complete system of normalizes and orthogonal functions, one from $\{\psi^{\partial}_{\mathbf{k}}\}_{\mathbf{k}}$ and the other one from $\{\psi_{\mathbf{n}}\}_{\mathbf{n}}$, are in general *not* orthogonal, the quasi-stationary state solution $p^{(2)}_{\text{q.s.}}$ contains, via $U^{(1)}_0$ and $U^{(1)}_L$, a double sum ranging over $\mathbf{k}$ and $\mathbf{n}$.

Suppose that the cylinder's geometric dimensions a_{cyl}, L are such that $a_{\text{cyl}} < L$ but $a_{\text{cyl}} \lll L$, for example a "short cylinder". This assumption is satisfied in the ICE context and implies the non-applicability of the modal cut-off criterion from duct acoustics. The latter states in the cylindrical geometry $\mathcal{Z}_{\text{stat}}$ that for suitably long but thin cavities other modes $\psi_{\mathbf{n}}$ than those depending only on the axial variable, i.e., here x, are evanescent modes. They decay exponentially in the quasi-stationary state such that the long but thin three-dimensional cylindrical cavity can be modeled as effectively one-dimensional, extending only along the cylindrical cavity's symmetry axis.

On the level of the boundary conditions to the acoustic wave equation on $\mathcal{Z}_{\text{stat}}$, effectively one-dimensional acoustic wave propagation may be achieved by replacing $u_0 \to \langle u_0 \rangle_{\mathcal{F}_0}$ and $u_L \to \langle u_L \rangle_{\mathcal{F}_L}$ where

$$\langle u_{x_0} \rangle_{\mathcal{F}_{x_0}} (t) \equiv \frac{1}{\text{Vol}_2 (\mathcal{F}_{x_0})} \int_{\mathcal{F}_{x_0}} d(r, \phi)\, r u_{x_0}(t, r, \phi) \tag{2.65}$$

denotes the average over the full $x = x_0$-face of $\mathcal{Z}_{\text{stat}}$ for a choice $x_0 \in \{0, L\}$.

On the level of the perturbation bundles $\mathcal{M}(t)$, the procedure results in replacing the endcaps by pistons. In the "bundle"-ish terminology, this leads to the *associated piston bundle*: $\langle \mathcal{M} \rangle (t) = \left\{ (x, y, z) \in \mathbb{R}^3 | y^2 + z^2 < a^2_{\text{cyl}}, -\langle u_0 \rangle_{\mathcal{F}_0}(t) < x < L + \langle u_L \rangle_{\mathcal{F}_L}(t) \right\}$. Let u_{x_0} denote the mollified null-continuation from Γ_{x_0} to $\mathcal{F}_{x_0}$ for $x_0 \in \{0, L\}$. The u_{x_0} obtained this way satisfies the equation of motion for the locally reacting surfaces but with Γ_{x_0} replaced by $\mathcal{F}_{x_0} \simeq D^2_{a_{\text{cyl}}}((y = 0, z = 0))$. We note that $D^2_{a_{\text{cyl}}}$ is a convex,
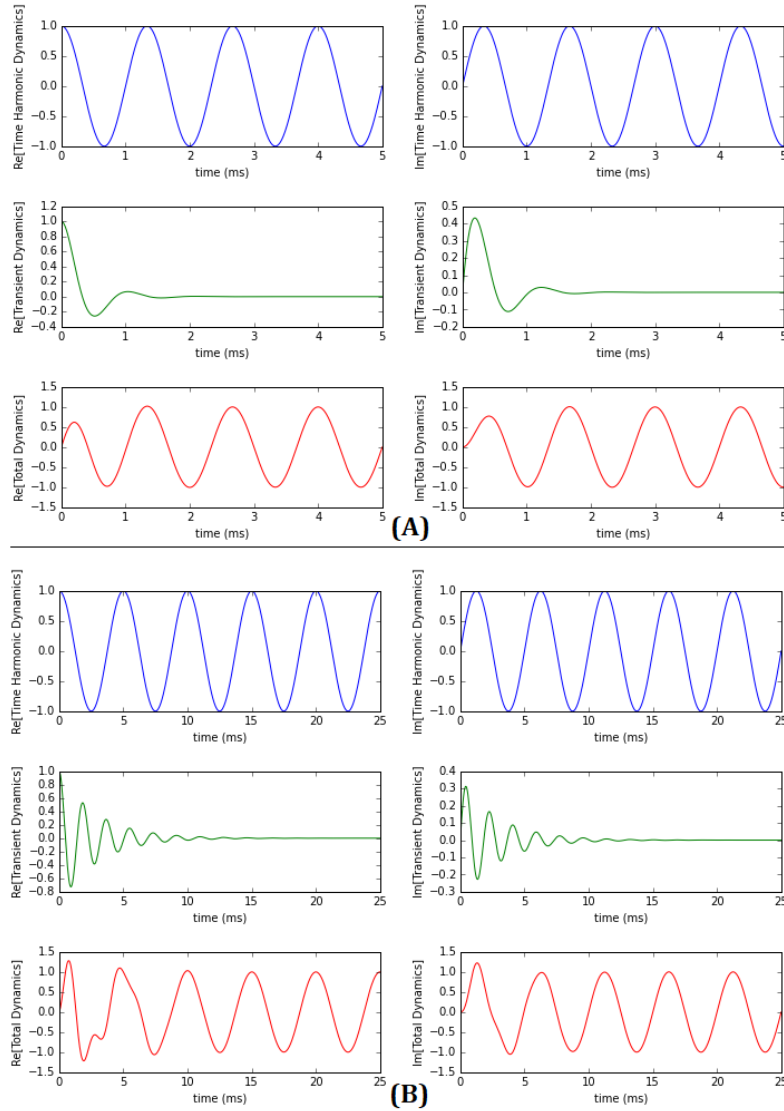
Figure 2.2: (A) Dynamics of the fundamental mode ψ_{11}^{∂} for *Gecko gekko* with $\omega_1^{\partial}1/(2\pi) = 1050\,\text{Hz}$, $\alpha = 1, \text{Hz}$ and $\kappa = 0$ during the first 5 ms for $\omega/(2\pi) = 750\,\text{Hz}$ after exposition to an external sound stimulus. The left column shows the real part ($\Re$) of the dynamics, the right one the imaginary part ($\Im$). The first row depicts the time-harmonic dynamics $\exp(i\omega t)$ in blue, the second one the transient dynamics $\exp(-\alpha t)t_{11}(t)$ in green and the third the total dynamics $\exp(i\omega t) - \exp(-\alpha t)t_{11}(t)$ in red. (B) Results of the analogous simulation for *Varanus salvator* with $\omega_{11}^{\partial}/(2\pi) = 550\,\text{Hz}$, $\alpha = 347\,\text{Hz}$ and $\kappa = 0$ for $\omega/(2\pi) = 200\,\text{Hz}$ during the first 25 ms after exposition to an external sound stimulus.

bounded Lipschitz domain, i.e., intuitively, a domain with suitably regular boundary. The physical regularity imposed on the displacements of the locally reacting surfaces and the mollification result in $u_{x_0}(t) \in W_0^{1,2}(\mathcal{F}_{x_0})$ for all $t > 0$, that is, the Sobolev space for function with Dirichlet boundary conditions at $\partial \mathcal{F}_{x_0}$.

The relative error made by replacing the locally reacting surfaces by the piston's can now be obtained in the L^2-norm by the Poincaré inequality [130], normalized to the 2-dimensional volume of $\mathcal{F}_{x_0}$, compared to the maximum amplitude $U_{\max} \simeq \epsilon L$:

$$\frac{\|u_{x_0} - \langle u_{x_0} \rangle_{\mathcal{F}_{x_0}}\|_{L^2}}{U_{\max}} \leq \sqrt{\frac{1}{\min_{\lambda \in \sigma(-\tilde{\Delta}^\partial)}\{\lambda\}}} \frac{\|\nabla u_{x_0}\|_{L^2}}{U_{\max}} \tag{2.66}$$

Due to the regularity of $\mathcal{F}_{x_0}$ as a domain, the optimal Poincaré constant in the inequality is given by the maximum, nonzero eigenvalue $-\lambda$ of the Dirichlet-Laplacian $\tilde{\Delta}^\partial$ on $\mathcal{F}_{x_0}$. As an order of magnitude estimate, the gradient ∇u_{x_0} can be written as $U_{\max}/a_{\mathrm{tymp}}$. MATHEMATICA allows the calculation of the first zero $\nu_{11} \approx 2.405$ of the first Bessel function of the first kind, J_1 and helps us to find

$$\frac{\|u_{x_0} - \langle u_{x_0} \rangle_{\mathcal{F}_{x_0}}\|_{L^2}}{U_{\max}} \leq \frac{1}{\nu_{11}} \frac{a_{\mathrm{cyl}}}{a_{\mathrm{tymp}}}. \tag{2.67}$$

In the "best" case $a_{\mathrm{cyl}} = a_{\mathrm{tymp}}$, the piston approximation introduces a relative error to the typical amplitude of the locally reacting surfaces of $\leq 42\,\%$. Observe that the figure only gives an upper bound on the error which needn't be the best upper bound despite the choice of the optimal Poincaré constant. Due to the non-applicability of the modal cut-off criterion to the ICE context, we propose a series expansion of (2.62).

Let $\mathbf{n} \in \mathbb{N}_0 \times \mathbb{Z} \times \mathbb{N}_0$ and let the squared stimulus frequency $\omega^2 \notin \sigma(-c^2\Delta)$. L^2-convergence of the series over $\mathbf{n}$ in (2.62) allows us to re-arrange the sum noting the identity

$$\mathbb{N}_0 \times \mathbb{Z} \times \mathbb{N}_0 = \biguplus_{n \in \mathbb{N}_0} \mathbb{N}_0 \times \mathbb{Z} \times \{n\}. \tag{2.68}$$

For $n \in \mathbb{N}_0$, a mode with label $(0, 0, n)$ is called $(n$-th) *axial mode*, a mode with label (n_1, n_2, n) with $(n_1, n_2) \in \mathbb{N} \times \mathbb{Z}$ for a $n \in \mathbb{N}_0$ is called $((n_1, n_2)$-) *spinning mode* (to the n-th axial mode).

Last, we define for all $\mathbf{n} \in \mathbb{N}_0 \times \mathbb{Z} \times \mathbb{N}_0$ the *spinning parameter* $\mathfrak{s}(\mathbf{n})$

$$\frac{1}{-\omega^2 + \omega^2_{\mathbf{n}=(n_1,n_2,n)}} = \frac{\mathfrak{s}(\mathbf{n})}{-\omega^2 + \omega^2_{\mathbf{n}=(0,0,n)}}. \tag{2.69}$$

It is a measure for the propagativity of a spinning mode compared to its basic axial mode.

In the ICE context, the stimulus' frequency satisfies $\omega < c\mu_{11}/a_{\mathrm{cyl}}$ on biological grounds, so that the spinning parameter is positive. For fixed axial mode label n, the spinning parameter attains its maximum for $(n_1, n_2) = (0, 0)$ and from the definition, $\mathfrak{s}((0, 0, n)) = 1$. Upon ordering of the Bessel functions' extrema, the sums in (2.62) can be arranged such that $\mathfrak{s}(\mathbf{n})$ is, as a function of the re-ordered label (n_1, n_2), strictly monotonously decreasing. In the limit $a_{\mathrm{cyl}}/L \to 0$, the conventional mode cut-off criterion is reproduced.

Inclusion of the radial integration in (2.62) accounts for a decrease of the coupling of higher spinning modes to a given membrane mode. Therefore, the non-dimensional quantity $a_{\mathrm{cyl}}^{-2}\mathfrak{s}(\mathbf{n})\langle J_{n_1}(a_{\mathrm{cyl}}^{-1}\mu_{n_1|n_2|}r)J_{q(k_1)}(a_{\mathrm{tymp}}^{-1}\nu_{k_1 k_2}r)\rangle_{L^2[0,a_{\mathrm{tymp}}]}$ with $q(k_1) \equiv k_1\pi/(2\pi - 2\beta)$ has been plotted for the first 5 $\mathbf{k}$-labeled and for the first 5 $\mathbf{n}$-labeled modes, see Fig. 2.3. The more red the parcels, the more important is the respective contribution to (2.62). The piston approximation corresponds to the dark red quadrilateral region in the upper left corner of each of the plots.

Although the piston approximation is far from being accurate in the sense of the Poincaré inequality method, the numerical assessment of its accuracy demonstrates that it captures at least the most dominant contribution to the acoustic pressure as given in (2.62).

2.4   Stationary domain approximation

Stationary domain approximation   By the preceding discussion, the perturbation operator V can be neglected altogether as yielding contributions out of range for the acoustic linearization process. This simplification permits us to focus on the system of integral equations on $\mathcal{Z}_{\mathrm{stat}}$, the so-called *stationary domain approximation*. It is the approximation underlying Beale's acoustic boundary conditions, see the assumptions in [8, 7]. The wave equation for p now lives on the reference bundle $\mathcal{M} = \mathbb{R}^+ \times \mathcal{Z}_{\mathrm{stat}}$ and is coupled to the displacements u_0 and u_L through acoustic boundary conditions.

The equations of motion for u_0, u_L feature p, evaluated at the $x = 0$ and $x = L$ endcap, explicitly in the source term. Green's theorem, applied to the acoustic wave equation, shows that equivalently

$$p = -\rho_0 c^2 \partial \mathsf{G}_0[\partial_t \dot{u}_0] - \rho_0 c^2 \partial \mathsf{G}_0[\partial_t \dot{u}_L] \tag{2.70}$$
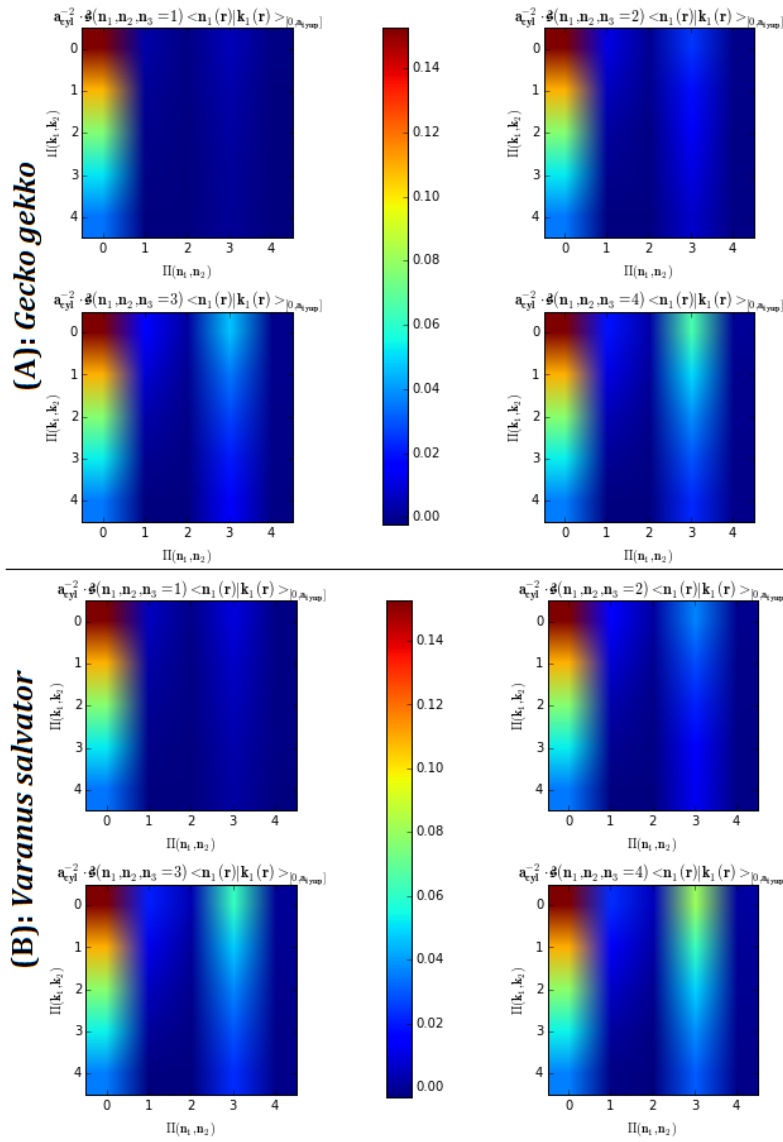
Figure 2.3: Simulation results of $a_{\mathrm{cyl}}^{-2}\mathfrak{s}(\mathbf{n})\langle J_{n_1}(a_{\mathrm{cyl}}^{-1}\mu_{n_1|n_2}|r)J_{q(k_1)}(a_{\mathrm{tymp}}^{-1}\nu_{k_1 k_2}r)\rangle_{L^2[0,a_{\mathrm{tymp}}]}$ for the lizards (A) *Gecko gekko* ($a_{cyl} = 6.6$ mm, $a_{tymp} = 2.6$ mm, $L = 22$ mm and $\beta = \pi/30$) at $\omega/(2\pi) = 750$ Hz (left) and (B) *Varanus salvator* ($a_{cyl} = 6$ mm, $a_{tymp} = 2.6$ mm, $L = 15.5$ mm and $\beta = \pi/(30)$) at $\omega/(2\pi) = 200$ Hz. As signified by the dark red color in the upper left corners of the individual plots, the piston mode is the dominant contribution to the spinning mode series for the internal pressure in each case. The plots only exemplify the generic situation. For data see [147, 148, 158].

where $\partial \mathcal{G}$ is the *boundary-to-cavity* propagator, that is, the Green's function which is evaluated on $x = 0$ or $x = L$ and integrated over the boundary to store the impact of the inhomogeneous Neumann boundary conditions on the internal acoustic pressure.

Likewise, the locally reacting surfaces inserted in the boundary $\partial \mathcal{Z}_{\text{stat}}$ can be expressed through the integral representation

$$u_0 = \sigma_m^{-1} \mathsf{H}_0[p_{\text{ex}}|_{x=0}] - \sigma_m^{-1} \mathsf{H}_0[p|_{x=0}], \tag{2.71}$$

$$u_L = \sigma_m^{-1} \mathsf{H}_0[p_{\text{ex}}|_{x=L}] - \sigma_m^{-1} \mathsf{H}_0[p|_{x=L}]. \tag{2.72}$$

Objective   Although it is possible to numerically iterate the equations or solve them together, an analytic solution, containing the physics underlying for instance the ICE model, is desirable. The goal of this paragraph is to decouple the equations such that one can iterate the resulting equations, one for p, u_0, u_L respectively, independent of each other.

Decoupling of the internal pressure   For p, an independent equation is obtained by insertion of the integral representations for u_0 and u_p:

$$p = -\frac{\mathfrak{g} c^2}{d} \sum_{x_0 \in \{0, L\}} \partial \mathsf{G}_0[\partial_t^2 \mathsf{H}_0[p_{\text{ex}}|_{x=x_0}]] + \frac{\mathfrak{g} c^2}{d} \sum_{x_0 \in \{0, L\}} \partial \mathsf{G}_0[\partial_t^2 \mathsf{H}_0[p|_{x=x_0}]] \tag{2.73}$$

where we have used linearity of the involved integral operators. Together with the starting point for the fixed-point iteration, $p^{(0)} = 0$, and contractivity because of damping of the locally reacting surfaces, the iteration is

$$p^{(k+1)} = -\frac{\mathfrak{g} c^2}{d} \sum_{x_0 \in \{0, L\}} \partial \mathsf{G}_0[\partial_t^2 \mathsf{H}_0[p_{\text{ex}}|_{x=x_0}]] + \frac{\mathfrak{g} c^2}{d} \sum_{x_0 \in \{0, L\}} \partial \mathsf{G}_0[\partial_t^2 \mathsf{H}_0[p^{(k)}|_{x=x_0}]]. \tag{2.74}$$

Obviously, one obtains a series in terms of powers of the coupling strength $\mathfrak{g}$ with the highest power of $\mathfrak{g}$ for, say $p^{(N+1)}$, being $\mathfrak{g}^{N+1}$ as is seen easily by mathematical induction. The coupling strength is small in air $\mathfrak{g} = \rho_0 / \rho_m \ll 1$ for solid or liquid interfaces - "*light-fluid assumption*" - and has been employed as convenient expansion parameter [83, 84].

Boundary-to-boundary propagator   Some additional notation is needed in order to handle the two locally reacting surfaces. For the Green's function expressions (2.70)

for the internal acoustic pressure evaluated at the $x = 0$ and $x = L$ endcap, we use the following "mnemonic" notation to express

$$p|_{x=0} = -\rho_0 d \left\{ (0 \rightsquigarrow 0)[u_0] + (L \rightsquigarrow 0)[u_L] \right\}, \tag{2.75}$$

$$p|_{x=L} = -\rho_0 d \left\{ (0 \rightsquigarrow L)[u_0] + (L \rightsquigarrow L)[u_L] \right\}. \tag{2.76}$$

Since $\psi_{\mathbf{n}}(r, \phi, x = 0) = (-1)^{n_3} \psi_{\mathbf{n}}(r, \phi, x = L)$, the integral kernel for the integro-differential operator is semi-independent of two axial variables in the following sense: $0 \rightsquigarrow L = L \rightsquigarrow 0$ and $0 \rightsquigarrow 0 = L \rightsquigarrow L$. However, $0 \rightsquigarrow L \neq L \rightsquigarrow L$. Note that it also contains a double partial derivative with respect to time.

Physically, the wiggling arrow shall indicate that the internal pressure carries information about the motion of one locally reacting surface to the other one. The coupling ensures that the two locally reacting surfaces "interact" through stimulation of a contribution to the internal pressure wave. We call it *boundary-to-boundary propagator* and its definition is possible due to the regularity behavior of the eigenfunctions of the Neumann Laplace-Beltrami operator. The dimensional re-scaling of the underlying Green's function has been chosen in order to obtain a dimensionless iteration parameter in the end, namely the coupling strength $\mathfrak{g} = \rho_0/\rho_m \lesssim 10^{-2}$ that has also been noted as a convenient expansion parameter in [83, 84].

We find

$$\begin{aligned} u_0 &= \sigma_m^{-1} \mathsf{H}_0[p_{\text{ex}}|_{x=0}] \\ &\quad + \mathfrak{g} \left(\mathsf{H}_0 \circ (0 \rightsquigarrow 0) \right)[u_0] + \mathfrak{g} \left(\mathsf{H}_0 \circ (L \rightsquigarrow 0) \right)[u_L], \end{aligned} \tag{2.77}$$

$$\begin{aligned} u_L &= \sigma_m^{-1} \mathsf{H}_0[p_{\text{ex}}|_{x=L}] \\ &\quad + \mathfrak{g} \left(\mathsf{H}_0 \circ (0 \rightsquigarrow L) \right)[u_0] + \mathfrak{g} \left(\mathsf{H}_0 \circ (L \rightsquigarrow L) \right)[u_L]. \end{aligned} \tag{2.78}$$

This can be re-arranged to make the form of a linear system of integral equations more obvious and provide us with the missing ingredient for the final decoupling. Denoting by $\mathbf{1}$ the identity operator for functions on Γ_0, Γ_L, we have

$$[\mathbf{1} - \mathfrak{g} \left(\mathsf{H}_0 \circ (0 \rightsquigarrow 0) \right)][u_0] + [-\mathfrak{g} \left(\mathsf{H}_0 \circ (L \rightsquigarrow 0) \right)][u_L] = \sigma_m^{-1} \mathsf{H}_0[p_{\text{ex}}|_{x=0}], \tag{2.79}$$

$$[-\mathfrak{g} \left(\mathsf{H}_0 \circ (0 \rightsquigarrow L) \right)][u_0] + [\mathbf{1} - \mathfrak{g} \left(\mathsf{H}_0 \circ (L \rightsquigarrow L) \right)][u_L] = \sigma_m^{-1} \mathsf{H}_0[p_{\text{ex}}|_{x=L}]. \tag{2.80}$$

The fact that Γ_0 and Γ_L differ only by translation along the symmetry axis of $\mathcal{Z}_{\text{stat}}$ permits us to act on with any of the operator-valued coefficients on an equation from the above set of two equations: The operator coefficients commute. For less symmetric locally reacting surfaces, this is not trivially possible.

Upon acting with $[1 - \mathfrak{g}\,(\mathsf{H}_0 \circ (L \rightsquigarrow L))]$ on the first of the two, and with $[-\mathfrak{g}\,(\mathsf{H}_0 \circ (L \rightsquigarrow 0))]$ on the second of the two equations, we can eliminate u_L such as to obtain an equation only for u_0. Observe that there is still one identity operator present in the resulting equation. Similarly, application of $[-\mathfrak{g}\,(\mathsf{H}_0 \circ (0 \rightsquigarrow L))]$ to the first and application of $[1 - \mathfrak{g}\,(\mathsf{H}_0 \circ (0 \rightsquigarrow 0))]$ to the second of the two equations permits us to eliminate u_0 and to obtain an equation for u_L. Noting $L \rightsquigarrow L = 0 \rightsquigarrow 0$ by the symmetry of the eigenfunctions, the results for u_0 and u_L are:

$$
\begin{aligned}
&[1 - \mathfrak{g}\,(\mathsf{H}_0 \circ (0 \rightsquigarrow 0))] \circ [1 - \mathfrak{g}\,(\mathsf{H}_0 \circ (0 \rightsquigarrow 0))]\,[u_0] \\
&+ [-\mathfrak{g}\,(\mathsf{H}_0 \circ (L \rightsquigarrow 0))] \circ \left(\sigma_m^{-1}\mathsf{H}_0[p_{\mathrm{ex}}|_{x=L}]\right) \\
&- [-\mathfrak{g}\,(\mathsf{H}_0 \circ (L \rightsquigarrow 0))] \circ [-\mathfrak{g}\,(\mathsf{H}_0 \circ (0 \rightsquigarrow L))]\,[u_0] \\
&= [1 - \mathfrak{g}\,(\mathsf{H}_0 \circ (0 \rightsquigarrow 0))] \circ \left(\sigma_m^{-1}\mathsf{H}_0[p_{\mathrm{ex}}|_{x=0}]\right),
\end{aligned}
\tag{2.81}
$$

$$
\begin{aligned}
&[1 - \mathfrak{g}\,(\mathsf{H}_0 \circ (L \rightsquigarrow L))] \circ [1 - \mathfrak{g}\,(\mathsf{H}_0 \circ (L \rightsquigarrow L))]\,[u_L] \\
&+ [-\mathfrak{g}\,(\mathsf{H}_0 \circ (0 \rightsquigarrow L))] \circ \left(\sigma_m^{-1}\mathsf{H}_0[p_{\mathrm{ex}}|_{x=0}]\right) \\
&- [-\mathfrak{g}\,(\mathsf{H}_0 \circ (0 \rightsquigarrow L))] \circ [-\mathfrak{g}\,(\mathsf{H}_0 \circ (L \rightsquigarrow 0))]\,[u_L] \\
&= [1 - \mathfrak{g}\,(\mathsf{H}_0 \circ (L \rightsquigarrow L))] \circ \left(\sigma_m^{-1}\mathsf{H}_0[p_{\mathrm{ex}}|_{x=L}]\right).
\end{aligned}
\tag{2.82}
$$

Decoupled equations for the displacements   Obviously, the two above equations satisfy the requirement of depending only on either u_0 or u_L as unknown functions. The next step is a slight re-arrangement such as to facilitate the fixed-point iteration akin to the one performed for the internal pressure. We find

$$
\begin{aligned}
u_0 = \;&\sigma_m^{-1}\mathsf{H}_0[p_{\mathrm{ex}}|_{x=0}] + 2\mathfrak{g}\mathsf{H}_0 \circ (0 \rightsquigarrow 0)\,[u_0] \\
&+ \mathfrak{g}\left\{(\mathsf{H}_0 \circ (L \rightsquigarrow 0)) \circ \left(\sigma_m^{-1}\mathsf{H}_0[p_{\mathrm{ex}}|_{x=L}]\right) - (\mathsf{H}_0 \circ (0 \rightsquigarrow 0)) \circ \left(\sigma_m^{-1}\mathsf{H}_0[p_{\mathrm{ex}}|_{x=0}]\right)\right\} \\
&+ \mathfrak{g}^2\left\{(\mathsf{H}_0 \circ (L \rightsquigarrow 0)) \circ (\mathsf{H}_0 \circ (0 \rightsquigarrow L)) - (\mathsf{H}_0 \circ (0 \rightsquigarrow 0)) \circ (\mathsf{H}_0 \circ (0 \rightsquigarrow 0))\right\}\,[u_0],
\end{aligned}
\tag{2.83}
$$

$$
\begin{aligned}
u_L = \;&+\sigma_m^{-1}\mathsf{H}_0[p_{\mathrm{ex}}|_{x=L}] + 2\mathfrak{g}\mathsf{H}_0 \circ (L \rightsquigarrow L)\,[u_L] \\
&+ \mathfrak{g}^2\left\{(\mathsf{H}_0 \circ (0 \rightsquigarrow L)) \circ (\mathsf{H}_0 \circ (L \rightsquigarrow 0)) - (\mathsf{H}_0 \circ (L \rightsquigarrow L)) \circ (\mathsf{H}_0 \circ (L \rightsquigarrow L))\right\}\,[u_L] \\
&+ \mathfrak{g}\left\{(\mathsf{H}_0 \circ (0 \rightsquigarrow L)) \circ \left(\sigma_m^{-1}\mathsf{H}_0[p_{\mathrm{ex}}|_{x=0}]\right) - (\mathsf{H}_0 \circ (L \rightsquigarrow L)) \circ \left(\sigma_m^{-1}\mathsf{H}_0[p_{\mathrm{ex}}|_{x=L}]\right)\right\}.
\end{aligned}
\tag{2.84}
$$

The equations simplify upon noting that the $\sim \mathfrak{g}^2$-term cancels because the eigenfunctions of the Neumann-Laplacian on $\mathcal{Z}_{\mathrm{stat}}$ evaluate identically up to a sign. The latter is canceled because the relevant values of the eigenfunctions appear in ever power.

Thus

$$
\begin{aligned}
u_0 &= \sigma_m^{-1}\mathsf{H}_0[p_{\mathrm{ex}}|_{x=0}] + 2\mathfrak{g}\mathsf{H}_0 \circ (0 \rightsquigarrow 0)\,[u_0] \\
&+ \mathfrak{g}\left\{(\mathsf{H}_0 \circ (L \rightsquigarrow 0)) \circ \left(\sigma_m^{-1}\mathsf{H}_0[p_{\mathrm{ex}}|_{x=L}]\right) - (\mathsf{H}_0 \circ (0 \rightsquigarrow 0)) \circ \left(\sigma_m^{-1}\mathsf{H}_0[p_{\mathrm{ex}}|_{x=0}]\right)\right\},
\end{aligned}
\tag{2.85}
$$

$$
\begin{aligned}
u_L &= \sigma_m^{-1}\mathsf{H}_0[p_{\mathrm{ex}}|_{x=L}] + 2\mathfrak{g}\mathsf{H}_0 \circ (L \rightsquigarrow L)\,[u_L] \\
&+ \mathfrak{g}\left\{(\mathsf{H}_0 \circ (0 \rightsquigarrow L)) \circ \left(\sigma_m^{-1}\mathsf{H}_0[p_{\mathrm{ex}}|_{x=0}]\right) - (\mathsf{H}_0 \circ (L \rightsquigarrow L)) \circ \left(\sigma_m^{-1}\mathsf{H}_0[p_{\mathrm{ex}}|_{x=L}]\right)\right\}.
\end{aligned}
\tag{2.86}
$$

Physical discussion Physically, the above two equations describe that one of the locally reacting surfaces is driven in leading order $\sim \mathfrak{g}^0$ by the external pressure. The next-to-leading order $\sim \mathfrak{g}^1$ encapsulates the feedback the surface gives to itself by either inducing at its location an acoustic pressure (first term $\sim \mathfrak{g}$ on the respective right-hand sides) or emitting a contribution to the internal acoustic pressure which is reflected back to the equilibrium position of the locally reacting surface. The last contribution $\sim \mathfrak{g}^1$ includes a drive by the external pressure p_{ex}. The latter is evaluated at the respective equilibrium positions of both locally reacting surfaces. These contributions do not cancel. It is the presence of both of them which leads in the model of internally coupled ears to a coupled vibration of the eardrums.

The corresponding iteration scheme, akin to the one for the internal pressure, reads:

$$
\begin{aligned}
u_0^{(k+1)} &= \sigma_m^{-1}\mathsf{H}_0[p_{\mathrm{ex}}|_{x=0}] + 2\mathfrak{g}\mathsf{H}_0 \circ (0 \rightsquigarrow 0)\,[u_0^{(k)}] \\
&+ \mathfrak{g}\left\{(\mathsf{H}_0 \circ (L \rightsquigarrow 0)) \circ \left(\sigma_m^{-1}\mathsf{H}_0[p_{\mathrm{ex}}|_{x=L}]\right) - (\mathsf{H}_0 \circ (0 \rightsquigarrow 0)) \circ \left(\sigma_m^{-1}\mathsf{H}_0[p_{\mathrm{ex}}|_{x=0}]\right)\right\},
\end{aligned}
\tag{2.87}
$$

$$
\begin{aligned}
u_L^{(k+1)} &= \sigma_m^{-1}\mathsf{H}_0[p_{\mathrm{ex}}|_{x=L}] + 2\mathfrak{g}\mathsf{H}_0 \circ (L \rightsquigarrow L)\,[u_L^{(k)}] \\
&+ \mathfrak{g}\left\{(\mathsf{H}_0 \circ (0 \rightsquigarrow L)) \circ \left(\sigma_m^{-1}\mathsf{H}_0[p_{\mathrm{ex}}|_{x=0}]\right) - (\mathsf{H}_0 \circ (L \rightsquigarrow L)) \circ \left(\sigma_m^{-1}\mathsf{H}_0[p_{\mathrm{ex}}|_{x=L}]\right)\right\}.
\end{aligned}
\tag{2.88}
$$

$u_{x_0}^{(1)}$ will include contributions which are to be trusted up to order $\mathfrak{g}^0$ for either choice of $x_0 \in \{0, L\}$. More generally, $u_{x_0}^{(N)}$ can be trusted up to order $\mathfrak{g}^{N-1}$ for $N \in \mathbb{N}$ and either choice $x_0 \in \{0, L\}$.

The first two iterations with starting point $u_0^{(0)} = 0 = u_L^{(0)}$ yield

$$u_0^{(1)} = \sigma_m^{-1} \mathsf{H}_0[p_{\text{ex}}|_{x=0}] + \mathcal{O}(\mathfrak{g}^1) \tag{2.89}$$

$$u_L^{(1)} = \sigma_m^{-1} \mathsf{H}_0[p_{\text{ex}}|_{x=L}] + \mathcal{O}(\mathfrak{g}^1) \tag{2.90}$$

$$\begin{aligned} u_0^{(2)} &= \sigma_m^{-1} \mathsf{H}_0[p_{\text{ex}}|_{x=0}] \\ &+ \sigma_m^{-1} \mathfrak{g} \left\{ (\mathsf{H}_0 \circ (L \rightsquigarrow 0)) \circ (\mathsf{H}_0[p_{\text{ex}}|_{x=L}]) + (\mathsf{H}_0 \circ (0 \rightsquigarrow 0)) \circ (\mathsf{H}_0[p_{\text{ex}}|_{x=0}]) \right\} \\ &+ \mathcal{O}(\mathfrak{g}^2) \end{aligned} \tag{2.91}$$

$$\begin{aligned} u_L^{(2)} &= \sigma_m^{-1} \mathsf{H}_0[p_{\text{ex}}|_{x=L}] \\ &+ \sigma_m^{-1} \mathfrak{g} \left\{ (\mathsf{H}_0 \circ (0 \rightsquigarrow L)) \circ (\mathsf{H}_0[p_{\text{ex}}|_{x=L}]) + (\mathsf{H}_0 \circ (L \rightsquigarrow L)) \circ (\mathsf{H}_0[p_{\text{ex}}|_{x=0}]) \right\} \\ &+ \mathcal{O}(\mathfrak{g}^2) \end{aligned} \tag{2.92}$$

Note that in practice, the summations hidden in the operator-notation need to be truncated sensibly to limit computational effort if a numerical treatment is desired.

The evolution of the real and imaginary part of the first iterate u_0 under the signal $p_{\text{ex}}(t) = p_0 \exp(i\omega t)$ with $\omega = 2\pi \cdot 200\,\text{Hz}$ and p_0 corresponding to a sound pressure level of $50\,\text{dB}$ is shown for the material parameters used for *Varanus salvator* [145] in Fig. 2.4 and Fig. 2.5. Fig. 2.4 displays the real and Fig. 2.5 the imaginary part for the first $18\,\text{ms}$ after stimulus exposition with time steps of $3\,\text{ms}$. Already the first iterate displays the correct scaling of the amplitude comparable to the order of a few nano-meters that is observed experimentally: It is $\lesssim \mathcal{O}(10^1\,\text{nm})$.

Fig. 2.6 shows the perturbation bundle $\mathcal{M}(t)$ respectively the undulating cylindrical cavity at different points in time with suitably re-scaled vibrational amplitudes up to contributions of order $\mathcal{O}(\mathfrak{g})$.

2.5 Summary

It is due time to discuss our findings. The notion of a perturbation bundle was defined and shown to be the natural geometric configuration space for vibrational acoustics problems in enclosures. The intuitive idea is to study a suitably regular, bounded manifold, say Ω, the boundary of which $\partial\Omega$ contains locally reacting surfaces described chartwisely as the graph of a transverse displacement function over the boundary $\partial\Omega$. For suitably small perturbations, the overall topological properties of Ω do not change in time, but only the local geometry is modified during the evolution of the perturbation bundle's undulation. In a mechanistic picture, the physically correct notion for
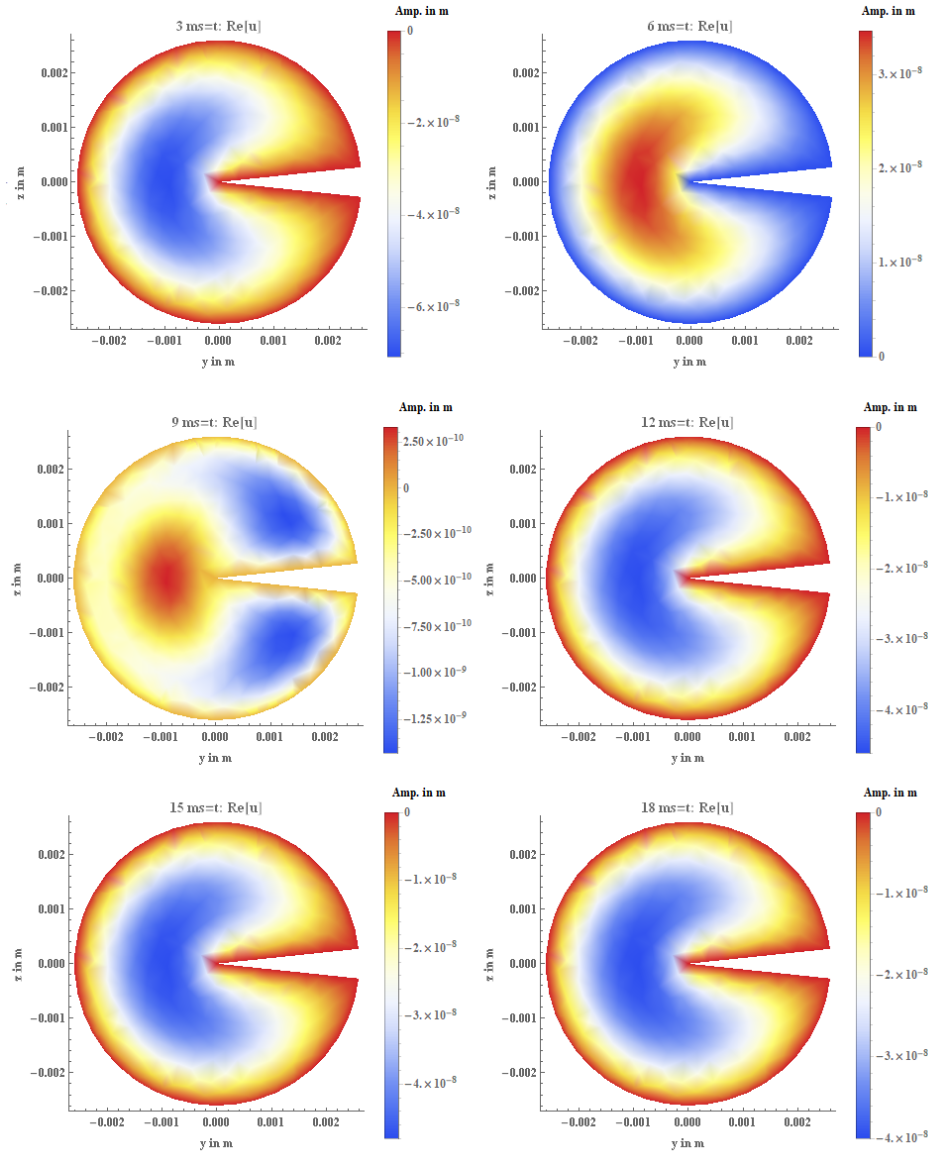
Figure 2.4: Simulation of a linearly damped (damping coefficient $\alpha = 350\,\text{Hz}$) flexible membrane (phase velocity of flexural waves $c_m = 2\,\text{ms}^{-1}$, $\kappa = 0$) on a sector with opening angle $\beta = \pi/30$ and radius $a_{\text{tymp}} = 2.6\,\text{mm}$ responding to an incident pressure signal $p_{\text{ex}}(t) = p_0 \exp(i\omega t)$ with $\omega = 2\pi \cdot 200\,\text{Hz}$ and p_0 corresponding to a sound pressure level of $50\,\text{dB}$: Real part at different times $3\,\text{ms} \leq t \leq 18\,\text{ms}$ in steps of $3\,\text{ms}$. Clamping (Dirichlet) boundary conditions have been used to match with findings on the lizard *Varanus salvator*.
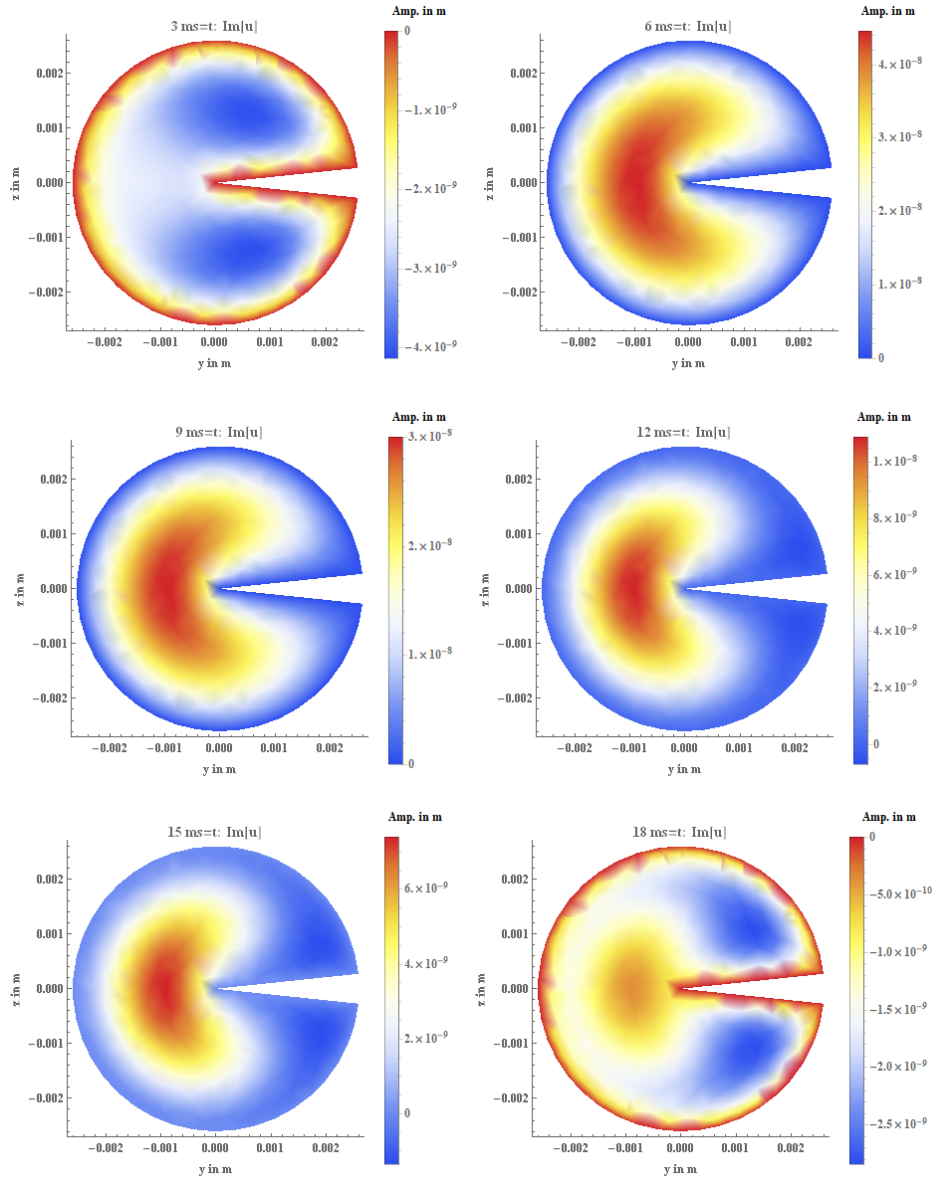
Figure 2.5: Simulation of a linearly damped (damping coefficient $\alpha = 350\,\text{Hz}$) flexible membrane (phase velocity of flexural waves $c_m = 2\,\text{ms}^{-1}$, $\kappa = 0$) on a sector with opening angle $\beta = \pi/30$ and radius $a_{\text{tymp}} = 2.6\,\text{mm}$ responding to an incident pressure signal $p_{\text{ex}}(t) = p_0 \exp(i\omega t)$ with $\omega = 2\pi \cdot 200\,\text{Hz}$ and p_0 corresponding to a sound pressure level of $50\,\text{dB}$: Imaginary part at different times $3\,\text{ms} \leq t \leq 18\,\text{ms}$ in steps of $3\,\text{ms}$. Clamping (Dirichlet) boundary conditions have been used to match with findings on the lizard *Varanus salvator*.
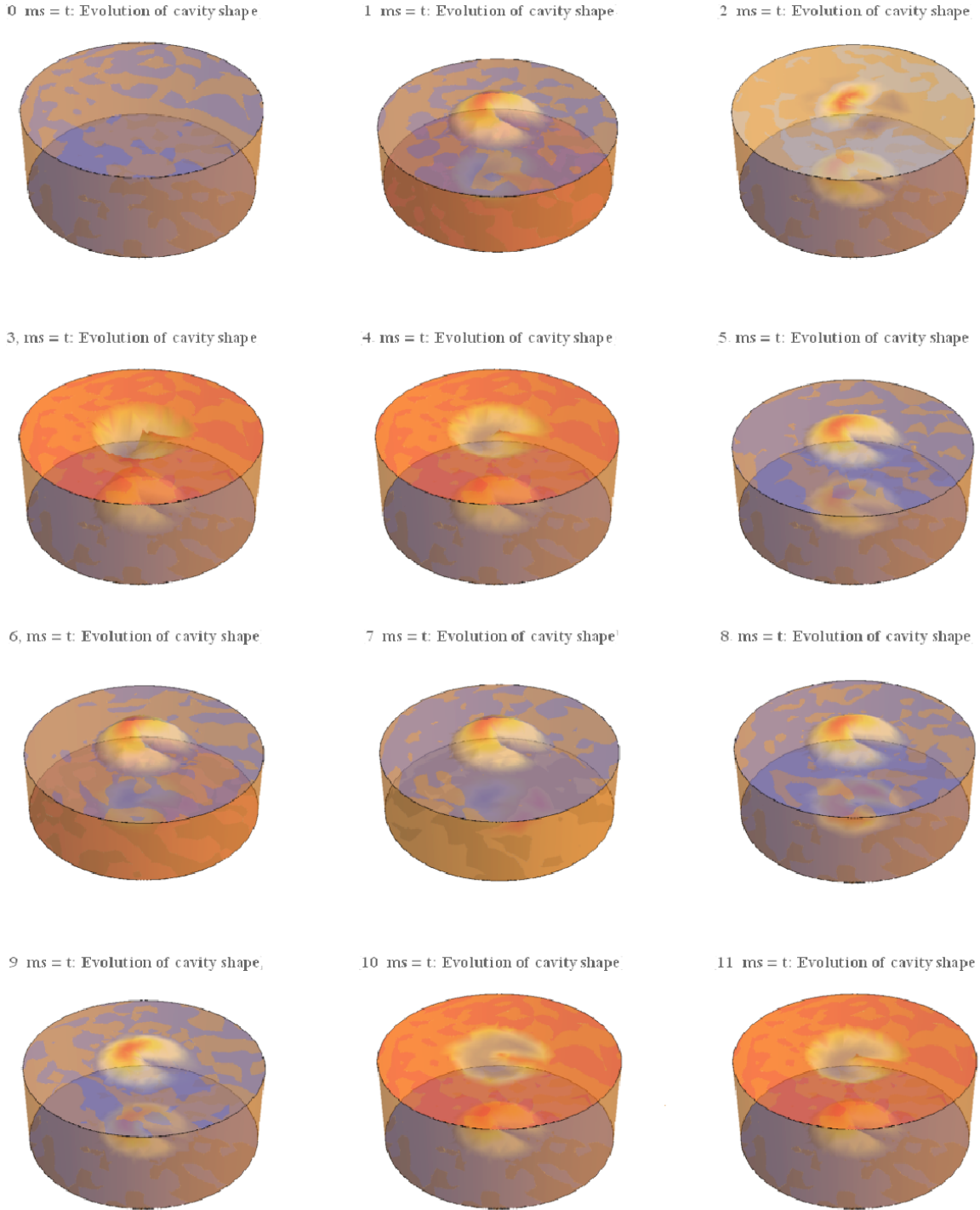
Figure 2.6: Evolution of the time-dependent cylinder $\mathcal{Z}(t)$ from $t = 0\,\mathrm{ms}$ to $t = 11\,\mathrm{ms}$ as indicated by the sub-plot labels. Locally reacting surface displacements $u_0^{(1)}$ and $u_L^{(1)}$ in the leading order of the coupling strength $\mathfrak{g}$. Amplitudes magnified by a factor of 10^5 for visualization. Geometrical data for the cavity setup as for the lizard *Varanus salvator*; cf. caption of Fig 2.4 and Fig. 2.5. $\phi_0 = -\pi/3$ and $\phi_L = \pi/3$ has been chosen as dummy phase shifts, corresponding to an external drive situated symmetrically between the membranes.

the force needed to trigger boundary displacement is that of acoustic pressure. The attribute "acoustic" signified a small perturbation to the mechanical equilibrium state of the geometric shape, i.e., the reference bundle associated to the perturbation bundle. The invariance of the topological properties of $\Omega(t)$ as functions of t played a crucial role for the existence of a t-family of diffeomorphisms. The diffeomorphism family maps the domain at rest, Ω, to its evolving counterpart at time t, symbolically for instance, $\Omega(t) = \Psi_t^{\mathrm{sp}}[\Omega]$. Non-conservation of topological properties of the evolving $\Omega(t)$ would constitute an obstruction to the existence of such a diffeomorphism family. The family of diffeomorphisms between the three-dimensional domains extends to a family of diffeomorphisms between the total spaces of the reference and perturbation bundle.

In the context of the ICE model, the diffeomorphism family could be specified easily. By consideration of the pull-back of the d'Alembertian from the perturbation to the reference bundle and imposing regularity assumptions on the perturbation, a time-dependent perturbation operator $\mathsf{V} = \mathsf{V}(t)$ could be derived. The coupling of the locally reacting surfaces and the acoustic pressure was incorporated at first in the boundary conditions to the acoustic wave equation and secondly through a force (per surface area) drive in the equations of motion for the surfaces' displacement. Consistency with the acoustic linearization required to drop the perturbation operator, which is noting but a derivation of Beale's acoustic boundary conditions, and the iteration technique decoupled the equations that had been coupled through acoustic boundary conditions before.

The equations were solved in the quasi-stationary state and, in the context of the ICE model, the relaxation time was shown to be only some ms. The piston approximation was investigated by an a priori error estimate, based on the Poincaré inequality, and by the spinning series expansion, a generalization of the duct acoustics' cut-off criterion. The two techniques demonstrates that although the piston approximation introduces according to the Poincaré estimate even in the best-case scenario $a_{\mathrm{tymp}} = a_{\mathrm{cyl}}$ a large $\lesssim 42\,\%$ error relative to the typical membrane vibration amplitudes, it captures at least the dominant contribution to the quasi-stationary state acoustic pressure $p_{\mathrm{q.s.}}^{(2)}$ in the simulated mode range.

Chapter 3

Biotremological model for elephants detecting tsunamis

Just after Christmas 2004, on December 26, elephants have been observed to take flight from tsunamis approaching coastal regions in South-Eastern Asia 15 min to 90 min before the first wave front reached the coast. This behavior is explained by an endogenous early-detection system for tsunamis based on infrasound detection. Such an early-detection system is used by a wide group of animals one which is the elephant.

While acoustic pathways have been discussed, biological findings support the notion that elephants use the tactile rather than the auditory pathway to detect seismic cues from the tsunami. However, the nature of this genuine tsunami-generated signal that induces the seismic cues, which the elephant can use for seismic localization, is so far unknown.

Here we show that the signal is constituted by a thin region of vortex dipoles generated by the tsunami that act as small but numerous hammers on the top layer of the continental plate. In contrast to the standard theory on seismic signal generation, the vortex dipole region forms exclusively due to turbulent effects at the interface between continental plate and oceanic fluid. Secondly, we demonstrate numerically that the seismic signal produced this way is detectable by elephants in terms of audible frequency as well as sound-pressure level. Last, we show that the arrival time difference between tsunami wave-front and seismic signal matches the experimental findings for a realistic oceanic height profile and that previous approximate results miss a factor of 2.

Our results show that although the infrasonic frequency range as well as seismic localization are biophysically in-experiencable for humans, animals, exemplified by the

largest land-living mammal, the elephant, can use these mechanisms to spot already
the onset of a natural hazard.

We anticipate that our results can serve as the starting point for a more detailed
investigation of the elasticity theoretic and hydrodynamic models for seismic cue for-
mation, applicable other animals as well. Knowledge of the physical origin of tsunami
cues can serve as a theoretical basis and thus is relevant for the emulation of natural
early-warning systems.

3.1   Introductory material

Motivation   The word "tsunami" originates from Japanese and translates to English
as "huge wave". Indeed, when in 2004 a tsunami struck Khao Lak, Thailand, the
tsunami wave was reported to have a peak amplitude of 30 m. Numerous reports in the
media claimed unusual animal behavior preceding the tsunami roll-up on the shoreline
of Kao Lak.

In this chapter, we focus on elephants' behavior prior to the roll-up event from the
perspective of theoretical physicists. It has been reported [159, 54, 66] that elephants ex-
hibited abnormal behavior (anxiety, nervousness etc.) several hours before the tsunami
hit the coast and took flight rampantly about $8 - 30\,\mathrm{min}$ before the tsunami finally
struck the coastal region.

We are led to asking: What is the most plausible physical process in the external
world which enables elephants but not humans to spot precursor signals of the tsunamis
and take flight just in time? The model we are about to discuss is not confined to
tsunamis since the governing equations can also be used to explain the responses of
elephants to earthquake signals [76, 99].

Tsunamis   Let us turn to a physical definition of a tsunami in order to build up a
prototypical mental image of the characteristics of a tsunami. We define a *tsunami* as a
perturbation of a volume of water from rest so that kinetic energy stored in the motion
of the perturbation is converted periodically into potential energy of the elevation of
the ocean's surface. Thus, a tsunami can be classified as a mechanical (water) wave.
Other definitions used for experimental purposes can be found in [87].

With a description of what a tsunami does in mind, we ask how a tsunami is gen-
erated. The standard trigger is a seaquake: At the junction of oceanic and continental

plates, the plates sometimes leap over each other abruptly. For instance, an oceanic plate can be stuck for some time while moving under the continental plate creating a plate tension in the oceanic plate. After a threshold value is exceeded, the oceanic plate literally leaps forward and moves several centimeters or even meters further on its way to dive beyond the continental plate. Due to the interplay of inertia of the water pillars above the oceanic sea floor, the water elements are propelled by an excess momentum transferred from the oceanic plate. The excess momentum propels water parcels away from the location of the injection of momentum into the ocean fluid and thus decreases the sea level beyond the standard reference value when the fluid is at rest (in the fluid rest frame).

In leading order, in particular neglecting the rotation of the earth around its axis of revolution, the gravitational force acts a homogeneous restoring force on the ocean's surface. It restores mechanical equilibrium, i.e., it makes the ocean's surface gradually relax into its equilibrium, which takes quite often the form of a minimal surface in physical approximation. The momentum is transferred by collisions of water molecules through the ocean fluid with the process at the surface of the ocean providing the "balance" for the periodic conversion of kinetic into potential energy and vice versa. In a theoretically idealized world, the so-created tsunami wave can travel without dissipation at its speed of propagation v_{ts} and phase velocity c_{ts} with dispersion velocity coincident with the phase velocity.

Checking dimensions of the physical quantity involved, the momentum transferal happens in a three-dimensional volume $\Delta V = H_0 \cdot \Delta A$ beneath a surface element ΔA which experiences the gravitational as a restoring force. Physically, the ocean floor is not at constant depth beyond sea level. Thus, we rather have $H_0 \rightarrow h_0(x)$ with a non-constant depth function h_0.

We will summarize oceanographic properties of the underwater region of the continental plate adjacent to the oceanic plate and recover a simple and well-known [87] fit model from these findings. A theoretical study on elephant tsunami sensing, assuming a somewhat less realistic constant depth profile, is available [54].

Oceanographic aspects of continental plates   According to a recent study [11], there are in total $N_{\text{p}} = 52$ plates. The plates can be divided into two classes: Heavier oceanic plates and lighter continental plates. We will focus on the latter because elephants typically live in regions on continental plates.
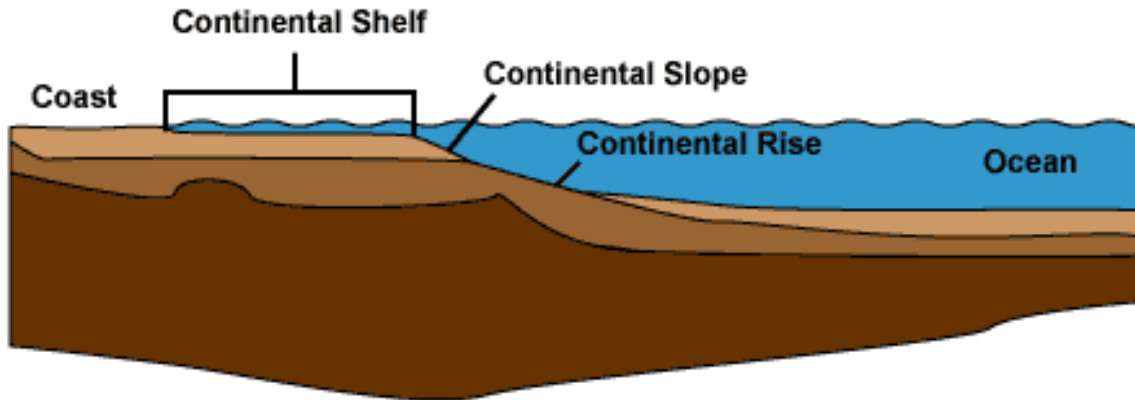
Figure 3.1: The oceanographic "standard model" for the continental margin and its subdivision into continental shelf (left), continental slope (middle) and continental rise (right). Figure from https://web.archive.org/web/20050217014801/http://www.onr.navy.mil/Focus/ocean/regions/oceanfloor2.htm.

Fig. 3.1 shows the division of the continental plate in three major regions classified by oceanographs and explained below. Fig. 3.2 shows a typical, yet fictitious, depth profile of the continental plate's region below sea level, called *continental margin* henceforth.

The continental margin is terminated by the *shoreline* which marks the boundary between land- and water-covered regions of the continental plate. The underwater region, the continental margin, is further divided into three regions according to the standard model of oceanography [58, 118, 21].

- *Continental shelf:* The *continental shelf* is the extended region from the shoreline to until the continental slope begins. It is characterized by a mostly almost uniform slope profile of $\beta_{csh} = 0.5°$ and a maximum depth of $H_{0csh} = 200\,\mathrm{m}$ averaged over all continental shelves. In the regions prone to tsunamis, i.e., at equatorial geographic height, the continental shelf is particularly narrow, cf. the topographic material in [58, 118, 21].

- *Continental slope:* The *continental slope* is characterized by a larger slope angle, $\beta_{csl} = 3°$ on average, than the continental shelf [58, 118, 21]. Notably, the angle $\beta_{csl} \in [1°, 10°]$ locally by a non-mildly varying fine-structure depth profile. The
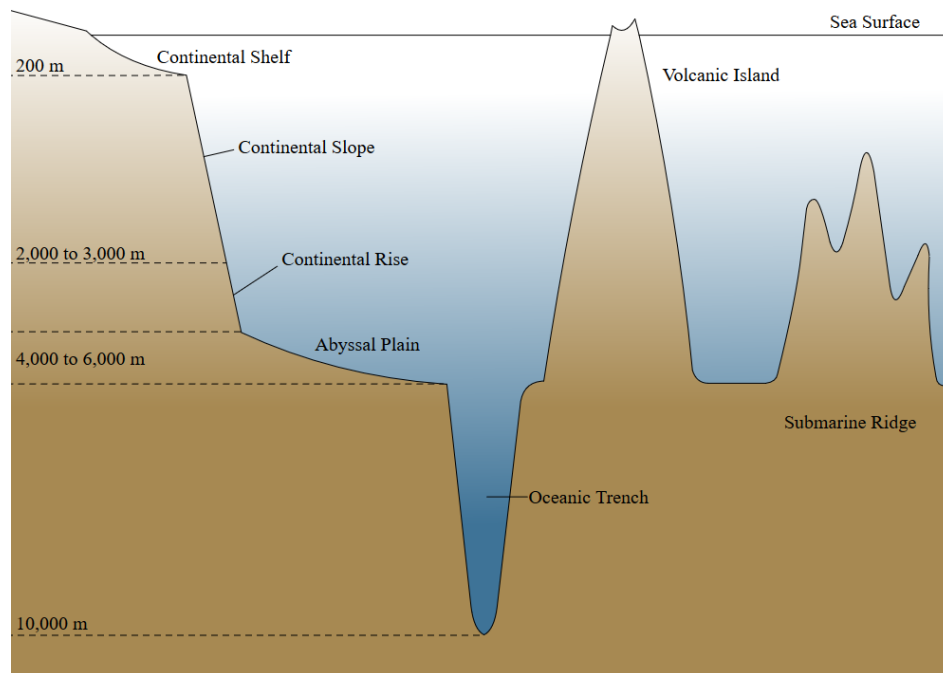
Figure 3.2: A re-scaled version of a realistic depth profile in the continental margin region and characteristic heights of the continental shelf, continental slope and continental rise. Figure from https://commons.wikimedia.org/wiki/File:Oceanic_ basin.svg.

Height	Slope	Length
$H_{0,\mathrm{csh}} = 0.2 \cdot 10^3\,\mathrm{m}$	$\beta_{\mathrm{csh}} = 0.50°$	$L_{\mathrm{csh}} = 7.2 \cdot 10^4\,\mathrm{m}$
$H_{0,\mathrm{css}} = 2.8 \cdot 10^3\,\mathrm{m}$	$\beta_{\mathrm{csl}} = 3.00°$	$L_{\mathrm{csl}} = 1.7 \cdot 10^5\,\mathrm{m}$
$H_{0,\mathrm{cr}} = 1.0 \cdot 10^3\,\mathrm{m}$	$\beta_{\mathrm{cr}} = 0.75°$	$L_{\mathrm{cr}} = 2.4 \cdot 10^5\,\mathrm{m}$
$H_0 = 4.0 \cdot 10^3\,\mathrm{m}$	$\beta = 1.50°$	$L = 4.8 \cdot 10^5\,\mathrm{m}$

Table 3.1: Geometric data of the continental margin used in the model: The index "csh" (first row) abbreviates continental shelf, "csl" (second row) indexes continental slope and "cr" stands for continental rise (third row). The fourth row contains the weighted summed values according to the prescriptions explained in the main text.

continental slope connects the shallow continental shelf regions at about 200 m to the continental rise starting at a depth of 3000 m.

- *Continental rise:* Little is known about detailed topographic properties of the *continental rise*. However, the average slope angle $\beta_{\mathrm{cr}} \in [0.5°, 1.0°]$ is agreed on to be a fair estimate [58, 118, 21]. We select the average value $\beta_{\mathrm{cr}} = 0.75°$ for calculations. The continental rise extends until a depth of 4000 m and connects the continental margin to the abyssal plains on the oceanic plate. It is covered by sediments.

The continental margin terminates underwater at the abyssal plains which are approximately flat plains, geologically situated on the oceanic plates.

In the small-angle approximation ($\tan \beta \approx \beta \approx \sin \beta$), the average slope angle β of the continental margin is found from $H_0 \beta^{-1} = \beta_{\mathrm{csh}}^{-1} H_{0,\mathrm{csh}} + \beta_{\mathrm{csl}}^{-1} H_{0,\mathrm{csl}} + \beta_{\mathrm{cr}}^{-1} H_{0,\mathrm{cr}}$ with the aid of the data in table 3.1 to be $\beta = 1.5°$. Using $H_0/L = \beta$, we find a horizontal extension of the continental margin of $L = 480\,\mathrm{km}$ as an order of magnitudes estimate using the overall depth $H_0 = 4\,\mathrm{km}$.

Selected topics in elephant tactile sensing   This paragraph serves to collect some facts and findings concerning the tactile sensing in elephants. To this end, we observe that typically the phase velocity of *seismic* waves are of the order of $2000\,\mathrm{ms^{-1}}$ for transversal seismic waves in standard solid material [64].

Defining a neural detectability criterion akin to the interaural time difference [157, 145, 42], the *inter-feet time difference* (IFTD) as $\mathrm{IFTD} = \Delta x / c_s$ where $\Delta x \simeq 2\,\mathrm{m}$ is the

characteristic distance between elephant feet and $c_s \simeq 2000\,\mathrm{ms}^{-1}$ is the phase velocity of a (transversal) seismic signal. The IFTD gives a time-scale which should be neurally resolvable by the elephant and thus be of the order of $\sim (0.5-3)\,\mathrm{ms}$ around the characteristic threshold value of $1\,\mathrm{ms}$. Signals with a higher IFTD are disadvantageous as cues because they are considerably slow. Signals with a lower IFTD are also disadvantageous because the neural anatomy forbids resolving all the information stored in them – The signal is too fast. With the previously introduced values, we find IFTD $\simeq 1\,\mathrm{ms}$ such that seismic cues are a priori detectable by the elephant *on anatomic basis*.

Numerous experimental investigations, e.g., [104, 102, 109, 106, 59, 4, 107, 103, 55, 92, 16, 97, 66, 65, 63, 64], have been performed to address which pathway the elephant can employ to detect seismic cues. It was found [104, 66] that the feet of elephants exhibit a fatty cushion comparable to the material constitution of subcutaneous layers of fat in dolphins. The latter has a so-called *impedance matching property* meaning that transmission of waves from the surrounding material into the body of the animal is maximized. Mathematically, this translates into using Euler's equation after linearization as boundary conditions at the feet of the elephant reacting to the vibration of the ground.

Furthermore, the feet skin of the elephant is known to be populated by mechano-receptor cells, the so-called *Pacinian* and *Meissner* cells. These act as pressure detectors and have been modeled in [9, 154, 37, 129], the most prominent model being the two-spring model to the author's knowledge [37].

The definite pathway employed by the elephant is so far uncertain and needs to be further assessed experimentally.

3.2 Presentation of the model

Introduction and model assumptions   The overall model assumption is the applicability of bio-tremology approach [66, 92, 97] rather than pure acoustics [54]. Sound generated at the location of the tsunami generation cannot transverse the water-air interface at a convingingly high enough intensity [56, 57]. The only acoustic model available to our knowledge [55] furthermore requires certain atmospheric conditions to be fulfilled, in order for a signal to reach the elephant via an acoustic pathway. No information on expected sound pressure level is given, most likely due to the non-availability of data and theoretical models. The acoustic pathway described in [54] definitely exists

but, more likely, plays a subsidiary role rather than being the dominant underlying physical process.

Inspired by [54], the present model builds upon the well-known [52, 51, 111, 87, 80] property of tsunamis to generate infrasound. By the acoustic intransparency of the air-water window, infrasound generated during the seaquake and, even more, underwater information of the tsunami cannot be transmitted through a purely acoustic pathway. Rather, we follow the findings of biologists [66, 104, 103] and assume that the feet of the elephant act as an "ear to the ground" as formulated in the title of [104]. The link between the tsunami and the elephant is constituted by the continental margin's surface vibrating in response to the tsunami.

Vortex force source term   Newton's second law states that in mechanical equilibrium, a force density corresponds to a temporal change in momentum density; cf. [127] in the context of acoustics. As noted in the introduction, the seabed floor is not aligned horizontally until the shoreline is reached but rather exhibits a non-zero slope $\beta \approx 3°$ on average. We interpolate the depth profile of the continental margin using the quantities of the last row in Tab. 3.1 through the affine-linear function

$$h : [0, L] \to [-H_0, 0], \, x \mapsto -H_0 + \frac{H_0}{L}x \tag{3.1}$$

and note that $1 \gg H_0/L = \tan\beta \approx \beta$ in the small angle approximation is consistent with the previous considerations. This is in contrast to the assumptions underlying the treatment [54] in which the so-called vertical wall approximation [87] has been utilized.

In case of the momentum disturbance that defines the tsunami traveling in, say, x-direction and enclosing a non-right angle with the seabed floor's outward unit normal **n** a thin turbulent layer forms. It extends as far as slightly above the seabed floor. The layer of vorticity results from forcing the motion of the viscous fluid "ocean water" being to abruptly alter its direction. This change in direction is due to the presence of a solid obstacle.

Note that while in the fluid rest frame, the full Navier-Stokes equations require the usage of the no-slip boundary conditions, these boundary conditions need no longer be satisfied in the presence of the tsunami excess momentum. Instead, the fluid parcels adjacent to the seabed floor are dragged along by the upper layers of fluid parcels, experiencing the full excess momentum handed to the ocean fluid by the tsunami generating seismic event. We refer to [87] for tsunami theory.

For the theory of vortex vibrations as used for the detection of tsunamis in elephants, we need a digression into the theories of aerodynamics and aero-acoustics which served as an inspiration. For the sake of better readability, a more detailed account is given in Appendix 3.A. The thin but extended region of turbulence slightly above the seabed floor can generate first of all underwater sound in the sense of Lighthill's theory [90, 91, 40] of sound generated aerodynamically - the formalism generalizes to sound in liquid media canonically. Neglecting viscous effects and using the lineaized thermal equation of state in water, we arrive at Howe-Powell's theory of vortex acoustics [127], a special case of Crocco's equation [33, 48].

Let us adopt the interpretation of the source of sound in this theory's governing equation as a force density of the same mathematical structure as a Coriolis force suggested in [127]. These qualitative considerations can be summarized in the following source term model for a force-per-volume density

$$\mathbf{f}_v = \rho_w \left(\boldsymbol{\omega} \times \mathbf{v} \right) \tag{3.2}$$

In this equation, we have utilized that the tsunami generating event only generates a small excess momentum density and thus constitutes merely a small perturbation to the oceanic fluid moving at the characteristic velocity $v = \|\mathbf{v}\| \sim (5 - 25)\,\mathrm{cm s}^{-1}$.

The symbol $\boldsymbol{\omega} = \nabla \times \mathbf{v}$ denotes the vorticity. Based on a physical interpretation of a weakened notion of a smooth manifold, the so-called manifolds with corners [77, 78, 79], the vorticity could be found to be confined mathematically to the solid-fluid interface, i.e., the seabed floor. See Appendix 3.B. for details. The building blocks of the vorticity $\boldsymbol{\omega}$ are small vortex dipoles as found with the aid of a decomposition of the depth profile (3.1) into step functions. This is consistent with other parts of our work, namely chapter 4 and the appendix to chapter 4, where we could derive vortex dipoles at geometric singularities, consistent with Ffowcs-Williams' approach [127] to deduce vortex dipoles at solid boundaries from Lighthill's equation [90, 91, 40] as an application of integration theorems to the leading-order quadrupole term in Lighthill's equation in integral formulation. The prediction of the vortices can be experimentally analyzed by placing underwater microphones close to the seabed floor during tsunamis.

Since the tsunami is a wave phenomenon, wherein kinetic and potential energy are periodically converted to the respective other form of energy, the orientation of the vortex dipoles cannot be treated as fixed in time. The restoring gravitational force triggers fluid parcels to oscillate back and forth around its equilibrium position which

is constant in the fluid rest frame. Thus, the fluid injected into the vortex whirls either positively or negatively around the vortex core in a planar cross-sectional model.

Let us understand the orientation of the individual vortices forming the dipole as small "spins" pointing either out of $(+1)$ or into (-1) the drawing plane. We assign an energy to them that is proportional to their orientation. Using the micro-canonical ensemble, we find in complete analogy to the standard treatment of magnetic materials that vortex dipoles aligned periodically maximize the entropy of the vortex system. Details on the treatment of the one-dimensional Ising model in the micro-canonical ensemble can be found in [155].

Short: The vortex force density in (3.2) naturally also exerts a load on the surface of the continental plate, see Appendices 3.A and 3.B. Metaphorically, the total of vortex dipoles behave physically as a superposition of small "hammers" knocking the surface of the continental margin. Mathematically, they are treated as a superposition of sinusoidal, due to periodically reversing their orientation, elementary loads on the surface of the continental plate.

Navier's equation in Hookian approximation   We let λ, μ denote the first and second Lamé constant respectively. Furthermore, we let ρ_s symbolize the mass-per-volume density of the material constitution of the continental plate. The constants are assumed homogeneous and we use a Hookian approximation for the stress-strain relation in the Cauchy stress tensor in the derivation of Navier's elastic equation. Following the argument exposed in the previous paragraph, we obtain a nonhomogeneous linear hyperbolic partial differential equation for the displacement vector $\mathbf{u}$.

The elephant's legs are aligned perpendicularly to the ground such that the detection of a transverse wave is most plausible. The solid-air interface is intransparent to transmission of longitudinal seismic waves: From [56, 57], using $p_s = -K\nabla\mathbf{u}$, the equation for the primary seismic waves degrees of freedom gives rise to an acoustic pressure in the solid material of the continental plate. Since the amplitude of the transmitted pressure wave $t \sim (\rho_a/\rho_s)$ at the solid-air interface grows with the ratio between mass-per-volume density of the air and the one of the solid, we find that $T = |t|^2 \sim 10^{-6}$ typically; cf. [127] for a detailed treatment of the reflexion problem or see the introduction in Appendix 3.A. Euler's equation on the other hand allows us to identify $\partial_n p = -\rho_a \partial_t v_n = -\rho_a \partial_t^2 u_s$ for the *secondary seismic wave* with wave function u_s. While the primary waves are longitudinal degrees of freedom, the secondary wave

is a transverse degree of freedom and thus can generate an acoustic pressure field by vibrational acoustics interaction at the solid-air interface. For an introduction, we refer the reader to chapter 1.3 and for details to [86]. Application of the Helmholtz decomposition theorem [64] results in the wave equation for a secondary seismic wave containing the *normal component* of the vortex force density source term as inhomogeneity:

$$\frac{\partial^2 u_s}{\partial t^2} - c^2 \Delta u_s = \mathfrak{g}_v(\aleph) \left\langle \mathbf{n}, \boldsymbol{\omega}, \mathbf{V} \right\rangle_{\mathbb{R}^3} . \tag{3.3}$$

We specify the quantities involved in the preceding equation and comment afterwards on the interpretation: The wave function for the secondary seismic wave is defined as the projection of the elastic displacement vector onto the direction of the outward unit normal of the interface of the continental plate with media in fluid or gaseous phase, $u_s \equiv \langle \mathbf{n}, \mathbf{u} \rangle_{\mathbb{R}^3} \mathbf{n}$. The object Δ is the Laplace-Beltrami operator on the *(hyper-) surface* of the continental plate. u_s describes a seismic surface wave as appropriate for a bio-tremological approach [66, 64]. The coupling constant $\mathfrak{g}_v(\aleph)$ depends via a Lorentzian functional dependence on the material parameter $\aleph$ defined below and the ratio $\mathfrak{g}_v^0 = \rho_a/\rho_s$ of the mass-per-volume densities of air and the solid constituents of the continental plate. More precisely, $\mathfrak{g}_v(\aleph) \equiv \mathfrak{g}_v^0/(1 + \aleph^2)$ where $\aleph$ is given as the positive solution of the equation $\aleph^2 \equiv \lambda/(2\mu)$. We recall that primary and secondary seismic waves exhibit different phase velocities [64], the slower of the two being the secondary wave with phase velocity c_s obtained from the material relation $c_s^2 \equiv \mu/\rho_s$.

The physical picture of the vortex region modeled as the source term on the right-hand side of equation (3.3) is that of small hammers knocking the surface of the continental plate. The tsunami generating event itself causes a short and temporally localized peak knock on the continental plate which travels too fast through the Earth's surface to be eligible for an explanation of the data [159]. On the contrary, the vortex region is the result of the tsunami wave fronts traveling gradually towards the shoreline. The tsunami builds up the vortex region in the course of propagation, and thus causes a seismic signal of increasing intensity. Based on the biological evidence of tactile sensing in the elephant, it may witness the cues so-generated while standing on the continental plate.

Metaphorically, the elephants' legs function as a tuning fork placed on a plate which is hammered on at an increasing area as the time (of tsunami propagation) passes.

Functional shape of the vortex source term   A detailed derivation of the function form of the vorticty $\boldsymbol{\omega}$ and the induced fluid velocity $\mathbf{v}$ is omitted here due to its length

but can be found in Appendix 3.B. The physically relevant part is the far field behavior as the leading order expansion the (dimensionless) slope parameter $\beta = H_0/L$. Here, we confine ourselves to sketch the derivation.

We define a cylindrical coordinate system such that in a cross sectional model of the tsunami region through the Earth's center, the direction from the tsunami generating event to the shoreline at sea level is the x-direction. The direction pointing away from the Earth's center is the y-direction. The x- and y-axis form the axes of a local Cartesian coordinate system which is termed drawing plane subsequently. The z-direction is defined such that the unit vector $\hat{e}_z$ points into the drawing plane and the negative z-axis goes out of the drawing plane. Introducing polar coordinates in the drawing plane and assuming that the depth profile h_0 defined in (3.1) stays quantitatively unchanged in a small neighborhood $(z_0 - \delta z, z_0 + \delta z)$ of a fixed z_0, a lengthy calculation, see appendix 3.B, permits the derivation of the dipoles' announced in the pre-to-last paragraph from the principle of angular momentum conservation in a far-field analysis in the potential theoretic framework of hydrodynamics. Viscosity is accounted for by using no-slip boundary conditions for the vortex core center positions at the surface of the underwater region of the continental plate. For $|x/y| \gg 1, H_0/L$, we recover the hydrodynamic far-field generated by a vortex in the vicinity of the shoreline at $x = L$. The expression can be Taylor expanded in a power series in the slope parameter β.

After a lot of algebra, we find

$$\boldsymbol{\omega} = -c_\omega \frac{\Gamma(t)\beta}{2\pi \cdot x^{5/2}} \hat{e}_z + \mathcal{O}(\beta^3 \hat{e}_z) \tag{3.4}$$

$$\boldsymbol{v} = c_v \frac{\Gamma(t)\beta}{2\pi \cdot x^2} \hat{e}_\phi + \mathcal{O}(\beta^3 \hat{e}_\phi) \tag{3.5}$$

in the cylindrical coordinate system defined by the polar coordinates introduced in drawing plane and the perpendicularly aligned z-axis. c_ω, c_v are two fit constants that cannot be derived. In terms of units, $[c_v] = 1\,\text{m}$ and $[c_\omega] = 1\,\text{m}^{1/2}$.

For the measurable amplitude U of the plate vibration, only the product $c_{\text{fit}} \equiv c_v c_\omega$ occurs and is the only free parameter. We emphasize that the expression is to be understood as a summation over all vortex dipoles allocated in the thin sheet of vorticity generated by the tsunami on top of the seabed floor.

Lighthill's V^8-law   The results on the expected sound pressure level equivalent from the vortex vibration theory can be estimated using *Lighthill's V^8-law*. It is derived as a far-field scaling of the *Lighthill equation* which is itself an exact rewriting of the

Navier-Stokes equations. We only give a very condensed account of the derivation of the V^8-law and refer to standard aero-acoustics textbooks such as [72] and the online textbook introduction [127].

The starting point is the integral formulation of Lighthill's equation: The mass density ρ of a fluid with speed of sound c_f can be expressed as a convolution of a Coulomb-like kernel and the double contraction of a "tensor-valued source term", the so-called *Lighthill stress tensor* evaluated at the retarded time t_{ret} defined below:

$$4\pi c_f^2 \rho(t, \mathbf{x}) = \partial_{i,j}^2 \int_{\mathbb{R}^3} \frac{d^3 x'\, T^{ij}(t_{\mathrm{ret}}, \mathbf{x}')}{\|\mathbf{x} - \mathbf{x}'\|} \tag{3.6}$$

The *retarded time* is defined through $t_{\mathrm{ret}} \equiv t - \|\mathbf{x} - \mathbf{x}'\|/c$. We implied Einstein summation convention on repeated indices in co- and contravariant index position. With the acoustic linearization of the thermal equation of state, $p = c_f^2 \rho$, and in the inviscid limit, $1/\mathrm{Re} \equiv 0$, the Lighthill stress tensor [127, 90, 91, 40] simplifies to

$$T^{ij} = \rho_0 v^i v^j \tag{3.7}$$

where we neglect contributions stemming from small mass density fluctuations in the stress tensor ("no back-reaction").

Acoustic multipole expansion [127] leads to the far-field scaling

$$p \simeq \frac{\rho_0 l v^4}{4\pi c_f^2 \|\mathbf{x}\|}. \tag{3.8}$$

Using the specific acoustic impedance $Z = \rho_0 c_f$ [127], we find for the power radiated through a spherical surface bounding the far-field region under consideration

$$\mathcal{P} \simeq \frac{\rho_0 l^2 v^8}{4\pi c_f^5}. \tag{3.9}$$

The next section contains analytic and numeric results obtained through application of the model specified in this and the previous section.

3.3   Results

Further parameter estimates   The equations (3.4) and (3.5) depend on the time t via the circulation $\Gamma(t)$. Using a Fourier transform, $\Gamma(t)$ is decomposed into spectral amplitudes $\hat{\Gamma}(\omega)$ and time-harmonic drives $\sim \exp(i\omega t)$ with $\omega \in 2\pi\mathbb{F}$ in the angular version of the frequency band $\mathbb{F} = [f_{\min}, f_{\max}]$.

At $t = 1/(2f)$, the vortex dipoles encapsulated in $\Gamma(t)$ will have reversed the orientation and performed a so-called *spin-flip* following the statistical interpretation of the vorticity region introduced in the preceding section. The goal is to bound the spin-flip frequency with known quantities from above and below and define the frequency band $\mathbb{F}$ this way.

A lower bound is established with the aid of basic tsunami theory [87]: Linear [134] water wave theory predicts a tsunami period $T_{\text{ts}} \sim (1.2 - 1.8) \cdot 10^3 \, \text{s}$ and thus, through its reciprocal, a minimal frequency $f_{\min} \simeq 2 \cdot 10^{-4} \, \text{Hz}$. Namely, the tsunami is a globally periodic phenomenon by definition. Translation invariance in t by periodicity causes the fluid mechanical properties of the vortex region to be at least of the same period as the tsunami. Otherwise the overall periodic tsunami structure would be broken.

A bound from above requires a result from turbulence theory. It is based on an analogy to the van Karmàn vortex street [98, 71, 128]: Assuming that the length of the continental margin is much larger than the characteristic length of a vortex dipole, a spin flip can be regarded as the shedding of a vortex monopole in the wake of a cylinder streamed by a real fluid. We refer to the appendix 3.B for the manifestation of the spin-flip as a time-dependent circulation. In the Karmàn vortex street picture, two conditions hold

$$\text{Re} = \frac{v l_c}{\nu} \geq \text{Re}_c = 90 \, \& \tag{3.10}$$

$$f = \text{St}_c \cdot \frac{v}{l_c} = 0.2 \cdot \frac{v}{l_c} \tag{3.11}$$

The symbol Re refers to the Reynolds number of the fluid flow which must exceed the threshold value of $\text{Re}_c = 90$ to permit the formation of a van Karmàn vortex street. The quantity $\text{St}_c = 0.2$ is the Strouhal number for the flow around the obstacle and found to vary for a variety of geometries and flows only mildly around the value $\text{St}_c = 0.2$ whence we take it as constant. v is the characteristic fluid velocity in the flow in the earth-fixed system, i.e, $v \in [5 \, \text{cms}^{-1}, 25 \, \text{cms}^{-1}]$. The kinematic viscosity of ocean water can be taken in first order as $\nu = 10^{-6} \, \text{m}^2\text{s}^{-1}$. l_c and f are unknown but can be specified from the 2×2-system of nonlinear equations in two unknowns.

Interested in an upper bound for f, we note that the l_c^{-1}-dependency on the right-hand side of (3.11) enables us to replace "$\geq$" by "$=$" in (3.10). The formula for $f_{\max}$ is

$$f_{\max} = \frac{\text{St}_c}{\text{Re}_c} \frac{v^2}{\nu} \in [3 \, \text{Hz}, 70 \, \text{Hz}] \tag{3.12}$$

with the lower value for $v = 25\,\text{cms}^{-1}$ and the higher value for $v = 5\,\text{cms}^{-1}$ respectively.

The values specified that way include the infrasonic regime $\lesssim 20\,\text{Hz}$ in terms of the orders of magnitudes calculation displayed above. We take the value $f_{\max} = 40\,\text{Hz}$ as a maximal value for the spin-flip frequency and specify the frequency band $\mathbb{F} \simeq [5 \cdot 10^{-4}\,\text{Hz}, 40\,\text{Hz}]$. The calculation yields a typical length scale $l_c \simeq (45 - 220)\,\text{nm}$ which is by two to three orders of magnitude above the threshold for quantum mechanics: $10^{-10}\,\text{m}$.

A calculation based on conservation of rotational energy shows that the core radius δ_c of a vortex monopole constituent of the dipole is slightly smaller. δ_c is defined through the prescription $\Gamma \simeq 2\pi\delta_c v$. The aforementioned calculation demonstrates that $2^{3/2}\delta_c = l_c$. From the above result (3.12), $\delta_c \sim 20\,\text{nm}$ follows using $v > 0$ from $v^2 = \text{Re}_c/\text{St}_c\nu f_{\max}$ at $f_{\max} = 40\,\text{Hz}$.

Arrival-time difference The phase velocity of a tsunami depends on the functional form of the depth profile [87] through $c_{\text{ts}}(x) = \sqrt{-gh(x)}$ with h given in (3.1) and $g \approx 9.81\,\text{ms}^{-2}$ being the near-field gravitational constant $g = GM_{\text{e}}/R_{\text{e}}$ derived from Newton's gravitational law for a mass probe placed at a distance $R_{\text{e}} \simeq 6.3 \cdot 10^6\,\text{m}$ of the point-mass of the mass of the earth M_{e}.

The *arrival-time difference* Δt is defined as the time difference between a tsunami wave front traveling the distance L at c_{ts} on the ocean's surface and the time the secondary seismic surface wave traveling along the shortest path of length $L\sqrt{1 + \beta^2}$ on the continental margin's surface at phase velocity $c_s = 3.5\,\text{kms}^{-1}$. Unlike [54, 55] we have an affine-linear depth profile (3.1) not using the somewhat unrealistic vertical-wall approximation [87] such that we expect the arrival time difference Δt to be firstly smaller than the one obtained in [54] and secondly to be given as an integral formula that should reproduce in the vertical-wall approximation, $\beta = 0$, the results in [54]. The arrival-time difference is given through the analytically tractable integral

$$
\begin{aligned}
(\Delta t)(\beta) &= \int_0^L dx \left(c_{\text{ts}}(x)^{-1} - c_s^{-1} \right) \\
&= \int_0^{H_0\beta^{-1}} dx \left(\frac{1}{\sqrt{gH_0(1 - \beta x/H_0)}} - \frac{1}{c_s} \right).
\end{aligned}
\tag{3.13}
$$

We find for the exact value of the integral as well as for the vertical-wall approxi-

mation indexed as "vv" $\beta = 0$ inside the integral

$$(\Delta t)(\beta) = \left(\frac{2}{\sqrt{gH_0}} - \sqrt{\frac{1 + \beta^2}{c_s^2}} \right) \frac{H_0}{\beta} \tag{3.14}$$

$$(\Delta t)_{\text{vv}} = \frac{L}{\sqrt{gH_0}} - \frac{L}{c_s}. \tag{3.15}$$

The latter equation (3.15) is the formula used in [54]. It differs from the exact value of the arrival time difference by almost a factor of 2 and thus leads to underestimating the arrival-time difference.

The authors of the article [54] rule out the seismic pathway as being eligible for tsunami early-detection in elephants. This conclusion is correct on the basis of their approach but incorrect in general due to (3.14) and (3.13). In particular, [54] obtained at $L = 10^2$ km an arrival-time difference of $(\Delta t)_{\text{vv}} = 8$ min. In contrast to that and for a considerably short distance to the shoreline equation, (3.14) produces for $H_0 = 4$ km at $L = 10^2$ km the value $\Delta t \approx 16$ min which is closer to the expected value of $\sim (20 - 60)$ min on the basis of the data [159].

Necessarily, replacing the phase velocity c_s with the speed of sound in air [54] one obtains $(\Delta t)_{\text{ac}} \sim 12$ min for a purely acoustic process by $c_s \rightarrow c_a \approx 343 \, \text{ms}^{-1}$ in (3.14). For $L = 10^3$ km we find $(\Delta t)_{\text{vv,ac}} \approx 160$ min as has to be compared to $(\Delta t)_{\text{vv}} = 35$ min in the vertical wall approximation for a seismic process.

As will be discussed in the next two paragraphs, a high Δt is advantageous because the seismic signal from the vortex layer forms gradually and thus has an advantageous signal-to-noise ratio for localization already built in.

Expected sound pressure level equivalent   In order to compare the strength of the signal that arrives at the elephant to an acoustic signal we exploit the fact that the feet of the elephant have an impedance matching function [104, 102]. The vibration of the continental plate respects conservation of energy and the impedance matching ensures that the elephants "puts an ear to the ground" [104] and detects the vibration in itself.

Mathematically, the impedance matching allows to identify $u_s = v_{\text{det}}$ where v_{det} denotes the normal speed of displacement of the detection surface which we take to be the feet of the elephants $r_{\text{det}} \sim 10$ cm. Physically, the impedance matching via the fatty cushions in the elephants feet provides a mechanism to circumvent reflective losses

that would occur at interfaces with a high difference in mass densities such as solid-air interfaces.

Since the mass-per-volume densities of water and solid are of the same order of magnitude, we can apply Lighthill's V^8-law (3.9) and multiply with the number of vortex monopoles in the turbulent vortex layer. We denote this number by N and use $N = 10^4 L_c L_v \cdot L/(L_v^3)$ where $L_v := 100 \cdot \delta_c$ denotes the spacing between individual vortices. L_c is the length of the shoreline and L its distance from the tsunami generating event. The factor 10^4 accounts for the vertical extension of the vortex layer since $L_v \sim 1\,\mu$m is by viscosity of water not a sufficient vertical extension of the turbulent vortex layer hammering the surface of the continental margin. Define $V_v = L_v^3 N$. Setting $l \to L_v$ in (3.9) and performing the multiplication with the number N, we find

$$\mathcal{P} \simeq \frac{\rho_0 V_v v^8}{4\pi c_f^5 L_v}. \tag{3.16}$$

which is seen to be independent of the precise value of L_v! The *sound pressure level* (SPL) is defined through normalizing the power $\mathcal{P}$ to $\mathcal{P}_c = I_c A_{\text{det}}$, that is,

$$\text{SPL}(\mathcal{P}|\mathcal{P}_c) = 10 \log_{10}\left(\frac{\mathcal{P}}{\mathcal{P}_c}\right) \tag{3.17}$$

where $A_{\text{det}} = \pi r_{\text{det}}^2$ is the area of detection and $I_c = 10^{-12}\,\text{Wm}^{-2}$ is the *hearing threshold for humans*. The reason for using a quantity related to humans is due to the field's conventions; See e.g. [55, 103, 64, 97].

Plugging the result (3.16) for $\mathcal{P}$ in (3.17), we find a formula that predicts which sound pressure level *equivalent* is to be expected:

$$\text{SPL}(\mathcal{P}|\mathcal{P}_c) \simeq 10 \log_{10}\left(\frac{\rho_0 V_v v^8}{4\pi c_f^5 L_v I_c A_{\text{det}}}\right). \tag{3.18}$$

The terminology features the addendum "equivalent" to mirror the fact that in reality we have a seismic cue which does not convert to sound without reflection losses at the solid-air interface; cf. the recent articles [56, 57] on the topic of reflection at interfaces.

The impedance matching via the fatty cushions [104] ensured that the elephant actually receives a cue at sound pressure level equivalent well-above the sound pressure level obtained for thermal ($T = 300\,$K) noise of a frequency band exhibiting a bandwidth of the order of $\sim 10\,$Hz. Choosing a detection area of $A_{\text{det}} \simeq 1\,\text{m}^2$ which corresponds roughly to the area covered by the elephants feet, this yields $I_{\text{therm}}\mathcal{P}_{\text{therm}}/A_{\text{det}} \sim$

$10^{-20}\,\mathrm{Wm}^{-2} \sim 10^{-8} \cdot I_c$ according to the Nyquist relation $\mathcal{P}_{\mathrm{therm}} = k_B T \Delta f$ with the Boltzmann constant $k_B \approx 1.38 \cdot 10^{-23}\,\mathrm{JK}^{-1}$! The excitement is dampened by the fact that the precise biological working mechanism of the fatty cushions in the elephants feet is up-to-date still a subject of ongoing experimental research in zoology [104].

Numerically and using the parameters in Tab. 3.2, we find the following values for the expected sound pressure level equivalent from (3.18) interpreted as a function of the fluid velocity v in the turbulent vortex layer region alone: $\mathrm{SPL}(v = 5\,\mathrm{cms}^{-1}) \simeq 30\,\mathrm{dB}$, $\mathrm{SPL}(v = 10\,\mathrm{cms}^{-1}) \simeq 50\,\mathrm{dB}$, $\mathrm{SPL}(v = 20\,\mathrm{cms}^{-1}) \simeq 70\,\mathrm{dB}$ and $\mathrm{SPL}(v = 25\,\mathrm{cms}^{-1}) \simeq 80\,\mathrm{dB}$.

The numbers are illustrated by the following analogous acoustic events in everyday human life: The sound pressure level equivalents correspond in the given order to the whisper of leaves in the wind, a somewhat medium-to-loud conversation, and traffic noise on a road and a highway, respectively. Inspection of the derivation of the numbers clarifies that they only substantiate the feasibility of the seismic pathway we modeled by the theory of vortex vibrations. however, they do *not* represent accurate figures because already Lighthill's V^8-law only aspires to give an order-of-magnitude estimate.

Numerical results In Fig. 3.3 the vortex core radius $\delta_c = 2^{-3/2} \cdot l_c$ and the maximum frequency $f_{\max} = \mathrm{St}_c/\mathrm{Re}_c v^2/(2\nu)$, i.e., cutting off at half the value according to (3.12), have been plotted against the fluid velocity v in the turbulent vortex layer in cms^{-1} on top of the solid-fluid interface of the continental margin. The core radius δ_c decreases with increasing v while the maximum frequency $f_{\max}$ increases. There are natural bounds from above by, first, the requirement that δ_c needs to be bigger than a quantum mechanical scale $\sim 10^{-10}\,\mathrm{m}$ for the classical turbulence theory as obtained from the Navier-Stokes equations to be applicable. Second, the maximum excited frequency $f_{\max} \in \mathbb{F}$ of the frequency band $\mathbb{F}$ should not exceed the high-infrasonic viz. very deep sonic frequency range. The latter is a consequence of elephants using [103, 104, 55] infrasonic frequencies in communication with peak sensitivity in the range $(30 - 50)\,\mathrm{Hz}$. Despite being already sonic frequencies, they are practically undetectable for humans and the majority of the frequency band below the frequency hearing threshold is inaccessible to human sound localization but accessible for the lucky elephant.

Fig. 3.4 shows the arrival time difference (3.14) in minutes at a fixed depth $H_0 = 4 \cdot 10^3\,\mathrm{m}$ in the top and at a fixed distance of the tsunami generating sea quake from the shoreline, $L = 10^5\,\mathrm{m}$ in the bottom plot. As exemplified by the part of the graph
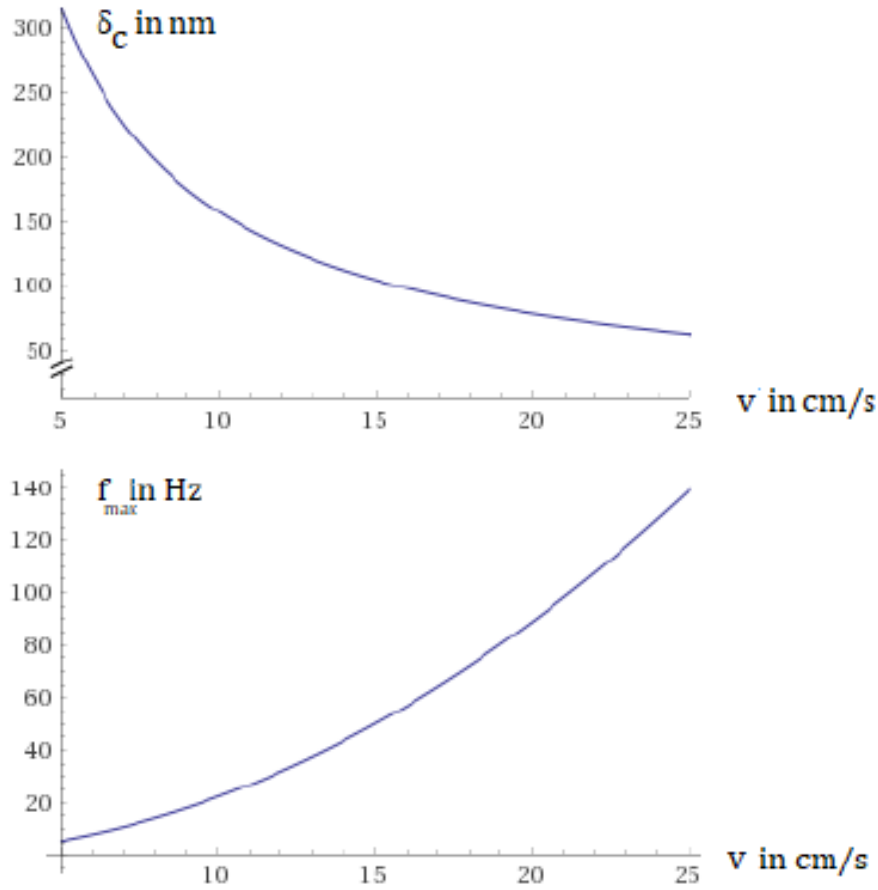
Figure 3.3: Top: Vortex core radius $\delta_c = \nu \cdot \text{Re}_c/(2\sqrt{2}v)$ as a function of the fluid velocity $v \in [5\,\text{cms}^{-1}, 25\,\text{cms}^{-1}]$ of the whirling fluid parcels in the layer of vorticity on top of the surface of the continental margin as obtained from (3.10) and (3.11) at minimal Reynolds number $\text{Re}_c = 90$ and characteristic Strouhal number $\text{St}_c = 0.2$ according to the van Karmàn vortex street analogy. Bottom: Maximum frequency $f_{\max} = \cdot \text{St}_c/\text{Re}_c \cdot v^2/\nu$ as a function of the fluid velocity $v \in [5\,\text{cms}^{-1}, 25\,\text{cms}^{-1}]$ of the whirling fluid parcels in the layer of vorticity on top of the surface of the continental margin as obtained from (3.10) and (3.11) at minimal Reynolds number $\text{Re}_c = 90$ and characteristic Strouhal number $\text{St}_c = 0.2$ according to the van Karmàn vortex street analogy.
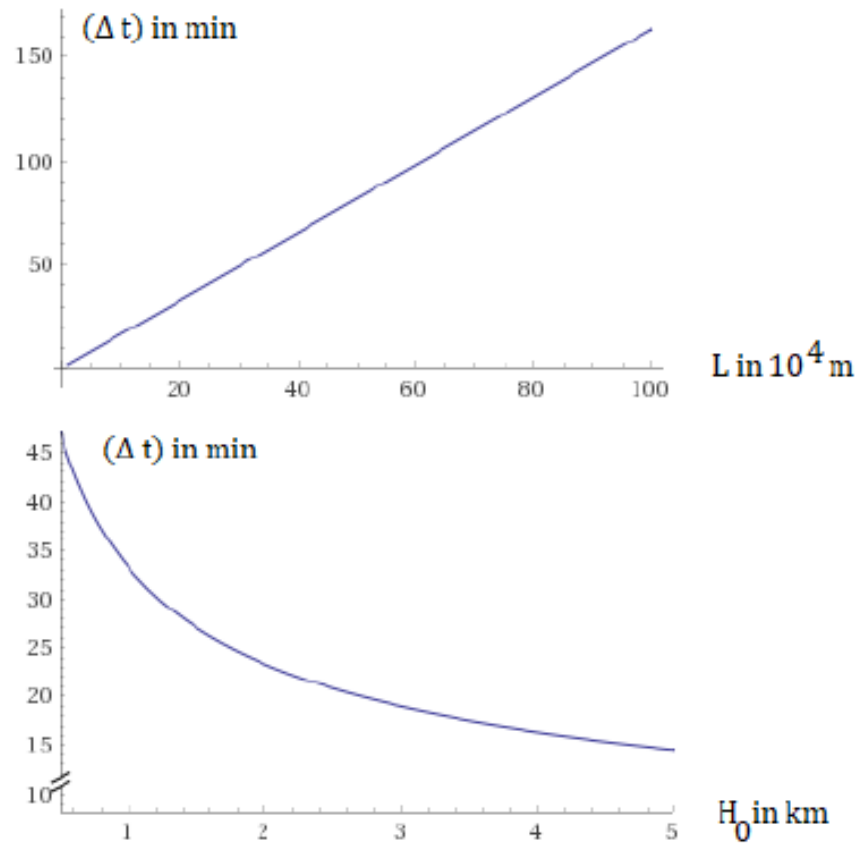
Figure 3.4: Top: Arrival-time difference Δt according to (3.14) at $H_0 = 4 \cdot 10^3$ m as a function of $L \in [10^4\,\text{m}, 10^6\,\text{m}]$. Bottom: Arrival-time difference Δt according to (3.14) at $L = 10^5$ m as a function of $H_0 \in [10^2\,\text{m}, 5 \cdot 10^4\,\text{m}]$.
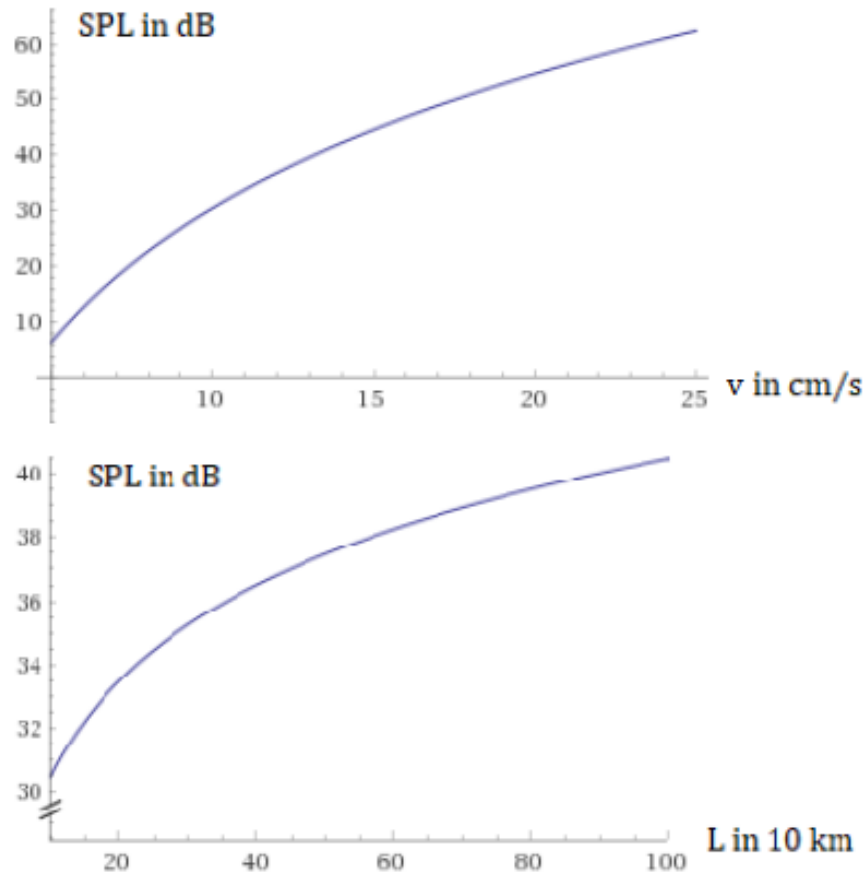
Figure 3.5: Top: The expected sound pressure level in [dB] equivalent according to (3.18) equivalent at fixed horizontal distance to the shoreline $L = 10^5$ m as a function of the fluid velocity in the turbulent vortex layer $v \in [5\,\mathrm{cms}^{-1}, 25\,\mathrm{cms}^{-1}]$. The other parameters are summarized in Tab. 3.2. Bottom: The expected sound pressure level equivalent in [dB] according to (3.18) equivalent at fixed fluid velocity in the vortex layer region $v = 10\,\mathrm{cms}^{-1}$ as a function of $L \in [10^4\,\mathrm{m}, 10^6\,\mathrm{m}]$. The other parameters are summarized in Tab. 3.2.

Name	Symbol	Value
Kinematic viscosity	ν	$\sim 10^{-2}\,\mathrm{cm^2 s^{-1}}$
Density water	ρ_0	$\approx 10^3\,\mathrm{kgm^{-3}}$
Speed of sound	c_f	$1481\,\mathrm{ms^{-1}}$
S-wave phase velocity	c_s	$\approx 3.5 \cdot 10^3\,\mathrm{ms^{-1}}$
Reynolds number	Re	$\geq 90 =: \mathrm{Re}_c$
Strouhal number	St_c	≈ 0.2
Threshold of hearing	I_c	$\sim 10^{-12}\,\mathrm{Wm^{-2}}$
Shoreline length	L_{coast}	$\sim 10^6\,\mathrm{m}$
Vortex length scale	L_v	$:= 100 \cdot \delta_c$
Vortex layer volume	V_v	$:= 10^4 \cdot L \cdot L_c \cdot L_v$
Slope parameter	β	$:= H_0/L$
Area of detection	A_{det}	$:= \pi r_{\mathrm{det}}^2$
Thermal noise	I_{therm}	$\sim 10^{-20}\,\mathrm{Wm^{-2}}$

Table 3.2: Parameters in numerical evaluation of the vortex vibration theory applied to tsunami sensing of elephants.

of the function in the plotting range, the arrival time difference $(\Delta t)(L, H_0)$ is strictly monotonously increasing with the distance to the shoreline L and strictly monotonously decreasing with the maximum depth of the continental margin, i.e., the depth at which the abyssal plains on the oceanic plate are located oceanographically. In particular, having found the missing factor of 2 [55], we find that the first signal of the tsunami arrived at about $(40-50)\,\mathrm{min}$ before the tsunami arrives at the coast. This agrees with the only published scientific data set [159] available to us as well as reports on such findings such as [104, 103, 66]. It is known that a repeated signal increasing in intensity (see the paragraph on the sound pressure level equivalent) increases the signal-to-noise ratio and thus allows better localization on the part of the elephants [104, 102, 103]. Since the turbulent layer of vorticity builds up as the tsunami propagates towards the shoreline and thus only generates a gradually increasing signal, even the difference in $\sim 10\,\mathrm{min}$ of the observed abnormal behavior of satellite collared elephants [159] is explained.

The "strength" of the signal has been assessed by mimicking the definition of the acoustic sound pressure level to define a sound pressure level equivalent for the seismic

signal. The motivation for the utilization of a joint measure of auditory and tactile loudness is that possibly the auditory pathway is used to process the seismic signal [104, 102]. Therefore, it is plausible to quantify the loudness of the seismic signal analogously to acoustic signals. See the previous paragraph for more details and selected numerical values. With the parameter choices summarized in Tab. 3.2, the expected sound pressure level equivalent according to (3.18) is depicted as a function of the fluid velocity v in the turbulent vortex layer region in the top plot of Fig. 3.5. The bottom plot in Fig. 3.5 shows the expected sound pressure level equivalent as a function of the distance L to the shoreline.

Outlook on Geometric Perturbation Theory (GPT)   Although not of primary interest to the study of elephants' endogenic tsunami localization system, we note that the vortex vibration theory (3.3) will in general be a complicated differential equation because the Laplace-Beltrami operator is defined on a somewhat "wildly" shaped embedded surface in, here, $\mathbb{R}^3$. In many cases, approximations can be performed. Indeed, geometric perturbation theory (GPT) in the style of chapter 2 can be applied to flatten the continental plate to a disk-shaped surface which is solvable again by standard techniques. This way one easily establishes through a lengthy but straightforward calculation an order-of-magnitude formula of the amplitude of continental plate vibration as a function of the circulation from (3.3) and (3.4). The interested reader is referred to Appendix 3.C for more details.

3.4   Summary and outlook

Summary   We have introduced the theory of vortex vibration as the implementation of vortex layers in flow, adjacent to a solid surface, acting as small hammers on that surface. They result in the excitation of seismic (surface) waves.

In the context of the propagating tsunami, the surface vibration transports a cue about the current position of the tsunami, encapsulated in the strength of the signal, to the shoreline. Assuming correctness of the current biological opinion on the impedance matching property of the elephant's feet, the elephant detects the cue and responds to the approaching hazard. An order-of-magnitudes estimate based on similarity results in turbulence theory together with an analogy to the von Karmàn vortex street showed that the high infrasonic and very deep sonic frequency range is covered by the

signal generated through vortex(-induced) vibrations ($\sim 15 - 45\,\text{Hz}$) and is in particular detectable by the elephant but closed to humans.

The predictions of the model yield plausible results in terms of the arrival-time difference also for secondary seismic surface waves, improving on a result established earlier [54]. The arrival-time difference as predicted by theory is shown to be sufficiently large to explain the (to the authors' knowledge only) available data set meeting scientific standards; See the closing remark.

The sound pressure level equivalent serves as a measure to compare the strength of the seismic signal to usual acoustic signals. The sound pressure level equivalent yielded values that are sufficiently high to be detected and most probably sufficiently high to cause arousal in elephants to trigger flight behavior. The fact that humans did not receive early-warning cues on the approaching tsunami is explained by the fact that the impedance matching function of the fatty material in the elephants' feet is absent in humans. Although the repetition, by the gradual formation, of the seismic signal ameliorates the signal-to-noise ratio to foster mammalian tsunami localization, the high reflection coefficient at the air-solid interface obstructs a detection by mammals lacking a well-adapted tactile sensing system featuring impedance matching or comparable mechanisms.

Outlook   Many questions remain unanswered due to a lack of experimental data. We name two of them: First the impedance matching function of elephants' feet awaits a thorough experimental investigation. Second the precise pathways in elephants, among other animals, to process seismic hearing cues are largely unexplored from both the theoretical an experimental side. The present work along with the bonus material from the appendix shall provide a theoretical foundation for research in the highly interdisciplinary field of bio-tremology.

Closing remark   The investigation of animals' ability to predict earthquakes and tsunamis is still a topical issue as also observed in [160]. The authors wish to reinforce the closing remark of the previously referenced article: In many animals, the data available are scarce. Quality standards for the data acquisition are rarely fulfilled in a satisfactory manner due to the – obvious – experimental difficulties to record animal responses to tsunamis and earthquakes under field study conditions. Nonetheless, the author wishes to express hereby his hope that the availability of data meeting scientific

standards increase in the future, e.g., by following the quality control checklist succinctly summarized in [160].

3.5 Appendices for Chapter 3

Appendix 3.A - Derivation of Vortex Vibration Theory

Introduction This section focuses on the derivation of the vortex theory equation. We start from the Howe-Powell's [70, 119] theory of vortex acoustics in ocean water.

The speed of sound in ocean water is tabulated at $c_f \approx 1560\,\mathrm{ms}^{-1}$, a lightly bigger value than for non-ocean water $c_f^{\mathrm{non-ocean}} \approx 1440\,\mathrm{ms}^{-1}$ [135, 127]. The vortex acoustics equation [72] is given by

$$\partial_t^2 p_f - c_f^2 \Delta_f p_f = \rho_f c_f^2 \nabla(\boldsymbol{\omega} \times \mathbf{v}) \tag{3.19}$$

where p_f denotes the acoustic pressure in the ocean water due to turbulent layer above the plate-ocean interface.

$\rho_f \approx 1.0 \cdot 10^3\,\mathrm{kg\,m}^{-3}$ denotes the equilibrium mass-per-volume density of ocean water [71], $\boldsymbol{\omega}$ and $\mathbf{v}$ denote the vorticity in the turbulent layer and $\mathbf{v}$ the fluid velocity therein, relative to the unperturbed motion of the ocean water.

Finally, Δ_f is the Laplace operator with matching boundary conditions [127] at the plate-ocean interface and hard-wall boundary conditions [135] at the acoustically almost intransparent [56, 57] water-air interface.

Preliminary considerations The origin of the matching boundary conditions is a consequence of the similarity of specific acoustic impedance of water and the stony composition of the underneath plate: Concrete for instance has a density of $\rho_s \approx 2.4 \cdot 10^3\,\mathrm{kg\,m}^{-3}$ [86]. Petro-physical tables show that sediment material in the ocean has a mass density, the detailed value depending on the micro-composition, which is comparable. The speed of sound in solids is larger than in water [86, 135] and, as an order of magnitudes estimate, we may take $c_s \approx 3600\,\mathrm{ms}^{-1}$.

The acoustic impedances $Z_s = \rho_s c_s$ and $Z_s = \rho_s c_s$ can be used to obtain the reflection coefficient [127]

$$R = \frac{Z_s - Z_r}{Z_s + Z_r} \approx 0.69 \tag{3.20}$$

in the case of normal plain wave incidence on the interface. The assumptions underlying the derivation are simplistic but sufficient for an order-of-magnitudes estimate.

The result for R yields that $T^2 = 1 - R^2 \approx 53\,\%$ of the intensity of a plane wave incident is transmitted through the ocean-plate interface. Performing the analogous computation for air, setting $Z_s = \rho_a c_a$ with $\rho_a \approx 1.2\,\mathrm{kgm}^{-3}$ and $c_s = 343\,\mathrm{ms}^{-1}$, the interface air-ocean is seen to be acoustically almost in transparent, $R \approx 1$. Thus, the interface of interest is the plate-ocean interface.

Mathematically, the interface is assumed to be a suitably regular, oriented hypersurface Γ in $\mathbb{R}^3$ and the orientation is chosen for physical reasons by choosing the normal that has a parallel rather than an anti-parallel component to the normal vector of a spherical Earth, i.e., pointing away from the Earth's core. The three-dimensional ocean region is denoted by V_f and supposed to be large enough to cover at least a patch of the turbulent layer of vorticity. The three-dimensional plate region is indicated as V_s and we consent on the consideration of sufficiently small volumes V_f, V_s. The right-hand side of the vortex acoustics equation can be re-written as $\rho_f c_f^2 \nabla(\boldsymbol{\omega} \times \mathbf{v}) = c_f^2 \nabla \mathbf{f}_v$ where $\mathbf{f}_v \equiv \rho_f(\boldsymbol{\omega} \times \mathbf{v})$ has the units of "force per volume" and the structure of a Coriolis force term [127].

Sound in solids   Unlike in liquids and gases, pressure waves, i.e., sound may travel not only as a longitudinal but also as a transversal wave in solid media [135]. We base the derivation on the longitudinal component. Let $\mathbf{u}$ denote an elastic displacement of the solid structure in V_f from its equilibrium position. Since sound waves typically give rise to small oscillations in the nanometer range in air at sonic frequencies and in liquids at sub-sonic frequencies as well, the target range for a classical description is the infrasound range at reasonable sound pressure level $\lesssim 110\,\mathrm{dB}$. The excess (longitudinal) pressure p_s in the solid, traveling as a direct solid analogue of a sound wave in fluids, is obtained from the material relation relation $p_s = -K\nabla\mathbf{u}$ [86] where K denotes the compressional modulus of the solid. Due to the divergence operator, transversal components are canceled immanently.

In Hookian approximation, for an isotropic, homogeneous medium, Cauchy-Navier's equation

$$\rho_s \partial_t^2 \mathbf{u} = (\lambda + \mu)\nabla(\nabla\mathbf{u}) + \mu\Delta_v\mathbf{v} + \mathbf{f} \qquad (3.21)$$

with a force density drive $\mathbf{f}$ provides a description of the displacement $\mathbf{u}$ of the solid, provided the vibrations of the molecular constituents are suitably small. λ, μ are the

first and second Lamé constant characterizing the solid. They are tabulated, see e.g. [86] for examples. The compressional modulus K is expressed in terms of the Lamé constants as $K = \lambda + 2/3\mu$.

The vector calculus identities $\nabla \cdot \Delta_v = \nabla^3 = \Delta(\nabla \cdot)$ and $\Delta_v = \nabla(\nabla) - \nabla \times \nabla \times$ together with the relation $p_s = -K\nabla\mathbf{u}$ yield

$$\rho_s \partial_t^2 p_s = (\lambda + 2\mu)\Delta p_s - K\nabla\mathbf{f}. \tag{3.22}$$

Re-arranging and defining the speed of sound $c_p^2 = \sqrt{(\lambda + 2\mu)/\rho_s}$, the latter equation becomes:

$$\partial_t^2 p_s - c_p^2 p_s = -\rho_s^{-1} K\nabla\mathbf{f}. \tag{3.23}$$

Hammer analogy Since the vortices are located in ultimate proximity to the the interface region, we would like to identify $\mathbf{f}$ with $\mathbf{f}_v$. This is an approximation because not all of the sound intensity stored in the ocean is transmitted to the solid. Rather, we adopt the picture that the vortex region effectively acts as a conglomerate of small hammers in place of the vortices hammering on top of the plate such that also the solid experiences at the interface the full force $\mathbf{f}_v$.

The problem is that we do not know $\mathbf{f}$ because the region of vorticity does not extend into the solid. Rather, we only know its value at the boundary. Let us define the primary and secondary components through $\mathbf{u} = \mathbf{u}_p + \mathbf{u}_s$ such that $\nabla\mathbf{u}_s = 0$ and $\nabla \times \mathbf{u}_p = \mathbf{0}$. The Helmholtz decomposition of the displacement is unique up to a harmonic function and gives a decomposition in compression and shear waves, or, as used in seismology, in primary and secondary waves. Indeed, direct insertion of the decomposition in primary and secondary waves into the Cauchy-Navier equation provides us with two individual wave equations for $\mathbf{u}_s$ and $\mathbf{u}_p$; See section 1.3. for details.

Next, we notice that $\mathbf{k} \parallel \mathbf{u}_p \perp \mathbf{u}_s \perp \mathbf{k}$ where $\mathbf{k}$ denotes the wave vector of a plane wave solution to the respective vector-valued wave equations. We assume that $\mathbf{u}_p$, $\mathbf{u}_s$ can be extended to a slightly bigger domain including ∂V_s such that we can define the restrictions to ∂V_s.

Last, we demand $\Delta = \Delta_\partial + \partial_z^2$ in the vicinity of ∂V_s where Δ_∂ is the Laplace-Beltrami operator of the hypersurface ∂V_s and $\partial_z \mathbf{u}_p = \mathbf{0}$, $\partial_z^2 \mathbf{u}_p = \mathbf{0}$ and analogously for $\mathbf{u}_s$. These requirements serve such as to obtain a wave traveling only along the surface $\Gamma \subset \partial V_s$ which is the direction relevant for studying the propagation of a tsunami cue from the ocean region to the shoreline.

Integration of the acoustic wave equation for p_s, eq. (3.23), yields upon noting once again $p_s = -K\nabla\mathbf{u}$ and Gauss' integration theorem

$$\int_{\partial V_f} d\mathbf{S}\ \left(c_s^{-2}\partial_t^2 u_s - \Delta_\partial u_s + (\lambda + 2\mu)^{-1}\langle\mathbf{n}, \mathbf{f}_v\rangle_{\mathbb{R}^3}\right) = 0. \qquad (3.24)$$

where $u_s = \langle\mathbf{n}, \mathbf{u}\rangle_{\mathbb{R}^3} = \langle\mathbf{n}, \mathbf{u}_s|_\Gamma\rangle_{\mathbb{R}^3}$, $c_s^2 = \mu/\rho_s$ is the phase velocity of a secondary wave and we assumed that $\mathbf{n}$ is approximately constant. The primary component is absent because on ∂V_s Δ_∂ denotes the induced Laplacian on $\partial V_s \supset \Gamma$.

We require the function inside the integral to be zero pointwisely and find upon definition $\mathfrak{g}_v(\aleph) \equiv c_s^{-2}(\lambda + 2\mu)^{-1}\rho_f\rho_s^{-1} = 1/2 \cdot \rho_f/\rho_s \cdot (1 + \aleph^2)^{-1}$ and $\aleph \equiv \sqrt{\lambda/(2\mu)}$ the vortex vibration theory

$$\partial_t^2 u_s - c_s^2\Delta_\partial u_s = \mathfrak{g}_v(\aleph)\,\langle\mathbf{n}, \boldsymbol{\omega}, \mathbf{v}\rangle_{\mathbb{R}^3} \qquad (3.25)$$

where we have used the notation $\langle\heartsuit, \clubsuit, \diamondsuit\rangle_{\mathbb{R}^3}$ to denote the triple product.

With $\mathfrak{g}_0 = \rho_f/\rho_s \approx 1/2$ denoting the mass density ratio of ocean water and solid, we have the formula $\mathfrak{g}_v(\aleph) = \mathfrak{g}_0 c_s^2/c_p^2 \approx 1/8 \approx 12.5\,\%$ for the conversion of the acceleration due to the vortex force density, $\boldsymbol{\omega} \times \mathbf{v}$, to simulate the displacement of the continental plate's surface in normal direction.

Comments on the derivation   The derivation is unfortunately only approximate. We do so to circumvent the treatment of a reflection-transmission problem for the acoustic pressure in a relatively complicated geometry, noting the choice of the linear depth profile.

Furthermore, it is of course not necessarily true that only surface waves are excited but also waves with a mathematically finite penetration depth. Since these are conceptually inappropriate for a model of cue propagation from the seabed floor to the elephant at the shoreline, assumptions have been chosen to rule this case out automatically.

Last, the idea to study seismic vibrations is due to the observation that in an ideal fluid dynamics framework $\partial_\mathbf{n} p_f = -\rho_f\partial_t v_{n,f} \neq 0$ at the solid boundary. In an idealization, the normal component of the fluid velocity vanishes at the solid interface. However, for the perturbation constituted by the tsunami, this is in general not the case such that the region of vorticity, one of the features of the tsunami, induces an excess momentum transfer to the continental plate and, for our purposes more importantly, its surface. The momentum $\rho_f v_{n,f}$ is not lost but transformed into momentum of vibration

of, at least, the surface of the continental plate by virtue of the requirement of local conservation of momentum $\rho_f v_{n,f} = \rho_s v_{n,s}$. Let $u_s = \|\mathbf{u}_s\|$ and $u_p = \|\mathbf{u}_p\|$.

The value for $\mathfrak{g}_v(\aleph)$ could have also been heuristically, equating $\rho_f \partial_t^2 u_f = \rho_f \partial_t v_{n,f} = \rho_s \partial_t v_{s,p} = \rho_s \partial_t^2 u_p$ at fixed ω. In addition, the force balance law $\rho_s \partial_t^2 u_s = \rho_s \partial_t^2 u_p$ is required at a fixed wave number k corresponding to different frequencies ω. This is because formation of both, primary and secondary waves takes place in the same medium with the same geometric dimensions such that the wave number k needs to be fixed instead of the angular frequency ω. Likewise, the acceleration due to the vortex force $\mathbf{f}_v$ is precisely $\boldsymbol{\omega} \times \mathbf{v}$. Thus, multiplication with the conversion derived just before hands us a theoretically plausible value for the accelaration of the surface of the continental plate after proection on the normal component which is just u_s, namely $\mathfrak{g}_v(\aleph) \langle \mathbf{n}, \boldsymbol{\omega}, \mathbf{v} \rangle_{\mathbb{R}^3}$. The right-hand side of (3.25) has been recovered.

Finally, the assumption that $\mathbf{n} \approx$ const. holds true when the surface of the continental plate doesn't deviate too wildly from a plane in the volume V_s. This will be used later on for geometric perturbation theory.

Appendix 3.B - Source term

Why a source term model In order to solve the vortex vibration theory for analytical insights, we need to specialize the source term $\langle \mathbf{n}, \boldsymbol{\omega}, \mathbf{v} \rangle_{\mathbb{R}^3}$. This will be done in several steps: First, we derive qualitatively the existence of counter-rotating vortices. Second, we derive the far- and near-field form of the velocity in the vortices and from that the vorticity. Third, we derive the total vorticity and the total velocity over the continental margin and expand them in leading order in the distance from the shoreline.

The results are used to evaluate the source term in (3.25) as an effective approximation akin to a mean field theory. Indeed, we neglect any reactions of the vortices with their fellow vortices which is of course present in reality as a direct ingredient of the turbulence behavior of the entire region that we model with a simple potential theoretic approach. It is precisely the spoken-of turbulence that necessitates a simple model for the source term, and possible simplifications, in order to make progress through analytic techniques.

We mention that Fig. 3.6 (A) illustrates step number one. Fig. 3.6 (B) serves as a visual backup for step two.
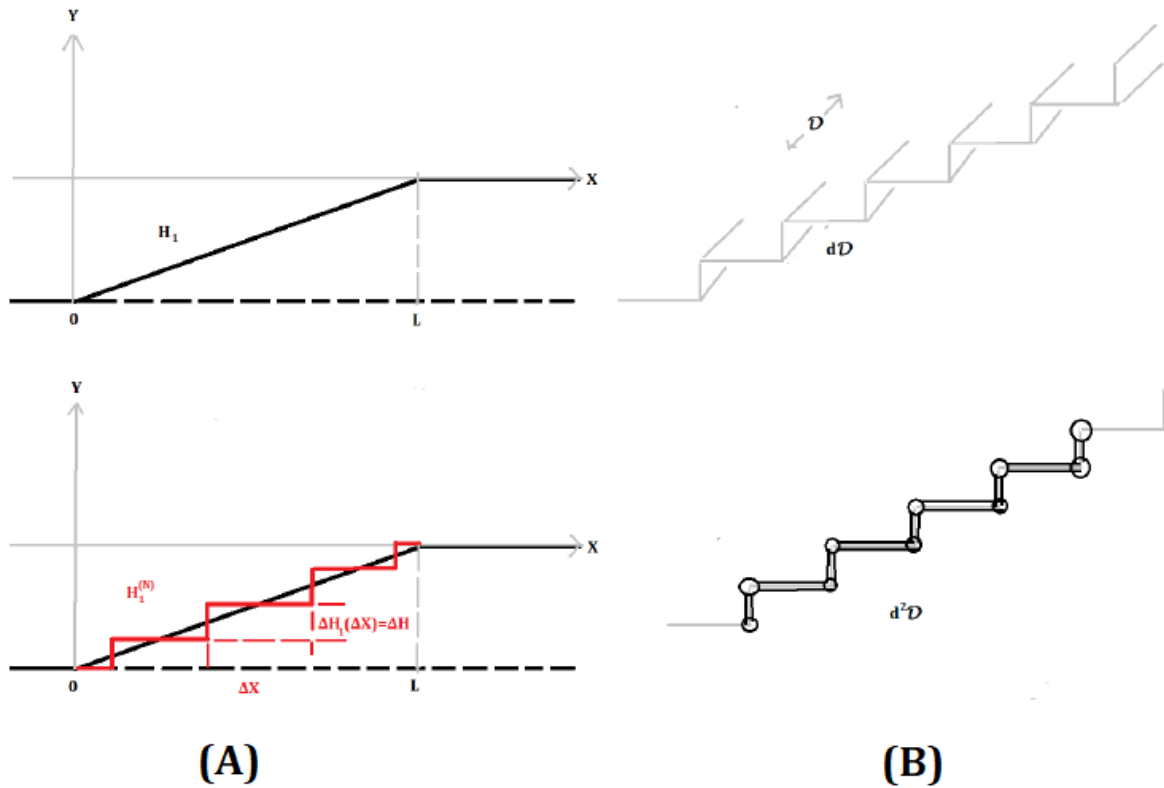
Figure 3.6: Derivation of the source term. (A) Discretization of the depth profile H_1 in a quasi-2-dimensional model, (B) Geometric regions and centers of vorticities in a planar model.

Step 1 - Existence of counter-rotating vortices   The step profile H_1 can be approximated arbitrarily accurate by a step function profile: The interval $[0, L]$ is partitioned into, say N, small intervals of length Δx such that the area enclosed by the graph of H_1 and its discretized version, say $H_1^{(N)}$, stays the same. The choice fixes the way of partitioning the interval. Schematically, it is shown in Fig. 3.6 (A).

Next, we imagine the motion of the fluid pointing in x direction, say $\mathbf{V} = V\hat{e}_x$ where typical velocities for the motion of oceanic fluid are about $\sim 10\,\mathrm{cm\,s^{-1}}$, a value that we also take for the tsunami perturbation. In the discretized setup this means that the fluid somehow has to wiggle its way over the points of discontinuity. In fact there are two such (two-dimensional) points in the drawing (x, z)-plane of Fig. 3.6 (A), one of them at either end of the intervals employed for the discretization.

Intuitively, at the lower of each of these candidates for vortex centers, say at x_k, the fluid has to move in positive z-direction *after* having moved in positive x-direction to stream further towards the shoreline. In terms of vortex orientation, this corresponds to a positive circulation. At the upper of the two points for a given discretized value x_k, the fluid has to move in positive x-direction *after* having moved in positive z-direction to stream further towards the shoreline. This corresponds to a negative circulation.

Let us consider the scenario that initially no perturbation of the ocean water is present. Thus, no tsunami-induced vorticity is present and the total vorticity stored in the region under consideration equates zero shown as the sufficiently small tubular neighborhood around the graph of the discretized depth profile $H_1^{(N)}$.

Let us extend the drawing plane by a small ϵ into the direction pointing inwards respectively outwards the drawing plane and call the resulting volume $\mathcal{D}$. Clearly, for suitable ϵ, the seabed can be approximated as translation invariant. Because of the vector calculus identity $\mathrm{div} \circ \mathrm{rot} = 0$, no region of vorticity is present in $\mathcal{D}$ in the sense that $\nabla\omega = 0$ almost everywhere in the volume $\mathcal{D}$. By application of Gauss' integration theorem

$$\int_{\mathcal{D}} dV\, \nabla\boldsymbol{\omega} = \int_{\partial\mathcal{D}} \langle d\mathbf{S}, \boldsymbol{\omega}\rangle_{\mathbb{R}^3}. \tag{3.26}$$

Next, we consider one face of $\partial\mathcal{D}$ aligned in parallel to the drawing plane. For simplicity, we will denote this face by $\partial_f\mathcal{D}$. Translational invariance of the setup serves as a physical basis for the assumption that $\boldsymbol{\omega}$ defines a suitably regular function also on $\partial_f\mathcal{D}$.

We require that total vorticity in $\partial_f\mathcal{D}$ vanishes and apply Stokes' theorem. In the notation of Fig. 3.6 (B), $\partial^2\mathcal{D}$ symbolizes the closed curve in the lower subplot

consisting of circles around the interesting points and two straight lines joining two adjacent circles. The quick calculation yields

$$0 = \int_{\partial_f \mathcal{D}} \langle d\mathbf{S}, \boldsymbol{\omega} \rangle_{\mathbb{R}^3} = \int_{\partial^2 \mathcal{D}} \langle d\mathbf{s}, \mathbf{v} \rangle_{\mathbb{R}^3} \tag{3.27}$$

because $\boldsymbol{\omega} = \nabla \times \mathbf{v}$.

We let the distance between the two lines shrink in such a way that each pair of lines does not contribute. This leaves us with the contributions from the two circles, say of radius $R > 0$. The smallness of slope, $\beta \ll 1$, supports the modeling that two vortices above each other, say at (x_k, y_k^-) and (x_k, y_k^+) cancel each other: Namely, the vertical distance between the centers of neighboring vortices are much smaller than the horizontal distance - the ratio being precisely β. Since the circles form the oriented closed curve $\partial^2 \mathcal{D}$, they are all endowed with the same orientation.

Introducing polar coordinates, denoting the velocity of the upper vortex as $\mathbf{v}^+$ and indicating the lower one by the superscript "$-$", the previous deliberations combine to the following equation

$$0 = R \int_0^{2\pi} d\phi \left(v_\phi^+(R, \phi) + v_\phi^-(R, \phi) \right). \tag{3.28}$$

Next, we make the simplifying assumption that the presence of the solid surface underneath the vortices does not affect the form of the angular components of the velocities in the previous equation. This means that the physical center of the vortices is a bit above the surface of the seabed, but at least by R. Realistically, this assumption is readily verified through observing the behavior of water channel flow through a channel with abruptly varying cross section - the vortices' centers are situated not directly at the solid-fluid interface but a bit in the channel.

The assumption we have just outlined ensures that v^ϕ is independent of the argument ϕ and as such we find

$$v_\phi^+(R) = -v_\phi^-(R). \tag{3.29}$$

Since for $H_1^{(N)}$, we have a total of N such equations, we have finally $2N$ candidates for vortices, giving rise to fluid motion around the edges as we had intuited in the beginning of the paragraph.

The functional form of $\mathbf{v}^\pm$ is the subject of the next paragraph which is to be understood as a more quantitatively inclined continuation of the discussion commenced in the present paragraph.

Step 2 - Individual vorticities & induced velocities   Let us assume we have a small massive probe, say a small rod of mass m, placed sufficiently far from two of the counter rotating vortices in the turbulent layer. In the potential theory framework employed here, the superposition principle allows us to treat the effects of pairs of vortices individually.

We denote the position of the probe by $\mathbf{r}$ and the locations of the two vortices by $\mathbf{r}^+$ and $\mathbf{r}^-$ following the convention for superscripts introduced in the paragraph before. As located in the hydrodynamic far field, we do not expect that the presence of vortices introduces an angular momentum to the mass m. That is, in the point-mass idealization,

$$
\begin{aligned}
m\left(\mathbf{r} - \mathbf{r}^+\right) \times \mathbf{v}^+(\|\mathbf{r} - \mathbf{r}^+\|_2) + \\
m\left(\mathbf{r} - \mathbf{r}^-\right) \times \mathbf{v}^-(\|\mathbf{r} - \mathbf{r}^-\|_2) = \mathbf{0}
\end{aligned}
\tag{3.30}
$$

where we assume, as in the previous paragraph, that the velocity fields $\mathbf{v}^\pm$ depends only on the distance of the mass to the centers of the respective vortices.

Further, we assume translational invariance in the drawing plane of Fig. 3.6 such that $\mathbf{v}^\pm \approx v_\phi^\pm \hat{e}_\phi$. The polar coordinates are chosen to be centered around the geometric mean of $\mathbf{r}^+$ and $\mathbf{r}^-$ such that the proximity but not coincidence of the centers of the vortices allows us to write only $\approx$ in the quantification of $\mathbf{v}^\pm$. Placing the mass m sufficiently upstream of the vortex centered at $\mathbf{r}^+$, we may assume that there is a $dr > 0$ such that $\mathbf{r} - \mathbf{r}^- \approx (r + dr)\hat{e}_r$ and $\mathbf{r} - \mathbf{r}^+ \approx (r - dr)\hat{e}_r$ where $r = \|\mathbf{r}\|_2$. Division by m recasts the only non-trivial component of the previous equation to

$$
v_\phi^-(r + dr) \cdot (r - dr) = -v_\phi^+(r - dr) \cdot (r - dr).
\tag{3.31}
$$

Expanding the equations up to linear order in dr, and comparing coefficients for powers of dr, we find

$$
\mathcal{O}\left((dr)^0\right) : v_\phi^-(r) = -v_\phi^+(r)
\tag{3.32}
$$

$$
\mathcal{O}\left((dr)^1\right) : r d_r v_\phi^-(r) + v_\phi^-(r) = 0.
\tag{3.33}
$$

The two equations are decoupled and can be solved such as to yield the profile of a vortex monopole in the hydrodynamic far field. Choosing the constant of integration to be $\Gamma(t)/(2\pi)$ and understanding $\Gamma(t)$ as a possibly time-dependent circulation, the solution reads

$$
v_\phi^+(t, r) = \frac{\Gamma(t)}{2\pi r} = -v_\phi^-(t, r).
\tag{3.34}
$$

It remains to assess the near field behavior. We do this by demanding that at $r = 0$, i.e., at the geometric mean of the vortices centers, the fluid should not be affected by the presence of vorticities in the sense that $v_\phi^+(t, r = 0) = 0 = v_\phi^-(t, r = 0)$. Letting δ_c denoting a threshold distance to signify the transition from hydrodynamic near to hydrodynamic far field, the continuity requirement at $r = \delta_c$ is satisfied most easily by a linear $v_\phi^\pm$-profile for $r \in [0, \delta_c]$.

Ultimately, the combined result for the polar velocity component is given by

$$v_\phi^\pm(t, r) = \begin{cases} \frac{\pm\Gamma(t)}{2\pi r} & r \geq \delta_c \\ \frac{\pm\Gamma(t)r}{2\pi\delta_c^2} & 0 \leq r \leq \delta_c \end{cases}. \tag{3.35}$$

We notice that the above equation characterizes a monopole.

Physically, a series of dipoles is required at the solid-fluid interface in order to establish a non-zero vorticity $\boldsymbol{\omega}$. We do this by choosing the point dipole limit and moving the centers of vortices to coincide such that in the hydrodynamic far field a non-zero velocity originates by requiring that $\Upsilon(t) \equiv 2\Gamma(t)\Delta z \neq 0$, with $\Delta z \equiv \|\mathbf{r}_+ - \mathbf{r}_-\|_2$, for almost all $t \geq 0$.

Since in the coordinate system under consideration $\mathbf{r}^+ = -\mathbf{r}^-$,

$$\begin{aligned} v_\phi^{\text{dip}}(t, r) &= \lim_{\mathbf{r}^+ \to 0} \left[v_\phi^+(t, \|\mathbf{r} - \mathbf{r}_+\|_2) + v_\phi^-(t, \|\mathbf{r} - \mathbf{r}_-\|_2) \right] \\ &= \begin{cases} \frac{\Upsilon(t)}{2\pi r^2} & r \geq \delta_c \\ \frac{\Upsilon(t)}{2\pi\delta_c^2} & 0 \leq r \leq \delta_c \end{cases} \end{aligned} \tag{3.36}$$

where $r = \|\mathbf{r}\|_2$ as usual. Expanding the vector operators in the definition $\boldsymbol{\omega} = \nabla \times \mathbf{v}$ in cylindrical coordinates such that the polar part matches with the polar coordinate system employed in this paragraph, the vorticity associated to the vortex point dipole follows from the previous equation by direct computation

$$\omega_y^{\text{dip}}(t, r) = \begin{cases} \frac{-\Upsilon(t)}{2\pi r^3} & r \geq \delta_c \\ 0 & 0 \leq r \leq \delta_c \end{cases} \tag{3.37}$$

where the y-direction is chosen such that the xz-plane and the y-axis span a positively oriented Cartesian coordinate system.

Step 3 - Total vorticity & induced velocity So far, we have taken advantage of the tight spacing of individual monopoles to obtain vortex dipoles. Since the depth profile $H_1^{(N)}$ is only an artificial discretization, we need to invert the discretization completely.

The dipole structure constituted only one half of the full procedure. We simplify the calculation by assuming that in the source term (3.25), only the full vorticity and the full induced fluid velocity contribute. By doing so, we rule out mutual feedback between different vortex dipoles but open up the possibility to conduct the analytic investigation further.

Noting that $\Upsilon(t) = 2\Gamma(t)\Delta z$ and $\Delta z = \beta\Delta x$ by virtue of the affine-linear depth profile H_1, the summation becomes in the limit $N \to \infty$ an integral over the distance between the tsunami generating event and the shoreline, i.e., an integral over the interval $x \in [0, L]$: Abbreviating $v_\phi^{\text{tot}} = v_\phi^{\text{tot}}(t, x, z)$ and $\omega_y^{\text{tot}} = \omega_y^{\text{tot}}(t, x, z)$,

$$
\begin{aligned}
v_\phi^{\text{tot}} &= \frac{\beta\Gamma(t)}{2\pi} \int_0^L dx' \, \frac{v_\phi^{\text{dip}}\left(t, \|(x,z) - (x', H_1(x'))\|_2\right)}{\Upsilon(t)} \\
&= \frac{\beta\Gamma(t)}{2\pi} \mathcal{I}(x, z),
\end{aligned}
\tag{3.38}
$$

$$
\begin{aligned}
\omega_y^{\text{tot}} &= \frac{\beta\Gamma(t)}{2\pi} \int_0^L dx' \, \frac{\omega_y^{\text{dip}}\left(t, \|(x,z) - (x', H_1(x'))\|_2\right)}{\Upsilon(t)} \\
&= \frac{-\beta\Gamma(t)}{2\pi} \mathcal{J}(x, z)
\end{aligned}
\tag{3.39}
$$

where the parameter-dependent integrals $\mathcal{I}$ and $\mathcal{J}$ are given through

$$
\mathcal{I}(x, z) \equiv \int_0^L \frac{dx'}{(x - x')^2 + (z + H_0 - \beta x')^2},
\tag{3.40}
$$

$$
\mathcal{J}(x, z) \equiv \int_0^L \frac{dx'}{\sqrt{(x - x')^2 + (z + H_0 - \beta x')^2}^3}.
\tag{3.41}
$$

and can be evaluated through direct analytic computation.

If the evaluation point (x, z) is far away from $\text{graph}(H_1)$ compared to the maximum depth of the ocean H_0, i.e., in the limit $z/x \to 0$ such that $\text{dist}((x, z), \text{graph}(H_1)) \approx x$, we can expand the solution obtained by the procedure described before in powers of z/x. We keep only the lowest order contribution. Upon the introduction of fitting constants c_v and c_ω, determined in principle through the series expansion but treated here as genuine fitting constants to ensure the correct physical dimensions, the results read

$$
v_\phi^{\text{tot}}(t, x, z) = c_v \frac{\Gamma(t)\beta}{2\pi x^2} + \mathcal{O}(\beta^3)
\tag{3.42}
$$

$$
\omega_y^{\text{tot}}(t, x, z) = -c_\omega \frac{\Gamma(t)\beta}{2\pi x^{5/2}} + \mathcal{O}(\beta^3).
\tag{3.43}
$$

where $[c_v^2] = 1\,\mathrm{m}^{-2}$ and $[c_\omega] = 1\,\mathrm{m}^{-1}$ for the aforementioned dimensional reasons.

By performing the expansion, we focus more on signals sourced far away from the elephant and not in the vicinity of the shoreline. This is a reflection of the overall goal to propose a model of the natural tsunami early warning system in elephants. Absorption of the effect of the projection onto the normal component at each point as an overall number into the constants c_v and c_ω, or rather their product $c_{\mathrm{fit}} = c_v c_\omega$, we obtain a strongly simplified version of the triple product in the source term of equation (3.25),

$$\langle \mathbf{n}, \boldsymbol{\omega}, \mathbf{v} \rangle_{\mathbb{R}^3} \simeq \frac{c_{\mathrm{fit}} \Gamma(t)^2 \beta^2}{4\pi^2 x^{9/2}} + \mathcal{O}(\beta^4), \tag{3.44}$$

which has the advantage of permitting further analytic investigations.

Comment Effectively, the model is a series of infinitesimally densely spaces counter-rotating vortices of Rankine type extending in the direction normal to the plane of Fig. 3.6 (A) & (B). Due to the small, namely $< 3°$ mostly, slope of the continental margin, one can also regard it as a series of equivalent vortex dipoles the constituents monopoles of which carry opposite circulation.

We would like to point out that the complexity of the phenomena requires us to follow very heuristic procedures. When someday accurate experimental data exist, it may be useful to model the plate vibration by a phenomenological input model and try to derive theoretical vortex models at the same time that are able to reproduce the phenomenology sufficiently well. At the present, this is out of reach.

The next subsection of the appendix focuses on an analytic treatment of the model on the macroscopic scale, i.e., on the scale of continental plates. The purpose is twofold. First, one obtains reference solutions to a first bio-tremological model. Second, one may derive a formula for the remaining fit parameter C from the zeroth order problem of the geometric perturbation theory. The equation can be used to match C with the experimentally better detectable amplitude of plate vibration. Since surface waves as generated during earthquakes can travel several times around the earth before ceasing to be detectable, we will neglect attenuation effects in (3.25), however, they could and, if the up to now non-existent data says so, should be included on phenomenological basis.

Appendix 3.C - Geometric Perturbation Theory

Introduction   Dropping the subscript ∂ in Δ_∂, the vortex vibration theory takes the form of a scalar $2 + 1$-dimensional inhomogeneous wave equation $\partial_t^2 u_s - c_s^2 \Delta u_s = \mathfrak{g}_v(\aleph)\langle \mathbf{n}, \boldsymbol{\omega}, \mathbf{V}\rangle_{\mathbb{R}^3}$ with an inhomogeneity on the right-hand side.

The top figure in Fig. 3.7 displays the plate tectonics of the earth according to the counting of the recent paper [11]. There are $N_p = 52$ plates.

In order to outline the ideas underlying a treatment of the vortex vibration equation by geometric perturbation theory, that is, reducing the non-flat plate profile to a flat one, we will make strong simplifications. On average, a plate spans an area of $A \approx 8 \cdot 10^{12}\,\mathrm{m}^2$, calculated from the Earth's surface which is approximately spherical at radius $R_e \approx 6 \cdot 10^6\,\mathrm{m}$. Interpreting each "average" plate as a spherical zone, this corresponds to an opening angle θ_0 in a spherical coordinate system (θ, ϕ) of $\theta_0 = \arccos\left(1 - 2N_p^{-1}\right) \approx 0.28\,\mathrm{rad} \approx 16°$, a value obtained through equating the area of the Earth's surface to the area of N_p "average" plates of the same zonal geometry: $4\pi R_e^2 = 2\pi(1 - \cos\theta_0)N_p R_e^2$. Since $\theta_0/\pi \ll 1$, we may try approximating the "average" plate as flat by introducing a cylindrical coordinate system in which the plate is represented as $\mathrm{graph}(H_{\mathrm{plate}})$ where $H_{\mathrm{plate}}(r, \phi) = \sqrt{R_e^2 - r^2}$ defines the height profile of the spherical zone with regards to the spherical coordinate system hinted at by symmetry reasons. The polar part of the spoken-of cylindrical coordinates defines a disk and, more precisely, we have $(r, \phi) \in [0, R_e \sin\theta_0] \times [0, 2\pi]$.

Since the deviation from the flat disk $\max|H(r, \phi) - R_e \cos\theta_0|/R_e = 2N_p^{-1} \ll 1$, we seek to replace the zone by the disk by geometric perturbation theory (GPT): Calling the metric on the disk $D_{R_e \sin\theta_0}^2$ g_0 and on the spherical zone g, we have $\|(g - g_0) \cdot g_0^{-1}\| \ll 1$ in a suitable matrix norm. This suggests to us to write express the algebraic Laplace-Beltrami operator Δ_g on the spherical zone and in the variables (r, ϕ) through the algebraic Laplace-Beltrami operator Δ_{g_0} for this disk plus a "small" perturbation operator $\mathsf{V} \equiv (\Delta_g - \Delta_{g_0}) \sim \mathcal{O}(g - g_0)$.

The advantage of this approach lies in the coordinate representation of the source term because the x from the previous sections corresponds through equality to $R - r$ where $R \equiv R_e \sin\theta_0$. As we will see through investigation of the eigenvalue problem for the Laplace-Beltrami operators for the Neumann problems for both Δ_{g_0} and Δ_g, the "flat" problem admits a much more convenient solution to work with.

We end this introductory paragraph by noting that the separation of the algebraic Laplace-Beltrami operator Δ_g on the zone in an unperturbed part Δ_{g_0}, i.e., just the
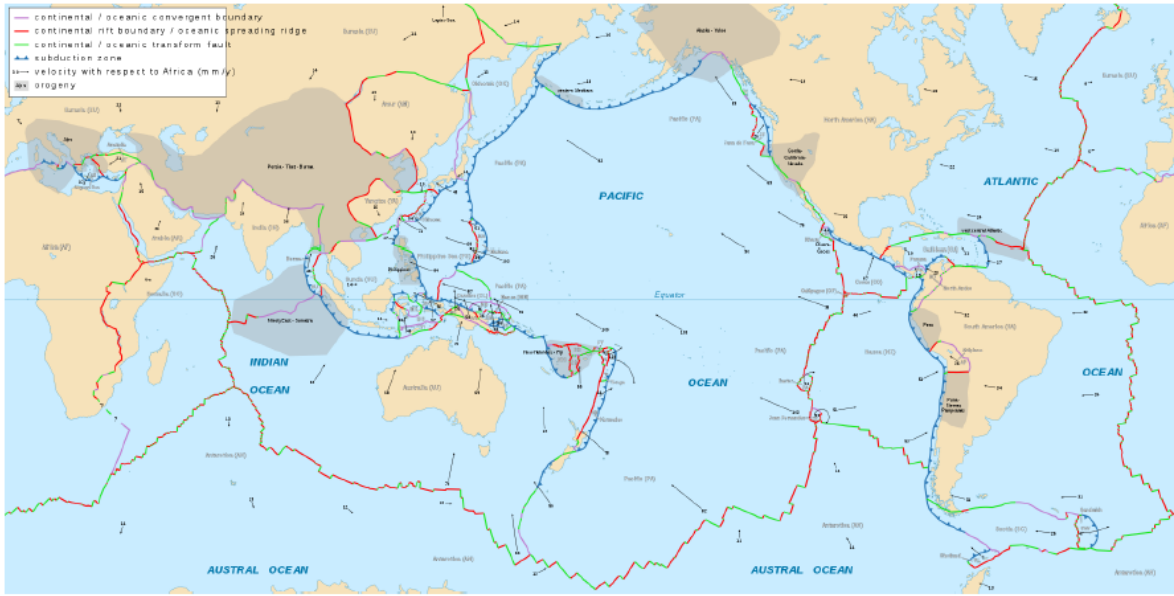
Figure 3.7: Plate tectonics of the earth according to [11] There are $N_p = 52$ plates on the earth's surface. Figure taken from [11].

Laplacian in polar coordinates, and a perturbation operator V reads as

$$\partial_t^2 u_s - c_s^2 \Delta_{g_0} u_s = c_s^2 \mathsf{V}[u_s] + \mathfrak{g}_v(\aleph)\langle \mathbf{n}, \boldsymbol{\omega}, \mathbf{v}\rangle_{\mathbb{R}^3}. \tag{3.45}$$

We will mainly be occupied with solving the "unperturbed" problem

$$\partial_t^2 u_s - c_s^2 \Delta_{g_0} u_s = \mathfrak{g}_v(\aleph)\langle \mathbf{n}, \boldsymbol{\omega}, \mathbf{v}\rangle_{\mathbb{R}^3} \tag{3.46}$$

with the Laplacian on the disk D_R^2 given algebraically by $\Delta_{g_0} = \partial_r^2 + r^{-1}\partial_r + r^{-2}\partial_\phi^2$. Instead of a complete specification of solutions to the vortex vibration theory equation, we confine the discussion to bits and pieces deemed relevant to, especially, the biological community.

It still remains to prepare the vortex source term on the right-hand side of (3.45) and (3.46) for further treatment.

Source term model   Since the source term (3.44) contains a multiplicative fit constant C, its strength may be adjusted such as to reproduce vibration amplitudes that can actually be sensed by Meissner and or Pacinian cells in the elephants feet. The interesting plate is a continental plate. Conceptually, of course not all of the flattened "average" plate gives rise to a non-zero source term. Rather, it is only a annular sector

defied through $\mathbb{A} \equiv \{(r, \phi) \in [0, R] \times [0, 2\pi] : R - L \leq r \leq R, \phi_0 \leq \phi \leq 2\pi - \phi_0\}$ which is struck by the tsunami.

ϕ_0 can be bounded from below by $5\pi/6$ and from above by $\pi/2$ if one regards the tsunami generating event situated directly at a point with $r = R$ and stimulating the formation of the turbulent layer responsible for the signal build-up spherically symmetrically and truncating the region when the first spherical wave front hits the center of the disk. The choice is somewhat arbitrary but also for realistic plates, the turbulent layer is most likely to form in the vicinity of the tsunami, say in the ocean surrounding Indonesia, but not, to stay with the hypothetical scenario, in the arctic sea on the west coast of Greenland where the tsunami plays virtually no role. For the present hypothetical model, we set $\phi_0 = 0$ for aesthetic rather than physical reasons.

One important phenomenon is stored in the expression $\Gamma(t)^2$. Recall that $\langle \mathbf{n}, \boldsymbol{\omega}, \mathbf{v} \rangle_{\mathbb{R}^3} \sim \Gamma(t)^2$, focusing only on time-dependencies. From the discussion of the frequencies excited in the vortices, we know that instead of a single frequency f a full frequency band $\mathbb{F} = [f_{\min}, f_{\max}]$ is excited. The time-dependent circulation's, $\Gamma(t)$'s, Fourier representation in $\omega = 2\pi f$-space is given by

$$\Gamma(t) = \int_{2\pi \mathbb{F} \uplus (-2\pi \mathbb{F})} \frac{d\omega}{\sqrt{2\pi}} \hat{\Gamma}(\omega) \exp(i\omega t). \tag{3.47}$$

It is well-known in functional analysis that the Fourier transform is a unitary operator on the Schwartz space of functions and that, moreover, it converts multiplication into convolution and vice verse, the so-called *morphism property*: For the Fourier transform denoted by the operator F, the equations $\mathsf{F}[f \cdot g](\omega) = (\mathsf{F}[f] * \mathsf{F}[g])(\omega)$ and $\mathsf{F}[f * g](\omega) = (\mathsf{F}[f] \cdot \mathsf{F}[g])(\omega)$ hold true for suitable functions $f, g \in \mathcal{S}(\mathbb{R} \to \mathbb{C})$, i.e., in the Schwartz space. Upon risking the unitarity of the Fourier transform, the properties extend to L^2-space in which we may assume the circulation Γ to live. Let us define the set $\mathbb{F}^f \equiv \mathbb{F} \uplus (-\mathbb{F})$. The morphism property yields that $\Gamma(t)^2$ can be represented as

$$\Gamma(t)^2 = \int_{2\pi \mathbb{F}^f + 2\pi \mathbb{F}^f} \frac{d\omega}{\sqrt{2\pi}} (\hat{\Gamma} * \hat{\Gamma})(\omega) \exp(i\omega t), \tag{3.48}$$

where $A + B = \{a + b | a \in A, b \in B\}$ for sets A, B.

In particular, we find $\sup(\mathbb{F}^f + \mathbb{F}^f) = 2f_{\max}$ which is biologically desirable: Suppose that a maximum frequency f is excited and carried to the shoreline where an arbitrary elephants peacefully awaits the tsunami. Further assume that the elephant can sensibly detect and process only frequencies above the threshold frequency $f_c < 2f$. Since the signal carried by the plate vibrations carries a frequency of $2f$, the elephant can detect

the signal as being above the threshold f_c. This explains why a low-frequency signal, say at $f \approx 20\,\text{Hz}$ which is just the hearing threshold for humans can suffice to produce a signal at frequency $2f \approx 40\,\text{Hz}$ which the elephant is much more likely to process, for it is not out of its typical communication channel.

Spherical cap vs. flat disk   Let us demand Neumann boundary conditions to the Laplace-Beltrami operators on the zone, Δ_g, and on the disk, Δ_{g_0}. In both cases, the eigenfunctions to the Neumann eigenvalue problem can be determined, for the zone in spherical and for the disk in polar coordinates.

For the zone, we find $\Psi_{\zeta m}(\xi, \phi) \propto P_\zeta^m(\xi) \exp(im\phi)$ where $\xi = \cos\theta$ and P_ζ^m denotes an associated Legendre function of the first kind. The latter is given through the hypergeometric function

$$P_\zeta^\eta(\xi) \equiv \frac{\left(\frac{1+\xi}{1-\xi}\right)^{\eta/2}}{\Gamma(1-\eta)}\,{}_2F_1\left(-\zeta, \zeta+1; 1-\eta, \frac{1-\xi}{2}\right). \tag{3.49}$$

The modal space is only given implicitly. Let $\mathcal{M}(m) \equiv \{\zeta \in \mathbb{C} : \partial_\xi P_\zeta^m(\xi = \cos\theta_0) = 0\}$. This set does only admit a numerical treatment. The corresponding modal space is then given as

$$\mathcal{M} = \bigcup_{m \in \mathbb{Z}} \mathcal{M}(m) \times \{m\}. \tag{3.50}$$

In contrast, the Neumann eigenvalue problem for the flattened plate gives rise to eigenfunctions $\Psi_{nm}^{(0)}(r, \phi) \propto J_{|m|}(\mu_{n|m|}\hat{r}) \exp(im\phi)$ with $\hat{r} = r/R$ and $R = R_e \sin\theta_0$. J_k denotes the Bessel function of the first kind of order k and μ_{nk} denotes its n-th non-negative extremum, labeled in ascending order. In the disk case, the modal space is simply $\mathbb{N} \times \mathbb{Z} \cup \mathbb{N}_0 \times \{0\} \ni (n, m)$. Conceptually, the disk model captures the biologically prominent picture that the elephant is "a tuning force standing on a vibrating disk" correctly.

For the next paragraph the disk approach has been used further to derive an estimation formula relating the fitting constant c_{fit} of the model to vibration amplitude U of the plate's surface.

Estimation formula for the fitting constant c_{fit}   In the notation introduced in the preceding paragraph, let us assume that a mode $\Psi_{n0}^{(0)}$ with $n \in \mathbb{N}$ is excited. The vortex vibration theory (3.46) can be solved by interpreting it as an operator differential

equation and applying Duhamel's principle for which we specify homogeneous initial conditions $u_s(t = 0, r, \phi) = 0 = \partial_t u_s(t = 0, r, \phi)$ in order to study exclusively the impact of the vortices on the continental plate's surface's vibrations.

Expanding the operator sine function produced by the operator differential equation approach by means of the spectral theorem and focusing on the aforementioned mode, it still remains to evaluate the projection of the source term $\mathfrak{g}_v(\aleph)\langle \mathbf{n}, \boldsymbol{\omega}, \mathbf{v}\rangle_{\mathbb{R}^3}$ onto $\Psi_{n0}^{(0)}$. The integral stemming from the aforementioned projection diverges.

Mathematically, the problem is circumvented by neglecting this contributions and replacing the integral by the length of the radial integration interval $R\epsilon_L$ times the value of the function inside the former integral evaluated at the "well-behaved" boundary, i.e., at $r = R(1 - \epsilon_L)$. The $\epsilon_L = L/R$ is supposed to be $\ll 1$ and means that only a sufficiently small annular region of the disk-shaped continental plate functions as the mathematical support of the source term.

Physically, the divergence is a result of the far-field expansion performed to arrive at (3.44) - the trade-off to use the far-field expansion instead of the full solution had to be made to make an analytic treatment feasible at all. The resulting algebraic expression is expanded in ϵ_L and only the leading contribution in ϵ_L is kept. The detailed analysis yielded the dominating contribution to be $\epsilon_L^{-7/2}$.

Finally, taking the modulus to cancel the phase factor stemming from the integration over the temporal variable, the following formula is the result of a bit of further but completely straightforward algebra:

$$U \simeq \frac{\rho_f c_s^2}{\rho_s c_p^2} \frac{\beta^2 |(\hat{\Gamma} * \hat{\Gamma})|(\mu_{n0} c_s R^{-1})}{J_0(\mu_{n0})\pi^2 c_s \mu_{n0} \sqrt{L}^7} \cdot c_{\text{fit}}. \tag{3.51}$$

Now, the fit constant c_{fit} can be estimated once the convolution $\hat{\Gamma} * \hat{\Gamma}$, geometric information on the continental plate, i.e., H_0 and L and a typical vibration amplitude U, for instance measured at the shoreline, are known. We mention that the inclusion of seismic attenuation effects in the vortex vibration theory leads to even more complicated parameter estimates for c_{fit}.

Chapter 4

Vortices, stopping spheres, and tone generation in organ pipes

The, quite often, majestic organ pipes have been the subject of intense physical investigations for more than 150 years; cf. [133, 1] and references therein. The as yet unresolved questions of physical interpretation lack a systematic treatment because of the non-availability of the correct mathematical medium for the appropriate formulation of both, questions and answers. Specifically, the mechanisms of harmonic and general tone production have been alleged to involve nonlinear processes which do however not provide the best possible results. Also, the open end of the organ pipes has not been investigated thoroughly from the perspective of fluid dynamics phenomena up to now to deepen the understanding of the interplay between fluid dynamics and acoustics.

Here, the existence of vortex structures in organ pipes during play is shown and the measured power spectrum is derived theoretically from a stochastic perspective. We show that a stable system of vortex rings exists at the open end of the organ pipe as a topological irregularity from both a theoretical and experimental viewpoint. We further show that upon utilizing non-equilibrium statistical turbulence modeling in the language of stochastic processes, a linear theory is sufficient to explain the radiated power spectrum as measured at the open end of the pipe.

The result and the universality of the underlying mechanism is in contrast to ongoing efforts in musical acoustics to search for nonlinear models accomplishing the same. The article exemplifies in the context of organ pipes and musical acoustics that the application of yet un-applied mathematics accompanies novel physical insights in the fields of science.

4.1   Introduction

It all began with a simple experiment...   Throughout the history of science, innovation was often preceded by observations from practice rather than initially standardized laboratory experiments. Indeed, the best "first guess" for boundary conditions at the circular endcaps of a cylindrical organ pipe by Helmholtz [156] had been paralleled by findings from "the practice" [27]. Today Helmholtz' imagination is accepted as the most adequate one, albeit still in need of several corrections. Fig. 4.1 visualizes Helmholtz' model (a), known corrections (b) and the explanation we present in section 5.2 (c) for the end-correction δ_0.

It was reported by *B. Edskes*[1] to *L. van Hemmen*[2] that, in sound quality checks in organ pipes after cleaning, a gold particle appeared to circulate slightly above the open end of the pipe during the test play. In order to understand the origin of the phenomenon in a satisfactory way, the organ pipe setup has been standardized as shown in the top plot of Fig. 4.2.

The organ pipe is installed perpendicularly to the laboratory floor and connected with the air bags supply system. The tube system for the air flow is indicated in green. The room is darkened and a diascope is installed to light a plane parallel or vertical to the open end of the pipe. A suction pump is connected to the air supply system to inject tobacco smoke in the pipe through the foot hole. A camera creates a film consisting of single pictures to record the vortex structures. The setup is combined with a microphone placed at distance 20 cm above the open end of the pipe to record the radiated sound. The electronics for spectrum recording and pre-processing is situated on the right table.

In the bottom plot of Fig. 4.2, the organ pipe is shown together withe the expected vortex structure and a horizontally lit plain. Minimization of external disturbances by smoke exiting the pipe through the labium and thus interfering with the vortices at the open end has been accomplished by a deflection rosette wrapped around the pipe above the organ pipe mouth. The experiment has been performed in a closed laboratory room with the requirement on the experimenters to stand still in order to avoid air disturbances and create a situation as close to the fluid rest frame as reasonably possible.

In the following paragraphs, we introduce the two phenomena which we will model

---

[1]Bernhardt Edskes, "Edskes Orgelbau", 5610 Wohlen, Switzerland.
[2]L. van Hemmen, T35 TUM Physik-Department.

in section two and three and test by the described experiment.

Open end of the organ pipe   In the general context of fluid dynamics, the study of *nozzle flow* belongs to the subject of great academic (e.g. [71]) and practical (e.g. [70]) interest alike: From an applied mathematician's perspective, nozzle flow is interesting because there is an abrupt change in qualitative geometry behavior - a formerly confined flow turns into a flow in an unbounded domain. In the engineering practice, the orifices interface the interior parts of the machine body with the outer world and thus are the exchange "stations" for numerous substances and quantities.

Recently, the authors of [20] have investigated certain fluid and aerodynamic properties of nozzle flow through a flanged orifice. The results agreed with experimental studies on vortex rings [85] and numerical assessments of the stability [101, 93, 94]. Also from the perspective of musical acoustics [28], the open end of the organ pipe has been found to be the geometric origin of the "acoustic enlargement" of resonating organ pipes [47, 28]: Since the air can emanate the organ pipe in the form of a jet, the notion of the pipe interior during resonance is ill-defined.

Together with the later Nobel laureate Schwinger, Levine [88] calculated via Wiener-Hopf methods the exact value of the end-correction for a semi-infinite unflanged circular pipe. The calculations have been extended to more complex geometries with one relevant result given by the numerical treatment in [2] accounting for a finite wall thickness. Two questions are natural: First, one may ask about the relation between the abrupt change in topology at the open end of the organ pipe and the existence of a vortex structure akin to [85]. Second, since both phenomena appear at the open end of the organ pipe, does there exist a link between the end-correction [88] and the hydrodynamic flow field induced by the vortex structure?

Tone generation   The search for mechanisms underlying the production of sound in organ pipes has developed into a subject of keen academic interest [36, 35, 31, 32, 38, 150, 153, 151, 152] as well as [43, 44, 45, 46, 137], not only to European research groups [161, 162]. The approaches presented in the above references share the basis of deterministic methods. Yet, only recently [28] the importance of aerodynamic and possibly turbulent processes has been recognized - less so in older treatments [47].

The geometric origin of tone production is the *upper labial lip* of the organ pipe; cf. the bottom plot in Fig. 4.2. The conceptually most straightforward way to account for the interplay between aerodynamic and aeroacoustic processes is given by the *vortex*
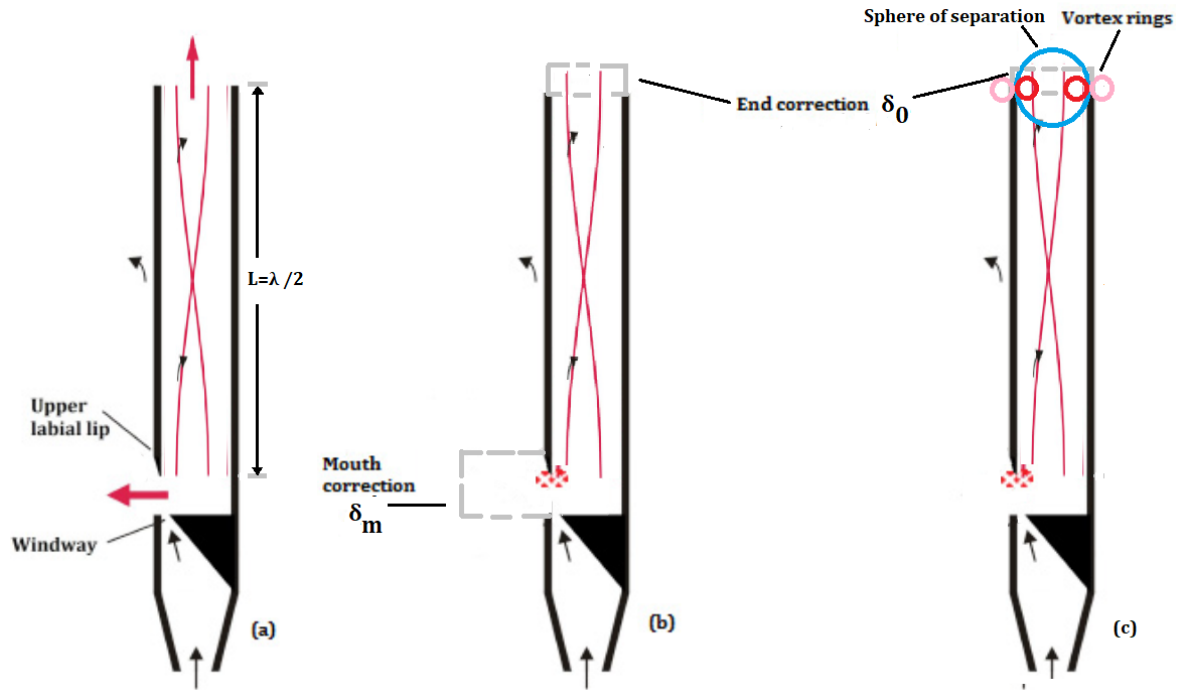
Figure 4.1: (a): Helmholtz' [156] creative imagination of how an organ pipe generates its fundamental frequency. The pipe length L between the mouth, or labium, at the bottom and the top of the pipe equals, for the air at resonance in the pipe, half the wavelength between two anti-nodes at the openings (symbolized by the "opening" of the solid red lines), where sound is radiated into free space, indicated by thick red arrows. Accordingly, since the wavelength λ equals the velocity of sound $c \approx 343\,\mathrm{ms^{-1}}$ divided by the fundamental frequency f_1 and $\lambda/2 = L$, we end up with $\lambda = 2L = c/f_1$. (b): The effective length L_{eff} to compute f_1 slightly exceeds the actual pipe length L, which in the past has been accounted for by phenomenological correction factors δ_0, the end-correction [88], and δ_m, the mouth correction [74]. Both corrections are symbolic in grey. The effective length finally is given through $L_{\mathrm{eff}} = L + \delta_0 + \delta_m$. Both the complicated geometry of and the turbulence at the labium preclude any simple physical explanation of δ_m. Only approximate, idealized results [74] exist that do, however, agree with earlier experimental findings [27]. (c): As will be explained below, the hydrodynamic mechanism underlying the end-correction is given through the existence of the sphere of separation (in light-blue) and a system of two counter-rotating vortex rings (stable inner one in dark red, unstable outer one in light red) at the open end.
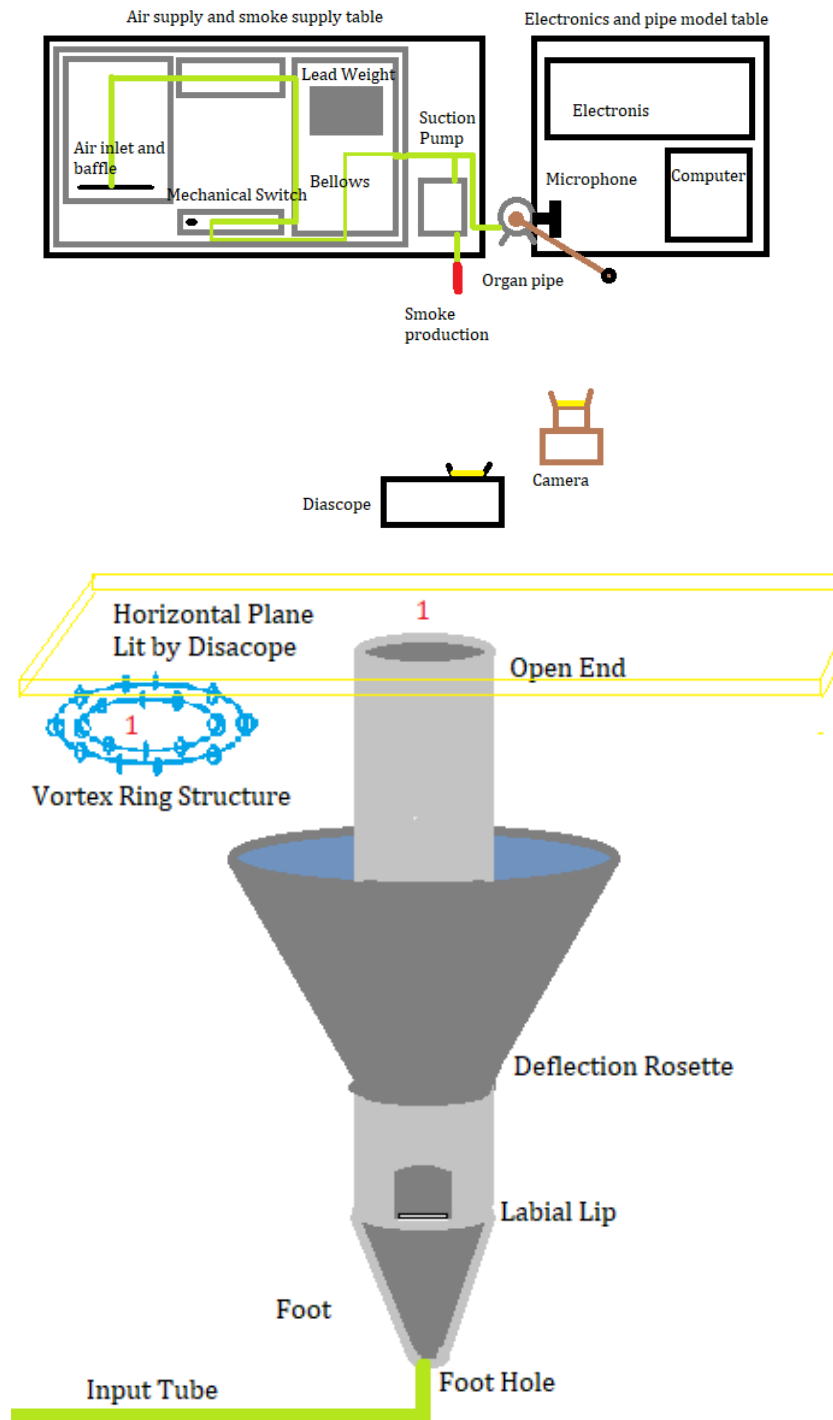
Figure 4.2: Top: Experimental setup for (A) observing a vortex structure at the open end of the organ pipe and (B) recording of the sound radiated from the open end of the pipe. Bottom: Schematic view on an organ pipe with conical deflection rosette, air supply tube, horizontally lit plane and the expected system of two concentric, counter-rotating vortex rings of equal strength at the open end of the pipe.

sound theory due to Howe [69] and Powell [120]. The applicability of the still fully deterministic theory is based on the production of *edge tones by vortices* [119]. Put simply, the interaction between the physical fluid "air" and the solid structure "labial lip" leads to the formation of sound-generating vortex dipoles [41, 119] which can be described by the Howe-Powell theory of vortex sound, itself a special case of the *Lighthill equation* as the governing equation of aerodynamics [90, 91]. The intricacy is rooted in the fluid dynamic nonlinearities in the governing equations of fluid and aerodynamics which makes an analytic treatment unfeasible at the present.

On the other hand, turbulence has been studies from a statistical point of view by Kolmogorov [82, 81], one of the founding fathers of modern probability theory. Given the statistical nature of turbulence, it is natural [100, 132] to ask about the nature of the relation between fluid and aerodynamics on the one hand and probability on the other hand. Based on the insufficiency of manifestly nonlinear modeling to explain tone generation [43, 44, 45, 46, 137], it is natural to ask whether a nonlinear treatment is actually necessary to explain quantitatively the measured power spectrum [15, 3] of the organ pipe.

Scope of the present work   The existence of a vortex structure at the open end of the pipe akin to [85] and its relation to the end-correction [88] is assessed in section two. Via a *linear, stochastic* theory based on Markov processes [53], the measured power spectrum as shown e.g. in the left plot of Fig. 4.5 from [3] is derived theoretically in section three. In the appendix, additional material is presented that would have distracted from the results but can be helpful for a better understanding of those.

4.2   Topological edge vortex phenomena in the open-ended organ pipe

Introduction   Not only organ pipes but also other brass musical instruments feature an open end functioning as junctions between an "interior" and an "exterior" of the instrument. We start the topological part of this article by defining explicitly what we mean when we speak of the interior of a musical instrument. This will be done in generality. We let $\partial\mathcal{G}$ denote a piecewisely suitably regular, oriented, connected and compactly embedded surface in the three-dimensional physical space $\mathbb{R}^3$. $\partial\mathcal{G}$ represents the walls of the musical instrument mathematically. We call $\partial\mathcal{G}$ a *musical instrument*

for brevity.

Next, we take a pair of points $(\mathbf{x}_1, \mathbf{x}_2) \in (\text{Conv}(\partial\mathcal{G})) \times (\text{Conv}(\partial\mathcal{G})^{\complement})$ with the property that the straight line $[\mathbf{x}_1, \mathbf{x}_2] \equiv \{(1-t)\mathbf{x}_1 + t\mathbf{x}_2 | t \in [0,1]\}$ connecting the two points has precisely one point in common with $\partial\mathcal{G}$. This ensures in conventional but yet ill-defined terminology that one point of the pair lies "inside" the instrument and the other one "outside". Since $\partial\mathcal{G} \hookrightarrow \mathbb{R}^3$ is compact, its complement is open and there is an $\epsilon_1, \epsilon_2 > 0$ such that, upon suitably decreasing the ϵ_1 and ϵ_2, the closed balls $\bar{B}^3_{\epsilon_i}(\mathbf{x}_i)$ and $\partial\mathcal{G}$ share no points. Next, let $\mathbf{p} = \mathbf{p}(\theta_i, \phi_i) \in \partial\bar{B}^3_{\epsilon_i}(\mathbf{x}_i) = S^2_{\epsilon_i}(\mathbf{x}_i)$ be the two-parameter family of the boundary points of the previously defined closed balls.

The strategy for the definition of the *acoustic volume* inside the musical instrument $\partial\mathcal{G}$ is to consider rays emanating from one of the two points $\mathbf{x}_i$ and passing through the points $\mathbf{p}(\theta_i, \phi_i)$. In ray acoustics, an acoustic wave is represented precisely by such a ray and is subject to the reflection law at the solid boundary ignoring the negligible transmission through the walls of $\partial\mathcal{G}$. Suppose that a ray in the direction $\mathbf{v}_i$ and through two point $\mathbf{p}_{i-1}$, $\mathbf{p}_i$ is reflected at $\mathbf{q}_i$. The reflection law then states that the reflected ray is emitted along the vector $s_{\partial\mathcal{G}}(\mathbf{q}_i)[\mathbf{v}_i]$ where $s_{\partial\mathcal{G}}(\mathbf{q}_i)$ denotes the reflection map on the so-called tangential space of $\partial\mathcal{G}$. Since the musical instrument is oriented, it is globally defined and by the choice of the pair $(\mathbf{x}_1, \mathbf{x}_2)$ we ensure that neither of the points is placed "on top of" one of the instrument's openings. The procedure yields for each $i \in \{1, 2\}$ and each (θ_i, ϕ_i) a polygonal arc $\mathcal{R}'((\theta_i, \phi_i))$ defined as the union of all rays emanating $\mathbf{x}_i$ and passing through $\mathbf{p}(\theta_i, \phi_i) \in S^2_{\epsilon_i}(\mathbf{x}_i)$ as first point. The reflection law construction from above allows a unique continuation of each of these rays by defining $\mathcal{R}(\theta_i, \phi_i) = \{\mathbf{x} \in \mathcal{R}'(\theta_i, \phi_i) | \mathbf{x} \in [\mathbf{q}_{j-1}, \mathbf{q}_j]\}$ where $\mathbf{q}_j \in \partial\mathcal{G}$ is a reflection point *in* $\partial\mathcal{G}$. Each of the $\mathbf{x}_i$'s is treated as the 0-the reflection point of a given ray $\mathcal{R}'(\theta_i, \phi_i)$. The polygonal arc defined this way naturally has finite length and is a, possibly closed, curve.

By the formalization of the intuitive picture of an "inside point" as $\mathbf{x}_1 \in \text{Conv}(\partial\mathcal{G})$, the *acoustic volume* of $\partial\mathcal{G}$ is well-defined through

$$\mathcal{G} \equiv \bigcup_{(\theta_1, \phi_1) \in S^2_{\epsilon_1}(\mathbf{x}_1)} \mathcal{R}((\theta_1, \phi_1)). \tag{4.1}$$

It is immediate that $\mathcal{G} \subseteq \text{Conv}(\partial\mathcal{G})$. Equality of sets holds if and only if $\partial\mathcal{G}$ is a subset of the boundary of a convex set, more precisely, $\partial\text{Conv}(\partial\mathcal{G}) \supseteq \partial\mathcal{G}$.

Last, the *acoustic volume inside* the musical instrument $\partial\mathcal{G}$ is defined as the com-

plement of $\partial\mathcal{G}$ in the acoustic volume $\mathcal{G}$ of $\partial\mathcal{G}$,

$$\text{Ins}(\partial\mathcal{G}) \equiv \mathcal{G} \setminus \partial\mathcal{G}. \tag{4.2}$$

We notice that $\text{Ins}(\partial\mathcal{G})$ is relatively open in $\mathcal{G}$ but not open as a subset in $\mathbb{R}^3$. Intuitively, one closes continuously the wall's holes by planes in $\mathbb{R}^3$ and fills the unique compact region bounded by this piecewisely Jordan-type surface. The solid body obtained this way is the acoustic volume $\mathcal{G}$. The inside volume $\text{Ins}(\partial\mathcal{G})$ is obtained by removing the walls $\partial\mathcal{G}$ from the previously obtained $\mathcal{G}$.

Despite the technical intricacies in the definition of the acoustic volume an implication is immediate: The manifest fundamental object from the topological perspective is $\partial\mathcal{G}$ from which the acoustic volume $\mathcal{G}$ can be derived as above. On the other hand, $\partial\mathcal{G}$ itself may have a nonzero boundary $\partial^2\mathcal{G} \equiv \partial(\partial\mathcal{G})$ because $\partial\mathcal{G}$ is only compactly embedded but not necessarily compact. We denote by $D^2_{R;z}((x_0, y_0, z_0))$ and $S^1_{R;z}((x_0, y_0, z_0))$ the closed disk, respectively the circle of radius $R > 0$ lying in a plane parallel to the xy-plane that contains (x_0, y_0, z_0). In the case of an open-ended organ pipe $\partial\mathcal{G}$, we have

$$\partial\mathcal{G} \equiv D^2_{R;z}((0,0,0)) \cup \{\mathbf{x} = (x, y, z) \in \mathbb{R}^3|$$
$$x^2 + y^2 = R^2,\, 0 \le z \le L\} \subset \mathbb{R}^3 \tag{4.3}$$

for $R, L > 0$.

For a closed organ pipe $\partial\mathcal{G}'$, we have

$$\partial\mathcal{G}' \equiv D^2_{R';z}((0,0,0)) \cup \{\mathbf{x} = (x, y, z) \in \mathbb{R}^3|$$
$$x^2 + y^2 = R'^2,\, 0 \le z \le L'\} \cup D^2_{R';z}((0,0,L')) \tag{4.4}$$

with $R', L' > 0$. In this case, the boundary of the musical instrument is

$$\partial^2\mathcal{G} = S^1_{R;z}((0,0,L)) \quad,\quad \partial^2\mathcal{G}' = \emptyset. \tag{4.5}$$

Due to a loss in regularity at the *opened edges* $\partial^2\mathcal{G}$ of a musical instrument $\partial\mathcal{G}$, we have an obstruction for the acoustic volume $\mathcal{G}$ to be a differentiable manifold if $\partial^2\mathcal{G} \ne \emptyset$. The converse is not true as exemplified by the closed organ pipe from above. Yet, the musical instrument is a *manifold with corners* [77] for which one has a generalized version of Stokes' theorem.

In a potential theoretic view on musical instruments in the physical sense, the overall *vorticity* defined as $\boldsymbol{\omega} = \nabla \times \mathbf{v}$ stays constant. Since *in initio* no vorticity is present is musical instruments, an $\epsilon > 0$ after the tone key is pressed, the total vorticity in $\mathcal{G}$

stays constant and equates to **0** and formalized in the solenoidality condition. Together with the algebraic *solenoidality condition* $\nabla\boldsymbol{\omega} = 0$ for the vorticity, the "manifold-with-corners" property enables us to devise the topological vortex model at the organ pipe's open end in the next paragraph.

Topological model   Real organ pipes have a finite wall-thickness $2r_w$ which is small compared to the interior diameter $2R$, i.e. $\delta \equiv r_w/R \ll 1$ in general and $\delta_w \approx 1/17$ for the plexiglass model in specific. Furthermore, $R/L \sim \delta \ll 1$ for sufficiently slender pipes. Yet, R/L, r_w/R are mathematically independent parameters. The finite-wall thickness requires us to use two analogues of the previous $\partial\mathcal{G}$ for the finitely long but infinitely thin pipe. Namely, denoting $\partial\mathcal{G} = \partial\mathcal{G}(R, L)$, we use

$$
\begin{aligned}
\partial\mathcal{G}_\delta \equiv -(0, 0, L) + \partial\mathcal{G}^-(R(1-\delta), L - \delta R) \\
\cup \partial\mathcal{G}^+(R(1+\delta), L + \delta R) \cup \mathcal{K}^{(o)}_{(1-\delta)R,(1+\delta)R;z}((0, 0, L))
\end{aligned}
\tag{4.6}
$$

with *opposite orientation* and join them by means of an annulus $\mathcal{K}^{(o)}_{(1-\delta)R,(1+\delta)R;z}((0, 0, L))$ in a plane parallel to the xy-plane containing $(0, 0, L) \in \mathbb{R}^3$ and oriented such that $\partial\mathcal{G}_\delta$ carries a globally orientation.

In the spirit of the experiment by Krutzsch [85], we choose R as the dominant length scale and idealize $R/L \to 0$, i.e., consider a semi-infinite pipe limit. This is also the model considered in [88]. The translation in (4.6) ensures that the pipe's open end is centered around the origin of the coordinate system. To avoid double-counting of edges, we identify $\partial^2\mathcal{G}(R(1-\delta), \infty) \cup \partial^2\mathcal{G}(R(1+\delta), \infty) = S^1_{(1-\delta)R;z}((0, 0, 0)) \cup S^1_{(1+\delta)R;z}((0, 0, 0)) = \partial\mathcal{K}_{(1-\delta)R,(1+\delta)R;z}((0, 0, 0))$. The 1-edges [77] are thus the disjoint union of two concentric and co-planar circles with the *same* orientation

$$
\partial^2\mathcal{G}_\delta = S^{1,+}_{(1-\delta)R;z}((0, 0, 0)) \cup S^{1,+}_{(1+\delta)R;z}((0, 0, 0)).
\tag{4.7}
$$

The co-orientedness of the circles is a consequence of the existence of a global orientation on $\mathcal{G}$: It is homeomorphic to a 2-sphere and the edges can be deformed into meridian circles at, say, $+45°$ and $-45°$ in geographic notation. These need to be co-oriented to ensure a global orientation via an almost everywhere smoothly defined pull-back of the well-defined Gauss map $N : S^2 \to S^2$ to $\mathcal{G}_\delta$.

By integration of the solenoidality condition over the complement of $\mathcal{G}_\delta$ and the classical Gauss' integration theorem:

$$
0 = \int_{\mathcal{G}_\delta^{\complement}} d^3x \, \nabla\boldsymbol{\omega} = \int_{\partial\mathcal{G}_\delta^{\complement}} d^2\mathbf{A} \, \boldsymbol{\omega} = -\int_{\partial\mathcal{G}_\delta} d^2\mathbf{A} \, \boldsymbol{\omega}.
\tag{4.8}
$$

By the definition $\boldsymbol{\omega} = \nabla \times \mathbf{v}$, the classical Stokes' integration theorem finally converts the surface to a contour integral over the edges (4.7):

$$0 = \int_{S^1_{(1-\delta)R}} d\mathbf{s}\, \mathbf{v} + \int_{S^1_{(1+\delta)R}} d\mathbf{s}\, \mathbf{v} \tag{4.9}$$

where we have canceled the overall minus from the orientation reversal and used disjointness of the the two edges to decompose the integral over the union of edges into a sum of integrals over the individual edges. The notation has been abbreviated slightly to ensure readability. The classical integration theorems are special cases of the general Stokes' theorem which remains valid upon generalization to manifolds with corners.

In the semi-infinite pipe limit, the setup is axisymmetric around the z-axis. Cylindrical coordinates are defined such that the xy-plane is covered by polar coordinates and the z-axis stays unchanged by the coordinate transform. The aforementioned so-called cylindrical symmetry of the setup translates into $\mathbf{v}^{\pm} = v_{\phi}^{\pm}(r, z = 0)\hat{e}_{\phi}$ where r denotes the polar distance to the z-axis and the super-script $\pm$ refers to whether the induced velocity fields from the vortex structure at $r_{\pm} = R(1 \pm \delta)$. The symmetry facilitates the evaluation of (4.9):

$$0 = 2\pi R(1-\delta)v_{\phi}^{-}(R(1-\delta)) + 2\pi R(1+\delta)v_{\phi}^{+}(R(1+\delta)). \tag{4.10}$$

In order to be able to match with the calculations in [88] and [47] for the value of the end-correction and in order to be able to evaluate the last equation further, we apply the so-called thin-wall approximation: By $0 < \delta \ll 1$, (4.10) admits a Taylor-expansion in δ around $r = R$ which may be truncated up to an error of order $\mathcal{O}(\delta^2)$ after the linear term $\sim \delta$. Indeed, cancellation of the pre-factor $2\pi R$ respectively $2\pi R\delta$ yields the system of equation for $v_{\phi}^{\pm}(R)$:

$$\mathcal{O}(\delta^0) : \; 0 = v_{\phi}^{+}(R) + v_{-}^{\phi}(R) \tag{4.11}$$

$$\mathcal{O}(\delta^1) : \; 0 = \partial_R \left(v_{\phi}^{+} - v_{\phi}^{-} \right)(R) + R \left(v_{\phi}^{+} - v_{\phi}^{-} \right)(R) \tag{4.12}$$

Re-arranging (4.11) and insertion of $v_{\phi}^{-}(R)$ in (4.12) and cancellation of an overall factor of 2 in the resulting equation leaves us with the ordinary differential equation $\partial_R v_{\phi}^{+}(R) + R v_{\phi}^{+}(R) = 0$. This is a separable differential equation in $\mathbb{R}^+ \times \mathbb{R}$ and has the general solution

$$v_{\phi}^{\pm}(R) = \frac{\pm\Gamma(t)}{2\pi\delta R} \implies \mathbf{v}^{\pm}(R) = \frac{\pm\Gamma(t)\hat{e}_{\phi}}{2\pi\delta R}. \tag{4.13}$$

It needs to be stressed that the expression exists in a plane in the z-plane. The integration constant has been specified to be a possibly time-dependent factor of $\Gamma(t)/(2\pi\delta)$ to match with the formal structure of axisymmetric, infinitely thin potential vortex rings [71] centered at $R(1 \pm \delta)$. The impacts of time-dependent circulations will be used in section three and discussion is outsourced to there.

By construction, the vorticity $\boldsymbol{\omega}^{\pm} \equiv \nabla \times \mathbf{v}^{\pm}$ inducing the above velocities vanishes, $\boldsymbol{\omega}^{\pm} = \mathbf{0}$. That is, the two potential vortex rings are irrotational: Heuristically generalizing (4.13) yields

$$v_{\phi}^{\pm}(\mathbf{x}) = \frac{\pm\Gamma(t)}{2\pi} \frac{1}{\left\| \mathbf{x} - \mathbf{x}_0^{\pm} \right\|} \tag{4.14}$$

where $\mathbf{x}_0^{\pm} \equiv R(1 \pm \delta)\hat{e}_r$ and for $\mathbf{x} = R\hat{e}_r$, we recover the special case derived above. For later purpose, we abbreviate $\mathbf{x}_0 = R\hat{e}_r$.

The vortex system containing two potential vortex rings with the above properties is shown in the top subplot of Fig. 4.3. A total of $N = 64$ vortex monopoles of equal strength have been distributed at equal distance on each of the two core circles of the rings. The vortices on the two rings differ in strength by a multiplicative minus sign each. Using the superposition principle in the context of the potential theoretic approach, the induced fluid velocity fields have been plotted as three-dimensional vector fields with the open end of the pipe (top row) and without (bottom row) from two different perspectives in either case.

Theoretical results   We discuss three implications of the vortex model resulting from the above topological deliberations.

- *Far-field quadrupole:* It is interesting to consider the total induced velocity field of the vortex rings starting from (4.14) in the thin-wall approximation: The definition $\mathbf{v}_{\text{tot}} \equiv v_{\phi}^{+}(R) + v_{\phi}^{-}(R)$ yields after expanding up to a linear order in a relative factor δ,

$$\mathbf{v}_{\text{tot}}(\mathbf{x}) = \frac{\Gamma(t)}{\pi} \frac{\left\langle \mathbf{x} - \mathbf{x}_0, \mathbf{x}_0 - \mathbf{x}_0^{\pm} \right\rangle_{\mathbb{R}^3} \hat{e}_{\phi}}{\left\| \mathbf{x} - \mathbf{x}_0 \right\|^3}. \tag{4.15}$$

  This is the far-field of a dipole of vortex rings and thus, since vortex rings themselves behave as dipoles [71] far-field, a quadrupole.

  Indeed, the vorticity $\boldsymbol{\omega}_{\text{tot}} = \nabla \times \mathbf{v}_{\text{tot}}$ exhibits a far-field scaling as $\boldsymbol{\omega}_{\text{tot}} \sim r^{-3}$ where r is the spherical distance from the open end's edge $\partial^2 \mathcal{G}$ for the idealized

infinitely thin organ pipe. The quadrupole behavior has also been observed in [10, 47] and thoroughly studied acoustically therein, a perspective dual to ours.

- *Meta-stationarity:* The vortex structure exhibits a stable behavior in the sense that the offhand and laboratory controlled experiments (see below) revealed vortex structures existing for $> 5\,\mathrm{s}$ at a fixed position without vortex dissolution or self-propulsion.

The well-known [71] formula for the self-propulsion velocity for an individual, infinitely thin, axisymmetric vortex ring of radius R and circulation Γ reads:

$$V_p(R;\Gamma) = \frac{\Gamma}{4\pi R}\left(\log\left(\frac{8R}{\epsilon}\right) - \frac{1}{4}\right). \tag{4.16}$$

The quantity ϵ is an infinitesimally small quantity describing the "infinitely thin" vortex core.

The total velocity $V_{\mathrm{tot}} = V_p(R(1-\delta), -\Gamma) + V_p(R(1+\delta), +\Gamma)$ of the vortex structure of can be obtained after expansion in powers of $0 < \delta \ll 1$. Inspection of the definition of V_{tot} reveals that it is an antisymmetric function in δ. Since the derivation of the vortices required an expansion up to including linear order in δ, we find

$$V_{\mathrm{tot}} = \frac{\Gamma\delta}{4\pi R}\left(\log\left(\frac{8R}{\epsilon}\right) - \frac{9}{4}\right) + \mathcal{O}\left(\delta^3\right). \tag{4.17}$$

From the stationary Bernoulli equation $v^2/2 = P/\rho_0$ at the foot for a blowing pressure $P_0 \simeq 7\,\mathrm{cmH_1O} \approx 687\,\mathrm{Pa}$ and conservation of kinetic energy $\rho_0/2v^2 A_{\mathrm{foot}} = \rho_0/2V_{\mathrm{pipe}}^2 A_{\mathrm{pipe}}$, we find for the mean flow in the pipe

$$V_{\mathrm{pipe}} = \sqrt{\frac{2P_0 A_{\mathrm{foot}}}{\rho_0 A_{\mathrm{pipe}}}} \simeq 18\,\mathrm{ms}^{-1} \tag{4.18}$$

which needs to compensate the V_{tot} by means of the *kinematic equilibrium condition*

$$0 \overset{!}{=} V_{\mathrm{tot}} + V_{\mathrm{pipe}}. \tag{4.19}$$

Setting $\epsilon \sim r_w$ in the hypothetical limit case of two vortex rings with non overlapping cores, we find from (4.17) and the general formula in (4.18) through

application of (4.19)

$$\Gamma \lesssim -\frac{4\pi RV}{\delta \log(8) - 2.25}\sqrt{\frac{2P_0 A_{\text{foot}}}{\rho_0 A_{\text{pipe}}}} \approx -71\,\text{m}^2\text{s}^{-1} \tag{4.20}$$

with the numerical value for V_{pipe} as in (4.18) and a generic but realistic choice of $R = 2.5\,\text{cm}$ for medium-sized organ pipes. The numerical test values are of acceptable order and hands a numerical feeling for the strength of circulation Γ in (4.14) which can most often only be found experimentally.

- *End-correction and sphere of separation (s.o.s.):* The end-correction due to the radiation of sound [88, 72, 71] can be obtained as

$$\delta_0 = \frac{-1}{\pi}\int_0^\infty \frac{dx\ \log\left(2K_1(x)I_1(x)\right)}{x^2} \approx 0.6127. \tag{4.21}$$

The bottom plot in Fig. 4.3 displays a cross section through the (infinitely thin) pipe's resonance body that contains the symmetry axis and the cross section through the two concentric vortex rings of opposite circulation. The setup is $\mathbb{Z}_2$-symmetric under reflection of *both* vortex dipoles centered at each ending of the wall.

Furthermore, the centers of the vortex dipoles at either wall end at $r = \pm R$ in the (r, z)-coordinate system and the two stagnation points of the flow field at $z = \pm R$ define a sphere. Indeed, since up to the signs needed for the dipoles at either end of the wall the vortices are equally strong, there is indeed a sphere in the bottom plot of 4.3 with the following noteworthy property. Fluid trapped inside the sphere will stay in this sphere as long as the vortices generate a flow field. Indeed, if fluid is transported in the jet flow from the resonance body of the pipe upstream towards the open end of the pipe it can enter the region bounded by the sphere.

The sphere is called *sphere of separation* because its upper cap extending into free-space functions as a correction surface to the acoustic volume of the organ pipe in the sense of the definition of the pre-to-last paragraph. Indeed the *acoustic volume* $\mathcal{G}$ of the organ pipe under play is enlarged precisely by the excess volume of the upper half ball $\text{Vol}(\bar{B}_R^3((0,0,0))) = 2\pi/3 \cdot R^3$. The latter has to be added to $\text{Vol}(\mathcal{G}) = \pi R^2 L$ for a cylindrical pipe.

This gives rise to a corrected volume

$$\mathrm{Vol}(\mathcal{G}'_c) \equiv \mathrm{Vol}(\mathcal{G}) + \mathrm{Vol}(\bar{B}^3_R(\mathbf{0})) = \pi R^2 \left(L + \frac{2}{3} R \right) \qquad (4.22)$$

and a topological prediction for the end-correction $\delta_0^{\mathrm{top}} = 2/3 \approx 0.6667$ with the error relative to the value of the Wiener-Hopf treatment being $< 10\,\%$. This error is significantly better than the value of the Rayleigh piston model [47, 28] which specified $\delta_0^{\mathrm{Ray.}} \geq 0.8$.

Now, $\mathcal{G}'_c$ is defined as the acoustic volume of an equivalent but stopped organ pipe $\partial \mathcal{G}'_c$, i.e., $\partial^2 \mathcal{G}'_c = \emptyset$; See the pre-to-last paragraph for details on the 1-edges of the stopped organ pipe.

The definition of an equivalent stopped organ pipe also explains why Neumann boundary conditions are to be used in order to calculate the eigenfrequencies of standing acoustic waves in the end-corrected acoustic volume. This result generalizes to other musical instruments with holes after appropriate, instrument-dependent modifications.

Experimental result   The major prediction of the topological deliberations leading to 4.14 is that a vortex structure of ring-like shape forms. Furthermore, the sphere of separation gives us a criterion to assess whether the prediction of the dipole structure is adequate: Monopoles would not admit the formation of a sphere of separation and the lowest possible hydrodynamic multiple in a cross-section model that allows a sphere of separation, as shown in the bottom plot of 4.3, is a dipole.

The experimental setup has already been described in the introduction, section 4.1. Tobacco smoke has been favored over conventional fog technology to avoid condensation of the liquid in fog on the solid walls of the pipe. Furthermore, it turned out that cigarillo smoke contains larger aerosol particles than cigarette smoke because despite pre-filtering the smoke, the jet exit slit connecting the pipe foot with the resonance body was prone to congestion by the solid constituents in cigarillo smoke requiring extensive cleaning after several experimental runs. In cigarette smoke, this was not the case and due to the lesser concentration in nicotine the walls of the plexiglass pipe did also not turn yellow to that extent. For the metal pipe, cigarillo smoke led to congestion almost every time so that cigarette smoke was injected into the pipe foot through the suction pipe connected as shown in the top plot of Fig. 4.2. Since a stream of smoke leaves
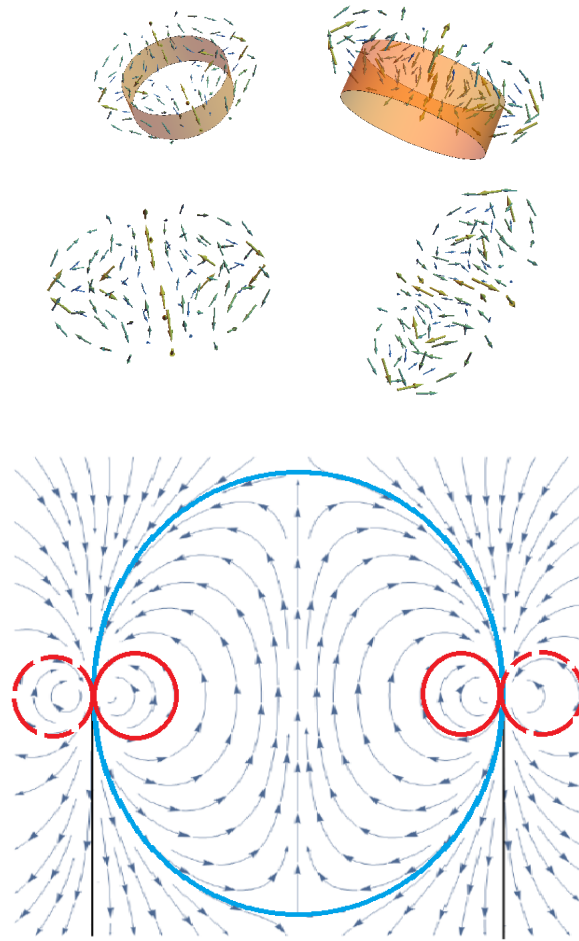
Figure 4.3: Top: Top row: Open end of the organ pipe with predicted vortex structure from two perspective angles; Bottom row: The system of two concentric counter-rotating vortex rings of equal strength. Bottom: Induced potential flow field in a cross-sectional plane containing the pipe symmetry axis with no-penetration boundary conditions at the pipe's walls (black lines). The local velocity is indicated by thin light-blue arrows. The cross section of the sphere of separation is indicated as the thick light-blue circle. Tangential to the sphere of separation are two red circles symbolizing the periodic trajectories a fluid parcel follows in close proximity to one vortex core. The cross section of the inner vortex ring which has been found to be stable in experiments is shown in solid red, the outer vortex ring has only allowed indirect observation via detection of the sphere of separation. The experimental instability of the outer vortex ring precludes a direct experimental observation.
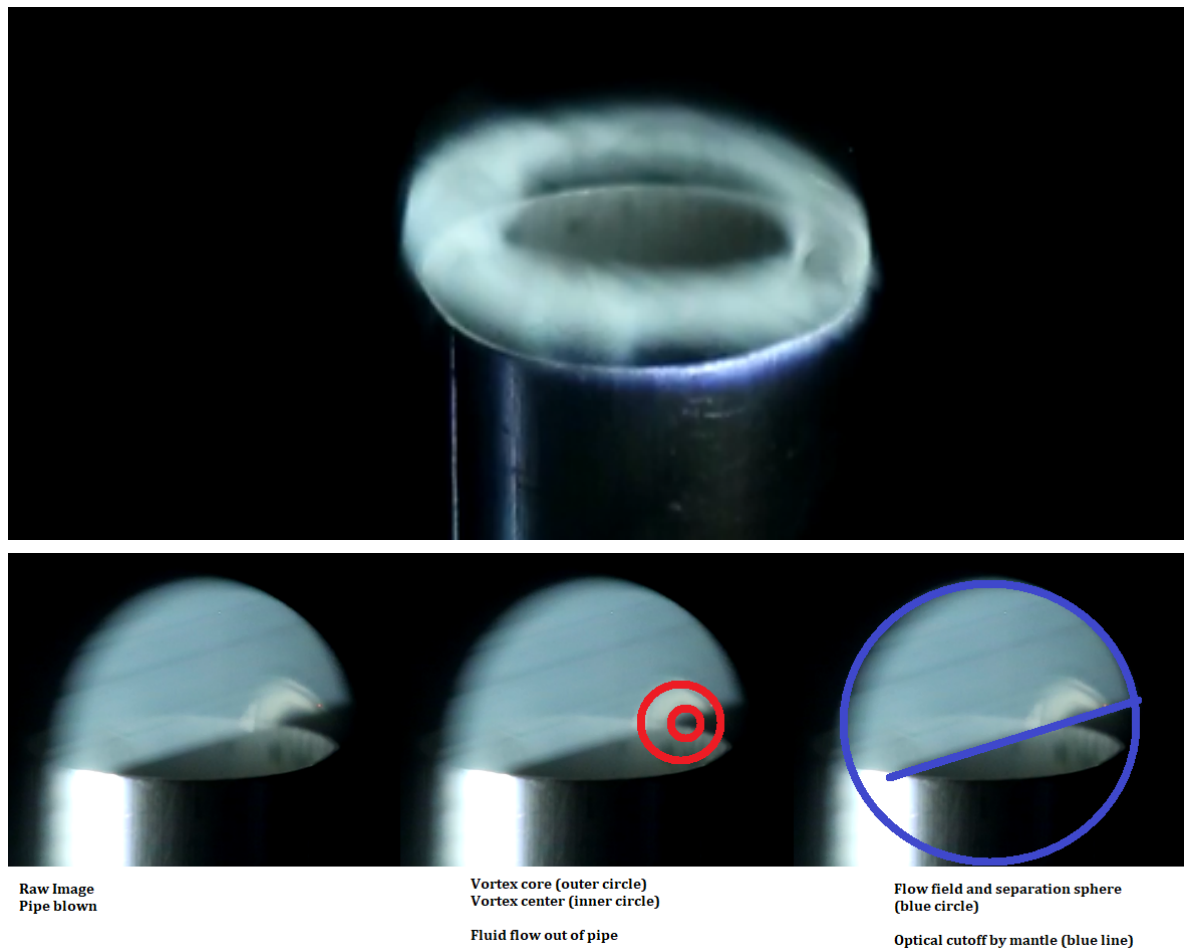
Figure 4.4: Top: Snapshot of the vortex ring system on top of a metal mantled organ pipe with a horizontally lit plane. Bottom: Sphere of separation created by the vortex dipoles at the pipe's open end: Left: Raw photo, Middle: Indication of the location of vorticity in red, Right: Indication of the circular cross section of the sphere of separation.

the labial mouth of the organ pipe, a deflection rosette has been wrapped around the resonance cavity to minimize disturbances from air velocity perturbations above the labial mouth; cf. the bottom plot in Fig. 4.2.

The experiment has been performed in two variants depending on the orientation of the plane lit by the diascope. The result of the experiment with a lit plane parallel to the floor of the laboratory is shown in the top plot of Fig. 4.4. A vortex ring-shaped structure is shown during pipe play. On the right-most part of the arc of the ring, two smaller arcs of lighter color can be found. They hint at the existence of a double vortex ring structure. The latter can be assessed more assertively by choosing the lit plane to be orthogonal to the laboratory's floor and containing the resonance body's symmetry axis. The result is shown in the bottom subplot of Fig. 4.4. One sees in the cross section of the pipe the sphere of separation in which the fluid is trapped. The photograph stems from a film of the sounding organ pipe and was $\approx (2-3)\,\mathrm{s}$ after the tone has ceased.

The shape of the sphere of separation agrees with the theoretical predictions visualized in the bottom subplot of Fig. 4.3.

The author has designed and conducted the experiment in collaboration with *B. Edskes*, *L. van Hemmen* and *B. Seeber*[3], listed in alphabetical order.

Closing remark   The central idea of this section that sharp edges admit the creation of acoustically "active" vortices can be combined with the theory of stochastic processes to obtain a quantitative model for the measured power spectrum of typical organ pipes. Such a spectrum is shown in the top left subplot (adapted picture from [3]) and bottom subplot of 4.5 (original measurements).

4.3   Stochastic mechanism of linear tone generation in the open-ended organ pipe

Introduction   Why are we in need of a universal mechanism of tone generation? With only two openings, the open end and the labial mouth, organ pipe are a geometrically easy-to-study flue-like instrument. This class of musical instruments is, in a simplistic picture, a refinement of organ pipes which share analogous constructions for the tone

---

[3]Bernhard Seeber, AIP TUM, Fakultät für Elektro- und Informationstechnik.

production [47, 28]. In that sense, the tone generation mechanism we will describe in this section is "universal".

The geometric location of tone generation [47, 28] is well-known to be the upper labial lip; cf. the lower plot in Fig. 4.2. Qualitatively, air bags are connected by tubes to the pipe foot. At a blowing pressure of $P_0 \approx 7\,\mathrm{cmH_2O} \simeq 687\,\mathrm{Pa}$ an air flow is injected through the *foot hole* in the *pipe foot*. The prism-like *languid* in the foot hole canalizes the air flow such that the air flow can leave the foot hole through so-called *(jet) exit slit* or *windway*. The jet exit slit is a thin $w_0 \sim 1\,\mathrm{mm}$ but long $W_0 \sim q \cdot 2\pi R$ rectangular orifice, adjacent to the pipe wall. It connects the, otherwise separated, foot hole with the *resonance body* of the pipe. The small effect of viscosity [28] canalizes the air flow such that it leaves the jet exit slit almost in the direction of the unit normal, i.e., propagates the distance $H_0 \lesssim 0.5\,\mathrm{cm}$ for medium sized pipes to the *upper labial lip*. The region of propagation, commonly referred to as *pipe mouth* or *labial region*, is opened towards the surrounding free space and thus provides the second of the two interfaces of the open-ended organ pipe with the environment. The upper labial lip itself is wedge-shaped and acts a sharp edge placed in the direction of the air flow. The pipe's tone is generated there [67, 119, 28].

Air jet and jet disturbance   Due to the interaction of the solid sharp edge with the hydrodynamic jet, a localized region of turbulence is created. It is known [133] that a plane jet admits an undulant, wave-like perturbation which also has been verified experimentally [150, 153, 151] and has been used extensively to study the tone production in organ pipes and related instruments, e.g., [38, 149, 152, 36, 35, 31, 32, 44, 45].

With the abbreviation $V_{\mathrm{jet}} = \sqrt{2P_0/\rho_0}$, the relevant low-frequency limit reads [133]

$$\zeta_k(t, z) = A \exp\left(\sqrt{\frac{kW_0}{2}} V_{\mathrm{jet}} t\right) \exp\left(i(\omega(k)t - kz)\right) \tag{4.23}$$

where the dispersion relation is quadratic, $\omega(k) = k^2 W_0 V_{\mathrm{jet}}/2 \sim k^2$, and A is an amplitude factor with the physical dimension of a length. The model is accurate for $f \lesssim 5.5\,\mathrm{kHz}$ for medium-sized typical organ pipes $L \sim 60\,\mathrm{cm}, \mathrm{R} \lesssim 3\,\mathrm{cm}$; cf. the practical book [1].

Theoretical refinements of the basic model by Rayleigh are available, see e.g. [47] and references therein.

Wave turbulence Since the jet velocity $V_{\text{jet}} = \sqrt{2P_0\rho_0^{-1}} \simeq 33.8\,\text{ms}^{-1} \lesssim c/10$ is considerably high for fluid flow and since the aforementioned experiments hint at a stable wave-like jet perturbation, it is more appropriate to use the notion of *wave turbulence* [98] rather than a complete turbulence [82, 81] which is indeed confined to a small region around the upper labial lip.

Wave turbulence is the study of the evolution of (mostly plane) linear waves in non-linear wave evolution such as the Navier-Stokes equations. The mathematical methods are similar to those used in modern field theories in physics for calculating correction terms to the wave solution and stochastic to study physical quantities such as dissipated energy [100, 132, 53]. A well-known [98] result due to Kolmogorov asserts that in full turbulence, energy is distributed according to the *Kolmogorov scaling* relation

$$E(k) \sim k^{-5/3} \tag{4.24}$$

where $k = \|\mathbf{k}\|$ is the (hydrodynamic) wave number of the wave in full turbulence.

Apart from a broad energy spectrum, (wave) turbulence features a so-called *inertial range* in which a dominant *forward* respectively sub-dominant *backward energy cascade* allows the transferal of energy from larger length scales to smaller length scales respectively vice-versa until a critical length λ_D is reached. The so-called dissipation length λ_D marks the threshold for dissipation of energy into heat. For instance, if an infinitely long wave-length, meaning $k \to 0^+$, is excited energy may be transferred to a non-zero wave number by virtue of the forward energy cascade. As an intermediate result of the preliminary deliberations, we note that once we have a turbulent flow we can via (4.24) ensure a broad energy scaling for the hydrodynamic wave number k and thus the hydrodynamic frequency $\omega = \omega(k)$ that the Rayleigh jet undulation carries.

Evolution of wave turbulence Naturally, the jet perturbation propagates along a coordinate, say z, which we choose to denote the distance from the jet exit slit, i.e., $0 \le z \le H_0$. At $z = 0$, the jet perturbation is purely potential and governed by the purely deterministic treatment [133]. The other extreme case is the upper labial lip where the full turbulence requires the replacement of the deterministic with a purely stochastic picture: The notion of a well-defined frequency ω or wave number k breaks down.

Both objects, ω and k, turn into so-called *random variables* Ω respectively K which are distributed according to a certain equilibrium probability distribution $\mathbb{P}_{\text{eq}}$. The

link between the fully deterministic and the fully stochastic quantities consists of using the notion of a *stochastic process*: Instead of taking a well-defined frequency and a well-defined wave number, we replace ω, k by the stochastic process counterparts $\Omega(z)$, $K(z)$,

$$k \rightarrow K = K(z) \in L^1([0, H_0] \rightarrow \mathbb{R}^+) \tag{4.25}$$

$$\omega(k) \rightarrow \Omega(z) = \omega(K(z)) \in L^1([0, H_0] \rightarrow \mathbb{R}^+) \tag{4.26}$$

and imply physical regularity behavior.

The stochastic process $K(z)$ is accompanied by a family of probability densities $\mathbb{P}_z(k) \equiv \mathbb{P}(k, z)$ so that the probability densities evolve in a quasi-stationary way according to a Fokker-Planck equation

$$\partial_z \mathbb{P}(k; z) = -\partial_k \left(\mathsf{a}_1(k) \mathbb{P}(k; z) \right) + \partial_k^2 \left(\mathsf{a}_2(k)/2 \cdot \mathbb{P}(k; z) \right) \tag{4.27}$$

in the coordinates z and k. The jump moments $\mathsf{a}_1, \mathsf{a}_2$ will be discussed after the next paragraph.

Here, we confine ourselves to specifying the limit behavior of the family $\mathbb{P}_z(k)$ for the two extreme cases $z \rightarrow 0$ and $z \rightarrow H_0$:

$$\lim_{z \to 0} \mathbb{P}_z(k) = \delta(k) \ \& \ \lim_{z \to H_0} \mathbb{P}_z(k) = \mathbb{P}_{\mathrm{eq}}(k) \tag{4.28}$$

An introduction to stochastic methods as applied to physical sciences is available e.g. in [53, 100].

Link to vortex acoustics   Finally, contact with aero-acoustics is made by using a Howe-Powell [70, 119] theory as suggested in [28], i.e.,

$$\partial_t^2 p - c^2 \Delta p = \rho_0 c^2 \nabla \left(\boldsymbol{\omega} \times \mathbf{v} \right) \tag{4.29}$$

We choose $\mathbf{v} = V_{\mathrm{jet}} \hat{e}_z$, inspired by the dominance of the jet propagation in z-direction towards the upper labial lip. The vorticity $\boldsymbol{\omega}$ contains the impact of turbulence and is supported in a small location at the labial lip.

In view of $H_0/L \lesssim 1/100$ in the plexiglass model and in view of the modal cut-off criterion in duct acoustics [72] for the low-frequency regime $f \lesssim 3.2\,\mathrm{kHz}$, we may confine ourselves to an effective one-dimensional model with a source condition at $z = 0$ and a hard-wall condition at $z = L_{\mathrm{eff}}$. The one-dimensional wave equation for the acoustic pressure reads [72]

$$\partial_t^2 p(t, z) - c^2 \partial_z^2 p(t, z) = 0. \tag{4.30}$$

In the language of mathematics, the boundary conditions [156] are implemented as Neumann boundary conditions

$$\partial_z p(t, z = 0) = -\rho_0 \partial_t^2 v_{z,\text{in}}(t) \,\&\, \partial_z p(t, z = L_{\text{eff}}) = 0. \tag{4.31}$$

The $z = 0$ condition stems from the linearized Euler's equation [72] where we "idealize" the labial lip to be at $z = 0$ and allowing an equivalent air mass flow $j_z(t) = \rho_0 v_{\text{in},z}(t)$ streaming in the pipe and capturing the effect of the vortex source term in (4.29).

In view of the discussion of the end-correction as above, the open-ended organ pipe is regarded as an effective pipe-shaped thin wave-guide of length $L_{\text{eff}} = L + \delta_0 R$ where we ignore the mouth correction; See section 4.2. Setting $\rho_0 \partial_t^2 v_{\text{in}} = \mathbf{f}_v \cdot \hat{e}_z$ with $\mathbf{f}_v = \rho_0(\boldsymbol{\omega} \times \mathbf{v})$, we have linked the broadband turbulent spectrum to the source condition at $z = 0$. Indeed, the results that will be presented below show that a simple inhomogeneity to the Helmholtz [156] model

$$\partial_z p(t, z = 0) = \mathcal{Q}_0 \cdot \langle \exp(i\Omega t) \rangle_{\Omega \sim \mathbb{P}_{\text{eq}}} \tag{4.32}$$

suffices in the source term.

Effectively, this model equates $\partial_z p$ at $z = 0$ to a superposition of $\exp(i\omega t)$'s, or, in the stochastic interpretation equivalently, to the average of the phase exponential $\exp(i\Omega t)$ with respect to the equilibrium probability distribution $\mathbb{P}_{\text{eq}}$ at the labial lip. The quantity $\mathcal{Q}_0$ is a parameter which quantifies the strength of the input and is treated as a free parameter in the model. It won't be needed in the further treatment explicitly and we comment that it serves to give a constant offset to the sound-pressure level, i.e., can be used to adjust vertical translations.

Stochastic model For the acoustics of the organ pipe and to explain the shape of the curve shown in the upper left subplot of (4.5), the jump moments a_1 and a_2 need to be specified. Natural boundary conditions are imposed on the Fokker-Planck equation (4.27).

The stationary solution, i.e., at $z = H_0$ is obtained [53] as

$$\mathbb{P}_{\text{eq}}(k) \propto \frac{1}{\mathsf{a}_2(k)} \exp\left(2 \int_0^k \frac{d\kappa\, \mathsf{a}_1(\kappa)}{\mathsf{a}_2(\kappa)}\right). \tag{4.33}$$

Using the Kolmogorov scaling (4.24), we derive the the scaling of the jump momenta from the assumption that

$$\frac{\rho_0 \partial_t \langle \zeta_K(t, z) \rangle_{K \sim \mathbb{P}_{\text{eq}}}^2}{2} \sim k^{-5/3} \sim E(k) \tag{4.34}$$

where we assume further that we may replace the average over wave-numbers by an average over a small interval $(-\Delta z + H_0, H_0)$; see Appendix 4.B for details of the rather lengthy calculation.

One may think of the replacement of averages as if we tracked the wave number over a suitably small interval close to the region of full turbulence and assign to K respectively k the character of a "quasi-ergodic" quantity. We note that the assumption is merely a calculational simplification yielding sensible results, though. Upon using the jump moments in the stationary ($\partial_z \mathbb{P} = 0$) state with natural boundary conditions $(-\mathsf{a}_1 + \mathsf{a}_2(k)/2\partial_k \mathbb{P}_{\text{eq}}(k) = 0)$ at $z = H_0$, we recover (4.33).

Using the simplifying assumptions sketched above, the precise but technical calculation presented in Appendix 4.B leads to the equilibrium probability density for the wave number, $\mathbb{P}_{\text{eq}}(k)$, and upon invoking the transformation theorem for probability densities [53], also the probability density for the (hydrodynamic) frequency $\omega = \omega(k) \propto k^2$ of the jet perturbation $\zeta = \zeta_k(t,z)$, denoted by $\mathbb{P}_{\text{eq}}(\omega)$:

$$dk\,\mathbb{P}_{\text{eq}}(k) = \frac{dk\,2\Theta(k)}{k_{\text{fit}}\beta(5/12,1/2)}\left(\frac{k_{\text{fit}}^2}{k^2 + k_{\text{fit}}^2}\right)^{\frac{11}{12}} \tag{4.35}$$

$$d\omega\,\mathbb{P}_{\text{eq}}(\omega) = \frac{d\omega\,\Theta(\omega)}{\sqrt{\omega\omega_{\text{fit}}}\beta(5/12,1/2)}\left(\frac{\omega_{\text{fit}}}{\omega + \omega_{\text{fit}}}\right)^{\frac{11}{12}} \tag{4.36}$$

The objects k_{fit} and ω_{fit} are fit constant which needed to be introduced in order to assure convergence.

The probability densities (4.35) and (4.36) are normalized. They belong to the class of Pearson-VII probability densities [114, 115, 116, 117].

Experimental and numerical testing Data for a plexiglass organ pipe of length $L = 0.6\,\text{m}$ and radius $R \approx 2.5\,\text{cm}$ have been gathered by placing a microphone above the open end of the organ pipe. Data have been gathered by the freeware AUDACITY and resolved at 4096 bins in the full measurement range $0\,\text{Hz}$ to $50\,\text{kHz}$. Finally, data from $200\,\text{Hz}$ to $3.7\,\text{kHz}$ have been exported as *.txt-file and processed further with the aid of the commercial software MATHEMATICA.

We state the final result of the statistical fit procedure and comment on the parameters and quantities involved. We let $\lg \equiv \log_{10}$. The *relative sound pressure level* is defined as $\text{SPL}(f|f_0) \equiv 10\log_{10}(\mathcal{P}(f)/\mathcal{P}(f_0))$ dB where $\mathcal{P}(f)$ is the value of the power spectrum at the frequency f. Equivalently, $\text{SPL}(f|f_0) = 20\log_{10}(|p(f)/p(f_0)|)$ dB. Choosing $p(f_0) = 20\,\mu\text{Pa}$, the *(absolute) sound pressure level* is recovered.

By the previous paragraphs, (4.30) admits a solution in frequency domain space, evaluated at the open end, given as $p(\omega, z = L_{\text{eff}}) \sim \omega^{-1}\mathbb{P}_{\text{eq}}(\omega)$ where the additional ω^{-1} stems from solving the $D = 1$-Helmholtz equation with the Neumann boundary conditions (4.32). Likewise, the $\mathbb{P}_{\text{eq}}$ as in (4.36) contains the broadband spectrum generated by the turbulence model at the upper labial lip which translates to the acoustic pressure by virtue of (4.29) respectively (4.30) and (4.32).

Data gathered by the author with *L. van Hemmen* and *B. Seeber* and independently in [3] are displayed in Fig. 4.5. In that figure, the maximum peak of sound pressure level is attained at the first harmonic $f_2 = 2 \cdot f_1$ for the fundamental frequency $f_1 \approx 262\,\text{Hz}$. The fit quality can be improved by setting $\omega \rightarrow \omega'(\omega) = \omega_p + |\omega - \omega_p|$ where ω_p is a *peak frequency* which can be fitted from the measurement data.

The width of the peaks is due to a physical and a technical reason: Physically, thermal-viscous effects lead to a small deviation from the perfect δ-peak structure predicted by the wave equations (4.30) and (4.29). Technically, the width of the peaks is influenced by the number of bins used in resolving the measurement range. The higher the number of bins, the smaller the peak width until the lower threshold due to the thermal-viscous effects is reached.

These deliberations are incorporated through *filters*. Following [47] on the function of the resonance body as a passive acoustic filter, these filters are regarded as the limit of a Dirac-sequence. I.e., they originate from a function sequence which converges weakly to the Dirac delta. The latter is the "perfect filter" in signal theory jargon: $\mu_\epsilon(\omega; \omega_n) \xrightarrow{\epsilon \to 0^+} \delta(\omega - \omega_n)$. The parameter ϵ serves so as to fine-tune the width of the peaks to match with the data. A small linear frequency dependency of the ϵ, the standard deviation in the case of Gaussian filters, improves the overall quality of the fit if we ignore normalization of the filters.

Last, we use a harmonic, e.g., f_{13} and calculate the relative sound pressure level to it. This is the frequency f_c at which $\text{SPL}(f = f_c | f_c) = 0$. Contact with the average sound pressure level of $\simeq 74\,\text{dB}$ as in several figures in [3] is made for our data by using an offset along the ordinate axis. Up to multiplicative constants, this is the strength parameter $\mathcal{Q}_0$ from (4.32) but we will treat it here just as an ordinate axis offset SPL_0.

Altogether, the model for the absolute sound pressure level is

$$\frac{\text{SPL}(\omega) - \text{SPL}_0}{20\,\text{dB}} = \lim_{\omega_{\text{fit}} \to 0} \lg\left(\frac{\sum_n \mu_\epsilon(\omega; \omega_n)\omega'(\omega)^{-1}\mathbb{P}_{\text{eq}}(\omega'(\omega))}{\sum_n \mu_\epsilon(\omega_c; \omega_n)\omega'(\omega_c)^{-1}\mathbb{P}_{\text{eq}}(\omega'(\omega_c))}\right). \tag{4.37}$$

For the $N_c = 13$ frequencies displayed in the lower subplot of (4.5), we find for Gaussian

filters $\mu(f; f_n) \simeq \sqrt{2\pi\epsilon_g^2(f_c/2)}^{-1} \exp(-|f - f_n|^2/(2\epsilon_g^2(f)))$ with $f_c = 3421.8\,\text{Hz}$, $f_p = 440\,\text{Hz}$ and the linear phenomologically adapted standard deviation $\epsilon_g(f) = 41\,\text{Hz} + 2\,\text{Hz} \cdot f/f_1$ from (4.37)

$$\frac{\text{SPL}(f) - 58\,\text{dB}}{20\,\text{dB}} = \lg\left(\frac{\sum_{k=1}^{N_c=13}(f_\text{p} + |f_c - f_\text{p}|)^{\frac{29}{12}} e^{-\frac{|f-f_n|^2}{2\epsilon_g^2(f)}}}{\sum_{k=1}^{N_c}(f_\text{p} + |f - f_\text{p}|)^{\frac{29}{12}} e^{-\frac{|f_c-f_n|^2}{2\epsilon_g^2(f_c)}}}\right). \qquad (4.38)$$

In (4.38), the impacts of the frequency dependence of ϵ_g have been ignored in the Gaussian filters according to the fit prescription from above.

The result of the simulation is shown in the top plot of Fig. 4.6. The raw data have been shifted around the model curve according to (4.38) and the green band denotes an absolute deviation band of $\pm 5\,\text{dB}$ between data and prediction, the orange one quantifies an absolute deviation of $10\,\text{dB}$ between data and prediction and the red band shows a deviation up to $\pm 15\,\text{dB}$. The data from the lower subplot of Fig. 4.5 have been interpolated and the dashed red curve has been used to obtain the offset value of $58\,\text{dB}$ in (4.38) to establish an average sound pressure level of $74\,\text{dB}$ in the frequency range $f \in [50\,\text{Hz}, 3700\,\text{Hz}]$ for the top plot Fig. 4.6.

From the lower plot of the same figure, it is seen that the absolute error is for the vast majority of frequencies below $10\,\text{dB}$ and for the majority even below $5\,\text{dB}$. The turbulence model predicted the exponent of $29/12$ in (4.38).

Concluding remark The results of the fitting procedure are better than expected originally by the authors. The authors regard this as *an* evidence that a linear stochastic instead of a nonlinear deterministic is fully sufficient to deduce the measured power spectrum in organ pipes.

4.4   Summary

Summary It is due time to step back and reflect on what has been accomplished.

In the chapter's second section, it was shown from topological considerations that the thorough modeling of the open end of organ pipes requires the usage of the pipe's walls, $\partial\mathcal{G}$, to define an (inside) acoustic volume. Inspired by the notion of a "manifold with corners" rather than a smooth manifold, we derived the existence of a vortex structure made up from two concentric, co-planar, counter-rotating vortex rings. By
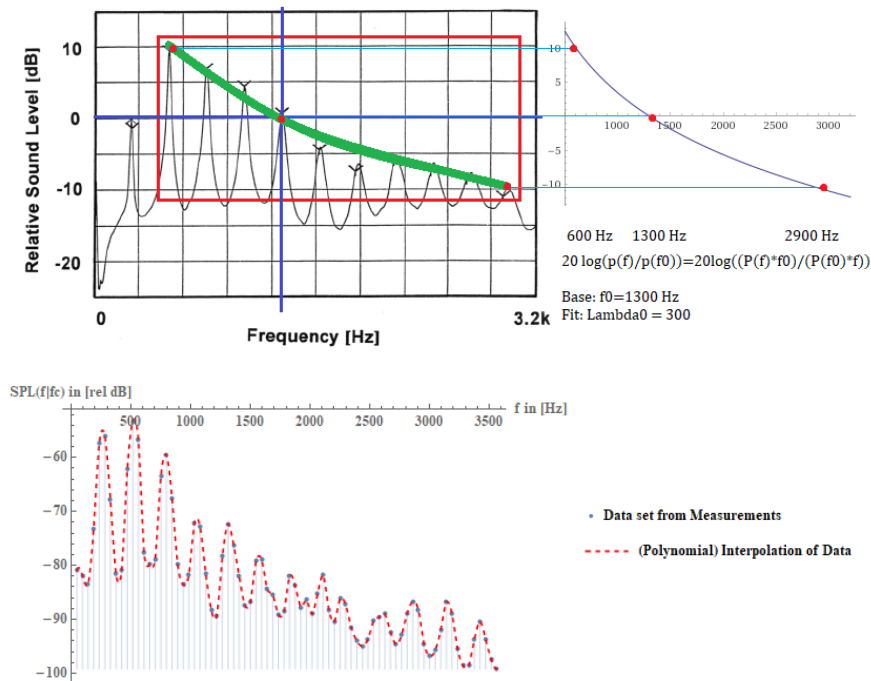
Figure 4.5: Top: Left: Data obtained independently and published in [3]: The maxima through which a green line is drawn have been extracted from these data and used within the frequency range contained in the red box to fabricate a preliminary test on the model; Right: Interpolating curve between the harmonic maxima. Bottom plot: Measured relative sound pressure level obtained from the experiment shown in Fig. 4.2. 4096 bins have been used to resolve the measurement range $[0, \text{kHz}, 50\,\text{kHz}]$. The data have been gathered for a circular plexiglass organ pipe with the geometric dimensions of $L = 58\,\text{cm}$ and $r = 25\,\text{mm}$.
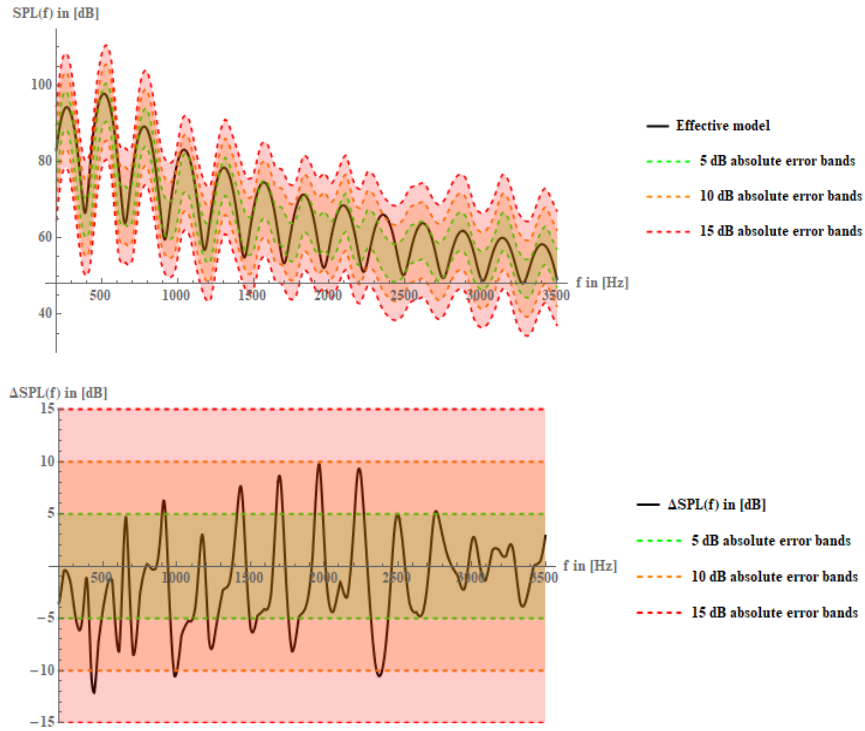
Figure 4.6: Top: The final plot of the theoretically predicted sound pressure level as fitted to the experimental data shown in the bottom subplot of Fig. 4.5. The overall normalization has been chosen to match with the one employed in [3] by a vertical shift of the data such that the average sound pressure level of $74\,\mathrm{dB}$ agrees with the value obtained from calibration measurements.,Bottom: Absolute error between the theoretically predicted sound pressure level (black curve) and the experimentally measured sound pressure level together with error bands placed covering the regions of $\pm 5\,\mathrm{dB}$ (green), $\pm 10\,\mathrm{dB}$ (orange) and $\pm 15\,\mathrm{dB}$ maximum absolute error.

studying the induced velocity field in the fluid rest frame, we saw that the vortex structure gives rise to a phenomenological sphere of separation. It induced an excess volume and thus elongates the pipe's resonance body by an end-correction.

Up to a small $\lesssim 10\,\%$ relative error, the excess volume was equivalent to the volume associated with the end-correction obtained by an exact Wiener-Hopf treatment. The advantage of the topological method is its flexibility to be generalized to other musical instruments with a more sophisticated geometry that prohibits a direct, exact Wiener-Hopf treatment. The existence of a vortex structure was tested by direct measurements through smoke injection into a sounding pipe. The double vortex ring structure was assessed indirectly by studying the sphere of separation which provides a necessary and, excluding higher than dipole moments in the cross-sectional plane, also sufficient criterion for the double structure.

The chapter's third section combined the finding that edges trigger the formation of turbulent vortex dipoles with a dynamic theory of turbulence evolution: Starting from a potential, fully deterministic flow, the evolution of turbulence was modeled by letting the probability density of a δ-distributed wave number, i.e., of a deterministic wave number, evolve during jet propagation towards the labium as a Markov process. We required the scaling of the turbulent energy spectrum to be reproduced at the upper labial lip by virtue of the formalism employed in this treatment. In the low-frequency limit with acoustic waves propagating only along the symmetry axis of the pipe, the governing equation of vortex sound was simplified to match with a time-harmonic input weighted by the equilibrium probability density $\mathbb{P}_{eq}$ which describes the broad-band frequency distribution due to wave turbulence. The vortices generated at the labium were modeled to carry the turbulent frequencies of the jet undulation.

From measurements, we tested the approach through a model fit containing the scaling exponent $1 + 17/12 = 29/12$ that the turbulent model predicts to appear in the sound pressure level. The model fit included phenomenological corrections to reproduce the positive harmonic peak width in the typical organ pipe spectra instead of just giving a zero peak width as predicted by a non-thermal-viscous theory. It was found that the peak width of the model needed to be increased by a slight frequency-dependent peak width to produce a fit of satisfactory quality. By the constancy of the resolution of the measurement data for processing, this reflects the thermal-viscous spread of harmonic peaks. The absolute error between the fit model predictions and the data have been found to be in the majority of frequencies below $\pm 5\,\text{dB}$.

Outlook   Given the simplicity of the end-correction re-derivation by the method presented in section 4.2, it would be interesting to study other musical instruments and compared the predictions from a vortex flow field analysis to acoustic measurements. This also includes other than circularly symmetric orifices. Furthermore, the author suggests testing the fit model for the sound pressure level for other types of organ pipes. This can reveal possible material dependencies affecting the proposed model which could not have been included in this work.

Closing remark   An unfortunate and persistent pattern accompanies the expansion of scientific knowledge and de-facilitates learning novel, especially mathematical tools, for scientists in the applied fields: The language barriers between the mathematical and the applied community have become less penetrable over the last century. Being both mathematician and physicist, the author hopes to have contributed to a revival of scientists' interest in modern mathematics in general and stochastic as well as topological tools in specific. The importance of availability of unprecedented introductions on "modern mathematics for applied scientists" written in a straightforward-to-apply manner is reinforced.

4.5   Appendices for Chapter 4

Appendix 4.A - Hydrodynamic aspects of the flow in the resonance body of the pipe

Introduction   This section shall collect some numerical results on the irrotational, ideal fluid dynamics in the resonance body of the organ pipe. Apart from the vortex structures at the openings of the pipe, the resonance body resembles a circularly symmetric, long channel truncating sharply at the open end.

Already in the middle of the last century, Levine and Schwinger [88] presented an "exact" treatment of the frequency-domain acoustics wave equation, i.e., the Helmholtz equation, for an unflanged axisymmetric pipe relying on the rather advanced technique of Wiener-Hopf analysis. The treatment is "exact" in the sense that it only required the specification of a massless piston model at the open termination of the duct corresponding to a plane wave mode propagating along its symmetry axis.

Staring from the Helmholtz operator, $\mathsf{H}_k \equiv \Delta + k^2$ with $k \in \mathbb{R}_0^+$ and the aforemen-

tioned treatment, Howe [70] considered the limit of vanishing k by letting the speed of sound c stored in $\omega^2 = c^2 k^2$ diverge: In conjunction with some algebra, this yielded a result for the Stokes' stream function characterizing the irrotational flow from a semi-infinite unflanged duct.

Curiously, the result has not been applied to study the flow from the axisymmetric organ pipe - this is what we will do. We sketch the result obtained by Howe [70] and discuss a potential theoretic cross-sectional model along the symmetry axis of the organ pipe which can be treated by the tools of complex analysis. See [71] for an introduction to the methods.

Stokes' stream function for the organ pipe   Letting $k^2 \to 0$ in the result of the Wiener-Hopf analysis of the Helmholtz equation, the Stokes' stream function ψ_{ac} for the irrotational background contribution to the ideal background flow is obtained in the non-dimensional variables $\hat{z} \equiv z/R$, $\hat{r} \equiv r/R$. The interior of the semi-infinite pipe idealization and the exterior requires usage of the Heaviside function which is defined here as $\Theta(x) \equiv 1$ for $x > 0$, $\Theta(x) \equiv 0$ for $x < 0$ and taken to be not defined if $x = 0$.

The result for ψ_{ac} reads [71, 70]

$$
\begin{aligned}
\frac{2\pi\psi_{\mathrm{ac}}}{AU} = {} & \frac{\Theta(R-r)r^2}{2R^2} + \frac{\Theta(r-R)}{2} \\
& - \frac{\Theta(R-r)r}{\pi R} \int_0^\infty \frac{d\lambda}{\lambda} \sqrt{\frac{2K_1(\lambda)}{I_1(\lambda)}} I_1(\lambda\hat{r}) \sin\left(\lambda(\hat{z} - \mathcal{F}(\lambda))\right) \\
& - \frac{\Theta(r-R)r}{\pi R} \int_0^\infty \frac{d\lambda}{\lambda} \sqrt{\frac{2I_1(\lambda)}{K_1(\lambda)}} K_1(\lambda\hat{r}) \sin\left(\lambda(\hat{z} - \mathcal{F}(\lambda))\right)
\end{aligned}
\tag{4.39}
$$

where AU has the physical dimensions of an area times a velocity and is shorthand for $AU \equiv 2\pi cR^2$ with the speed of sound c and the radius R of the pipe.

For $\lambda > 0$, the phase contribution $\mathcal{F}(\lambda)$ is defined through the integral representation

$$
\mathcal{F}(\lambda) \equiv \frac{1}{\pi} \int_0^\infty \frac{dx \, \log\left(\frac{K_1(\lambda)I_1(\lambda)}{K_1(x)I_1(x)}\right)}{x^2 - \lambda^2}.
\tag{4.40}
$$

As $\delta_0 \equiv \lim_{\lambda\to 0^+} \mathcal{F}(\lambda) \approx 0.6127$, Howe noted correctly that this provides another derivation of the end-correction through a hydrodynamically inspired approach.

Cross section model   The geometry of the cross section model for the flow in the semi-infinite cross section of the organ pipe is shown in Fig. 4.7. The goal is to find the complex velocity potential $w = \Phi + i\Psi$ with a monopole source placed at $z_s = -\infty + iR$.

In the two-dimensional potential theory, the toolkit of complex analysis becomes applicable since $\Delta\Psi = 0 = \Delta\Phi$ are harmonic functions and thus define a holomorphic complex velocity potential w. In particular, the complex velocity potential can be transformed by bi-holomorphic maps between the physical coordinate system, say z, and a mathematically more tractable one, say ζ. This serves the purpose to reduce the intricate geometry $\mathcal{D}$ in the z-coordinate system to a more basic one in ζ-coordinates.

The bi-holomorphic transformation in question is established by the Schwarz-Christoffel mapping theorem [71] and the requirement that $z_A \mapsto -\infty$, $z_B \mapsto -1$, $z_C \mapsto 0$, $z_E \mapsto 1$, $z_F \mapsto \infty$ and the identification $z_C = z_D$. The latter identification yields a polygonal arc in the z-plane and ensures the applicability of the Schwarz-Christoffel mapping theorem, namely, the existence of a bi-holomorphic transformation that sends the polygonal arc $(AB(C = D)EF)$ to the real line in the ζ-coordinate system. Following [71], the inverse map is obtained from $d_\zeta z = K(\zeta + 1)(\zeta - 1)\zeta^{-1} = K(\zeta - \zeta^{-1})$ to be $z(\zeta) = -K\zeta^2/2 - K\log\zeta + C$. The constants $K, C \in \mathbb{C}$ are found from $(z_B = iR, \zeta_B = -1)$, $(z_E = -iR, \zeta_E = 1)$ through insertion and solution of a 2×2 system of linear equations: $K = -2R/\pi$, $C = -iR + R/\pi$. The source is located at $\zeta = 0$ corresponding to a planar source input at $z = -\infty$ in physical coordinates.

The complex velocity potential is given through $w(\zeta) = 2RV_{\text{jet}}/\pi \log\zeta - iRV_{\text{jet}}$ after having imposed $w(\zeta(z) = i) = 0$, that is, equating the complex velocity potential to zero at $z = (0,0)$ which fixes the additive constant up to which the complex velocity potential is determined. Using $w(\zeta) = \Phi(\zeta) + i\Psi(\zeta)$ the mathematical ζ-coordinate as a function of ζ follows from inversion of w:

$$\zeta = i \exp\left(\frac{\pi\Phi}{2RV_{\text{jet}}}\right)\exp\left(\frac{i\pi\Psi}{2RV_{\text{jet}}}\right). \tag{4.41}$$

Insertion into $z = z(\zeta)$ and taking the real part $x \equiv \Re[z]$ and $y \equiv \Im[z]$, the final equations for the planar stream line plot are obtained

$$\frac{x}{R} = \frac{1}{\pi} + \frac{\Phi}{V_{\text{jet}}R} + \frac{1}{\pi}\exp\left(\frac{\pi\Phi}{RV_{\text{jet}}}\right)\cos\left(\frac{\pi\Psi}{RV_{\text{jet}}}\right), \tag{4.42}$$

$$\frac{y}{R} = \frac{\Psi}{V_{\text{jet}}R} + \frac{1}{\pi}\exp\left(\frac{\pi\Phi}{RV_{\text{jet}}}\right)\sin\left(\frac{\pi\Psi}{RV_{\text{jet}}}\right). \tag{4.43}$$

The resulting planar streamline plot is shown in Fig. 4.9.

Using rotational invariance of the setup to rotate the planar plot around the x, axis the plot 4.8 is produced. The blue lines respectively the blue surfaces in Fig. 4.9 and
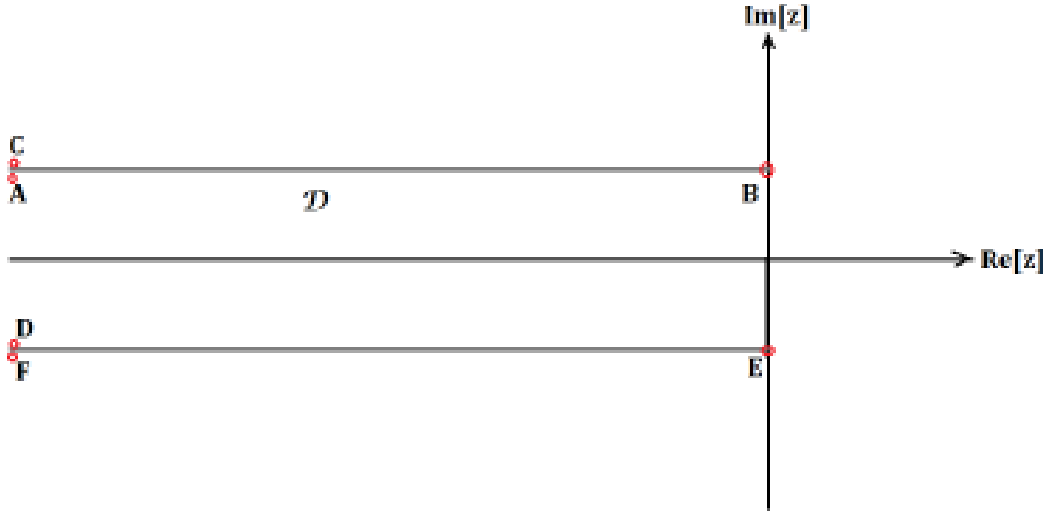
Figure 4.7: Cross section model of the organ pipe containing the symmetry axis of the resonance body: The points B and E are at $z_B = iR$ and $z_E = -iR$ respectively. The points A and C are situated at $z_A = -\infty + iR^-$ and $z_B = -\infty + iR^+$. Finally, B and F correspond to $z_B = -\infty - iR^+$ and $z_F = -\infty - iR^-$. The acoustic volume inside the pipe is called $\mathcal{D}$. The formerly radial and axial variables correspond, in this order, to $\Im[z]$ and $\Re[z]$.

4.8 represent the loci of constant $\Psi/(RV_{\text{jet}}) \in \{-0.8, -0.6, -0.4, -0.2, 0, 2, 0, 4, 0.6, 0.8\}$ and constant $\Psi/(RV_{\text{jet}}) \in \{0.2, 0.4, 0.6, 0.8\}$.

The curvature modulus of the curves of constant Ψ in Fig. 4.9 around the pipe wall terminations at $x = 0, y = \pm R$ increases for increasing $|\Psi|$. Analogously for Fig. 4.8 originating from Fig. 4.9 by revolution around the x-axis.

Appendix 4.B - Derivation of the input distribution through a Fokker-Planck approach

Introduction The purpose of this appendix section is to offer a more detailed derivation of the probability density used in the turbulent source term model presented in the main body of the article. The derivation is performed from an utilitaristic point of view, namely, the assumption of quasi-ergodicity announced in the main text will simply be used and deemed to be appropriate because of providing sensible numerical
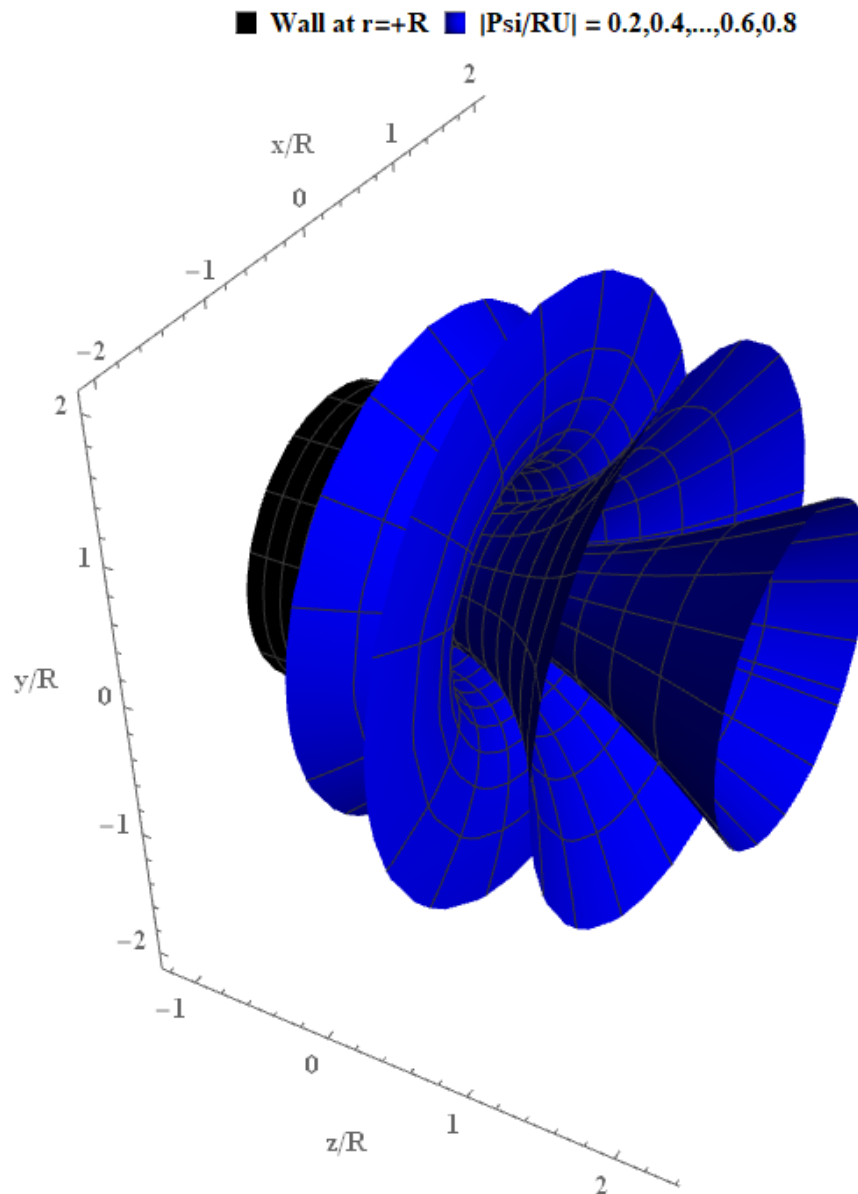
Figure 4.8: Family of surfaces of constant stream function Ψ for $\Psi/(RV_{\text{jet}}) \in \{0.2, 0.4, 0.6, 0.8\}$ for the axisymmetric potential flow out of the circular pipe orifice. The parameters are the non-dimensional real velocity potential $\Phi/(RV_{\text{jet}}) \in [-1.5, 0.5]$ and the azimuthal angle $\phi \in [0, 2\pi]$ for all surfaces of constant Ψ.
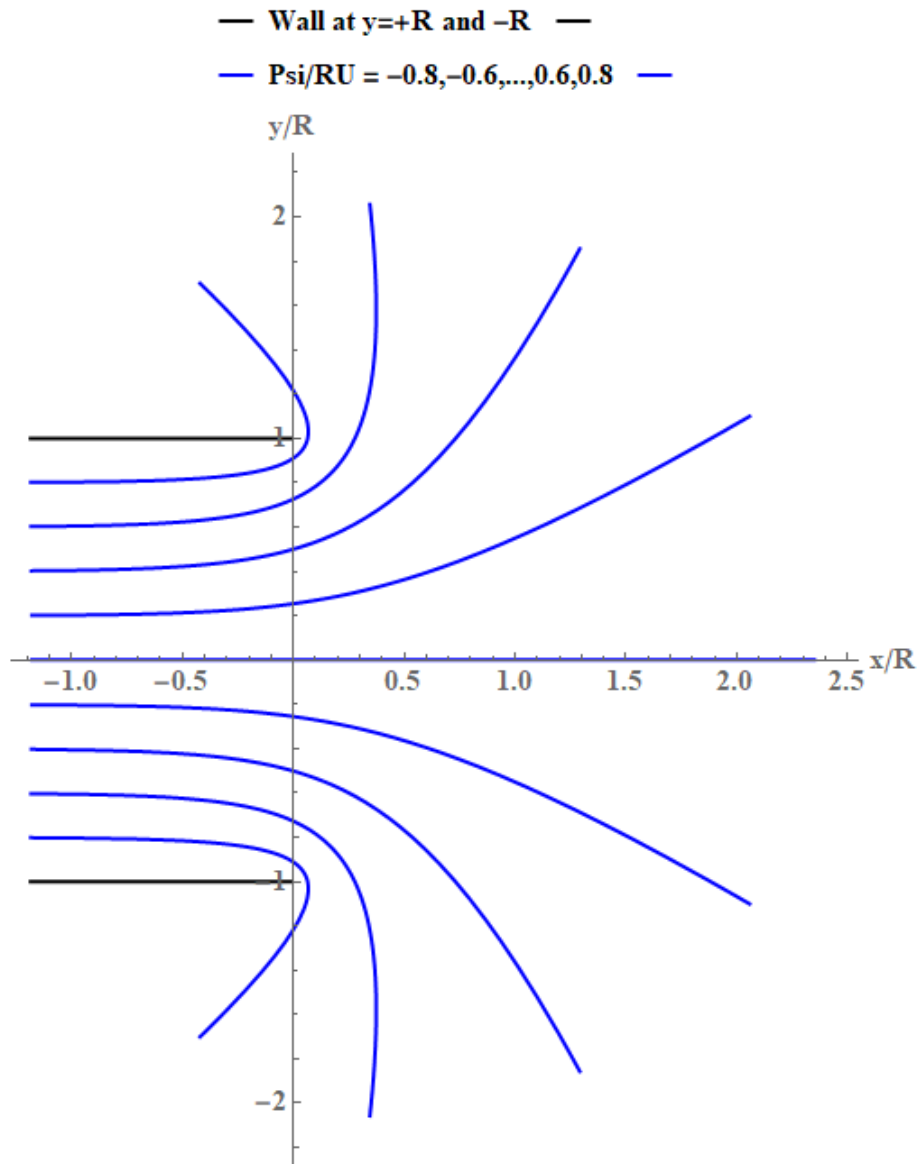
Figure 4.9: Family of curves of constant stream function Ψ for $|\Psi/(RV_{\text{jet}})| \in \{0, 0.2, 0.4, 0.6, 0.8\}$ for the planar potential flow out of the cross section model of the organ pipe. The simulation parameter is the non-dimensional real velocity potential and $\Phi/(RV_{\text{jet}}) \in [-1.5, 0.5]$ for all curves of constant Ψ.

results.

Fokker-Planck equation and Kolmogorov scaling The dynamic object of the approach presented in the main body of this chapter is the reduced frequency ω which is modeled as the realization of a stochastic process Ω and evolves as a Markovian stochastic process as a given point moves from the jet exit slit ("windway") towards the upper labial lip. We take $z = 0$ as the position of the windway and $z = H_0$ as the position of the upper labial lip and require K to be distributed such that the velocity of the undulating jet perturbation, $\partial_t \xi_K(t, z = H_0)$, with random wavenumber $K(z = H_0)$ reproduces the Kolmogorov scaling for the kinetic energy $E_{\text{kin}} \sim k^{-5/3}$ for sufficiently large wave numbers but small enough to ensure the applicability of the quadratic dispersion relation $\Omega \propto K^2$.

Upon assuming the requirements of the Kramers-Moyal-expansion to be satisfied and assuming a quasi-stationary process, we can model the probability density corresponding to the distribution of $K(z)$ as $\mathbb{P}(z, k)$. The evolution coordinate $\chi \equiv z/H_0/(1 - z/H_0)$ facilitates the investigation of the probability density's asymptotic behavior.

In (χ, k)-coordinates, we take the (dynamic) Fokker-Planck equation [53]

$$\partial_\chi \mathbb{P} = -\partial_k(\mathsf{a}_1(k)\mathbb{P}) + \frac{1}{2}\partial_k^2\left(\mathsf{a}_2(k)\mathbb{P}\right). \tag{4.44}$$

and investigate its quasi-stationary state at $\chi \to \infty$, i.e., $\partial_\chi \mathbb{P} = 0$. The equilibrium probability density to which $\mathbb{P}_{\text{eq}}$ converges in the limit $\chi \to \infty$ is denoted by $\mathbb{P}_{\text{eq}}$. We impose natural boundary conditions for the quasi-stationary state, $-\mathsf{a}_1(k)\mathbb{P}) + \frac{1}{2}\partial_k\left(\mathsf{a}_2(k)\mathbb{P}\right) = 0$ at $\chi \to \infty$, meaning there is no "flux of probability" beyond the quasi-stationary state.

It remains to solve the ordinary differential equation

$$-\mathsf{a}_1(k)\mathbb{P}_{\text{eq}} + \frac{1}{2}\partial_k\left(\mathsf{a}_2(k)\mathbb{P}_{\text{eq}}\right) = 0 \tag{4.45}$$

and we find

$$\mathbb{P}_{\text{eq}}(k) \propto \frac{\exp\left(\int_{k_0}^k \frac{dk'\,\mathsf{a}_1(k)'}{\mathsf{a}_2(k')}\right)}{\mathsf{a}_2(k)}. \tag{4.46}$$

By $\langle \heartsuit \rangle_t$ we denote the average with respect to the wave number of the quantity in brackets up to the threshold time t.

Let us take the formula $E(k) \sim k^2 \langle \bar{\mathbf{v}}(k,t), \mathbf{v}(k,t) \rangle_t$ for the averaged, up to time t, kinetic energy stored in a flow with isotropic wave vector distribution, whence the k^2, in three dimensions. As simplest model, we choose a plane wave Ansatz $\mathbf{v}(k) \sim \mathbf{A} \mathbb{P}_{\text{eq}}(k) \exp(i\omega(k)t)$ for the velocity field induced from the jet perturbation only at the upper labial lip. $\mathbf{A}$ is a constant amplitude and the remaining ω-dependent factor has been chosen such as to conform with the corresponding factor from the jet perturbation profile $\xi_k(t, z = H_0)/\exp(-ikH_0)$ excluding the exponential amplification.

Finally, we need to assume quasi-ergodicity such that we can relate the $E(k)$ to the Kolmogorov scaling $E_{\text{Kol}}(k) \sim k^{-5/3}$. Under quasi-ergodicity, we understand that the kinetic energy averaged over a suitably short time interval of the duration τ_{erg} should follow the Kolmogorov scaling if measured at the region of full turbulence, the upper labial lip. Then

$$E_{\text{Kol}}(k) \sim \langle \bar{\mathbf{v}}(k,t), \mathbf{v}(k,t) \rangle_t \sim |\mathbb{P}_{\text{eq}}|^2 k^2. \tag{4.47}$$

Since $\mathbb{P}_{\text{eq}}(k)$ is a probability density, insertion of the scaling result due to Kolmogorov, $E(k) \sim k^{-5/3}$, yields the scaling

$$\mathbb{P}_{\text{eq}}(k) \sim k^{-11/6}. \tag{4.48}$$

Comparison of (4.48) to (4.46) and the Ansatz $\mathsf{a}_1(k) \sim k^{\delta_1}$ and $\mathsf{a}_2(k) \sim k^{\delta_2}$ with $\delta_2 - \delta_1 = 1$ to cancel the exponential in (4.46) fixes $\delta_1 = -7/6$ and $\delta_2 = -1/6$.

Normalization issues - Pearson's differential equation In order to obtain a probability density, we need to ensure integrability of $\mathbb{P}_{\text{eq}}$ over $\mathbb{R}^+ \ni k$. Additionally, the scaling derived previously should be respected.

The above two requirements are satisfied by employing the *Pearson differential equation* [114, 115, 116, 117] and seeking for a probability density which reproduces the above scaling $\mathbb{P}_{\text{eq}}(k) \sim k^{-11/6}$. The result transfers to the non-dimensional $\kappa \equiv (k - k_0)/k_0$ where we regard k_0 as a start wave number. It will be let small enough later on to perform the expansion needed for the comparison.

Heuristically, we seek a probability density that looks similar to the Cauchy probability density $\propto (1 + ((k - k_0)/k_0)^2)^{-1} \sim k^{-2}$. To this end, we consider (4.45) in the non-dimensional wave number κ and rename the moments, $\mathsf{a}_l \to \tilde{\mathsf{a}}_l$ ($l \in \{1, 2\}$). The procedure leaves the mathematical structure of the equation (4.46) invariant,

$$0 = \frac{d\mathbb{P}_{\text{eq}}(\kappa)}{\mathbb{P}_{\text{eq}}(\kappa)} + \frac{\partial_\kappa \tilde{\mathsf{a}}_2(k) - 2\tilde{\mathsf{a}}_1(\kappa)}{\tilde{\mathsf{a}}_2(\kappa)}. \tag{4.49}$$

Next, we make the general Ansatz $\tilde{\mathsf{a}}_1 = \kappa^{-7/6}(a_{10} + a_{11}\kappa^{-1} + ...)$ and $\tilde{\mathsf{a}}_2(\kappa) = \kappa^{-1/6}/(a_{20} + a_{21}\kappa^{-1} + ...)$ such that $(\partial_\kappa\tilde{\mathsf{a}}_2(\kappa) - 2\tilde{\mathsf{a}}_1(\kappa))/(\tilde{\mathsf{a}}_2(\kappa))$ equates to $\kappa/(b_2\kappa^2 + b_0)$. b_2 and b_0 are yet undetermined. The differential equation to solve becomes

$$0 = \frac{d\mathbb{P}_{\text{eq}}(\kappa)}{\mathbb{P}_{\text{eq}}(\kappa)} + \frac{\kappa}{b_2\kappa^2 + b_0}. \tag{4.50}$$

Up to a normalization pre-factor, the solution to the above differential equations reads

$$\mathbb{P}_{\text{eq}}(\kappa) \propto \left(1 + \frac{\kappa^2}{\kappa_{\text{fit}}^2}\right)^{-\delta} \tag{4.51}$$

where $\delta = (2|b_2|)^{-1}$ and $\kappa_{\text{fit}}^2 = |b_0|/|b_2|$. δ can be determined by letting $\kappa_{\text{fit}} \ll \kappa$ and investigating the resulting scaling behavior in k. This procedure gives $\delta = 11/12$. κ_{fit}^2 will be used as a small (non-dimensional) wave number which is, for our purposes, only needed to ensure the existence of a normalization constant.

The normalization prescription that $\mathbb{P}_{\text{eq}}(\kappa)$ should integrate to unity over $\mathbb{R}^+$ yields finally

$$\mathbb{P}_{\text{eq}}(\kappa) = \frac{2}{\kappa_{\text{fit}}\beta(5/12, 1/2)}\left(1 + \frac{\kappa^2}{\kappa_{\text{fit}}^2}\right)^{-\frac{11}{12}} \tag{4.52}$$

where $\beta(x, y)$ is Euler's β-function. The pre-factor of 2 stems from the one-sidedness of normalization. The probability densities in the physical variables k and $\omega \propto k^2$ are specified in the main text and obtained through successively application of the transformation theorem for probability densities [53].

Vortices   We clarify the existence of vortices at the upper labial lip. Intuitively speaking, the latter partitions the jet emanating from the windway into two halves; cf. [28] for models inspired by this observation. It functions a sharp obstacle to the free jet propagation. The incident oscillatory jet with displacement ξ given in the main text has to wiggle its way around the edges of the tip. By convection and stickiness of air, vortices emerge.

Suppose, the tip has length, say ϵ, and we choose the coordinate system defined by the direction of jet propagation and the extension of the upper labial lip's tip in transverse direction. Suppose further $\epsilon/H_0 \ll 1$ and denote the respective positions of the tip's edges by $\mathbf{r}_+$ and $\mathbf{r}_-$. Placing an air probe of mass m at a sufficiently distant position $\mathbf{r}$, the angular momentum induced on the probe should equate to zero.

Namely, the air wiggling around the edges needs to do so with opposite orientation and due to symmetry considerations, we may assume that equal portions of fluid move around each of the two edges of the tip.

Let us denote the induced velocity field by the presence of the vortices as $\mathbf{v}^{\pm}$ and assume it does only depend on the distance of the probe to the center of the respective vortex. The angular momentum condition reads

$$m(\mathbf{r} - \mathbf{r}_-) \times \mathbf{v}^-(|\mathbf{r} - \mathbf{r}_-|) + m(\mathbf{r} - \mathbf{r}_+) \times \mathbf{v}^+(|\mathbf{r} - \mathbf{r}_+|) = \mathbf{0}. \tag{4.53}$$

Introducing polar coordinates around the midpoint of $\mathbf{r}_-$ and $\mathbf{r}_+$, upon a slight dislocation of the probe closer to either of the tips, we may assume $\mathbf{r} - \mathbf{r}_{\pm} = (r \pm dr)$ where $dr > 0$ is a small length compared to R. Due to the cross product, we may take $\mathbf{v}^{\pm} \parallel \hat{e}_{\phi}$. (4.53) features only one non-trivial component, namely for the direction perpendicular to the planar coordinate system defined in the beginning of the present paragraph.

The equation under consideration turns into

$$(r - dr)v_{\phi}^-(r - dr) = -(r + dr)v_{\phi}^+(r + dr). \tag{4.54}$$

Taylor expansion up to linear order in dr and requiring the coefficients to vanish individually yields the following two equations:

$$\mathcal{O}((dr)^0): \ v_{\phi}^-(r) = -v_{\phi}^+(r), \tag{4.55}$$

$$\mathcal{O}((dr)^1): \ r\partial_r v_{\phi}^-(r) + v_{\phi}^-(r) = -(r\partial_r v_{\phi}^+(r) + v_{\phi}^+(r))). \tag{4.56}$$

The latter can be solved to yield $v_{\phi}^+(r;t) = \Gamma(t)/(2\pi \cdot r) = -v_{\phi}^-(r;t)$ where $\Gamma(t)$ originates mathematically as an integration constant and physically plays the role of a time-dependent circulation. The vorticities $\boldsymbol{\omega}^{\pm} \equiv \nabla \times \mathbf{v}^{\pm}$ in a three-dimensional cylindrical coordinate system stay zero at the present.

However, this changes as soon as we consider the total velocity field $\mathbf{v}_{\text{tot}} = \mathbf{v}_- + \mathbf{v}_+$ and let $\epsilon \to 0$ but keep $\Upsilon(t) \equiv \Gamma(t)\epsilon$ nonzero for almost all t. In physics, this is known as the point dipole limit [75].

Keeping only the dipole contribution, we find

$$v_{\text{tot}}^{\phi}(y, z; t) \simeq \frac{-\Upsilon(t)}{2\pi} \frac{y}{\sqrt{y + (z - H_0)^2}^3} \tag{4.57}$$

where y is the coordinate transverse to the coordinate along the direction of jet propagation, z. Note that the vorticity $\boldsymbol{\omega}_{\text{tot}} \equiv \nabla \times \mathbf{v}_{\text{tot}}$ does not vanish identically. Letting

$y \simeq \sqrt{y + (z - H_0)^2}$ and working in the cylindrical coordinate system introduced before, $\boldsymbol{\omega}$ points into the axial direction of the cylindrical coordinate system.

Comments   Since the axial direction is along the direction in which the upper labial lip extends physically, $\boldsymbol{\omega}$ points in azimuthal direction in the global organ pipe system. In the vortex force density contribution to the vortex acoustics equation, $\mathbf{f}_{\text{vort}} = \rho_0(\boldsymbol{\omega} \times \mathbf{V}_{\text{jet}})$ holds in acoustic linearization. Since the jet itself propagates in parallel to the symmetry axis of the organ pipe, we have $\mathbf{f}_{\text{vort}} \propto \hat{e}_r$, i.e., pointing towards the symmetry axis of the organ pipe or away from it.

The dynamics of the circulation is modeled as

$$
\begin{aligned}
\Gamma(t) &= \Gamma \int_0^\infty \frac{d\omega}{\sqrt{2\pi}} \mathbb{P}_{\text{eq}}(\omega) \exp(i\omega t) \\
&= \Gamma \left\langle \exp(i\Omega t) \right\rangle_{\Omega \sim \mathbb{P}_{\text{eq}}}
\end{aligned}
\tag{4.58}
$$

where $\mathbb{P}_{\text{eq}}$ is the probability density for the distribution of hydrodynamic, and thus acoustic, frequencies due to turbulence and has been specified in the main text.

Appendix 4.C - Nonlinear acoustic effects and filter theorem

Introduction   In this appendix section, we assess the approach to use a linear in place of a nonlinear theory. Recent approaches to the acoustics and fluid dynamics of the organ pipe focus on nonlinear effects to explain the generation of higher harmonics [38, 44, 137, 43]. Numerical studies focus on the *ab initio* solution of the governing Navier-Stokes equations for compressible flow in realistic organ pipe geometries; See [20] for a fluid dynamic perspective on the flow from an orifice.

The authors hold the opinion that a linear acoustics theory [28, 71] in conjunction with turbulence modeling [98, 53] is sufficient to explain also the generation of higher harmonics from the broadband signal generated by turbulence. Geometrical filter properties of the pipe's resonance body [28, 47] will be explained at the end of this section as well.

Lighthill's and Westervelt's equations   Let us consider the scenario that we only know that the Navier-Stokes equations [71] are valid inside the organ pipe. *Lighthill's equation* [72, 28, 90, 91] is an exact rewriting of the compressible Navier-Stokes equa-

tions and reads:

$$\partial_t^2 p - c^2 \Delta p = c^2 (\nabla \otimes \nabla) :: \mathsf{T} + \partial_t^2 (p - c^2 \rho) \tag{4.59}$$

where $\mathsf{T} \equiv \rho(\mathbf{v} \otimes \mathbf{v}) - \sigma$ denotes the *reduced Lighthill stress tensor* and σ is the *Cauchy-Navier stress tensor* storing viscous contributions to the Navier-Stokes equations.

The Lighthill's equation is a somewhat impractical place to start looking for analytic solutions. However, it forms the starting point for systematic derivations of acoustic theories.

A non-standard acoustic theory is obtained by using a quadratic equation of state that is keeping second-order effects in the last contribution on the right-hand side of the previous equation. Furthermore, thermo-acoustic damping can be included phenomenologically in the expanded form of the equation of state.

The textbook [12] result is

$$c^2 \rho = p - \frac{\gamma_{\mathrm{ad}} - 1}{2\rho_0 c^2} p^2 - \frac{\kappa_T}{\rho_0 c^2} \left(\frac{1}{c_V} - \frac{1}{c_p} \right) \frac{\partial p}{\partial t} \tag{4.60}$$

In the above equation, $\gamma_{\mathrm{ad}} = 1.4$ is the adiabtic index for a diatomic ideal gas, $\rho_0 \approx 1.2\,\mathrm{kg\ m^{-3}}$ denotes the reference mass density of air and $c \approx 343\,\mathrm{m\ s^{-1}}$ the reference speed of sound. $\kappa_T \approx 26\,\mathrm{mW \cdot (K\ m)^{-1}}$ is the thermal conductivity of air and $c_V = \gamma_{\mathrm{ad}}^{-1} c_p$, $c_p \approx 1005\,\mathrm{J(kg\ K)^{-1}}$ denote the specific heat capacities at constant volume (c_V) respectively pressure (c_p).

Thermal and viscous damping effects are assumed to be so small that they give rise to quadratic contributions. Furthermore, we keep only overall linear contribution from the reduced Lighthill stress tensor such that the contribution to the theory due to turbulence takes the form of the vortex acoustics source term $\rho_0 c^2 \nabla(\boldsymbol{\omega} \times \mathbf{V}_{\mathrm{jet}})$ where we treat $\mathbf{V}_{\mathrm{jet}}$ as a background zeroth order effect.

Following the standard derivation of the governing equation of linear acoustics through series expansion [72], the plane wave relations from linear acoustics are imposed to convert between acoustic pressure p and acoustic velocity field $\mathbf{v}$ as if the quantities were taken from a linear acoustics theory. The final result is *Westervelt's equation* with a vortex acoustics source term, the latter not being present in the textbook result [12]. The equation is given first, afterwards the parameters are specified:

$$\partial_t^2 p + \wp(-\Delta)\partial_t p - c^2 \Delta p = \aleph \partial_t^2 p^2 + \rho_0 c^2 \nabla(\boldsymbol{\omega} \times \mathbf{V}_{\mathrm{jet}}). \tag{4.61}$$

$c \approx 343 \, \text{m s}^{-1}$ denotes the speed of sound in air under reference conditions as in the corresponding linear theory. $\aleph$ is the *coefficient of nonlinearity* given through

$$\aleph = \frac{\gamma_{\text{ad}} - 1}{2\rho_0 c^2}. \tag{4.62}$$

$\wp$ is called *thermal-viscous damping coefficient* and given through

$$\wp = \frac{\lambda + 2\mu}{\rho_0} + \frac{\kappa_T}{\rho}\left(\frac{1}{c_V} + \frac{1}{c_p}\right) \tag{4.63}$$

where $\lambda = -2/3 \cdot \mu$ (by Stokes' hypothesis [71]) denotes the bulk and $\mu = 18.2 \cdot 10^{-6} \, \text{Pa s}$ denotes the shear viscosity. $\wp$ is proportional to the sound diffusivity introduced in [12].

A perturbation theory perspective on Westervelt's equation   The drawback of the Westervelt-like equation lies in its manifest nonlinearity. However, if the nonlinearity is small, one may do a perturbation theory or neglect it altogether.

The key idea is to observe that $\sim \partial_t^2 p^2$ and the usual wave equation contribution $\sim \partial_t^2 p$ both feature a double partial derivative with respect to time. We refer to the contributions as nonlinear respective linear dynamic contribution. Choosing a plane wave Ansatz for the order of magnitudes estimate, we need to assess $\aleph \|\partial_t^2 p^2\| / \|\partial_t^2 p\|$. If the expression exceeds unity, the nonlinear dynamic contribution dominates over the linear one and for values $\gg 1$, we may even neglect the usual linear dynamic contribution against the nonlinear one.

The plane-wave Ansatz yields a characteristic amplitude $p \sim (4\aleph)^{-1}$ when the linear and nonlinear dynamic contributions become equally important. Approximately, this corresponds to a sound pressure level $\text{SPL}(p = (4\aleph)^{-1} | p_{\text{ref}} = 20 \, \mu\text{Pa}) \gtrsim 200 \, \text{dB}$.

Letting the organ pipe peak at a sound pressure level $p = 120 \, \text{dB}$ for one frequency, we still have $\aleph \|\partial_t^2 p^2\| / \|\partial_t^2 p\| \approx 10^{-4}$ which is negligibly small compared to the pure linear acoustics contribution. Thus, nonlinear acoustic effects can be neglected and a linear acoustics theory is preferable.

Using Dirac perturbation theory, the nonlinear effects can be accounted for mathematically although no interesting result shows up in the present context.

Geometrical filter theorem   Upon neglection of the nonlinear contributions and damping effects, we arrive at the vortex acoustics equation as a sensible model - cf. [28] for the same view - for the acoustic wave propagation in the organ pipe: $\partial_t^2 p - c^2 \Delta p =$

$\rho_0 c^2 \nabla (\boldsymbol{\omega} \times \mathbf{V}_{\text{jet}})$. The source term has been investigated in the previous section. We focus on the filter property of the pipe interior $\mathcal{G}$.

To this end, let us investigate the quasi stationary state behavior and the more general problem

$$-\omega^2 \hat{p}_n(\omega) + \omega_n^2 \hat{p}_n(\omega) = \hat{f}_n(\omega) \tag{4.64}$$

in frequency-domain space for all mode labels n for the Neumann Laplace operator Δ. Neumann boundary conditions at the ends of the acoustic volume, to stay with the jargon introduced in the main text, have already been seen to be the most sensible choice for boundary conditions by Helmholtz. $\hat{p}_n(\omega)$ and $\hat{f}_n(\omega)$ denote the projections onto the n-th eigenfunction of the Neumann Laplacian of the frequency-domain pressure $\hat{p}(\omega, \mathbf{x})$ and the frequency-domain "dummy" input $\hat{f}(\omega, \mathbf{x})$.

Under suitable regularity assumptions on $\hat{f}_n$ and $\hat{p}_n$, the functions of a real argument can be continued uniquely to the complex plane according to the holomorphy principle. Furthermore, we can expand the fraction such as to have only simple poles in the complex plane for all eigenmodes of nonzero eigenfrequency.

Invoking Cauchy's integral theorem, the Fourier back transform becomes simple

$$p_n(t) = \sum_{s=0}^{1} \frac{(-1)^s}{2\omega_n} \int_{-\infty}^{\infty} \frac{d\omega}{2\pi} \frac{\hat{f}_n(\omega) \exp(i\omega t)}{\omega - (-1)^s \omega_n} \tag{4.65}$$

$$= \sum_{s=0}^{1} (-1)^s \frac{i}{2\omega_n} \hat{f}_n((-1)^s \omega_n) \exp((-1)^s i\omega_n t). \tag{4.66}$$

On the other hand, we can also write the "insertion of an eigenfrequency" by means of the Dirac-δ-distribution:

$$p_n(t) = i \sum_{s=0}^{1} \int_{\mathbb{R}} \frac{d\omega \, \hat{f}_n(\omega) \exp(i\omega t)}{2(-1)^s \omega} \delta(\omega - (-1)^s \omega_n) \tag{4.67}$$

where we agree on $\omega_n > 0$ and discard the constant mode due to lack of dynamics.

In this, admittedly very ideal, model, the geometry acts as a perfect δ-filter. The damping effects lead in general to a deviation from the above formula, but, even more so, the frequency resolution capabilities of the software package that we use.

The appearance of the δ-distribution inside the integral suggests us to use a Dirac sequence, say $(\delta_\epsilon)_{\epsilon > 0}$ of smooth functions, which converges to the Dirac distribution, that is, in the weak sense. The prototypical example is that of a Gaussian $\delta_\epsilon(\omega - \omega_n) \equiv (\sqrt{2\pi}\epsilon)^{-1} \exp(-(\omega - \omega_n)^2/(2\epsilon^2))$ which produces $\delta = \lim_{\epsilon \to 0} \delta_\epsilon$ in the weak limit.

This is what we call geometrical fit filter theorem because it allows us to tune the observed width of the signals' peaks in frequency space.

Comments   Via the solution of the vortex acoustics like wave equation $\partial_t^2 p - c^2 \Delta p = c^2 \nabla \mathbf{f}_v$ with $\mathbf{f}_v = \boldsymbol{\omega} \times \mathbf{V}_{\mathrm{jet}}$ in the quasi-one-dimensional approximation, the geometrical fit filter theorem becomes applicable to the quasi-stationary state of the organ pipe.

We conclude the appendix by mentioning that the Westervelt like (4.61) features a built-in cut-off similar to a second-order phase transition for weak nonlinearities (in terms of amplitude) at high frequencies. Namely, the angular frequency stored in the argument of the sinusoidal contribution to the damped wave solution reads $\sim \exp(\Xi_{\pm}(\omega)t)$ where $\Xi_{\pm}(\omega) = (\wp\omega^2 \pm \sqrt{4c^4\omega^2 - \wp^2\omega^2})/(2c^2)$. If $\omega > \omega_c \equiv 2c^2/\wp \approx 8.5\,\mathrm{GHz}$ for air, the argument of the square root turns negative and the square root takes a purely imaginary value. Due to the pre-factor i in front of the square root, this leads to an additional damping contribution. Here, the complex phase of the square root is chosen such as to exclude exponential growth of the amplitude of the pressure signal.

The imaginary part of $\Xi_{+}(\omega)$ is shown for air in Fig. 4.10 as an example. By analysis of the functional form of $\Xi_{\pm}$ and analogizing with thermodynamic potentials, $\Xi_{\pm}(\omega)$ exhibits a second-order phase transition behavior – "*Stokes-Kirchhoff phase transition*" – at $\omega = \omega_c = 2c^2/\wp$.

The consequence of the finding is that unlike the linear acoustics theories, the Westervelt theory predicts its own fail shortly before the onset of quantum mechanical scales where the classical theory should cease to be applicable altogether: An acoustic wave guide at ω_c as a reduced fundamental frequency has the length $L \approx c\pi/\omega_c \approx 127\,\mathrm{nm}$ which is still three order of magnitudes above the typical quantum mechanical length scale of $10^{-10}\,\mathrm{m}$. It is remarkable that a classical, mechanical theory exhibits this sort of consistency behavior and predicts its non-applicability at reasonably small scales.

Appendix 4.D - Mouth correction

Observation   In the top plot of Fig. 4.6, the fundamental frequency is at $f_1 \approx 258\,\mathrm{Hz}$, rounded to an integer frequency in Hertz. The organ pipe that was used to gather the data had a resonance body of length $L = 58\,\mathrm{cm}$ and a radius of $R = 2.5\,\mathrm{cm}$. A theory that builds exclusively on the end-correction $\delta_0 \approx 2/3 \cdot R$ produces a fundamental frequency $f_1 = c/(2L_{\mathrm{corr}}) \approx 288\,\mathrm{Hz}$ that is still too high. How comes?
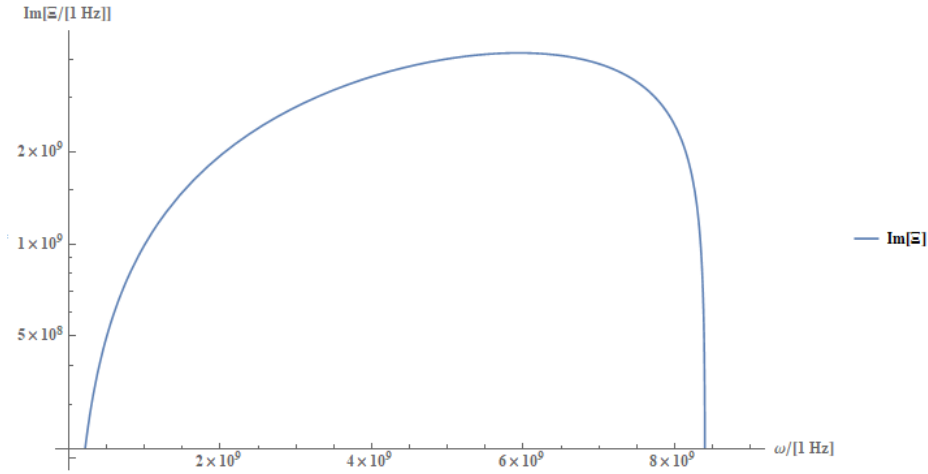
Figure 4.10: Evolution of the imaginary part of the phase "potential" $\Xi_+ = \Xi_+(\omega)$, $\Im[\Xi_+]$, as a function of the input reduced frequency $\omega \in [0\,\text{Hz}, 9\,\text{GHz}]$ plotted decadically logarithmically on the abscissa axis. At $\omega = \omega_c = 2c^2/\wp \approx 8.5\,\text{GHz}$ the imaginary part vanishes. In this case, a genuine wave behavior as stored in undulant dynamics such as $\exp(i\omega t)$ is no longer supported by the theory (4.61).

Mouth correction Phenomenologically [47, § 17.3], the end-correction δ_0 is the smaller of two corrections that lead to an acoustic "elongation" of the resonance body. In 1947, Ingerslev and Frobenius [74] derived another correction formula. Let H_0 denote the height of the labium and W_0 its width. Usually, $H_0/W_0 = 1/4$ is chosen by the organ pipe builder [47, § 17.3]. According to B. Edskes, $W_0 = q \cdot 2\pi R$ where $q = 1/4$. The rectangular labium has area $A = \sqrt{W_0 H_0}^2 = \pi^2/4(R/2)^2$. Ingerslev and Frobenius [74] specify

$$\delta_m \approx \frac{2.3 \cdot R^2}{\sqrt{A}} = \frac{9.2}{\pi} R \approx 3R. \tag{4.68}$$

such that $\delta_m \gg \delta_0$ by a factor of about 5.

Plexiglass pipe For the plexiglass pipe model under consideration, an effective length including both end- and mouth-correction, $L_{\text{eff}} = L + \delta_0 + \delta_m \approx L + 11/3R$, yields $f_{1,\text{corr}} = c/(2L_{\text{eff}}) \approx 255\,\text{Hz}$ which is close to the measured value $f_1 \approx 258\,\text{Hz}$ given in the first paragraph of this appendix section.

Chapter 5

Concluding remarks

This final chapter is devoted to a quick combined summary (section 5.1). After the collection of the results of the projects with regard to geometric perturbation theory, a short conclusion (section 5.2) is appropriate: The conclusion is intended as a verbalization of (research) intuition so that a reader may avoid some pitfalls on his quest for other phenomena generated by or generating geometric perturbations. For the sake of concreteness, future research directions, where the methods developed in the thesis can be applied, are indicated at the very end of the thesis, namely in section 5.3. Naturally, the choice of research questions is inspired by the author's individual taste.

5.1 Thesis summary

Overall summary for chapter two In chapter two, we derived a perturbation theory in the context of the ICE model to investigate Beale's acoustic boundary conditions [8, 7] from a physical mathematics viewpoint, i.e., a perspective which gives rise to concrete calculational methods. Under the assumption that the vibrations of the locally reacting surfaces in Beale's terminology, or the eardrum vibrations in Vedurmudi et al.'s jargon [147, 148, 146, 145], are suitably small compared to the characteristic axial length scale of the cavity, one can neglect the impact of the domain undulations for the solution of the model as being out of the range of acoustic linearization.

The above finding was central for the thesis as it substantiated the "stationary domain" approximation widely used in the modeling of acoustic systems. The technique of Picard iterations allowed us to decouple the, formerly coupled, equations of motion for the displacement of the locally reacting surfaces and the acoustic pressure inside

the ICE cavity. Through formal equation re-arrangement, the ICE equations were shown to admit a complete decoupling in the sense that the fixed-point iteration can be performed for each of the three ICE equations individually in the stationary domain approximation.

The piston approximation which effectively results in replacing the locally reacting surfaces at the endcaps of the ICE cavity was investigated from two different perspectives. First of all, we have seen that a "global" estimate involving the Poincaré inequality permits us to obtain an estimate for an upper bound of the relative error caused by the approximation.

The spinning mode series expansion [61] as a generalization of the modal cut-off criterion from duct acoustics allowed a numerical assessment of whether the piston approximation is the dominant contribution in the coupling between duct and membrane modes.

Overall summary for chapter three   In chapter three, we focused on the interaction of the velocity perturbation due to the tsunami and the part of the surface of the continental plate that is underwater. We derived a layer of vorticity in the framework of potential fluid mechanics slightly above the underwater part of the continental plate.

A similarity number estimate the tsunami frequency empowered us to obtain an estimated frequency band for the spinning frequencies of vorticities. The frequency band covered mostly the infrasound spectrum and did not extend significantly into frequency range audible for humans. Vortex vibration theory served as the link between physical vortices and the geometric perturbation of the continental plate: It modeled the vibrations of the surface of the plate in response to the layer of vorticity. The corresponding transverse seismic wave propagated to the shoreline and could be detected (possibly, due to lack of consensus among biologists about the precise biological pathway used for detection) by the elephant [66, 65, 63, 64].

The "seismic" explanation based on the perturbation of the surface geometry and its advantage rooted in the circumvention of the impedance mismatch for sound propagation from an underwater source to air. The water-air interface is acoustically an almost perfect reflector in the high infrasound regime of interest to elephants.

From a mechanical point of view, the expected sound-pressure level and the arrival time difference calculated and compared to (scarce) experimental data the seismic pathway is possible: The maximum arrival time difference was seen to be between

$30 \, \text{min} - 75 \, \text{min}$ which agrees with the (scarce, [159]) experimental data.

In terms of sound pressure level, reasonable parameters led to a maximum sound pressure level equivalent at the shoreline corresponding to $\sim 60 \, \text{dB}$, i.e., traffic-level noise [131]. Thus, arousal in elephants as observed by everyday observers and reported in some scientific studies due to the seismic precursor signal is plausible.

Overall summary for chapter four In chapter four, two aspects of organ pipe physics were investigated.

First, the focus was on an understanding of the geometry of the organ pipe. The notion of "acoustic volume inside the pipe" was introduced as a measure to specify when a parcel of air can be regarded as "inside" the open pipe. At the boundary of the walls of the pipe, vortices were seen to form out.

A theoretic derivation resulted in two counter-rotating vortex rings slightly inside respectively outside the pipe endcap circle. The derivation was similar to the case of elephants, but differed in the sense that it yielded two vortex rings instead of a layer of vortex dipoles. In the planar cross section model, the flow-field of the vortex dipole pair was seen to admit a sphere of separation. By simulating the flow-field, the "outside" of the pipe could be discerned from its "inside".

Counting the excess volume stored inside the sphere of separation to the acoustic volume inside the pipe, the end-correction was reproduced with the less than $10 \, \%$ error compared to the literature value [28, 88]: The physical perturbation of the air velocity caused by the edges of the open end leads to an elongation of the pipe by $\delta_0(R) = 2/3R$, i.e., causes a perturbation of the geometry of the open-ended organ pipe in the idealized picture due to Helmholtz [156].

The second aspect concerned the sound production in the organ pipe. Consensus exists on the role of the resonance body of the pipe as a passive filter element selecting the eigenfrequencies. We proposed a model based on the gradual onset of turbulence (see [132, 100] for attempts in a different physical context) of the geometric perturbation of the jet exiting the windway and propagating towards the upper labial lip. The wavenumber was interpreted as a position dependent random variable.

Via a phenomenological probability model, a broadband frequency distribution at the upper labial lip was derived. Subject to two corrections for the maximum existed frequency and to ensure realistic filter properties of the organ pipe, the recorded power spectrum (see [3] for more measurement data) of a plexiglass organ pipe was reproduced

with $\lesssim 15\,\mathrm{dB}$ maximum discrepancy and $\lesssim 10\,\mathrm{dB}$ for most of frequencies.

5.2   Conclusion: Interrelation of physical and geometric perturbations

From the projects, we have seen that perturbations of a mechanical system can happen as a consequence of a perturbation of certain geometric features and, conversely, mechanical processes can alter geometric properties of the mechanical system under consideration. Even more, the cues generated by the mechanical system convey information about the geometric perturbation.

- The latter statement is manifest in directional hearing, or more concretely, the ICE model. Without eardrum vibrations, no directional hearing cues are produced by virtue of the pressure wave inside the cavity.

  Also in organ pipes, without the geometric perturbation by the excess volume stored inside the sphere of separation, Helmholtz zeroth order guess of a stationary cylindrical cavity with Neumann boundary conditions (and the possibility of a mouth correction) would have been fully accurate. Furthermore, without the geometric perturbation to the ideal jet profile, no starting frequency would have been generated for stochastic evolution of frequencies that generate the broadband spectrum from which the pipe filters its resonance frequencies.

  Without the geometric perturbation of the surface of the continental plate, elephants would not be able to gather geometric information about how much they are in danger by the approaching tsunami.

- The conclusion named first becomes more approachable if its manifestations in concrete situations is studied.

  In organ pipes, the blowing of the organ pipe leads to the formation of a pressure wave and the generation of a vortex structure at the open end. The latter creates the sphere of generation which gives an excess volume to the organ pipe - the end-correction. On the other hand, the perturbation of the frequency of the ideal, Helmholtz open-ended organ pipe is directly implied by the change in organ pipe geometry, more precisely, the acoustic volume its resonance body encloses.

In the ICE model used to study acoustic boundary conditions as a formalization of geometric perturbation, the external perturbation given by a sound stimulus altered the geometric state of the eardrum membranes from "equilibrium position" to "oscillation of a curved surface". Precisely this information is forwarded to the interaural cavity and generates the internal pressure inside the cavity. The latter is connected to the geometric properties of the cavity in which it lives through boundary conditions and, finally, connects the vibrations of the two membranes.

In the case of cues generated by tsunamis, the momentum disturbance by the tsunami generating event manifested in the form of a layer of vorticity slightly above the continental plate. The latter perturbs the geometry of the surface of the continental plate. This information can be conveyed to and detected by the elephant.

Precisely the interplay between small changes in geometrical properties of mechanical systems and the perturbations to mechanical equilibrium processes served as the motivation for the thesis and, conversely, the thesis served as a case study of how these small changes harmonize to yield, in the author's opinion, interesting physical phenomena that can be observed in the real world and, even better, described with the aid of, both, physical techniques and geometric concepts.

5.3   Outlook

Here, different projects are proposed that could be used to push further the research presented in this thesis. The description is in some parts technical. The intention is to ease the translation process between open research question and work-flow for a reader who wants to build on this thesis. Some additional suggestions have already been sketched in the summaries of the individual chapters. We discuss some of these questions in the form of preliminary project descriptions.

How do we extend geometric perturbation theory to multi-cavity systems?
The geometric perturbation theory developed in chapter two is well-adapted to one cylindrical cavity for extraordinarily small perturbations (boundary vibration amplitudes in the nanometer range versus a cavity of typical length of centimeters). Thus two directions of investigation are immediately possible. The first question concerns a comparison of exact solutions to ICE-like coupled systems with the perturbation theory.

A former ICE-model comprised Dirichlet boundary conditions for the acoustic wave equation in radial direction and two circularly symmetric membranes covering all of the endcaps of the cavity, one at either side respectively. In this simple model case, separability of the Laplacian in cylindrical coordinates allows to reduce the partial differential equations in two and three spatial dimensions to a countably infinite number of differential equations in zero respectively one spatial dimension. Since the problem has been solved exactly already in the stationary domain approximation, the decoupling argument can be tested against the exact solution.

Second, there may not even be only one cavity but several cavities connected via membrane or plate like locally reacting surfaces. In the case of a large number of locally reacting surfaces ≥ 3 and a large number of connecting cavities ≥ 2, an extension of the systematic decoupling argument presented in chapter two would be of interest.

A possible application would be for instance directional hearing in crickets, see [145] for details on directional hearing and references specific to crickets in the outlook. Crickets feature two symmetrical cavities interfaced by a septum membrane partitioning the tracheal system into the two symmetric halves. To be even more realistic, the pressure input on the septum membrane is amplified by a horn.

Are there more tractable formulations of geometric perturbation theory in simple examples? Another question concerns a "mathematical heresy" but is interesting intuitively. Suppose, we have an elastic strip $[0, L]$ which forms the configuration space of our acoustic wave equation in response to external stimulation in time. In scenario number one, the strip-cavity supports Neumann boundary conditions at fixed end. The problem is solvable by standard techniques.

In scenario number two, the size of the cavity is can be shrunk by a small perturbation in time, that is, we let $[-x_0(t), L + x_L(t)]$ with $\|x_0(t)\|, \|x_L(t)\| \ll L$ and x_0, x_L. Suppose Neumann boundary conditions hold true. Obviously, the eigenvalue problem for the Laplacian can be solved for all fixed t and one obtains a t-parameterized family of eigenvalues and associated eigenfunctions. What coefficients $c_n(t)$ for all eigenfunctions $\psi_{n,t}(x) \propto \cos(n\pi x/L(t))$ are we to choose in $p_n(t, x) = c_n(t) \cos(n\pi x/L(t))$ with $L(t) = L + (x_0(t) + x_L(t))$ such that the equation $\partial_t^2 p_{n,t} - c^2 n^2 \pi^2/(L(t)) p_{n,t} = 0$ is fulfilled? Is there a consistent perturbation procedure to determine the c_n's?

A much more challenging question concerns to what extent the intuition of a "time-evolving" eigenvalue by "minimal substitution $\lambda_n = -n^2\pi^2/L^2 \rightarrow -n^2\pi^2/(L(t))^2 =:$

$\lambda_n(t)$ carries over to more realistic higher dimensional cavities where x_0, x_L depend also on other variables than just time.

What is the best choice for an unperturbed domain to minimize the "strength" of the perturbation operator?   As described in the appendix to chapter four, difficulties in solving partial differential equations occur already when the spatial arguments live on a time-independent but non-standard co-dimension one sub-manifold $\Omega \subset \mathbb{R}^n$. For the sake of concreteness, we stay with a membrane equation of the scalar form $\partial_t^2 u - c_m^2 \Delta u = f$. Suppose that an eigenfunction set of the Laplacian is known on a different co-dimension one sub-manifold $\Omega_0 \subset \mathbb{R}^n$ [68, 96]. Furthermore, assume that there is a sufficiently regular diffeomorphism $\Psi : \Omega_0 \to \Omega$ between the manifolds.

The perturbation theory developed in chapter two thus reduces to the case of a time-independent perturbation theory, see [122, 123, 124] for a formal discussion of time-independent perturbation theory. The formal question concerns good, or possibly even the best choice, of the reference, i.e., unperturbed manifold Ω: How are we to choose the reference manifold such as to minimize the "strength" of the perturbation operator V?

When is a geometric pertubation small in the language of operator theory? In the case of time-independent perturbations as well as time-independent perturbations, a more rigorous formulation of the geometric perturbation theory as designed in chapter two should be achievable: Suppose a time-independent or a time-dependent perturbation of the (fixed) domain Ω_0 to $\Omega(t)$ such that the involved geometric objects stay well-behaved and topological properties are preserved under the perturbation. What can be said about the perturbation operator V in the time-independent case and about $\mathsf{V}(t)$ in the time-dependent case? In particular, which requirements are needed to ensure that $\mathsf{V}(t)$ really is a perturbation operator of suitably small strength compared to the Laplacian Δ in the time-independent or the d'Alembertian $\square$ in the time-dependent case?

How does a layer of vorticity form at a surface when a fluid impinges from a non-parallel direction and what happens to the background boundary layer in this case?   A formalization of the theoretical argument leading to the vortices is desirable: Consider a two-dimensional regular and oriented surface $\Gamma \hookrightarrow \mathbb{R}^3$ diffeomorphic to a domain in $\mathbb{R}^2$. Physically, the surface shall correspond to a solid boundary.

Assume that fluid impinges on the surface with "perturbation" velocity $\mathbf{V}(t) \in \mathbb{R}^3$ at a given time $t \geq 0$ such that $\mathbf{V}(t) \not\parallel T_{\mathbf{y}}\Gamma$ for almost all $\mathbf{y} \in \Gamma$. Paralleling the derivation presented in the appendix to chapter three, one obtains that on all of Γ, small vortex dipoles should exist.

Further investigations could concern a detailed relation of the vortex dipoles to boundary layers [128], that is, considering an abrupt perturbation of a background ocean flow (with boundary layer in the vicinity of Γ) which fails to satisfy the standard no-slip boundary conditions. In other words, the perturbation should lead to a disruption of a laminar boundary layer such that the boundary layer ultimately can produce sound [72].

The author emphasizes that this project may or may not work: Little details are known about how the boundary layer actually supports the formation of acoustic respectively vortical disturbances in boundary layers.

What is the impact of geometric perturbations on the reference organ geometry on the fundamental frequencies of the pipe and the sphere of separation? An interesting application to organ pipes is the study of end-correction phenomena by smoke experiment for "perturbed" organ pipe: It is well-known that the organ pipe can change the fundamental frequency to lower respectively higher frequencies by increasing the surface area of the organ pipe at the open end or decreasing it, see [1, 136].

Given that axial wave propagation is supported in sufficiently long pipes only below the cut-off frequency $f_c = c\mu_{11}/(2\pi R)$, a one-dimensional wave equation effectively becomes a Webster equation, [131]: $\partial_t^2 p - c^2 \mathsf{D}^2 p = 0$ where $\mathsf{D}^2 = \Sigma(x)^{-1}\partial_x(\Sigma(x)\partial_x)$ is of Sturm-Liouville type and $\Sigma(x) = \pi R(x)^2$ denotes the cross-section of the pipe at distance $x \in (0, L)$ from the bottom of the resonance body. For the organ pipe practice [1, 136], $\Sigma(x)$ is non-constant only on $(L - \delta L, L)$ and R denotes the radius of the "unperturbed" pipe. The smallness of the perturbation can be encapsulated as $\partial_x\Sigma(x)/(\pi R^2/L) \ll 1$ as well as $(\Sigma(x) - \pi R^2) \ll \pi R^2$.

The question is first to what extent the eigenfrequencies $\pi^2 n^2/L^2$ of the pipe without any corrections are affected by the perturbation in cross section. The second question concerns a theoretical and experimental study of the behavior of a sphere of separation in this modified geometry, e.g., for a linear approximation of the perturbation, that is $\Sigma(x) = \pi R^2 + \delta A(x - L + \delta L)$ for $x \in (L - \delta L, L)$ and $\Sigma(x) = \pi R^2$.

It is hypothesized that a sphere of separation forms out experimentally as it did in the "unperturbed" case as long as the perturbation is sufficiently small. Given that the end-correction $\delta_0(R)/L \ll 1$ for sufficiently thin pipes, corrections to the end-correction are expected to be negligible. The mouth correction of the organ pipe is by construction not affected by the change of cross section area in the vicinity of the open end of the pipe. The impact of the perturbation operator V for the organ pipe setup then accounts for deviations of the fundamental frequency of the organ pipe modified according to the above prescription from the fundamental frequency of the conventional "unperturbed" organ pipe that was studied in chapter four.

Bibliography

[1] W. ADELUNG, *Einführung in den Orgelbau*, Breitkopf & Härtel, Wiesbaden, 2nd ed., 2003.

[2] Y. ANDO, *On the radiation of sound from a semi-infinite circular pipe of certain wall-thickness*, Acustica, 22 (1969-1970), pp. 219–225.

[3] J. ANGSTER, P. RUCZ, AND A. MIKLÓS, *Acoustics of organ pipes*, Acoustics Today, 13 (2017), pp. 10–18.

[4] B. T. ARNASON, L. A. HART, AND C. E. O'CONNELL-RODWELL, *The properties of geophysical fields and their effects on elephants and other animals*, Journal of Comparative Psychology, 116 (2002), pp. 123–132.

[5] H. AUTRUM, *Über Lautäusserungen und Schallwahrnehmungen bei Anthropoden II. Das Richtungshören von Locusta und Versuch einer Hörtheorie für Tympanalorgane vom Locustidentyp*, Zeitschrift für Vergleichende Physiologie, 28 (1940), pp. 326–352.

[6] ——, *Schallempfang bei Tier und Mensch*, Naturwissenschaften, 30 (1942), pp. 69–85.

[7] J. T. BEALE, *Spectral properties of an acoustic boundary condition*, Indiana Univerity Mathematics Journal, 25 (1976), pp. 895–917.

[8] J. T. BEALE AND S. I. ROSENCRANS, *Acoustic boundary conditions*, Bulletin of the American Mathematical Society, 80 (1974), pp. 1276–1278.

[9] J. BELL AND M. HOLMES, *Model of the dynamics of receptor potential in a mechanoreceptor*, Mathematical Biosciences, 110 (1992), pp. 139–174.

[10] S. BERGWEILER, *Körperoszillation und Schallabstrahlung akustischer Wellenleiter unter Berücksichtigung von Wandungseinflüssen und Kopplungseffekten. Verändern Metalllegierung und Wandungsprofil des Rohrresonators den Klang der labialen Orgelpfeife?*, PhD thesis, University of Potsdam, 2005.

[11] P. BIRD, *An updated digital model of plate boundaries*, G3 – Geochemistry, Geophysics, Geosystems. An electronic journal of the earth sciences., 4 (2003), pp. 1–52. doi:10.1029/2001GC000252.

[12] D. T. BLACKSTOCK AND M. F. HAMILTON, *Nonlinear Acoustics*, Academic Press, Cambridge, MA, USA, 1st ed., 1997.

[13] S. BLANES, F. CASAS, J. A. OTEO, AND J. ROS, *The Magnus expansion and some of its applications*, Physics Reports, 470 (2009), p. 151–238.

[14] ——, *A pedagogical approach to the Magnus expansion*, European Journal of Physics, 31 (2010), pp. 907–918.

[15] C. P. BONER, *Acoustic spectra of organ pipes*, Journal of the Acoustical Society of America, 10 (1938), pp. 32–40.

[16] E. BORG, *Cutaneous senses for detection and localization of environmental sound sources: A review and tutorial*, Scandinavian Audiology, 26 (1997), pp. 195–206.

[17] L. BRILLOUIN, *Remarques sur la méchanique ondulatoire*, Journal de Physique et le Radium, 7 (1926), pp. 353–368.

[18] ——, *Perturbation d'un problème de valeurs propres par déformation de la frontière*, Comptes Rendus de l'Académie des Sciences de Paris, 204 (1937), pp. 1863–1865.

[19] G. B. BROWN, *Organ pipe and edge tones*, Nature, 141 (1938), pp. 11–13.

[20] J. M. BUICK, M. ATIG, D. J. SKULINA, D. M. CAMPBELL, J. P. DALMONT, AND J. GILBERT, *Investigation of nonlinear acoustic losses at the open end of a tube*, Journal of the Acoustical Society of America, 129 (2011), pp. 1261–1272.

[21] C. A. BURK AND C. L. DRAKE, eds., *Geology of Continental Margins*, Springer, Berlin, 1974.

[22] N. Cabrera, *Sur la perturbation d'un problème de valeurs propres par déformation de la frontière*, Comptes Rendus de l'Académie des Sciences de Paris, 208 (1938).

[23] ——, *Perturbation par changement des conditions aux limites*, Cahiers de Physique, 31 (1948), pp. 24–62.

[24] V. Casarino, K.-J. Engel, R. Nagel, and G. Nickel, *A semigroup approach to boundary feedback systems*, Integral Equations and Operator Theory, 47 (2003), pp. 289–306.

[25] V. Casarino, K.-J. Engel, R. Nagel, and S.Piazerra, *Decoupling techniques for wave equations with dynamic boundary conditions*, Discrete and Continuous Dynamical Systems, 12 (2005), pp. 761–772.

[26] F. Casas, *Sufficient conditions for the convergence of the Magnus expansion*, Journal of Physics A: Theoretical and Mathematical, 40 (2007), pp. 1–17.

[27] M. Cavaillé-Coll, *Etudes expérimentales sur les tuyaux d'orgue: De la détermination des dimensions des tuyaux en rapport avec l'intonation des mêmes tuyaux*, Comptes Rendus Hebdomadaires des Séances de l'Académie des Sciences, 55 (1860), pp. 176–180.

[28] A. Chaigne and J. Kergomard, *Acoustics of Musical Instruments*, Springer, New York, 1st ed., 2016.

[29] J. Christensen-Dalsgaard, *Directional hearing in non-mammalian tetrapods*, in Sound Source Localization, A. N. Popper and R. R. Fay, eds., Springer Handbook in Auditory Research, Springer, New York, 2005, pp. 67–123.

[30] J. Christensen-Dalsgaard, Y. Tang, and C. E. Carr, *Binaural processing by the gecko auditory periphery*, Journal of Neurophysiology, 105 (2011), pp. 1992–2004.

[31] J. W. Coltman, *Sounding mechanism of the flute and organ pipe*, Journal of the Acoustical Society of America, 44 (1968), pp. 983–992.

[32] ——, *Jet drive mechanisms in edge tones and organ pipes*, Journal of the Acoustical Society of America, 60 (1976), pp. 725–733.

[33] L. Crocco, *Eine neue Stromfunktion für die Erforschung der Gase mit Rotation*, ZAMM - Journal of Applied Mathematics and Mechanics, 17 (1937), pp. 1–7.

[34] P. A. M. Dirac, *Quantum Mechanics*, Oxford University Press, Oxford, 4th ed., 1958.

[35] S. A. Elder, *On the mechanism of sound production in organ pipes*, Journal of the Acoustical Society of America, 54 (1973), pp. 1554–1564.

[36] ——, *The mechanism of sound production in organ pipes and cavity resonators*, Journal of the Acoustical Society of Japan (E), 13 (1992), pp. 11–23.

[37] M. Escudé, M. K. Rigozzi, and E. M. Terentjev, *How cells feel: Stochastic model for a molecular mechanosensor*, Journal of Biophysics, 106 (2014), pp. 124–133.

[38] B. Fabre, *Sound production in flute-like instruments: Aeroacoustic modeling and time-domain simulation*, PhD thesis, Université du Maine, Le Mans, 1992.

[39] H. Feshbach, *On the perturbation of boundary conditions*, Physical Review Letters, 65 (1944), pp. 307–318.

[40] J. E. Ffowcs Williams, *The acoustics analogy - thirty years on.*, IMA Journal of Applied Mathematics, 32 (1984), pp. 113–124.

[41] J. E. Ffowcs Williams and D. L. Hawkings, *Sound generated by turbulence and surfaces in arbitary motion*, Philosophical Transactions of the Royal Society of London, A264 (1969), pp. 321–342.

[42] N. H. Fletcher, *Auditory patterns*, Reviews of Modern Physics, 12 (1940), pp. 47–65.

[43] ——, *Nonlinear interactions in flue organ pipes*, Journal of the Acoustical Society of America, 56 (1974), pp. 645–652.

[44] ——, *Jet-drive mechanism in organ pipes*, Journal of the Acoustical Society of America, 60 (1976), pp. 481–483.

[45] ——, *Sound production by organ flue pipes*, Journal of the Acoustical Society of America, 60 (1976), pp. 929–936.

[46] ——, *Harmonic generation in organ pipes, recorders and flutes*, Annual Review of Fluid Mechanics, 11 (1979), pp. 123–146.

[47] N. H. Fletcher and T. D. Rossing, *The Physics of Musical Instruments*, Springer, New York, 2nd (reprinted) ed., 2010.

[48] A. Friedmann, *An essay on hydrodynamics of compressible fluid*, University of St. Petersburg (Petrograd), St. Petersburg (Petrograd), 1st ed., 1922.

[49] H. Froehlich, *A solution of the Schrödinger equation by a perturbation of the boundary conditions*, Physical Review Letters, 54 (1938), p. 945.

[50] C. G. Gal, G. R. Goldstein, , and J. A. Goldstein, *Oscillatory boundary conditions for acoustic wave equations*, Journal of Evolution Equations, 3 (2003), pp. 623–635.

[51] M. Garces and A. Le Pichon, *Encyclopaedia of complexity and systems science*, Springer, 2009, pp. 4839–4855.

[52] ——, *Extreme environmental events - Complexity in forecasting and early warning*, Springer, 2011, pp. 663–679.

[53] S. Gardiner, *Stochastic Methods: A Handbook for the Natural and Social Sciences*, Springer, New York, 4th ed., 2009.

[54] M. Garstang, *Precursor tsunami signals detected by elephants*, The open conservation biology journal, 3 (2009), pp. 1–3.

[55] M. Garstang, D. Larom, and M. Raspet, R.and Lindeque, *Atmospheric controls on elephant communication*, Journal of Experimental Biology, 198 (1995), pp. 939–951.

[56] O. A. Godin, *Sound transmission through water–air interfaces: New insights into an old problem*, Journal of Contemporary Physics, 49 (2008), pp. 105–123.

[57] ——, *Low frequency sound transmission through a gas-solid interface*, Journal of the Acoustical Society of America, 129 (2011), pp. EL45–EL51.

[58] M. G. Gross, *Oceanography - A View on the Earth*, Prentice Hall, Upper Saddle River, NJ, 7th ed., 1995.

[59] R. H. Günther, C. E. O'Connell-Rodwell, and S. L. Klemperer, *Seismic waves from elephant vocalizations: A possible communication mode*, Geophysical Research Letters, 31 (2004), p. L11602.

[60] S. Hassani, *Mathematical Physics: An Introduction to its Foundations*, Springer, Berlin, 2 ed., 2013.

[61] D. T. Heider, *Störungstheoretische Behandlung zeitabhängiger Randwertprobleme aus der Akustik - Perturbative treatment of time-dependent boundary value problems from acoustics*, Master's thesis, Technische Universität München & Ludwig-Maximilians-Universität München, 2014/2015.

[62] P. Hertel, *Continuum Physics*, Springer, Berlin, 2012.

[63] P. S. M. Hill, *Vibration as a communication channel. A symposium*, American Zoologist, 41 (2001), pp. 1133–1240.

[64] ——, *Vibrational Communication in Animals*, Cambridge University Press, Cambridge, 1 ed., 2008.

[65] ——, *How do animals use substrate-borne vibrations as an information source?*, Naturwissenschaften, 96 (2009), pp. 1355–1371.

[66] P. S. M. Hill and P. Wessel, *Biotremology*, Current Biology, 26 (2016), pp. R181–R191.

[67] D. K. Holger, T. A. Wilson, and G. S. Beavers, *Fluid mechanics of the edge-tone*, Journal of the Acoustical Society of America, 62 (1977), pp. 1116–1128.

[68] B.-Y. Hou and B.-Y. Hou, *Differential Geometry for Physicists*, World Scientific, Singapore, 1997.

[69] M. S. Howe, *Contributions to the theory of aerodynamic sound, with applications to excess jet noise and the theory of the flute*, Journal of Fluid Mechanics, 71 (1975), pp. 625–673.

[70] ——, *The compression wave produced by a high-speed train entering a tunnel*, Proceedings of the Royal Society of London A - Mathematical, Physical and Engineering Sciences, 454 (1998), p. 1974.

[71] ——, *Hydrodynamics and Sound*, Cambridge University Press, Cambridge, 1st ed., 2006.

[72] ——, *Acoustics and Aerodynamic Sound*, Cambridge University Press, Cambridge, 1st ed., 2014.

[73] G. A. HUFFORD, *An integral equation approach to the problem of wave propagation over an irregular surface*, Quarterly of Applied Mathematics, 9 (1952), pp. 391–404.

[74] F. INGERSLEV AND W. FROBENIUS, *Some measurements of the endcorrections and acoustic spectra of cylindrical open flue organ pipes*, Transactions of the Danish Academy of Technical Science, 1 (1947), pp. 1–44.

[75] J. D. JACKSON, *Classical Electrodynamics*, Wiley, Hobolen, NJ, USA, 3rd ed., 1998.

[76] V. A. JACKSON, *Panic in elephants during an earthquake*, Journal of Bombay Natural Historic Society, 26 (1918), p. 285.

[77] D. D. JOYCE, *On manifolds with corners*, (2009). https://arxiv.org/abs/0910.3518.

[78] ——, *A generalization of manifolds with corners*, (2016). https://arxiv.org/abs/1501.00401.

[79] ——, *On manifolds with analytic corners*, (2016). https://arxiv.org/abs/1605.05913.

[80] R. KIND, A. RAVELOSON, F. WANG, AND X. YUAN, *Seismic and infrasound signals from the 2004 Sumatra-Andaman and the 2011 Tohoku-Oki tsunamis*, Geophysical Research Abstracts, 15 (2013), pp. EGU2013–2263).

[81] A. N. KOLMOGOROV, *Dissipation of energy in locally isotropic turbulence*, Proceedings of the Royal Society of London A - Mathematical, Physical and Engineering Sciences, 434 (1991), p. 15.

[82] ——, *The local structure of turbulence in incompressible viscous fluid for very large Reynolds numbers*, Proceedings of the Royal Society of London A - Mathematical, Physical and Engineering Sciences, 434 (1991), p. 9.

[83] G. A. KRIEGSMANN, A. NORRIS, AND E. L. REISS, *Acoustic scattering by baffled membranes*, Journal of the Acoustical Society of America, 75 (1984), pp. 685–694.

[84] ——, *Acoustic pulse scattering by baffled membranes*, Journal of the Acoustical Society of America, 79 (1986), pp. 1–8.

[85] C.-H. KRUTZSCH, *Über eine experimentell beobachtete Erscheinung an Wirbelringen in ihrer translatorischen Bewegung durch wirkliche Flüssigkeiten*, Annalen der Physik, 35 (1939), pp. 497–523.

[86] B. LAUTRUP, *Physics of Continuous Matter: Exotic and Everyday Phenomena in the Macroscopic World*, Taylor & Francis, New York, 2nd ed., 2011.

[87] B. W. LEVIN AND M. NOSOV, *Physics of Tsunamis*, Springer, New York, 2008.

[88] H. LEVINE AND J. SCHWINGER, *On the radiation of sound from an unflanged circular pipe*, Reviews of Physics, 73 (1948), pp. 383–406.

[89] D. LI, C. C. DOUGLAS, T. KAKO, S. MASABUMI, AND H. ICHIRO, *A novel perturbation expansion method for coupled system of acoustics and structures*, Computers and Mathematics with Applications, 51 (2006), pp. 1689–1704.

[90] M. J. LIGHTHILL, *On sound generated aerodynamically I. General theory.*, Proceedings of the Roal Society London A, 211 (1952), pp. 564–587.

[91] ——, *On sound generated aerodynamically II. Turbulence as a source of noise.*, Proceedings of the Royal Society London A, 222 (1954), pp. 1–32.

[92] H. MARKL, *Vibrational communication*, in Neuroethology and behavioral physiology, Springer, 1983, pp. 332–353.

[93] T. MAXWORTHY, *The structure and stability of vortex rings*, Journal of Fluid Mechanics, 51 (1972), pp. 15–32.

[94] ——, *Turbulent vortex rings - With an appendix on an extended theory of laminar vortex rings*, Journal of Fluid Mechanics, 64 (1974), pp. 227–240.

[95] P. C. MOAN AND J. NIESEN, *Convergence of the Magnus expansion*, Foundations of Computer Mathematics, 8 (2008), pp. 291–301.

[96] M. NAKAHARA, *Geometry, Topology and Physics*, Francis & Taylor, London, 2nd ed., 2003.

[97] P. M. NARINS, E. R. LEWIS, J. J. JARVIS, AND J. O'RIAIN, *The use of seismic signals by fossorial southern African mammals: A neuroethological gold mine*, Brain Research Bulletin, 44 (1997), pp. 641–646.

[98] S. NAZARENKO, *Wave Turbulence*, Springer, New York, 1st ed., 2011.

[99] F. NICHOLLS, *Effects of earthquakes on elephants*, Journal of Bombay Natural Historic Society, 53 (1955), p. 585.

[100] D. NICKELSEN, *Markov processes linking thermodynamic and turbulence*, PhD thesis, Universität Oldenbourg, 2014.

[101] M. NITSCHE AND R. KRASNY, *A numerical study of vortex ring formation at the edge of a circular tube*, Journal of Fluid Mechanics, 276 (1994), pp. 139–161.

[102] C. E. O'CONNEL-RODWELL, P. M. NARINS, AND N. LOSIN, *Seismic and vibrational signals in animals*, Encyclopedia of Neuroscience, 8 (2009), pp. 555–559.

[103] C. E. O'CONNELL, B. T. ARNASON, AND L. A. HART, *Seismic transmission of elephant vocalizations and movement*, PhD thesis, ASA, 1997.

[104] C. E. O'CONNELL-RODWELL, *Keeping an ¨ear¨ to the ground: Seismic communication in elephants*, Physiology, 22 (2007), pp. 287–294.

[105] ——, *The use of vibrations in communication: Properties, mechanisms and function across taxa*, Transworld Research Network, Kerala, India, 2010.

[106] C. E. O'CONNELL-RODWELL, B. T. ARNASON, AND L. A. HART, *Seismic properties of Asian elephant (Elephans maximus) vocalizations and locomotion*, Journal of the Acoustical Society of America, 108 (2000), pp. 3066–3072.

[107] C. E. O'CONNELL-RODWELL, L. A. HART, AND B. T. ARNASON, *Exploring the potential use of seismic waves as a communication channel by elephants and other large mammals*, American Zoologist, 41 (2001), pp. 1157–1170.

[108] C. E. O'CONNELL-RODWELL, J. D. WOOD, C. KINZLEY, T. C. RODWELL, J. H. POOLE, AND S. PURIA, *Wild African elephants (Loxodonta africana) discriminate seismic alarm calls of familiar versus unfamiliar conspecifics*, Journal of the Acoustical Society of America, 122 (2007), pp. 823–830.

[109] C. E. O'CONNELL-RODWELL, J. D. WOOD, T. C. RODWELL, S. PURIA, S. R. PARTAN, R. KEEFE, D. SHRIVER, B. T. ARNASON, AND L. A. HART, *Wild elephant (Loxodonta africana) breeding herds respond to artificially transmitted seismic stimuli*, Behavioral Ecolog and Sociobiology, 59 (2006), pp. 842–850.

[110] C. E. O'CONNELL-RODWELL, J. D. WOOD, M. WYMAN, S. REDFIELD, S. PURIA, AND L. A. HART, *Antiphonal vocal bouts associated with departures in free-ranging African elephant family groups (Loxodonta africana)*, Bioacoustics, 21 (2012), pp. 215–224.

[111] E. A. OKAL, *Advances in geophysics Vol. 49*, Springer, 2008, ch. Generation of T-waves by earthquakes, pp. 1–65.

[112] J. PAN AND D. A. BIES., *The effect of fluid-structural coupling on sound waves in an enclosure – Experimental part*, Journal of the Acoustical Society of America, 87 (1990), pp. 708–717.

[113] ——, *The effect of fluid-structural coupling on sound waves in an enclosure – Theoretical part*, Journal of the Acoustical Society of America, 87 (1990), pp. 691–707.

[114] K. PEARSON, *Contributions to the mathematical theory of evolution*, Proceedings of the Royal Society, 54 (1893), pp. 329–333.

[115] ——, *Contributions to the mathematical theory of evolution, II: Skew variation in homogeneous material*, Philosophical Transactions of the Royal Society, 186 (1895), pp. 343–414.

[116] ——, *Mathematical contributions to the theory of evolution, X: Supplement to a memoir on skew variation*, Philosophical Transactions of the Royal Society A - Mathematical, Physical and Engineering Sciences, 197 (1901), pp. 443–459.

[117] ——, *Mathematical contributions to the theory of evolution, XIX: Second supplement to a memoir on skew variation*, Philosophical Transactions of the Royal Society A - Mathematical, Physical and Engineering Sciences, 216 (1916), pp. 429–457.

[118] P. R. Pinet, *An Invitation to Oceanography*, Jones and Bartlett Learning, Burlington, MA, 6th ed., 2012.

[119] A. Powell, *On the edgetone*, Journal of the Acoustical Society of America, 33 (1961), pp. 395–406.

[120] ——, *Theory of vortex sound*, Journal of the Acoustical Society of America, 36 (1964), p. 177.

[121] F. Press and M. Ewing, *Ground roll coupling to atmospheric compressional waves*, Geophysics, 16 (1951), pp. 416–430.

[122] M. C. Reed and B. Simon, *Methods of Modern Mathematical Physics I: Functional Analysis*, Academic, San Diego, CA, 1972.

[123] ——, *Methods of Modern Mathematical Physics II: Fourier Analysis, Self-Adjointness*, Academic, San Diego, CA, 1975.

[124] ——, *Methods of Modern Mathematical Physics IV: Analysis of Operators*, Academic, San Diego, CA, 1978.

[125] T. Reuter, S. Nummela, and S. Hemilä, *Elephant hearing*, The Journal of the Acoustical Society of America, 104 (1998), pp. 1122–1123.

[126] O. Reynolds, *Papers on mechanical and physical subjects-the sub-mechanics of the Universe, Collected Work, Volume III*, Cambridge University Press, Cambridge, 1903.

[127] S. Rienstra and M. Hirschberg, *An Introduction to Acoustics*, tech. rep., Eindhoven University of Technology, 2017. https://www.win.tue.nl/ sjoerdr/papers/boek.pdf.

[128] H. Schlichting and K. Gersten, *Boundary Layer Theory*, Springer, Berlin, 9th ed., 2016.

[129] U. S. Schwarz, T. Erdmann, and I. B. Bischofs, *Focal adhesions as mechanosensors: The two-spring model*, Biosystems, 83 (2006), pp. 225–232.

[130] M. Shearer and R. Levy, *Partial Differential Equations: An Introduction to Theory and Applications*, Princeton University Press, Princeton, 2015.

[131] E. J. Skudrzyk, *Foundations of Acoustics: Basic Mathematics and Basic Acoustics*, Springer, Berlin, 1971.

[132] R. Stresing, *Stochastic analysis of turbulence*, PhD thesis, Universität Oldenbourg, 2010.

[133] J. W. Strutt (Lord Rayleigh), *Scientific Papers Vol. I.*, Cambridge University Press, Cambridge, 1899.

[134] C. E. Synolakis, *Tsunami rump on deep slopes - How good linear theory really is*, Natural Hazards, 4 (1991), pp. 221–234.

[135] S. Temkin, *Elements of Acoustics*, Wiley, New York, 1981.

[136] N. Thistlethwaite and G. Webber, eds., *The Cambridge Companion to the Organ*, Cambridge University Press, Cambridge, 2003.

[137] S. Thwaites and N. H. Fletcher, *Harmonic generation in organ pipes, recorders and flutes*, Journal of the Acoustical Society of America, 68 (1980), pp. 767–771.

[138] S. Timoshenko and J. N. Goodier, *Theory of Elasticity*, McGraw-Hill Education (India), Noida, IN, 3 ed., 2010.

[139] S. Timoshenko and S. Woinowsky-Krieger, *Theory of Plates and Shells*, McGraw-Hill College, New York, USA, 2 ed., 1959.

[140] J. L. van Hemmen, *Acoustic Boundary-Condition Dynamics and Internally Coupled Ears*, SIAM News, 49/8 (2016), pp. 1–3.

[141] J. L. van Hemmen, J. Christensen-Dalsgaard, C. E. Carr, and P. M. Narins, *Animals and ICE: Meaning, origin and diversity*, Biological Cybernetics, 110 (2016), pp. 237–246.

[142] J. L. van Hemmen and C. Leibold, *Elementary excitations of biomembranes: Differential geometry of undulations in elastic surfaces*, Physics Reports, 444 (2007), pp. 51–99.

[143] ———, *Elementary excitations of biomembranes: Differential geometry of undulations in elastic surfaces*, Physics Reports, 444 (2007), pp. 51–99.

[144] V. V. Vasil'ev, S. Krein, and S. I. Piskarev, *Operator semigroups, cosine operator functions, and linear differential equations*, Journal for Soviet Mathematics, 54 (1991), pp. 1042–1129.

[145] A. P. Vedumurdi, *General Aspects of Sound Localization through Intenally Coupled Ears*, PhD thesis, Technische Universität München, 2018.

[146] A. P. Vedurmudi, J. Christensen-Dalsgaard, and J. L. van Hemmen, *Modeling underwater hearing and sound localization in the frog Xenopus laevis*, Journal of the Acoustical Society of America, 144 (2018), pp. 3010–3021.

[147] A. P. Vedurmudi, J. Goulet, J. Christensen-Dalsgaard, B. A. Young, R. Williams, and J. L. van Hemmen, *How internally coupled ears generate temporal and amplitude cues for sound localization*, Physical Review Letters, 116 (2016), p. 028101.

[148] A. P. Vedurmudi, B. Young, and J. L. van Hemmen, *Internally coupled ears: Mathematical structures and mechanisms underlying ICE*, Biological Cybernetics, 110 (2016), pp. 359–382.

[149] M. P. Verge, *Aeroacoustics of confined jets with applications to the physical modeling of recorder-like instruments*, PhD thesis, Eindhoven University of Technology, 1995.

[150] M. P. Verge, R. Caussé, B. Fabre, A. Hirschberg, A. P. J. Wijnands, and A. van Steenberge, *Jet oscillations and jet drive recorder-like instruments*, Acustica Acta Acustica, 2 (1994), pp. 403–419.

[151] M. P. Verge, B. Fabre, A. Hirschberg, and A. P. J. Wijnands, *Sound production in recorder-like instruments I. Dimensionless amplitude of the internal acoustic field*, Journal of the Acoustical Society of America, 101 (1997), pp. 2914–2924.

[152] M. P. Verge, B. Fabre, and A. Mahu, W. E. A. Hirschberg, *Feedback excitation mechanism in organ pipes*, Journal of the Acoustical Society of America, 95 (1994), pp. 1119–1132.

[153] M. P. Verge, B. Fabre, W. E. A. Mahu, A. Hirschberg, R. R. van Hassel, A. P. J. Wijnands, J. J. de Vries, and C. J. Hogendoor, *Jet formation and jet velocity fluctuations in a flue organ pipe*, Journal of the Acoustical Society of America, 95 (1994), pp. 1119–1132.

[154] R. T. Verrillo, *Psychophysics of vibrotactile stimulation*, Journal of the Acoustical Society of America, 77 (1985), pp. 225–232.

[155] M. Vojtja and G. Vojtja, *Teubner-Taschenbuch der statistischen Physik*, B. G. Teubner, Stuttgart, 2000.

[156] H. von Helmholtz, *Theorie der Luftschwingungen in Röhren mit offenen Enden*, Journal für die reine und die angewandte Mathematik, 57 (1860), pp. 1–72.

[157] C. Vossen, *Auditory Information Processing in Systems with Internally Coupled Ears*, PhD thesis, Technische Universität München, 2010.

[158] C. Vossen, J. Christensen-Dalsgaard, and J. L. van Hemmen, *Analytical model of internally coupled ears*, Journal of the Acoustical Society of America, 128 (2010), pp. 909–918.

[159] E. Wikramanayake, P. Fernando, and P. Leimgruber, *Behavioral response of satellite collared elephants to the tsunami in southern Sri Lanka*, Biotropica, 38 (2006), pp. 775–777.

[160] H. Woith, G. M. Petersen, S. Hainzl, and T. Dahm, *Review: Can animals predict earthquakes?*, Bulletin of the Seismological Society of America, 108 (2018), pp. 1031–1045.

[161] S. Yoshikawa, *Harmonic generation mechanism in organ pipes*, Journal of the Acoustical Society of Japan (E), 5 (1984), pp. 17–29.

[162] S. Yoshikawa and J. Saneyoshi, *Feedback excitation mechanism in organ pipes*, Journal of the Acoustical Society of Japan (E), 1 (1980), pp. 175–191.

LEBENSLAUF DAVID THOMAS HEIDER

PERSÖNLICHE DATEN

Name, Vornamen	Heider, David Thomas
Geburtsdatum	23.04.1993
EMail	davidthomasheider@online.de

AUSBILDUNG

Okt. 2016 – Mär. 2020	Studium Lehramt Gymnasium Mathematik & Physik
	Ludwig-Maximilians-Universität München
	(Universitäre Note Mathematik 1,16 & Physik 1,91)
Mär. 2016 – Jun. 2019	Promotion in Theoretischer Physik
	Technische Universität München (Bestanden)
Okt. 2011 – Sep. 2015	Studium Physik (BSc, Note 2,02 & MSc, Note 1,41)
	Ludwig-Maximilians-Universität München
Sep. 2003 – Jul. 2011	Abitur (Sprachlicher Zweig, Note 1,2)

BERUFSERFAHRUNG[1]

01. Aug. 2019 – 30. Sep. 2019	Praktikum im Bereich Corporate Underwriting
	Munich Re (Group)
15. Mai 2019 – 14. Sep. 2019	E-Learning Tutor (Theoretische Physik)
	Ludwig-Maximilians-Universität München
01. Okt. 2018 – 30. Sep. 2019	Tutor & Korrektor (Mathematik)
	Ludwig-Maximilians-Universität München
01. Mär. 2016 – 14. Jun. 2019	Doktorand in Theoretischer Physik
	Technische Universität München, T35
01. Aug. 2017 – 30. Sep. 2017	Praktikum im Vertrieb

---

[1]Verpflichtende Praktika im Studium an Schulen bzw. im Labor sind nicht aufgeführt.

	H. Hugendubel GmbH, Filliale München Stachus
01. Apr. 2017 – 31. Mär. 2018	Tutor & Korrektor (Theoretische Physik)
	Ludwig-Maximilians-Universität München (Sommer)
	Technische Universität München (Winter)
01. Jul. 2016 – 30. Sep. 2016	Wissenschaftliche Hilfskraft Software-Entwicklung
	Ludwig–Maximilians-Universität München
15. Sep. 2015 – 15. Mär. 2016	Forschungspraktikum AdS/CFT
	Ludwig-Maximilians-Universität München
02. Sep. 2013 – 27. Sep. 2013	Forschungspraktikum Physik
	Technische Universität München, E15
01. Apr. 2012 – 30. Sep. 2012	Studentische Hilfskraft (Theoretische Physik)
	Ludwig-Maximilians-Universität München
11. Aug. 2011 – 30. Aug. 2011	Praktikum angewandte Statistik
	Bayerisches Landesamt für Statistik und Datenverarbeitung (BayLfStaD)
23. Aug. 2009 – 07. Sep. 2009	Schülerpraktikum Physik
	Technische Universität München, E15

Sprachen[2]

Deutsch	Muttersprache (C2)
Englisch	Verhandlungssicher (C1)
Französisch	Gut (B1)

IT

| MS Word, MS Powerpoint, LaTeX inkl. Beamer, Mathematica, Python | Fortgeschritten |
| LabView, C++ inkl. Root | Grundkenntnisse |

---

[2]Sprachniveaus laut Abiturzeugnis.

Sonstiges

Biophysik	Zertifikat Schwerpunktstudium MSc Physik
Medizinphysik	Nebenfach zur Biophysik
Erster Platz beim Science Slam	74. Kick-Off Seminar TUM Graduate School, Gruppe "Elephantastic" – Tsunami-Ortung in Elefanten, Preis: 15 € -Gutschein für "Hans-Im-Glück"
Model United Nations	Teilnahme an 3 Model United Nations Konferenzen in München, Stuttgart und Amsterdam in Q11/Q12.